

UC Berkeley

UC Berkeley Electronic Theses and Dissertations

Title

Electronic Tunings in Biomimetic Iron Complexes for Small Molecule Activation

Permalink

<https://escholarship.org/uc/item/3vj7h7sj>

Author

Chantarojsiri, Teera

Publication Date

2015

Peer reviewed|Thesis/dissertation

Electronic Tunings in Biomimetic Iron Complexes for Small Molecule Activation

By

Teera Chantarojsiri

A dissertation submitted in partial satisfaction of the

requirements for the degree of

Doctor of Philosophy

in

Chemistry

in the

Graduate Division

of the

University of California, Berkeley

Committee in Charge:

Professor Christopher J. Chang, Chair

Professor Jeffrey R. Long

Professor Seung-wuk Lee

Summer 2015

Abstract

Electronic Tunings in Biomimetic Iron Complexes for Small Molecule Activation

By Teera Chantarojsiri

Doctor of Philosophy in Chemistry

University of California, Berkeley

Professor Christopher J. Chang, Chair

The ever-increasing global energy consumption drives the search for sustainable, alternative, carbon-neutral energy sources. Chemists approach these problems taking inspiration from nature, which utilizes various metalloenzymes for different types of small molecule activations, including proton reduction (hydrogenases), water oxidation (oxygen-evolving complexes), methane oxidation (methane monooxygenases), and carbon dioxide fixation (carbon monoxide dehydrogenases). Several small-molecule model systems have been developed to mimic the reactivity and structures of active sites in these enzymes. The main advantage of molecular inorganic catalysts in this vein includes the ability to chemically modify the electronic properties of the molecule, eliciting changes in physical properties and catalytic reactivity. Using traditional synthetic methods, the reactivity of the modified catalysts can be studied in order to elucidate the mechanisms of small molecule transformations. Iron (Fe) complexes are also good candidates due to iron's high abundance in the earth crust and rich redox reactivity.

For hydrocarbon oxidation, high-valent iron-oxo intermediates play important roles in both chemical and biological oxidations. Their rich reactivity inspires the development of synthetic analogs, especially Fe(IV)-oxo complexes. In contrast to their enzymatic counterparts, however, the vast majority of biomimetic Fe(IV)-oxo complexes have been prepared and studied in organic solution. A series of water-soluble Fe complexes supported by PY5Me₂-X ligand with substituents on the axial pyridine (X = -NMe₂, -Me, -H and -CF₃) were synthesized to study the ligand's electronic effects their oxidative reactivity. Crystal structures of Fe(II) complexes showed small variation in bond lengths between different derivatives. Mössbauer spectroscopy confirmed the identity of Fe(II) and small variation in electronic properties as the quadrupole splitting increase as the electron-donating ability of the ligand increase. Electrochemical studies of [Fe(L)(PY5Me₂-X)]²⁺ in MeCN and water showed drastic decrease of Fe(III/II) redox potentials (300 mV in MeCN and 200 mV in water when changing substituents from electron-withdrawing (-CF₃) to electron-donating group (-NMe₂) and linear correlation with Hammett parameters (σ_p). We observe that Fe(III/II) redox potentials also significantly less positive in aqueous media, resulting from the proton-coupled electron transfer process.

Oxidation in water using outersphere oxidant, cerium ammonium nitrate (CAN), produced clean Fe(IV)-oxo species, verified by UV-vis and Mössbauer Spectroscopy. Fe(IV)-oxo species produced is stable in water at room temperature for 2 hours with an exception of -NMe₂ derivatives as its Fe(IV)-oxo species is only detectable transiently at low temperature by mass spectrometry. Labeling study with H₂¹⁸O showed a m/z shift of 1 Da in mass spectrometry of ¹⁸O-labeled Fe(IV)-oxos and a peak shift in IR which corresponds to the harmonic oscillator model, proving that the water is the source of oxygen atom. Furthermore, Fe(IV)-oxo can also be

generated photochemically using $\text{Ru}(\text{bpy})_3^{2+}$ as a photosensitizer, $\text{K}_2\text{S}_2\text{O}_8$ as a sacrificial quencher and 13 W blue CFL light bulb as a light source. Photochemically-generated Fe(IV)-oxo can be used to probe oxidative reactivity by hydrocarbon oxidation in aqueous solution. Three substrates were used to evaluate oxidative reactivity of each derivatives: benzyl alcohol, 4-ethylbenzene sulfonate sodium salt, and 4-styrenesulfonate sodium salt. Second-order rate constants were measured by observing decay of the characteristic Fe(IV)-oxo signature centered at 710 nm in the UV-vis spectra upon substrate oxidation. Among this systematic series, we observe that the $[\text{Fe}^{\text{IV}}(\text{O})\text{PY5Me}_2\text{-X}]^{2+}$ derivative containing the most electron-withdrawing group, the $-\text{CF}_3$ congener, shows the fastest rates of oxidation for both HAT and OAT reactions with the substrates tested. Reaction rate differences also correlate to Hammett parameters (σ_p) of the ligand's substituents.

Extending the concept of biomimetic chemistry, Fe complexes that mimic heme enzymes were studied as a CO_2 reduction catalyst as Fe porphyrins have been demonstrated to reduce CO_2 electrochemically. Square planar Fe salen complexes were synthesized and characterized for their CO_2 reactivity. Unlike the porphyrins, these ligands can be synthesized in large scale and easily tuned the electronics by changing substituents. Exploring redox reactivity of Fe salen complexes electrochemically under Ar reveals a Fe(II/I) redox couple for all the complexes in that family that shifts more positive upon substitution with electron withdrawing groups. Upon exposure to CO_2 atmosphere, cyclic voltammetry showed current enhancement at the Fe(II/I) and Fe(I/0), which is indicative of a catalytic process for all complexes. Catalytic onsets can also be shifted more positively by using ligand with electron-withdrawing substituents.

Controlled potential electrolysis experiments under a CO_2 atmosphere of FePhsalenCl showed remarkable selectivity toward CO production over H_2 production, with Faradaic efficiency of 40% and less than 1% respectively. Because no other C1 product was found, we postulated that some product, CO, was trapped at the Fe center, which then proceed to deactivate the catalyst. To prove this hypothesis, CV experiments in the presence of a CO scavenger molecule, $[\text{Ni}(\text{TMC})](\text{PF}_6)_2$, was conducted. The increased catalytic current supports the hypothesis. Furthermore, electrolysis of Fe catalyst with $[\text{Ni}(\text{TMC})](\text{PF}_6)_2$ also increased the amount of CO produced. CV of Fe salen complex under a CO atmosphere also produced a new feature that resembles the redox couple of Fe complex after controlled potential electrolysis. IR spectroscopy of the electrolysis solutions showed small changed of Fe complex upon applied potentials, suggesting that the catalyst remains intact during the reaction.

Taken together, this body of work displays the potential of biomimetic iron catalysts for both oxidative and reductive transformations of small molecules. Understanding the molecular basis through electronic tunings of metal catalysts for these reactions will further aid the development of robust and efficient catalysts in homogeneous catalysis.

Dedications

To my dear family,
Dr. Teerachai Chantarojanasiri, Dr. Worapan Chantarojsiri, and Dr. Tanyaporn Chantarojsiri,
for their unwavering supports from 8,000 miles away

Table of Contents

Acknowledgements xiii

Chapter 1 Metal-Polypyridyl Catalysts for Electro- and Photochemical Reduction of Water to Hydrogen 1

1.1	<i>Conspectus</i>	2
1.2	<i>Introduction</i>	2
1.3	<i>Polypyridyl Ligands for Catalysis in Water</i>	3
1.4	<i>A Water-Compatible Tetrapyridyl-Cobalt Catalyst</i>	4
1.5	<i>Electrocatalytic Proton Reduction in Neutral Water using [(PY5Me₂)MoO]²⁺</i>	4
1.6	<i>[(PY5Me₂)MoS₂]²⁺ as an Functional Molecular Mimic of Molybdenum Disulfide</i>	5
1.7	<i>[(PY5Me₂)Co(H₂O)]²⁺ as a Tunable Platform for Water Reduction in Neutral Water</i>	5
1.8	<i>Redox-Active Ligands for Redox-Leveling and Facilitating Multi-Electron Electrocatalysis</i>	6
1.9	<i>Optimizing Photocatalytic Hydrogen Generation</i>	6
1.10	<i>Concluding Remarks</i>	7
1.11	<i>References</i>	7

Chapter 2. Water-Soluble Iron(IV)-Oxo Complexes Supported by Pentapyridine Ligands: Axial Ligand Effects on Hydrogen Atom and Oxygen Atom Transfer Reactivity 26

2.1	<i>Abstract</i>	27
2.2	<i>Introduction</i>	27
2.3	<i>Results and Discussion</i>	28
2.4	<i>Concluding Remarks</i>	32
2.5	<i>Experimental Section</i>	32
2.6	<i>References</i>	36

Chapter 3 Reactivity of Fe Salen Complexes in Electrocatalytic CO₂ Reduction 94

3.1	<i>Abstract</i>	95
3.2	<i>Introduction</i>	95
3.3	<i>Results and Discussions</i>	95
3.4	<i>Conclusions</i>	97
3.5	<i>Experimental</i>	97

3.6	<i>References</i>	99
Appendix A Toward the Synthesis of Mo and V Imido Complexes Supported by PY5Me₂ Ligand		
	Ligand	118
A.1.	<i>Synopsis</i>	119
A.2.	<i>Motivation and Design</i>	119
A.3.	<i>Results and Discussion</i>	119
A.4.	<i>Conclusion and Future Directions</i>	122
A.5.	<i>Experimental</i>	123
Appendix B Assorted Synthesis of Ligand for Fe Complexes		
	Ligand	149
B.1.	<i>Synopsis</i>	150
B.2.	<i>Motivation and design</i>	150
B.3.	<i>Results and Discussions</i>	150
B.4.	<i>Experimental</i>	152
B.5.	<i>References</i>	157
Appendix C Syntheses and Characterizations of Ir-Based Water-Soluble Photosensitizers		
	Ligand	166
C.1.	<i>Synopsis</i>	167
C.2.	<i>Motivation and Design</i>	167
C.3.	<i>Results and discussions</i>	167
C.4.	<i>Experimental</i>	167
C.5.	<i>References</i>	169
Appendix D Mössbauer Spectroscopy of Linear Fe(I) complexes and Fe(0) complexes....		
	Ligand	176
D.1.	<i>Synopsis</i>	177
D.2.	<i>Motivation and Design</i>	177
D.3.	<i>Results and Discussion</i>	177
D.4.	<i>Experimental</i>	177
D.5.	<i>References</i>	178
Appendix E Glovebox Guidelines and Basic Troubleshooting		
	Ligand	185
D.1.	<i>Glovebox Guidelines</i>	186

D.2.	<i>Policies Regarding N₂</i>	186
E.3.	<i>Operation and Maintenance</i>	187
E.4.	<i>Troubleshootings</i>	193
Appendix F Mössbauer Guidelines		195
F.1.	<i>Parts and Pieces</i>	196
F.2.	<i>How to align the instruments</i>	200
F.3.	<i>How to do iron metal calibration</i>	201
F.4.	<i>How to expand velocity scale and How to set up higher velocity data collection ...</i>	201
F.5.	<i>General Guidelines for data collection</i>	201
F.6.	<i>How to prepare solid sample</i>	202
F.7.	<i>How to prepare frozen solution sample</i>	202
F.8.	<i>How to work up the data</i>	202
F.9.	<i>Experimental write-up for Mössbauer experiments</i>	203
F.10.	<i>Source Installation</i>	204
F.11.	<i>Contacts</i>	205
Appendix G Photolysis Setup		206
G.1.	<i>Parts and Pieces</i>	207
Appendix H. Variable Temperature UV-visible Spectroscopy with Unisoku Cryostat Setup		209
H.1.	<i>UV-vis Spectrometer with Unisoku cryostat</i>	210
H.2.	<i>How to operate</i>	210

Table of Figures

- Figure 1.1.** Hydrogenase enzymes (far left) and MoS₂ (molybdenite, second from left) are proton reduction catalysts from biology and materials, respectively. Black circles delineate the small and sparse active sites among the large, overall structures: the [NiFe] cofactor of [NiFe]-hydrogenase enzymes (molecular weight ~60,000 kDa), and the disulfide-terminated (1 0 -1 0) edge of MoS₂. Molecular catalysts (right) can capture the functional essence of these biological and materials systems in a compact and tunable active site..... 13
- Figure 1.2.** Molecular metal-polypyridyl H₂ evolution catalysts from our laboratories..... 14
- Figure 1.3.** Cyclic voltammogram of 1 in a 1:1 water/CH₃CN (v/v) mixture (black), with a glassy carbon working electrode. The Co(II/I) couple occurs *ca.* -1.4 V versus the ferrocenium/ferrocene couple (Fc⁺⁰). Increasing concentrations of TFA give corresponding rises of catalytic current (red, green blue, cyan, and purple). The inset shows the crystal structure of 1, R₁ (wR₂) = 5.20% (13.3%)..... 15
- Figure 1.4.** a) CV of 2 in CH₃CN at a glassy carbon electrode (black). Addition of acetic acid causes current enhancement at the third reduction, with plateaus occurring at *ca.* -2.25 V vs Fc⁺⁰. The inset shows the crystal structure of 2, R₁ (wR₂) = 3.64% (9.82%). b) Rotating disk electrode voltammograms (100 to 3600 rpm) of 2 in CH₃CN (glassy carbon). Traces show three distinct plateaus, indicating three reduction processes. c) CV in a 0.6 M aqueous phosphate buffered to pH 7 at a Hg pool electrode in the absence (red), and presence of 2 (black). d) CPE at -1.40 V vs SHE in the absence (red) and presence of 2 (2 μM, black) in 3.0 M phosphate buffered to pH 7. Complex 2 remains catalytically active after 72 h of electrolysis. 16
- Figure 1.5.** Gibbs free energy diagram for the liberation of H₂ from H, which is formed by the reduction of 2..... 17
- Figure 1.6.** a) CVs of 3 in 0.05 M phosphate buffered to pH ranging from 3 to 7. The first reductive wave shifts by *ca.* 60 mV per unit change in pH, suggesting that the reduction is proton-coupled. Inset shows the crystal structure of 3, R₁ (wR₂) = 2.85% (6.08%). b) CVs of 1 M acetate buffer at pH 3 at a mercury pool electrode (red) with 2 (130 μM, black) and 3 (130 μM, blue). c) CPE of 3 (66 μM) in 3 M aqueous acetate buffer (blue) versus the buffer alone (red) at -0.96 V vs SHE (η = 0.78 V)..... 18
- Figure 1.7.** a) Crystal structures of 4, 5, and 6, R₁ (wR₂) = 3.04% (8.19%), 2.62% (6.67%), and 6.11% (18.9%). b) Normalized CVs of 4 (red), 5 (black) and 6 (blue) in 1 M phosphate buffer at pH 7 at a Hg pool electrode. c) CPE at -1.30 V vs SHE of 4 (black), [(PY5Me₂)Zn(H₂O)]²⁺ (green), PY5Me₂ ligand (red) and without additives (blue). Control experiments show that the ligand or metal alone or an isostructural PY5Me₂ complex with Zn(II) are inactive for catalysis. Only the CoPY5Me₂ unit shows competent reactivity. All electrolyses were performed in 2 M phosphate buffer at pH 7. 19
- Figure 1.8.** Photochemical generation of H₂ by 5 photosensitized with either [Ru(bpy)₃]²⁺ (left) or GaP nanowires (right), with ascorbate as a sacrificial reductant. 20
- Figure 1.9.** a) To reduce a weak acid such as water, catalysis may involve a Co(II/0) process, with a driving force of E1 (red). Introduction of a ligand-based redox state gives a new driving force E2 that can afford catalysis at less extreme potentials (blue). b) Crystal

- structures of 7 and 8, R_1 (wR_2) = 3.61% (9.25%) and 3.32% (7.83%). Blue areas highlight one of the redox-active bpy moieties. c) Photocatalytic H₂ evolution in water by 7 and 8. Once catalysis levels off, addition of [Ru(bpy)₃]²⁺ regenerates activity. 21
- Figure 1.10.** Crystal structures of 9, 11, 14, and 15, R_1 (wR_2) = 2.53% (6.58%), 2.75% (11.3%), 2.77% (6.60%), and 2.96% (7.01%). 9, 11 and 14 contain two *cis* open sites while 16 has two *trans* open sites. 22
- Figure 1.11.** a) Photocatalytic hydrogen production versus time of different Co catalysts. b) Catalysis is limited by photosensitizer stability. c) Transient absorption difference spectra shows formation of a Co(I) species of 9 coinciding with disappearance of [Ru(bpy)₃]⁺. d) TONs of different Co catalysts at their respective optimal pH. 23
- Figure 2.1.** Crystal structures of **1-X** and **2-X**. Anions and hydrogen atoms are omitted for clarity, except for OH groups. Orange, blue, red, grey, green and white represent Fe, N, O, C, F and H respectively. Structure of **2-NMe₂** was reported previously. 40
- Figure 2.2.** Linear free energy relationship of Fe(III/II) redox couples of **1-X** and Hammett Parameters (σ_p) with ρ 2.24×10^{-1} , $R^2 = 0.99$. Fe(III/II) redox couples were measured with 1 mM of **1-X** in 0.1 M NBu₄PF₆ MeCN using glassy carbon as a working electrode, Ag/AgCl as a reference electrode and Pt wire as a counter electrode. Ferrocene was used as an external standard and the potential was corrected to vs SCE by addition of 0.4 V. Experimental details on the synthesis of **1-pyr**, **1-Cl**, and **1-NH₂** can be found in the Supplementary Information. Pyr = 2,5-dimethylpyrrole. 41
- Figure 2.3.** Cyclic voltammograms of **1-CF₃** (black), **1-pyr** (red), **1-Cl** (blue), **1-H** (green), **1-Me** (magenta), **1-NH₂** (dark yellow), and **1-NMe₂** (purple) in 0.1 M NBu₄PF₆ MeCN solution using glassy carbon as a working electrode, 1 mM Ag/AgNO₃ as a reference electrode and Pt wire as a counter electrode. Ferrocene was added as an external standard. **1-pyr** redox couple showed slight irreversibility due to oxidation of the ligand. 42
- Figure 2.4.** Linear free energy relationship of Fe(III/II) redox couples of **2-X** in water with ρ of 1.51×10^{-1} , $R^2 = 0.99$ (pH 3), 1.46×10^{-1} , $R^2 = 0.99$ (pH 4), 1.48×10^{-1} , $R^2 = 0.99$ (pH 5), 1.45×10^{-1} , $R^2 = 0.99$ (pH 6). The Fe(III/II) redox couples were measured with 1 mM of **2-X** in 0.1 M Potassium Acetate (KOAc) buffer at pH 3-6, using glassy carbon as a working electrode, Ag/AgCl as a reference electrode and Pt wire as a counter electrode. Black circle, red square green triangle and blue diamond represent redox potential measured at pH 3, 4, 5, and 6 respectively (top). Pourbaix diagram of **2-X** at pH 3 to 6 (bottom). The slopes of all lines match the theoretical value of 59 mV/pH, $R^2 = 0.99$. Black circle, red square, green triangle and blue diamond represent redox potential of **2-CF₃**, **2-H**, **2-Me**, and **2-NMe₂** respectively. 43
- Figure 2.5.** Cyclic voltammograms of **2-CF₃** (black), **2-H** (red), **2-Me** (green), and **2-NMe₂** (blue) in 0.1 M KNO₃ aqueous solution (non-buffered) using glassy carbon as a working electrode, Ag/AgCl as a reference electrode and Pt wire as a counter electrode. **2-CF₃** and **2-H** showed second oxidation event around 0.9 V. 44
- Figure 2.6.** Cyclic voltammograms of **2-CF₃** with increasing scan rate from 25 mV/s (black), 50 mV/s (red), 100 mV/s (blue), 250 mV/s (green), 500 mV/s (cyan), 1000 mV/s (magenta), 2500 mV/s (yellow), 5000 mV/s (purple), to 10000 mV/s (wine), in 0.1 M KNO₃ aqueous

<p>solution (non-buffered) using glassy carbon as a working electrode, Ag/AgCl as a reference electrode and Pt wire as a counter electrode. Background currents were subtracted from the voltammogram.....</p>	45
<p>Figure 2.7. Cyclic voltammograms of 2-H with increasing scan rate from 25 mV/s (black), 50 mV/s (red), 100 mV/s (blue), 250 mV/s (green), 500 mV/s (cyan), 1000 mV/s (magenta), 2500 mV/s (yellow), to 5000 mV/s (purple), in 0.1 M KNO₃ aqueous solution (non-buffered) using glassy carbon as a working electrode, Ag/AgCl as a reference electrode and Pt wire as a counter electrode. Background currents were subtracted from the voltammogram.....</p>	46
<p>Figure 2.8. Cyclic voltammograms of 2-Me with increasing scan rate from 25 mV/s (black), 50 mV/s (red), 100 mV/s (blue), 250 mV/s (green), 500 mV/s (cyan), 1000 mV/s (magenta), 2500 mV/s (yellow), 5000 mV/s (purple), to 10000 mV/s (wine), in 0.1 M KNO₃ aqueous solution (non-buffered) using glassy carbon as a working electrode, Ag/AgCl as a reference electrode and Pt wire as a counter electrode. Background currents were subtracted from the voltammogram.....</p>	47
<p>Figure 2.9. Cyclic voltammograms of 2-NMe₂ with increasing scan rate from 25 mV/s (black), 50 mV/s (red), 100 mV/s (blue), 250 mV/s (green), 500 mV/s (cyan), 1000 mV/s (magenta), 2500 mV/s (yellow), 5000 mV/s (purple), to 10000 mV/s (wine), in 0.1 M KNO₃ aqueous solution (non-buffered) using glassy carbon as a working electrode, Ag/AgCl as a reference electrode and Pt wire as a counter electrode. Background currents were subtracted from the voltammogram. A redox couple around 0.76 V indicates ligand oxidation that occurs before the oxidation at the Fe center.....</p>	48
<p>Figure 2.10. Zero-field Mössbauer spectra of solid 1-CF₃ (top), 2-CF₃ (middle), and 3-CF₃ (bottom) (black squares) acquired at 5 K. A least-square fit (blue line) provided the parameters listed in Tables 2.2 and 2.4.</p>	49
<p>Figure 2.11. Mössbauer spectra of 1-CF₃ and 2-CF₃ at 5 K and 295 K. Black square represents the collected spectra and blue line represents a least square fit.....</p>	50
<p>Figure 2.12. A Mössbauer spectrum of 3-CF₃ at 5 K. Black square represents the collected spectra and blue line represents a least square fit.....</p>	51
<p>Figure 2.13. Mössbauer spectra of 1-H and 2-H at 5 K and 295 K. Black square represents the collected spectra and blue line represents a least square fit.</p>	52
<p>Figure 2.14. A Mössbauer spectrum of 3-H at 5 K. Black square represents the collected spectra and blue line represents a least square fit.</p>	53
<p>Figure 2.15. Mössbauer spectra of 1-Me and 2-Me at 5 K and 295 K. Black square represents the collected spectra and blue line represents a least square fit.....</p>	54
<p>Figure 2.16. A Mössbauer spectrum of 3-Me at 5 K. Black square represents the collected spectra and blue line represents a least square fit.....</p>	55
<p>Figure 2.18. Mössbauer spectra of 1-CF₃ and K₂S₂O₈ at 5 K. Line broadening is caused by thickness of frozen solution sample. Black square represents the collected spectra and blue line represents a least square fit. $\delta = 0.242$ mm/s, $\Delta E_Q = 1.852$ mm/s.....</p>	57
<p>Figure 2.19. Infrared spectra of 3-CF₃. Solid traces: Fe^{IV}(¹⁶O), dotted traces: Fe^{IV}(¹⁸O). Asterisks denote assignments to $\nu(\text{Fe-O})$ stretches.</p>	58

Figure 2.20. Difference Infrared spectra of 3-CF₃ . Asterisks denote assignments to $\nu(\text{Fe-O})$ stretches, $\text{Fe}^{\text{IV}}(^{16}\text{O})$ (black), $\text{Fe}^{\text{IV}}(^{18}\text{O})$ (red).....	59
Figure 2.21. Infrared spectra of 3-H . Solid traces: $\text{Fe}^{\text{IV}}(^{16}\text{O})$, dotted traces: $\text{Fe}^{\text{IV}}(^{18}\text{O})$. Asterisks denote assignments to $\nu(\text{Fe-O})$ stretches	60
Figure 2.22. Difference Infrared spectra of 3-H . Asterisks denote assignments to $\nu(\text{Fe-O})$ stretches, $\text{Fe}^{\text{IV}}(^{16}\text{O})$ (black), $\text{Fe}^{\text{IV}}(^{18}\text{O})$ (red).....	61
Figure 2.23. Infrared absorption spectra of the $\text{Fe}(\text{IV})$ -oxo PY5Me_2 complex 3-Me synthesized from H_2^{16}O (black) and H_2^{18}O (red). Asterisks denote the Fe-oxo vibration $\nu(\text{Fe-O})$. Difference Spectra are shown in Figure 2.24	62
Figure 2.24. Difference Infrared spectra of 3-Me . Asterisks denote assignments to $\nu(\text{Fe-O})$ stretches, $\text{Fe}^{\text{IV}}(^{16}\text{O})$ (black), $\text{Fe}^{\text{IV}}(^{18}\text{O})$ (red).....	63
Figure 2.25. Mass spectra of 3-CF₃-¹⁶O and 3-CF₃-¹⁸O . A mass shift of $m/z = 1$ Da was observed when H_2^{18}O is employed, consistent with water as the source of the oxo ligand. .	64
Figure 2.26. Mass spectra (a) and simulated mass spectra (b) of 3-CF₃-¹⁶O (top left), 3-CF₃-¹⁸O (top right), 3-H-¹⁶O (middle left), 3-H-¹⁸O (middle right), 3-Me-¹⁶O (bottom left), and 3-Me-¹⁸O (bottom right).....	65
Figure 2.27. Mass spectra (top) and simulated mass spectra (bottom) of 3-NMe₂ that formed and decomposed quickly at 0°C	66
Figure 2.28. Photochemical oxidation of $\text{Fe}(\text{II})$ -aqua 2-CF₃ to $\text{Fe}(\text{IV})$ -oxo 3-CF₃ in water using a flash-quench $[\text{Ru}(\text{bpy})_3]^{2+}/\text{K}_2\text{S}_2\text{O}_8$ system.....	67
Figure 2.29. UV-visible spectra of formation of 3-CF₃ by CAN in water at room temperature. 68	
Figure 2.30. UV-visible spectra of 3-CF₃ (dotted blue trace) and 3-H (dashed red trace) in comparison to $\text{Ru}(\text{bpy})_3^{3+}$ background (solid black trace) during photolysis. The inset shows the characteristic weak band of $\text{Fe}^{\text{IV}}(\text{O})$ at 710 nm, which does not overlap with Ru^{3+} absorption at 680 nm.....	69
Figure 2.31. UV-visible spectra of 2-CF₃ (black solid trace), 2-H (red dashed trace), 2-Me (dotted green trace), and 2-NMe₂ (blue dotted-dashed trace) and excess $\text{K}_2\text{S}_2\text{O}_8$ in water at room temperature, showing the absence of features around 300-500 nm which is characteristic of Fe^{II} species.....	70
Figure 2.32. UV-visible spectra of 2-CF₃ (black solid trace), 2-H (red dashed trace), 2-Me (green dotted trace), and 2-NMe₂ (blue dotted-dashed trace) in water at room temperature.71	
Figure 2.33. Linear free energy relationship of oxidation reaction rate constants (pseudo first-order) of hydrocarbon substrates by 3-X and Hammett Parameters (σ_p). Black squares, red circles, green triangles represent oxidation rate of benzyl alcohol (ρ 0.79, $R^2 = 0.98$), 4-ethylbenzene sulfonate (ρ 1.06, $R^2 = 0.95$) and 4-styrene sulfonate (ρ 0.49, $R^2 = 0.94$) respectively.....	72
Figure 2.34. Concentration dependent of apparent rate (k_{obs}) of oxidation of Benzylalcohol with 3-CF₃ (black circle), 3-H (red square), and 3-Me (blue triangle).....	73
Figure 2.35. Concentration dependent of apparent rate (k_{obs}) of oxidation of 4-Ethylbenzene Sulfonate with 3-CF₃ (black circle), 3-H (red square), and 3-Me (blue triangle).....	74
Figure 2.36. Concentration dependent of apparent rate (k_{obs}) of oxidation of 4-Styrene Sulfonate with 3-CF₃ (black circle), 3-H (red square), and 3-Me (blue triangle).....	75

Figure 3.1. Cyclic voltammogram (CV) of 0.5 mM of 1 under Ar atmosphere (black), CO ₂ atmosphere (red), CO ₂ atmosphere with water added (blue) and Ar atmosphere with water added (green).	103
Figure 3.2. CVs of 1 (black), 2 (red), and 3 (blue) in MeCN under Ar atmosphere (left) and CO ₂ atmosphere (right). The most electron withdrawing group (NO ₂) shifts the Fe(II/I) redox couple to the most positive potential.	104
Figure 3.3. CVs of 2 (black), 4 (red), 5 (blue), and 6 (green) in MeCN under Ar atmosphere (left) and CO ₂ atmosphere (right). 5 with the most electron-deficient head group shows the most positive Fe(II/I), Fe(I/0) redox potentials and gave rise to the highest catalytic current.	105
Figure 3.4. Solid state structure of 5 (left) and 6 (right).	106
Figure 3.5. CVs of 5 with 0 eq (black), 1 eq (red), 2 eq (blue), 3 eq (cyan), 4 eq (pink) and 5 eq (yellow) of [Ni(TMC)](PF ₆) ₂ in MeCN under CO ₂ atmosphere. Catalytic current increases with the increasing amount of [Ni(TMC)](PF ₆) ₂ which serves as a CO scavenger.	107
Figure 3.6. CVs of 5 under CO ₂ (black) and CO (red) atmosphere. New features around -1.2 V developed under CO atmosphere matched the peaks that appeared after controlled potential electrolysis, suggesting some Fe complex trapped CO as metal carbonyl species.	108
Figure 3.7. CV of 0.5 mM of 5 under Ar atmosphere (black), CO ₂ atmosphere (red), CO ₂ atmosphere with water added (blue) and Ar atmosphere with 0.1 M water added (green).	109
Figure 3.8. CV of 0.5 mM (red), 1.0 mM (blue), 1.5 mM (cyan), 2.0 mM (pink), and 2.5 mM (dark yellow) [Ni(TMC)](PF ₆) ₂ in MeCN under CO ₂ atmosphere, showing no background current when it is added to the solution of 5	110
Figure 3.9. IR spectra of MeCN of 5 before (black) and after (red) controlled potential electrolysis experiment.	111
Figure 3.10. CV of 5 before (black) and after (red) controlled potential electrolysis experiment.	112
Figure 3.11. UV-visible spectra of MeCN of 5 before (black) and after (red) and 5 with 5 eq before (blue) and after (green) controlled potential electrolysis experiment. Spectra of [Ni(TMC)](PF ₆) ₂ before (pink) and after (cyan) controlled potential electrolysis experiment.	113
Figure 3.12. solid state structure of dinuclear μ -oxo species of 5 isolated after the electrolysis.	114
Figure A.1. Cycloaddition product of MoPY5Me ₂ (N ₃)(OTf) ₂ with MeCN (3). Hydrogen atoms and counter ions are omitted for clarity.	127
Figure A.2. IR spectra for the reaction of 1 with adamantylazide (black) and with adamantylamine (red) reaction. The two spectra show the same fingerprint pattern with the exception of the azide N=N stretching peak, 2085 cm ⁻¹ (arrow), indicating similarity of products from both reactions.	128
Figure A.3. UV-vis spectra of MoPY5Me ₂ (OTf) ₂ (1) (black), MoO(PY5Me ₂)(OTf) ₂ (3) (blue), product from reaction of 1 with PhINNs (red). These spectra indicate that the product from reaction of 1 with PhINNs is not the same as 3	129

Figure A.4. Mass spectrum of MoPY5Me ₂ NNs ²⁺ (<i>m/z</i> of 370.553) and the isotopic simulation of MoPY5Me ₂ NNs ²⁺ showing (<i>m/z</i> of 370.552).....	130
Figure A.5. Solid state structure showing atom connectivities of product from reaction of 1 with PhINNs. The ambiguous atom (X1) is shown on top. Hydrogen atoms and counter ions are omitted for clarity. Mo-X bond length is 1.689(3) Å.....	131
Figure A.6. UV-vis spectra of MeCN solution of dark brown crystal from reaction of 1 with PhINNs (solid line) and MoO(PY5Me ₂)(OTf) ₂ (4) (dashed line). Absorption at 492 nm (arrow) is indicative of the yellow product.	132
Figure A.7. CV of [MoNNs(PY5Me ₂)](OTf) ₂ (4 , black) and [MoO(PY5Me ₂)](OTf) ₂ (5 , red) in 0.1 M (ⁿ Bu) ₄ NPF ₆ in MeCN on glassy carbon electrode at 100 mV/s, showing that the 5 is not a clean product and suggested that it contained 4 as impurities.....	133
Figure A.8. Solid State structure of 7 (left) and 9 (right). Hydrogen atoms and counter ions are omitted for clarity. V-O bond length is 1.588(5) Å in 7 and 1.597(6) Å in 9 , compared to 1.595(2) Å in [V ^{IV} (O)(PY5Me ₂)](OTf) ₂ . Ellipsoid in 9 is 20% probability.	134
Figure A.9. Cyclic voltammogram of [V ^{IV} (O)(PY5Me ₂ -X)] ²⁺ derivatives. When X = CF ₃ , V ^{IV} (O)/V ^{III} (O) redox couple is the most positive and the most negative when X = NMe ₂ . The redox couple around 0 V is ferrocene which is an external standard.....	135
Figure A.11. Solid state structure of 11 (left), 12 (middle) and 13 (right). Hydrogen atoms and counter ions are omitted for clarity. V-N bond length is 1.618(8) Å in 12 and V-F bond length is 1.789(4) Å in 13	137
Figure A.12. Squid Magnetometry of V ^{IV} (O) (TC3-194, black) and V ^{III} (F) (TC3-193, red, 13), showing S = 1/2 and S = 1 spin state.....	138
Figure B.1. Crystal Structure of Fe(PY5Me ₂ -BF ₃ ⁻).....	158
Figure B.2. Crystal Structure of Fe(NMe ₂ -PY5Me ₂).....	159
Figure B.3. Crystal Structure of [Fe(sulfonamide)] ₂	160
Figure C.1. Photophysics of Ir(N-mppy) ₃ in CH ₃ CN.....	170
Figure C.2. Cyclic Voltammograms of complex 2-4 . Redox couple at 0 V is an external standard, ferrocene.....	171
Figure D.1. Zero-field ⁵⁷ Fe Mössbauer spectra of 1 at 5, 25 and 50 K respectively (black square). A least-squares fit (blue line) provided the parameters listed in Table D.1.	179
Figure D.2. Zero-field ⁵⁷ Fe Mössbauer spectra of 1 acquired at 75, 100, 150, 200, 250 and 290 K (black squares). A least-squares fit (blue line) provided the parameters listed in Table D.2.	180
Figure D.3. Zero-field ⁵⁷ Fe Mössbauer spectra of 5 acquired at 5, 25, 50, 75, 100, and 150 K (black squares). A least-squares fit (blue line) provided the parameters listed in Table D.3.	181
Figure D.4. Zero-field ⁵⁷ Fe Mössbauer spectra of 5 acquired at 200, 250, and 290 K and at 5 K right after a room temperature experiments (black squares). A least-squares fit (blue line) provided the parameters listed in Table D.2. Green and red lines represent least-square fits of 2 iron species, 5 and decomposed product respectively.....	182

Table of Schemes

Scheme 2.1. Synthesis of $[\text{Fe}^{\text{II}}(\text{L})(\text{PY5Me}_2\text{-X})]^{2+}$, 1-X and 2-X . a) $\text{Fe}(\text{OTf})_2$ in MeCN yielded $[\text{Fe}^{\text{II}}(\text{MeCN})(\text{PY5Me}_2\text{-X})(\text{OTf})_2]$ (1-X), b) $\text{Fe}(\text{OH}_2)_6(\text{BF}_4)_2$ in acetone/water mixture yielded $[\text{Fe}^{\text{II}}(\text{OH}_2)(\text{PY5Me}_2\text{-X})](\text{BF}_4)_2$ (2-X).....	76
Scheme 2.1. Oxidation of Fe(II)-PY5Me ₂ complexes to their Fe(IV)-oxo counterparts by chemical or photochemical routes. a) CAN in H ₂ O, b) $\text{Ru}(\text{bpy})_3^{2+}$, $\text{K}_2\text{S}_2\text{O}_8$ and hv (blue light). L = H ₂ O or MeCN.	77
Scheme 2.3. Ligand synthesis for PY5Me ₂ -X (X = pyr, Cl, and NH ₂).....	78
Scheme 2.4. Synthesis Procedure for 1-pyr , 1-Cl , and 1-NH₂	78
Scheme 3.1. Fe supported by porphyrin ligand reported as electrocatalyst for CO ₂ reduction (left) and Fe supported by salen ligand complex.....	101
Scheme 3.2. Fe(salen)Cl complex and its derivatives were studied as electrochemical CO ₂ reduction catalyst in this report.	102
Scheme A.1. Nitrido complex (a) and imido complex (b) of Mo(PY5Me ₂).....	139
Scheme A.2. Syntheses of 7 and 9	140
Scheme A.3. Synthesis of 11 and 12	141
Scheme A.4. Synthesis of 13 by oxidation of 11 with NOBF ₄	142
Scheme B.1. Synthesis of PY5Me ₂ -BF ₃ ⁻	161
Scheme B.2. Synthesis of DMAP5.....	162
Scheme B.3. Synthesis of NMe ₂ -PY5Me ₂	163
Scheme B.4. Synthesis of bis-sulfonamide ligand.....	164
Scheme B.5. Synthesis of Dipyrrin-phenoxide platform.....	165
Scheme C.1. Derivatives of phenylpyridine which can be used to make water-soluble photosensitizer (top). $\text{Ir}(\text{ppy})_3$ (1) and target molecules, 2 , 3 , 4 , and 5	172
Scheme C.2. Synthesis of N-mppy and C-mppy.....	173
Scheme C.3. Two-step synthesis of <i>fac</i> - $\text{Ir}(\text{N/C-mppy})_3$, methyl esters can then be hydrolyzed to give <i>fac</i> - $\text{Ir}(\text{N/C-cppy})_3$	174
Scheme D.1. Linear Fe(I) (1) and the reduction product Fe(0) (5).....	183

Table of Tables

Table 1.1. CPE Data of Hydrogen-Producing Catalysts.....	24
Table 1.2. Photolytic Hydrogen Production by Molecular Cobalt Catalysts.*	25
Table 2.1. Fe(III)/Fe(II) reduction potentials of 1-X and 2-X in MeCN and water, respectively.	79
Table 2.2. Mössbauer parameters of Fe(II)-PY5Me ₂ complexes of the 1-X and 2-X series at 295 and 5 K. The quadrupole splitting ($ \Delta E_Q $) values increase with the electron-donating ability.	80
Table 2.3. Comparison of Fe(III/II) reduction potentials of various Fe complexes supported by pyridine-amine ligands. All but 1-H , which exhibits the most positive potential, can be oxidized to Fe(IV)-oxo species using OAT reagents.	81
Table 2.4. Mössbauer, UV-visible, and infrared spectroscopic parameters for Fe(IV)-oxo PY5Me ₂ complexes 3-X	82
Table 2.5. Second-order rate constants of substrate oxidation by Fe ^{IV} (O) PY5Me ₂ species 3-X at 25°C in aqueous solution at pH 5.5 (non-buffered water).....	83
Table 2.6. Fe ^{III/II} Reduction potentials of 1-X . Fe(III/II) redox couples were measured with 1 mM of 1-X in 0.1 M NBu ₄ PF ₆ MeCN using glassy carbon as a working electrode, Ag/AgCl as a reference electrode and Pt wire as a counter electrode. Ferrocene was used as an external standard.....	84
Table 2.7. Fe ^{III(OH)/Fe^{II(OH₂)} Reduction potentials of 2-X. Fe(III/II) redox couples were measured with 1 mM of 2-X in 0.1 M KNO₃ H₂O using glassy carbon as a working electrode, Ag/AgCl as a reference electrode and Pt wire as a counter electrode.}	85
Table 2.8. Mass spectrometry of reaction mixtures after photolysis confirming that all 3-X complexes are successfully generated.	86
Table 2.9 Crystal Structure Tables.....	87
Table 3.1. Summary of electrolysis results of 5 in the absence and presence of CO scavenger molecule.....	115
Table 3.2. Crystal data and structure refinement for 5	116
Table 3.3. Crystal data and structure refinement for 7	117
Table A.1. Crystallographic Data of Mo(2-methyltetrazole) (PY5Me ₂)(OTf) ₂ (3)	143
Table A.2. Crystallographic Data of V(O) (PY5Me ₂ -CF ₃)(OTf) ₂ (7).....	144
Table A.3. Crystallographic Data of V(O) (PY5Me ₂ -NMe ₂)(OTf) ₂ (9).....	145
Table A.4. Crystallographic Data of V(N ₃) (PY5Me ₂)(OTf) ₂ (11).....	146
Table A.6. Crystallographic Data of V(F) (PY5Me ₂)(OTf) ₂ (13).....	148
Table C.1. Latimer diagrams and solubility properties of complex 2-4	175
Table D.1. Mössbauer parameters of 1 at 5, 25 and 50 K.....	184
Table D.2. Mössbauer parameters of 1 at 75, 100, 150, 200, 250 and 290 K.....	184
Table D.3. Mössbauer parameters of 5 at 5, 25, 50, 75, 100, 150, 200, 250, and 290 K.....	184
Table D.4. Mössbauer parameters of 5 at 5 K after room temperature experiment, 50% of 5 decomposes into another product (specie 2).....	184

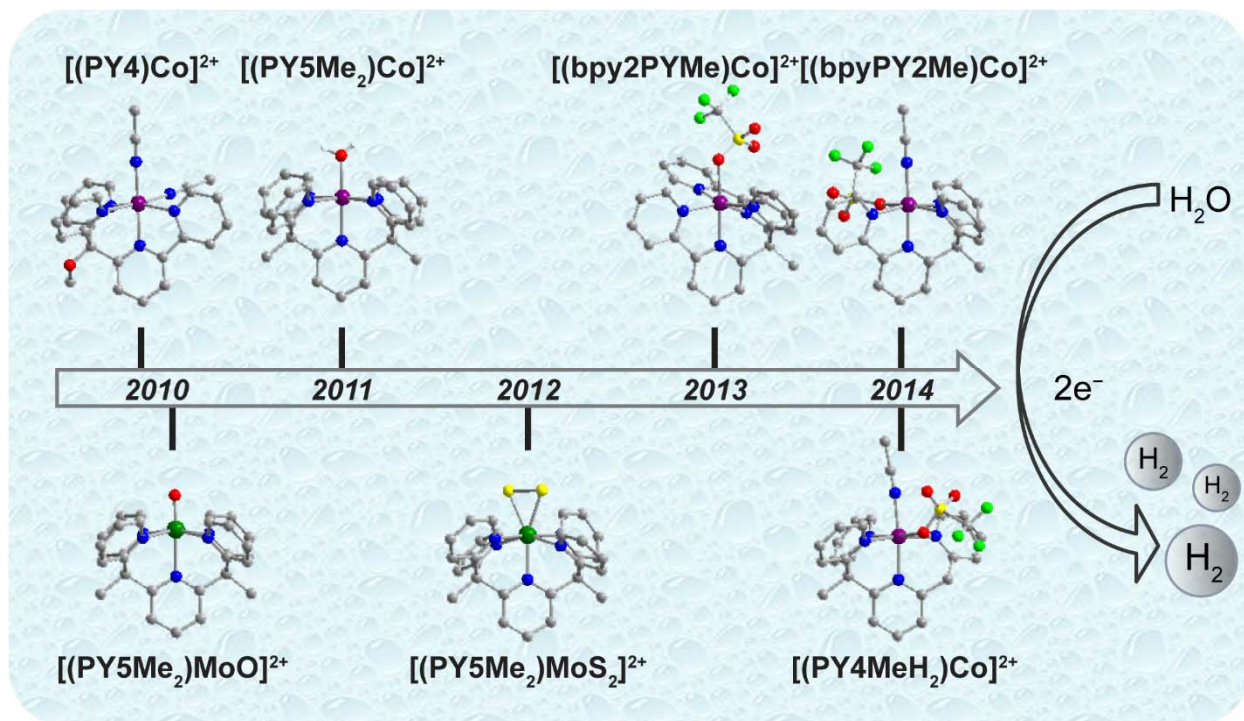
Acknowledgements

Someone once told me that getting a PhD is a team effort; I have come to appreciate this saying as I am going through my PhD program. First, I would like to express my gratitude to my advisor, Professor Chris Chang, for his support and the opportunities to explore different areas of research. Along the process, I learned how to operate various scientific equipments as well as design and customize them to be suitable for my experiments. I thank my labmates, former and current, for helpful discussions and new perspectives on different scientific problems. In particular, I want to thank Dr. Sara Thoi, Dr. Julian Bigi and Dr. Nick Piro who helped me started out my PhD career.

I am fortunate to be a part of Chemistry Department at Berkeley. I am very grateful to Professor Jeff Long and Professor Don Tilley for their scientific supports and collaborations, and Professor Bob Bergman and Professor Dick Andersen for helpful discussions. I also want to thank Dr. Heinz Frei at the Physical Bioscience Division, Lawrence Berkeley National Laboratory for his help with IR spectroscopy. I want to extend my appreciation to my collaborators, David Zee and Dr. Mike Lipschutz for their feedbacks, supports and patience. I also want to thank Dianne Xiao for working closely with me in maintaining the Mössbauer spectrometer. Supporting staff of the College of Chemistry, particularly, Eric Granlund from the machine shop, Jim Breen from the glass shop, Clif Marshall and Manny Druga from the electrical shop, and Mike Brateng and his crews from the wood shop help me multiple times with instrumentations and engineering problems that I had during my experiments. All of my friends in the Chemistry department, I owe them for their moral supports throughout this past five years.

Finishing a PhD is already challenging by itself but Mananya Tantiwivat did it while battling cancer; I thank her for being my inspirations. Dr. Sucheewin Chotchatchawankul is always with me during the ups and downs of my PhD career. I thank him for listening, supporting me in the most difficult times, and for helpful discussions. Last but definitely not least, I am grateful to have my sister, my Mom, and my Dad, for all their unconditional love and support

Chapter 1 Metal-Polypyridyl Catalysts for Electro- and Photochemical Reduction of Water to Hydrogen



This chapter includes work published in: Zee, D. Z., [Chantarojsiri, T.](#), Long, J. R., Chang, C. J. *Acc. Chem. Res.* **2015**, ASAP.

1.1 Conspectus

Climate change, rising global energy demand, and energy security concerns motivate research into alternative, sustainable energy sources. In principle solar energy can meet the world's energy needs, but the intermittent nature of solar illumination means that it is temporally and spatially separated from its consumption. Developing systems that promote solar-to-fuel conversion, such as via reduction of protons to hydrogen, could bridge this production-consumption gap, but this effort requires invention of catalysts that are cheap, robust, efficient, and use earth-abundant elements. In this context, catalysts that utilize water as both an earth-abundant, environmentally benign substrate and a solvent for proton reduction are highly desirable. This Account summarizes our studies of molecular metal-polypyridyl catalysts for electrochemical and photochemical reduction of protons to hydrogen. Inspired by concept transfer from biological and materials catalysts, these scaffolds are remarkably resistant to decomposition in water, with fast and selective electrocatalytic and photocatalytic conversions that are sustainable for several days. Their modular nature offers a broad range of opportunities for tuning reactivity by molecular design, including altering ancillary ligand electronics, denticity, and/or incorporating redox-active elements. Our first generation complex $[(\text{PY}4)\text{Co}(\text{CH}_3\text{CN})_2]^{2+}$ catalyzes the reduction of protons from a strong organic acid to hydrogen in 50% water. Subsequent investigations with the pentapyridyl ligand PY5Me₂ furnished molybdenum and cobalt complexes capable of catalyzing the reduction of water in fully aqueous electrolyte with 100% Faradaic efficiency. Of particular note, the complex $[(\text{PY}5\text{Me}_2)\text{MoO}]^{2+}$ possesses extremely high activity and durability in neutral water, with turnover frequencies at least 8,500 moles of H₂ per mole of catalyst per hour and turnover numbers over 600,000 moles of H₂ per mole of catalyst over three days at an overpotential of 1.0 V, without apparent loss in activity. Replacing the oxo moiety with a disulfide affords $[(\text{PY}5\text{Me}_2)\text{MoS}_2]^{2+}$, which bears a molecular MoS₂ triangle that structurally and functionally mimics bulk molybdenum disulfide, improves the catalytic activity for water reduction. In water buffered to pH 3, catalysis by $[(\text{PY}5\text{Me}_2)\text{MoS}_2]^{2+}$ onsets at 400 mV of overpotential, while $[(\text{PY}5\text{Me}_2)\text{MoO}]^{2+}$ requires an additional 300 mV of driving force to operate at the same current density. Metalation of the PY5Me₂ ligand with an appropriate Co(II) source also furnishes electrocatalysts that are active in water. Importantly, the onset of catalysis by the $[(\text{PY}5\text{Me}_2)\text{Co}(\text{H}_2\text{O})]^{2+}$ series is anodically shifted by introducing electron-withdrawing functional groups on the ligand. With the $[(\text{bpy}2\text{PYMe})\text{Co}(\text{CF}_3\text{SO}_3)]^{1+}$ system, we showed that introducing a redox-active moiety can facilitate the electro- and photochemical reduction of protons from weak acids such as acetic acid or water. Using a high-throughput photochemical reactor, we examined the structure-reactivity relationship of a series of cobalt(II) complexes. Taken together, these findings set the stage for the broader application of polypyridyl systems to catalysis under environmentally benign aqueous conditions.

1.2 Introduction

Increasing global demand for energy and concerns over anthropogenic climate change drive the search for sustainable, alternative energy sources. Solar energy is a preeminent candidate as it achieves the scale needed to meet the demand, but suffers from critical problems in energy storage and transport.¹ One attractive solution to this problem is solar-to-fuel

conversion, where energy is stored by converting energy-poor molecules into energy-rich ones. In particular, hydrogen is an appealing carbon-neutral fuel as both its feedstock and combustion product are water.² Platinum can catalyze the reduction of water to hydrogen at fast rates near thermodynamic equilibrium, but its low abundance and high cost prohibit its widespread use.³ As such, it is attractive to develop inexpensive, earth-abundant hydrogen-evolution catalysts that can, when interfaced with electrodes or photoelectrodes, convert solar energy into chemical energy in a sustainable manner.⁴

In this context, biology and materials provide unifying concepts to drive the development of new solar-fuel chemistry. Within the framework of hydrogen production, hydrogenase enzymes can convert protons and electrons to hydrogen utilizing only iron and/or nickel in their active sites with high speed and efficiency on a per molecule basis.^{5,6} However, the activity of enzymes on a per volume basis is limited by size constraints, as most of the protein structure is devoted to its biological regulation for cellular function while critical catalytic reactions occur at relatively small active sites within these larger scaffolds (Figure 1.1). A similar situation is observed in heterogeneous materials, where catalytically active sites are often restricted to minor edges or faces and the bulk of the material is inert and provides but a scaffold for stability purposes. With these principles in mind, molecular catalysts can retain the small, functional units of their biological or materials counterparts, but achieve higher volumetric activities by discarding the superfluous regulatory or stabilizing scaffolds. Indeed, molecular proton reduction catalysis is a vibrant area of research and has been the subject of numerous excellent and comprehensive reviews.⁷⁻¹⁵ A key challenge is achieving efficient and sustainable catalysis in water, and we focus this Account on strategic efforts from our laboratories to meet this goal by employing metal-polypyridyl complexes.

1.3 Polypyridyl Ligands for Catalysis in Water

An important goal of proton reduction catalysis is to use water as both substrate and solvent, as water is the most abundant source of protons and offers the benefit of maintaining high substrate concentrations without organic waste produced during fuel generation or combustion. In this regard, many elegant examples of molecular proton reduction catalysts have been reported, but aqueous compatibility remains a challenge, as many molecular catalysts lack solubility in water while others are irreversibly decomposed by water and cannot be funneled back into the catalytic pathway. Our research program has centered on multidentate polypyridine ligands to address these issues. First, the use of a neutral polypyridyl scaffold coordinated to a metal ion gives a charged complex, which, combined with an appropriate charge-balancing anion, provides aqueous solubility. Moreover, being aromatic and possessing strong bonds, pyridine ligands are resistant to hydrolysis. Finally, we reasoned that the strong σ -donor capabilities of pyridines coupled with their ability to participate in metal-to-ligand π back-bonding should stabilize reduced metal species. Figure 1.2 summarizes water-compatible polypyridyl scaffolds we have successfully applied in the catalytic reduction of protons to hydrogen.

1.4 A Water-Compatible Tetrapyrrolyl-Cobalt Catalyst

Our initial foray into electrocatalytic proton reduction centered on the cobalt(II) complex $[(\text{PY}4)\text{Co}(\text{CH}_3\text{CN})_2]^{2+}$ (**1**, Figure 1.2).¹⁶ The cyclic voltammogram (CV) of **1** in acetonitrile displays a reversible Co(II)/(I) redox couple at modest reduction potentials. Addition of trifluoroacetic acid (TFA) triggered proton reduction catalysis, with ~99% Faradaic yield (Table 1.1). Importantly, we found that electrocatalytic reduction of TFA by **1** was observed even when the water content in the electrolyte solution was increased to 50%, although the complex was insoluble at higher water levels (Figure 1.3). Nevertheless, the results established the viability of our strategy.

1.5 Electrocatalytic Proton Reduction in Neutral Water using $[(\text{PY}5\text{Me}_2)\text{MoO}]^{2+}$

Concurrently, longstanding efforts in molecular magnetism led us to explore polypyridyl capping ligands to prepare coordination clusters. In particular, we became interested in the PY5 ligand investigated by Stack and coworkers for bioinorganic model chemistry,¹⁷⁻¹⁹ but found its preparation synthetically challenging. As such, we developed a convenient, multigram-scale preparation for the related ligand PY5Me₂,²⁰ which enabled us to pursue parallel investigations in both molecular magnetism and reactivity.

Inspired by elegant water activation studies in the organometallic literature,²¹⁻²⁵ particularly the work of Yoon and Tyler²³ on MCp₂ fragments, we focused on low-valent molybdenum chemistry supported by PY5Me₂. We reasoned that substituting the neutral PY5Me₂ for the anionic cyclopentadienyls would leave at least one open coordination site available for chemistry and shift reductions to more positive potentials, enabling reactivity nearer the thermodynamic potential for water reduction. Indeed, the Mo(II) complex $[(\text{PY}5\text{Me}_2)\text{Mo}(\text{CF}_3\text{SO}_3)]^{1+}$ reacts with water to form the molybdenum(IV)-oxo ion $[(\text{PY}5\text{Me}_2)\text{MoO}]^{2+}$ (**2**, Figure 1.2), with concomitant release of H₂.²⁶ This quantitative stoichiometric reactivity encouraged us to test **2** as an electrocatalyst and we were delighted to observe that it is capable of reducing acetic acid to hydrogen in acetonitrile at 100% Faradaic efficiency (Figure 1.4a, Table 1.1).²⁷ Cyclic and rotating disk voltammetry experiments unambiguously establish the active catalyst to be molecular in nature. Complex **2** proved to be sufficiently soluble and active in water, displaying two reduction events preceding a sharp rise in current corresponding to catalysis. Controlled-potential electrolyses (CPE) of **2** at -1.40 V versus the standard hydrogen electrode (SHE) showcase its activity and durability in water, with turnover frequencies (TOF) of at least 8,500 moles of H₂ per mole of catalyst per hour, turnover numbers (TON) over 600,000 moles of H₂ per mole of catalyst after 72 h without loss of activity, and 100% Faradaic efficiency (Figure 1.4d, Table 1.1). Computational investigations suggest that in aqueous solution the first two reductions are proton-coupled and those electrons are placed into orbitals antibonding in character with respect to the Mo–O bond to make the oxo moiety more nucleophilic and basic.²⁸ A third electron yields a Mo(I) center that cleaves the H–OH bond of the ligated water to form a seven-coordinate Mo(III) complex $[(\text{PY}5\text{Me}_2)\text{Mo}(\text{H})(\text{OH})]^{1+}$ (Figure 1.5). Finally, the catalyst was found to be highly active in unpurified seawater, suggesting that the PY5Me₂ ligand not only provides a catalytically active molybdenum site, but also prevents catalyst poisoning by adventitious impurities.

1.6 [(PY5Me₂)MoS₂]²⁺ as an Functional Molecular Mimic of Molybdenum Disulfide

While investigating **2** for water reduction, we recognized growing efforts in using nanoparticulate and amorphous MoS₂ for this same purpose,²⁹⁻³⁴ where catalysis is postulated to occur at MoS₂ triangular edges.^{29,30} These observations prompted us to prepare the Mo(IV)-disulfide [(PY5Me₂)MoS₂]²⁺ (**3**, Figure 1.2) with a molecular MoS₂ triangle that not only structurally resembles the active edge sites of MoS₂, but also functionally supports catalytic activity for reduction of protons to hydrogen in water.³⁵ The CV of **3** in acetonitrile displays a set of well-defined and reversible reduction events at potentials more positive than those of **2**, presaging that stabilization of the reduced states by the S₂²⁻ moiety could result in a catalyst with lower overpotentials. Indeed, catalysis by **3** in acetonitrile or acidic water initiates at 400 mV of overpotential, whilst **2** requires an additional 300 mV of driving force to operate at similar current densities (Figure 1.6, Table 1.1). This redox tuning emphasizes the molecular nature of **3**, which is additionally confirmed by complementary electrochemical and spectroscopic experiments that show no evidence of Mo deposits. The catalyst also retains activity for at least one day with 100% Faradaic efficiency, and its sustained activity in untreated seawater again highlights the ability of the PY5Me₂ ligand to furnish robust transition metal catalysts in aqueous media. In a broader sense, this work establishes a path towards functional molecular mimics of heterogeneous catalysts, in analogy to the use of coordination complexes as models for enzyme active sites.

1.7 [(PY5Me₂)Co(H₂O)]²⁺ as a Tunable Platform for Water Reduction in Neutral Water

Given the structural similarities between PY5 and PY5Me₂, as well as the established use of the former as a ligand for first-row transition metals, we reasoned that the PY5Me₂ ligand could support first-row transition metal water reduction catalysts with the reactivity, durability, and solubility necessary to function in aqueous media. Indeed, CVs collected in water with [(PY5Me₂)Co(H₂O)]²⁺ (**4**, Figure 1.2)³⁶ show an irreversible reduction followed by hydrogen evolution catalysis (Figure 1.7b). Like its molybdenum predecessors, electrolysis with **4** generates H₂ with 100% Faradaic efficiency for at least 60 h (Figure 1.7c, Table 1.1), suggesting that the PY5Me₂ ligand helps prevent decomposition via non-productive pathways.

Although **4** operates at a fairly high overpotential, the most salient feature of this system is the ability to tune potentials in a rational molecular manner. Introduction of an electron-withdrawing trifluoromethyl substituent at the 4-position of the central pyridine affords the electronically deficient complex **5** (Figure 1.2) and anodically shifts the initial one-electron reduction and subsequent catalysis without loss in Faradaic efficiency (Figure 1.7b, Table 1.1). By voltammetry, catalysis by **5** reaches 2.25 mA at -0.80 V vs SHE ($\eta = 390$ mV), whereas the unsubstituted parent complex **4** requires -0.97 V vs SHE ($\eta = 560$ mV). Introduction of an electron-donating dimethylamino substituent (**6**, Figure 1.2) increases the requisite driving force by another 100 mV. Independent preparation of the Co(I) complex [(PY5Me₂)Co]⁺ reveals that it shares its square pyramidal coordination geometry and its intense blue coloration with the cobaloxime anions,³⁷⁻⁴⁰ but instead possesses a high-spin d⁸ electron configuration. In addition, we established that **5** can generate hydrogen from neutral water under photocatalytic conditions with visible light irradiation, [Ru(bpy)₃]²⁺ as a molecular photosensitizer and ascorbic acid as a sacrificial reductant (Figure 1.8).⁴¹ Likewise, **5** enhanced the hydrogen photolysis yield of GaP nanowires in water, demonstrating that this molecular catalyst platform can be interfaced with

heterogeneous photosensitizers.⁴¹ Taken together, these results suggest that judicious modifications of the ancillary ligand can furnish catalysts active in water, utilizing either sustainable solar or electrical input.

1.8 Redox-Active Ligands for Redox-Leveling and Facilitating Multi-Electron Electrocatalysis

The prevalence of molecular cobalt-based proton reduction catalysts,^{9,39,40,42-63} including contributions from our laboratories,^{11,16,36,37,41,64,65} has attracted many experimental and computational mechanistic investigations. Though the operative mechanism for these catalysts can vary widely, formation of a cobalt-hydride is commonly invoked.^{37,48} With interest in minimizing catalyst overpotentials, Co(I) centers capable of deprotonating water (or H⁺_(aq)) are more desirable than resorting to the undoubtedly more basic Co(0) species, which require an additional reducing equivalent, and thus more negative potentials (Figure 1.9a). In cases where protonation of Co(I) is inefficient, however, we reasoned that introduction of another ligand-based redox event between the Co(II/I) and Co(I/0) couples may lower catalyst overpotentials. This concept is challenging to put into practice, however, as incorporation of a redox-active ligand can have detrimental effects. For example, the delocalization of spin onto the ligand framework in Co-bisglyoxime^{39,40,42} and trisglyoxime⁶⁶ catalysts have been shown to promote ligand hydrogenation⁶⁷⁻⁷⁰ during catalysis, significantly reducing catalyst longevity.

We therefore designed the complex [(bpy)2PYMe)Co(CF₃SO₃)]¹⁺ (**7**, Figure 1.2),⁶⁴ which contains two 2,2'-bipyridine (bpy) moieties that are not only redox-active, but also expected to be robust against hydrogenation, vis-à-vis oximes, owing to their aromatic nature (Figure 1.9b). Indeed, the CV of **7** in acetonitrile displays a metal-centered Co(II/I) couple followed by two bpy^{0/+} reductions. Addition of acetic acid, which possesses a H⁺/H₂ reduction potential midway of the Co(II/I) and bpy^{0/+} couples, engenders electrocatalysis. Complex **7** can also reduce water photocatalytically in fully aqueous conditions with [Ru(bpy)₃]²⁺ and ascorbic acid. Though the catalyst is not indefinitely stable under irradiation, this photocatalytic system is apparently limited by the durability of the photosensitizer. Addition of [Ru(bpy)₃]²⁺ after catalysis levels off restores activity (Figure 1.9c), while addition of fresh catalyst in parallel experiments did not. Photocatalysis by **4** and **5**, which are devoid of redox-active ligands, result in *ca.* six-fold decrease in activity relative to **7** (Table 1.2), showcasing synergy between ligand and metal redox activity.

1.9 Optimizing Photocatalytic Hydrogen Generation

The foregoing results prompted us to evaluate the photocatalytic performance of other cobalt(II)-based molecular catalysts. Importantly, these experiments required catalyst concentrations only at the micromolar level, enabling us to interrogate complexes that were not soluble enough for conventional aqueous electrochemistry. Again, using [Ru(bpy)₃]²⁺ and an aqueous ascorbate buffer, we evaluated the photocatalytic properties of ten cobalt-polypyridyl catalysts, including **9**, **11**, **14**, and **16** (Figure 1.10), using a high-throughput photochemical reactor developed by Castellano.⁶⁵ These findings highlighted several trends. First, Co(II) complexes bearing tetradentate ligands that enforce *cis* divacant coordination sites, such as **1**, **9**, **10**, and **11**, show higher activity for photocatalytic hydrogen generation compared those with

ligands that enforce *trans* sites, **15** and **16** (Figure 1.11a). Second, sustained photochemical hydrogen production is limited by the stability of $[\text{Ru}(\text{bpy})_3]^{2+}$, not the catalyst (Figure 1.11b). Third, transient absorption measurements suggest that a putative Co(I) intermediate forms during photocatalysis (Figure 1.11c). Finally, changes in pH had different effects on the activity for each catalyst. With each catalyst evaluated at its optimal pH, comparison of TONs reveal that catalysts with tetradentate ligands exhibit higher activity than those bearing pentadentate ligands, without losses in stability (Figure 1.11d, Table 1.2). The performance of **14**, which does not contain redox-active ligands, exemplifies the importance of denticity and implies that the operative photocatalytic mechanism in water substantially differs from the electrochemical mechanism utilizing weak organic acids.

1.10 Concluding Remarks

In this Account, we have summarized recent progress in our laboratories in the creation of molecular catalysts for electrochemical and photochemical water reduction. Specifically, we have developed a family of molybdenum- and cobalt-polypyridyl proton reduction catalysts that operate in pure water with high, selective, and robust activity. The foregoing examples highlight how molecular systems can conceptually and practically shed large portions of enzymatic and heterogeneous catalysts while retaining the minimal chemical unit needed for catalytic function. As such, molecular systems provide a useful, complementary approach to biological and materials catalysts for sustainable solar-to-fuel conversion. This work sets the stage for the broader application of polypyridyl systems to catalysis under environmentally benign aqueous conditions.

1.11 References

- (1) Bard, A. J.; Fox, M. A. Artificial Photosynthesis: Solar Splitting of Water to Hydrogen and Oxygen. *Acc. Chem. Res.* **1995**, *28*, 141–145.
- (2) Turner, J. A. Sustainable Hydrogen Production. *Science* **2004**, *305*, 972–974.
- (3) Gordon, R. B.; Bertram, M.; Graedel, T. E. Metal Stocks and Sustainability. *Proc. Natl. Acad. Sci. U.S.A.* **2006**, *103*, 1209–1214.
- (4) Lewis, N. S.; Nocera, D. G. Powering the Planet: Chemical Challenges in Solar Energy Utilization. *Proc. Natl. Acad. Sci. U.S.A.* **2006**, *103*, 15729–15735.
- (5) Armstrong, F. Hydrogenases: Active Site Puzzles and Progress. *Curr. Opin. Chem. Biol.* **2004**, *8*, 133–140.
- (6) Fontecilla-Camps, J. C.; Volbeda, A.; Cavazza, C.; Nicolet, Y. Structure/Function Relationships of [NiFe]- and [FeFe]-Hydrogenases. *Chem. Rev.* **2007**, *107*, 4273–4303.
- (7) Barton, B. E.; Olsen, M. T.; Rauchfuss, T. B. Artificial Hydrogenases. *Curr. Opin. Biotechnol.* **2010**, *21*, 292–297.
- (8) Cook, T. R.; Dogutan, D. K.; Reece, S. Y.; Surendranath, Y.; Teets, T. S.; Nocera, D. G. Solar Energy Supply and Storage for the Legacy and Nonlegacy Worlds. *Chem. Rev.* **2010**, *110*, 6474–6502.
- (9) Artero, V.; Chavarot-Kerlidou, M.; Fontecave, M. Splitting Water with Cobalt. *Angew. Chem. Int. Ed.* **2011**, *50*, 7238–7266.

- (10) Wang, M.; Chen, L.; Sun, L. Recent Progress in Electrochemical Hydrogen Production with Earth-Abundant Metal Complexes as Catalysts. *Energy Environ. Sci.* **2012**, *5*, 6763–6778.
- (11) Thoi, V. S.; Sun, Y.; Long, J. R.; Chang, C. J. Complexes of Earth-Abundant Metals for Catalytic Electrochemical Hydrogen Generation Under Aqueous Conditions. *Chem. Soc. Rev.* **2013**, *42*, 2388–2400.
- (12) McKone, J. R.; Marinescu, S. C.; Brunschwig, B. S.; Winkler, J. R.; Gray, H. B. Earth-Abundant Hydrogen Evolution Electrocatalysts. *Chem. Sci.* **2014**, *5*, 865–878.
- (13) Bullock, R. M.; Appel, A. M.; Helm, M. L. Production of Hydrogen by Electrocatalysis: Making the H–H Bond by Combining Protons and Hydrides. *Chem. Commun.* **2014**, *50*, 3125–3143.
- (14) Han, Z.; Eisenberg, R. Fuel From Water: the Photochemical Generation of Hydrogen From Water. *Acc. Chem. Res.* **2014**, *47*, 2537–2544.
- (15) DuBois, D. L. Development of Molecular Electrocatalysts for Energy Storage. *Inorg. Chem.* **2014**, *53*, 3935–3960.
- (16) Bigi, J. P.; Hanna, T. E.; Harman, W. H.; Chang, A.; Chang, C. J. Electrocatalytic Reduction of Protons to Hydrogen by a Water-Compatible Cobalt Polypyridyl Platform. *Chem. Commun.* **2010**, *46*, 958–960.
- (17) Goldsmith, C. R.; Jonas, R. T.; Stack, T. D. P. C-H Bond Activation by a Ferric Methoxide Complex: Modeling the Rate-Determining Step in the Mechanism of Lipxygenase. *J. Am. Chem. Soc.* **2002**, *124*, 83–96.
- (18) Klein Gebbink, R. J. M.; Jonas, R. T.; Goldsmith, C. R.; Stack, T. D. P. A Periodic Walk: a Series of First-Row Transition Metal Complexes with the Pentadentate Ligand PY5. *Inorg. Chem.* **2002**, *41*, 4633–4641.
- (19) Goldsmith, C. R.; Jonas, R. T.; Cole, A. P.; Stack, T. D. P. A Spectrochemical Walk: Single-Site Perturbation Within a Series of Six-Coordinate Ferrous Complexes. *Inorg. Chem.* **2002**, *41*, 4642–4652.
- (20) Bechlers, B.; D'Alessandro, D. M.; Jenkins, D. M.; Iavarone, A. T.; Glover, S. D.; Kubiak, C. P.; Long, J. R. High-Spin Ground States via Electron Delocalization in Mixed-Valence Imidazolate-Bridged Divanadium Complexes. *Nature Chem.* **2010**, *2*, 362–368.
- (21) Parkin, G.; Bercaw, J. E. (η^5 -C₅Me₅)₂W=O: an Exceptionally Reactive Organometallic Oxo Derivative. Reduction with Dihydrogen and Reaction with Dioxygen Resulting in Insertion of Oxygen Into a Tungsten-Carbon Bond. *J. Am. Chem. Soc.* **1989**, *111*, 391–393.
- (22) Silavwe, N. D.; Bruce, M. R. M.; Philbin, C. E.; Tyler, D. R. Descriptive Photochemistry and Electronic Structure of the Cp₂MoO and (MeCp)₂MoO Complexes (Cp = η^5 -C₅H₅; MeCp = η^5 -CH₃C₅H₄). *Inorg. Chem.* **1988**, *27*, 4669–4676.
- (23) Yoon, M.; Tyler, D. R. Activation of Water by Permethyltungstenocene; Evidence for the Oxidative Addition of Water. *Chem. Commun.* **1997**, 639–670.
- (24) Baxley, G. T.; Avey, A. A.; Aukett, T. M.; Tyler, D. R. Photoactivation of Water by Cp'₂Mo and Photochemical Studies of Cp₂MoO. Investigation of a Proposed Water-Splitting Cycle and Preparation of a Water-Soluble Molybdocene Dihydride. *Inorg. Chim. Acta* **2000**, *300*, 102–112.

- (25) Blum, O.; Milstein, D. Oxidative Addition of Water and Aliphatic Alcohols by $\text{IrCl}(\text{Trialkylphosphine})_3$. *J. Am. Chem. Soc.* **2002**, *124*, 11456–11467.
- (26) Karunadasa, H. I.; Chang, C. J.; Long, J. R. A Molecular Molybdenum-Oxo Catalyst for Generating Hydrogen From Water. *Nature* **2010**, *464*, 1329–1333.
- (27) Thoi, V. S.; Karunadasa, H. I.; Surendranath, Y.; Long, J. R.; Chang, C. J. Electrochemical Generation of Hydrogen From Acetic Acid Using a Molecular Molybdenum–Oxo Catalyst. *Energy Environ. Sci.* **2012**, *5*, 7762–7770.
- (28) Sundstrom, E. J.; Yang, X.; Thoi, V. S.; Karunadasa, H. I.; Chang, C. J.; Long, J. R.; Head-Gordon, M. Computational and Experimental Study of the Mechanism of Hydrogen Generation From Water by a Molecular Molybdenum-Oxo Electrocatalyst. *J. Am. Chem. Soc.* **2012**, *134*, 5233–5242.
- (29) Hinnemann, B.; Moses, P. G.; Bonde, J.; Jørgensen, K. P.; Nielsen, J. H.; Horch, S.; Chorkendorff, I.; Nørskov, J. K. Biomimetic Hydrogen Evolution: MoS_2 Nanoparticles as Catalyst for Hydrogen Evolution. *J. Am. Chem. Soc.* **2005**, *127*, 5308–5309.
- (30) Jaramillo, T. F.; Jørgensen, K. P.; Bonde, J.; Nielsen, J. H.; Horch, S.; Chorkendorff, I. Identification of Active Edge Sites for Electrochemical H_2 Evolution From MoS_2 Nanocatalysts. *Science* **2007**, *317*, 100–102.
- (31) Zong, X.; Yan, H.; Wu, G.; Ma, G.; Wen, F.; Wang, L.; Li, C. Enhancement of Photocatalytic H_2 Evolution on CdS by Loading MoS_2 As Cocatalyst Under Visible Light Irradiation. *J. Am. Chem. Soc.* **2008**, *130*, 7176–7177.
- (32) Li, Y.; Wang, H.; Xie, L.; Liang, Y.; Hong, G.; Dai, H. MoS_2 Nanoparticles Grown on Graphene: an Advanced Catalyst for the Hydrogen Evolution Reaction. *J. Am. Chem. Soc.* **2011**, *133*, 7296–7299.
- (33) Merki, D.; Fierro, S.; Vrubel, H.; Hu, X. Amorphous Molybdenum Sulfide Films as Catalysts for Electrochemical Hydrogen Production in Water. *Chem. Sci.* **2011**, *2*, 1262–1267.
- (34) Lukowski, M. A.; Daniel, A. S.; Meng, F.; Forticaux, A.; Li, L.; Jin, S. Enhanced Hydrogen Evolution Catalysis From Chemically Exfoliated Metallic MoS_2 Nanosheets. *J. Am. Chem. Soc.* **2013**, *135*, 10274–10277.
- (35) Karunadasa, H. I.; Montalvo, E.; Sun, Y.; Majda, M.; Long, J. R.; Chang, C. J. A Molecular MoS_2 Edge Site Mimic for Catalytic Hydrogen Generation. *Science* **2012**, *335*, 698–702.
- (36) Sun, Y.; Bigi, J. P.; Piro, N. A.; Tang, M. L.; Long, J. R.; Chang, C. J. Molecular Cobalt Pentapyridine Catalysts for Generating Hydrogen From Water. *J. Am. Chem. Soc.* **2011**, *133*, 9212–9215.
- (37) King, A. E.; Surendranath, Y.; Piro, N. A.; Bigi, J. P.; Long, J. R.; Chang, C. J. A Mechanistic Study of Proton Reduction Catalyzed by a Pentapyridine Cobalt Complex: Evidence for Involvement of an Anation-Based Pathway. *Chem. Sci.* **2013**, *4*, 1578–1587.
- (38) Shi, S.; Daniels, L. M.; Espenson, J. H. Molecular Structure of a Cobalt(I) Complex Lacking a Carbonyl Ligand. A Unique Example of Cobalt-Nitrogen Bond Shortening. *Inorg. Chem.* **1991**, *30*, 3407–3410.
- (39) Hu, X.; Cossairt, B. M.; Brunschwig, B. S.; Lewis, N. S.; Peters, J. C. Electrocatalytic Hydrogen Evolution by Cobalt Difluoroboryl-Diglyoximate Complexes. *Chem. Commun.* **2005**, 4723–4725.

- (40) Hu, X.; Brunschwig, B. S.; Peters, J. C. Electrocatalytic Hydrogen Evolution at Low Overpotentials by Cobalt Macrocyclic Glyoxime and Tetraimine Complexes. *J. Am. Chem. Soc.* **2007**, *129*, 8988–8998.
- (41) Sun, Y.; Sun, J.; Long, J. R.; Yang, P.; Chang, C. J. Photocatalytic Generation of Hydrogen From Water Using a Cobalt Pentapyridine Complex in Combination with Molecular and Semiconductor Nanowire Photosensitizers. *Chem. Sci.* **2013**, *4*, 118–124.
- (42) Razavet, M.; Artero, V.; Fontecave, M. Proton Electroreduction Catalyzed by Cobaloximes: Functional Models for Hydrogenases. *Inorg. Chem.* **2005**, *44*, 4786–4795.
- (43) Baffert, C.; Artero, V.; Fontecave, M. Cobaloximes as Functional Models for Hydrogenases. 2. Proton Electroreduction Catalyzed by Difluoroborylbis(Dimethylglyoximato)Cobalt(II) Complexes in Organic Media. *Inorg. Chem.* **2007**, *46*, 1817–1824.
- (44) Fourmond, V.; Jacques, P.-A.; Fontecave, M.; Artero, V. H₂ Evolution and Molecular Electrocatalysts: Determination of Overpotentials and Effect of Homoconjugation. *Inorg. Chem.* **2010**, *49*, 10338–10347.
- (45) McCrory, C. C. L.; Uyeda, C.; Peters, J. C. Electrocatalytic Hydrogen Evolution in Acidic Water with Molecular Cobalt Tetraazamacrocycles. *J. Am. Chem. Soc.* **2012**, *134*, 3164–3170.
- (46) Jacobsen, G. M.; Yang, J. Y.; Twamley, B.; Wilson, A. D.; Bullock, R. M.; Rakowski DuBois, M.; DuBois, D. L. Hydrogen Production Using Cobalt-Based Molecular Catalysts Containing a Proton Relay in the Second Coordination Sphere. *Energy Environ. Sci.* **2008**, *1*, 167–174.
- (47) Fang, M.; Wiedner, E. S.; Dougherty, W. G.; Kassel, W. S.; Liu, T.; DuBois, D. L.; Bullock, R. M. Cobalt Complexes Containing Pendant Amines in the Second Coordination Sphere as Electrocatalysts for H₂ Production. *Organometallics* **2014**, *33*, 5820–5833.
- (48) Dempsey, J. L.; Brunschwig, B. S.; Winkler, J. R.; Gray, H. B. Hydrogen Evolution Catalyzed by Cobaloximes. *Acc. Chem. Res.* **2009**, *42*, 1995–2004.
- (49) Dempsey, J. L.; Winkler, J. R.; Gray, H. B. Kinetics of Electron Transfer Reactions of H₂-Evolving Cobalt Diglyoxime Catalysts. *J. Am. Chem. Soc.* **2010**, *132*, 1060–1065.
- (50) Stubbert, B. D.; Peters, J. C.; Gray, H. B. Rapid Water Reduction to H₂ Catalyzed by a Cobalt Bis(Iminopyridine) Complex. *J. Am. Chem. Soc.* **2011**, *133*, 18070–18073.
- (51) Marinescu, S. C.; Winkler, J. R.; Gray, H. B. Molecular Mechanisms of Cobalt-Catalyzed Hydrogen Evolution. *Proc. Natl. Acad. Sci. U.S.A.* **2012**, *109*, 15127–15131.
- (52) McNamara, W. R.; Han, Z.; Alperin, P. J.; Brennessel, W. W.; Holland, P. L.; Eisenberg, R. A Cobalt–Dithiolene Complex for the Photocatalytic and Electrocatalytic Reduction of Protons. *J. Am. Chem. Soc.* **2011**, *133*, 15368–15371.
- (53) McNamara, W. R.; Han, Z.; Yin, C.-J. M.; Brennessel, W. W.; Holland, P. L.; Eisenberg, R. Cobalt–Dithiolene Complexes for the Photocatalytic and Electrocatalytic Reduction of Protons in Aqueous Solutions. *Proc. Natl. Acad. Sci. U.S.A.* **2012**, *109*, 15594–15599.
- (54) Probst, B.; Guttentag, M.; Rodenberg, A.; Hamm, P.; Alberto, R. Photocatalytic H₂ Production From Water with Rhenium and Cobalt Complexes. *Inorg. Chem.* **2011**, *50*, 3404–3412.

- (55) Rodenberg, A.; Oraziotti, M.; Probst, B.; Bachmann, C.; Alberto, R.; Baldrige, K. K.; Hamm, P. Mechanism of Photocatalytic Hydrogen Generation by a Polypyridyl-Based Cobalt Catalyst in Aqueous Solution. *Inorg. Chem.* **2015**, *54*, 646–657.
- (56) Chen, L.; Wang, M.; Han, K.; Zhang, P.; Gloaguen, F.; Sun, L. A Super-Efficient Cobalt Catalyst for Electrochemical Hydrogen Production From Neutral Water with 80 mV Overpotential. *Energy Environ. Sci.* **2013**, *7*, 329–334.
- (57) Zhang, P.; Wang, M.; Gloaguen, F.; Chen, L.; Quentel, F.; Sun, L. Electrocatalytic Hydrogen Evolution From Neutral Water by Molecular Cobalt Tripyridine-Diamine Complexes. *Chem. Commun.* **2013**, *49*, 9455–9457.
- (58) Singh, W. M.; Baine, T.; Kudo, S.; Tian, S.; Ma, X. A. N.; Zhou, H.; DeYonker, N. J.; Pham, T. C.; Bollinger, J. C.; Baker, D. L.; Yan, B.; Webster, C. E.; Zhao, X. Electrocatalytic and Photocatalytic Hydrogen Production in Aqueous Solution by a Molecular Cobalt Complex. *Angew. Chem. Int. Ed. Engl.* **2012**, *51*, 5941–5944.
- (59) Lee, C. H.; Dogutan, D. K.; Nocera, D. G. Hydrogen Generation by Hangman Metalloporphyrins. *J. Am. Chem. Soc.* **2011**, *133*, 8775–8777.
- (60) Singh, W. M.; Mirmohades, M.; Jane, R. T.; White, T. A.; Hammarström, L.; Thapper, A.; Lomoth, R.; Ott, S. Voltammetric and Spectroscopic Characterization of Early Intermediates in the Co(II)–Polypyridyl-Catalyzed Reduction of Water. *Chem. Commun.* **2013**, *49*, 8638–8640.
- (61) Mandal, S.; Shikano, S.; Yamada, Y.; Lee, Y.-M.; Nam, W.; Llobet, A.; Fukuzumi, S. Protonation Equilibrium and Hydrogen Production by a Dinuclear Cobalt–Hydride Complex Reduced by Cobaltocene with Trifluoroacetic Acid. *J. Am. Chem. Soc.* **2013**, *135*, 15294–15297.
- (62) Tong, L.; Zong, R.; Thummel, R. P. Visible Light-Driven Hydrogen Evolution From Water Catalyzed by a Molecular Cobalt Complex. *J. Am. Chem. Soc.* **2014**, *136*, 4881–4884.
- (63) Letko, C. S.; Panetier, J. A.; Head-Gordon, M.; Tilley, T. D. Mechanism of the Electrocatalytic Reduction of Protons with Diaryldithiolene Cobalt Complexes. *J. Am. Chem. Soc.* **2014**, *136*, 9364–9376.
- (64) Nippe, M.; Khnayzer, R. S.; Panetier, J. A.; Zee, D. Z.; Olaiya, B. S.; Head-Gordon, M.; Chang, C. J.; Castellano, F. N.; Long, J. R. Catalytic Proton Reduction with Transition Metal Complexes of the Redox-Active Ligand bpy2PYMe. *Chem. Sci.* **2013**, *4*, 3934–3945.
- (65) Khnayzer, R. S.; Thoi, V. S.; Nippe, M.; King, A. E.; Jurss, J. W.; Roz, El, K. A.; Long, J. R.; Chang, C. J.; Castellano, F. N. Towards a Comprehensive Understanding of Visible-Light Photogeneration of Hydrogen From Water Using Cobalt(II) Polypyridyl Catalysts. *Energy Environ. Sci.* **2014**, *7*, 1477–1488.
- (66) Voloshin, Y. Z.; Dolganov, A. V.; Varzatskii, O. A.; Bubnov, Y. N. Efficient Electrocatalytic Hydrogen Production From H⁺ Ions Using Specially Designed Boron-Capped Cobalt Clathrochelates. *Chem. Commun.* **2011**, *47*, 7737–7739.
- (67) Anxolabéhère-Mallart, E.; Costentin, C.; Fournier, M.; Nowak, S.; Robert, M.; Savéant, J.-M. Boron-Capped Tris(Glyoximato) Cobalt Clathrochelate as a Precursor for the Electrodeposition of Nanoparticles Catalyzing H₂ Evolution in Water. *J. Am. Chem. Soc.* **2012**, *134*, 6104–6107.

- (68) Ghachtouli, El, S.; Fournier, M.; Cherdo, S.; Guillot, R.; Charlot, M.-F.; Anxolabéhère-Mallart, E.; Robert, M.; Aukauloo, A. Monometallic Cobalt–Trisglyoximato Complexes as Precatalysts for Catalytic H₂ Evolution in Water. *J. Phys. Chem. C* **2013**, *117*, 17073–17077.
- (69) Ghachtouli, El, S.; Guillot, R.; Brisset, F.; Aukauloo, A. Cobalt-Based Particles Formed Upon Electrocatalytic Hydrogen Production by a Cobalt Pyridine Oxime Complex. *ChemSusChem* **2013**, *6*, 2226–2230.
- (70) Anxolabéhère-Mallart, E.; Costentin, C.; Fournier, M.; Robert, M. Cobalt-Bisglyoximato Diphenyl Complex as a Precatalyst for Electrocatalytic H₂ Evolution. *J. Phys. Chem. C* **2014**, *118*, 13377–13381.
- (71) Artero, V.; Savéant, J.-M. Toward the Rational Benchmarking of Homogeneous H₂-Evolving Catalysts. *Energy Environ. Sci.* **2014**, *7*, 3808–3814.

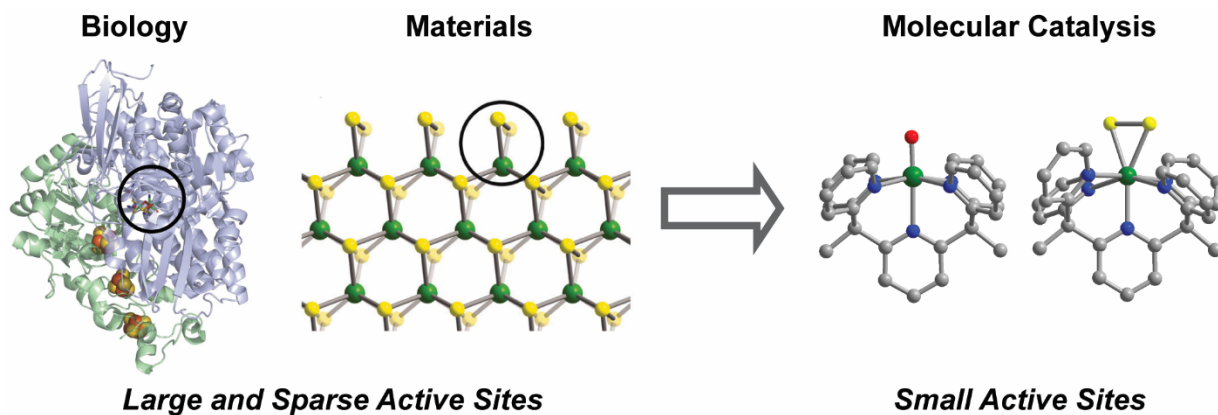


Figure 1.1. Hydrogenase enzymes (far left) and MoS₂ (molybdenite, second from left) are proton reduction catalysts from biology and materials, respectively. Black circles delineate the small and sparse active sites among the large, overall structures: the [NiFe] cofactor of [NiFe]-hydrogenase enzymes (molecular weight ~60,000 kDa), and the disulfide-terminated (1 0 -1 0) edge of MoS₂. Molecular catalysts (right) can capture the functional essence of these biological and materials systems in a compact and tunable active site.

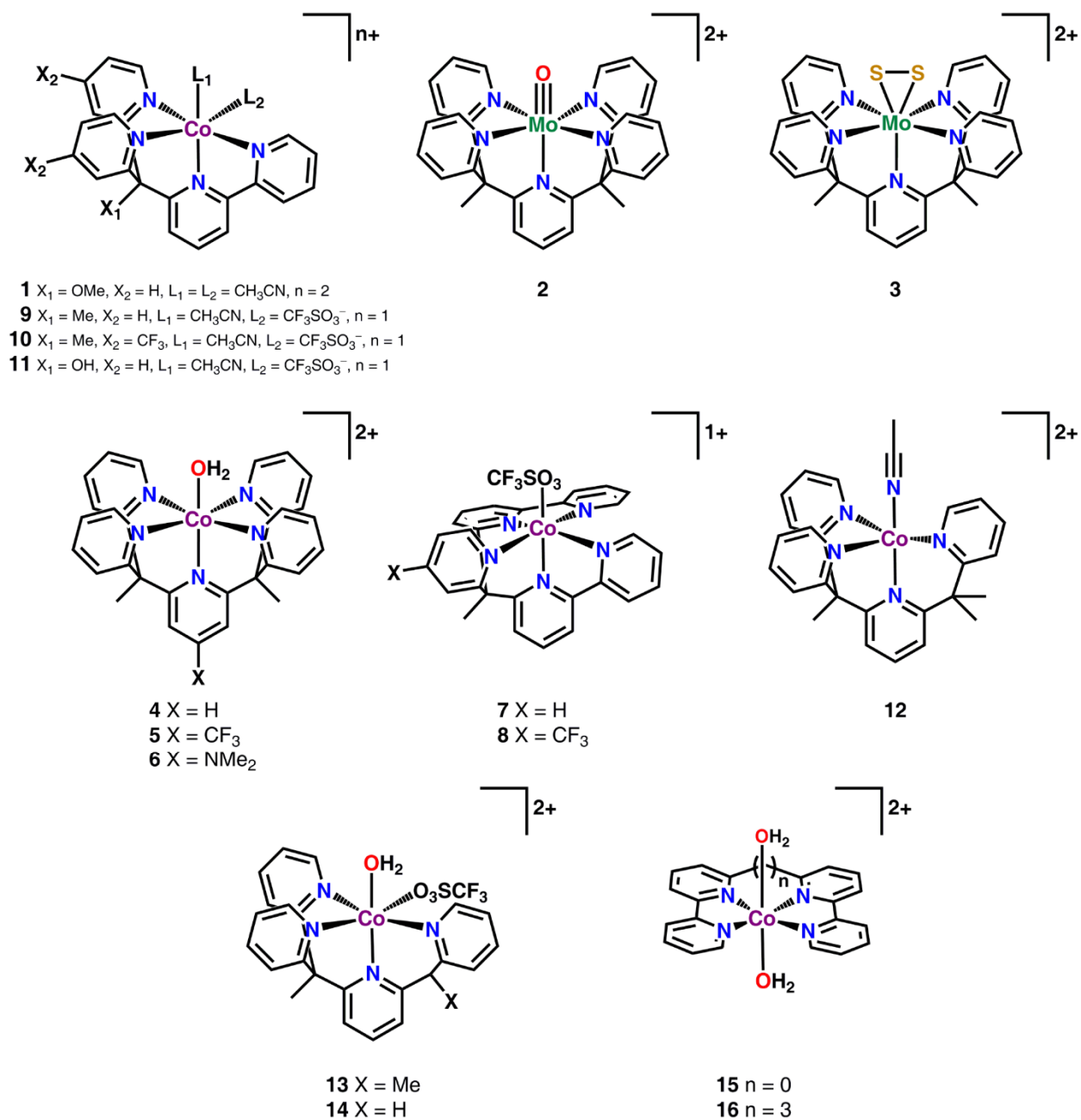


Figure 1.2. Molecular metal-polypyridyl H_2 evolution catalysts from our laboratories.

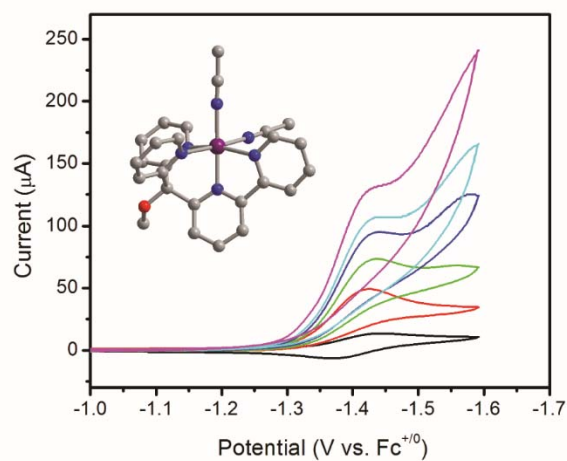


Figure 1.3. Cyclic voltammogram of **1** in a 1:1 water/CH₃CN (v/v) mixture (black), with a glassy carbon working electrode. The Co(II/I) couple occurs *ca.* -1.4 V versus the ferrocenium/ferrocene couple (Fc⁺⁰). Increasing concentrations of TFA give corresponding rises of catalytic current (red, green blue, cyan, and purple). The inset shows the crystal structure of **1**, R₁ (wR₂) = 5.20% (13.3%).

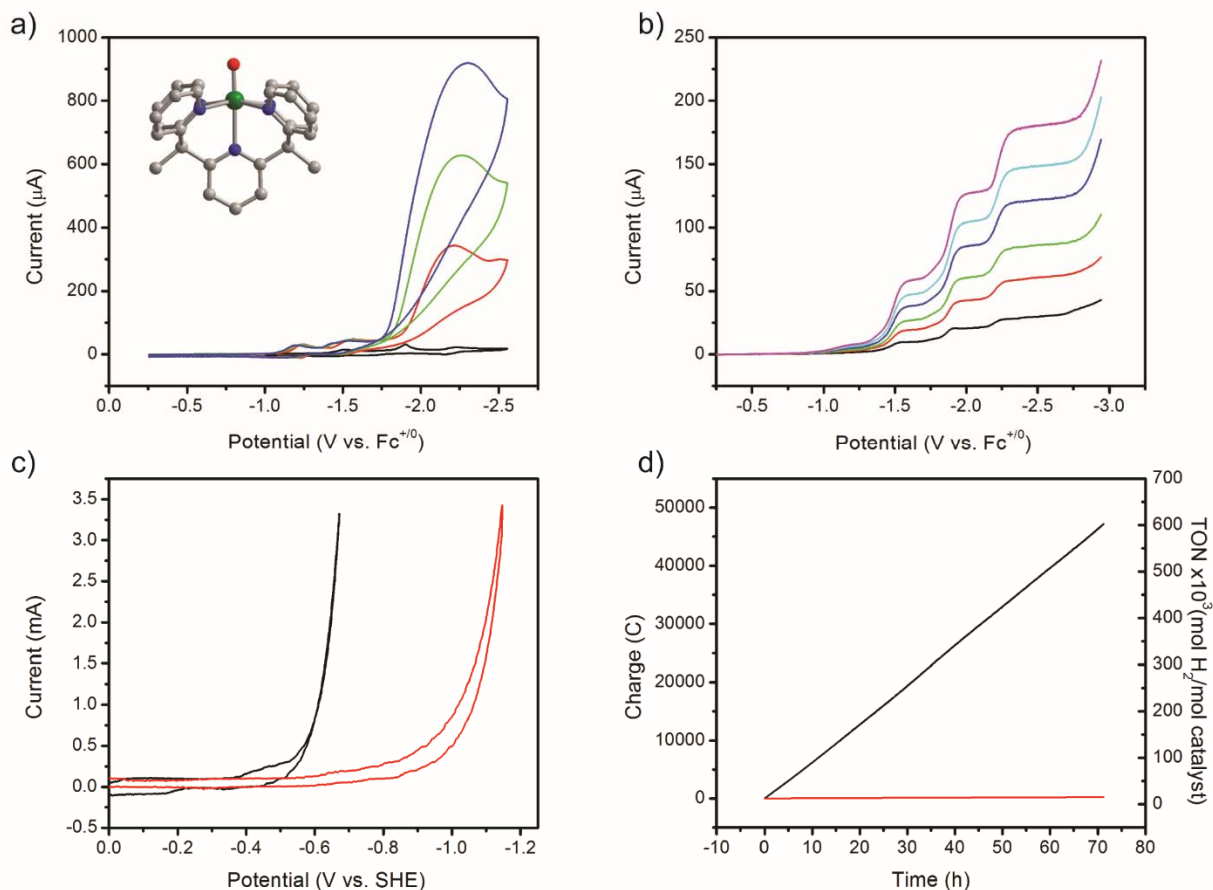


Figure 1.4. a) CV of 2 in CH₃CN at a glassy carbon electrode (black). Addition of acetic acid causes current enhancement at the third reduction, with plateaus occurring at *ca.* -2.25 V vs Fc⁺⁰. The inset shows the crystal structure of 2, R_1 (wR_2) = 3.64% (9.82%). b) Rotating disk electrode voltammograms (100 to 3600 rpm) of 2 in CH₃CN (glassy carbon). Traces show three distinct plateaus, indicating three reduction processes. c) CV in a 0.6 M aqueous phosphate buffered to pH 7 at a Hg pool electrode in the absence (red), and presence of 2 (black). d) CPE at -1.40 V vs SHE in the absence (red) and presence of 2 (2 μM, black) in 3.0 M phosphate buffered to pH 7. Complex 2 remains catalytically active after 72 h of electrolysis.

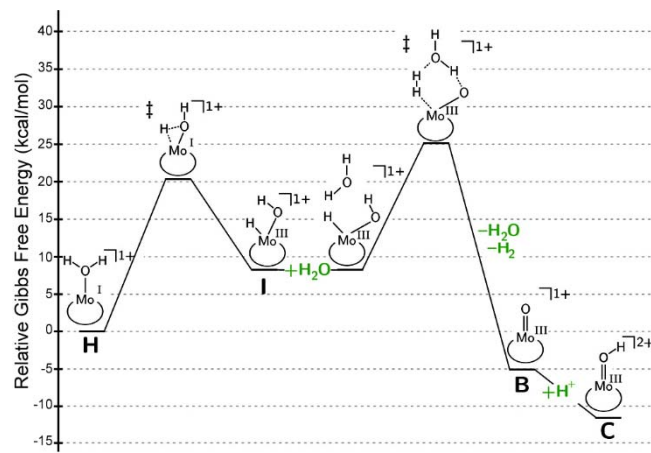


Figure 1.5. Gibbs free energy diagram for the liberation of H₂ from H, which is formed by the reduction of 2.

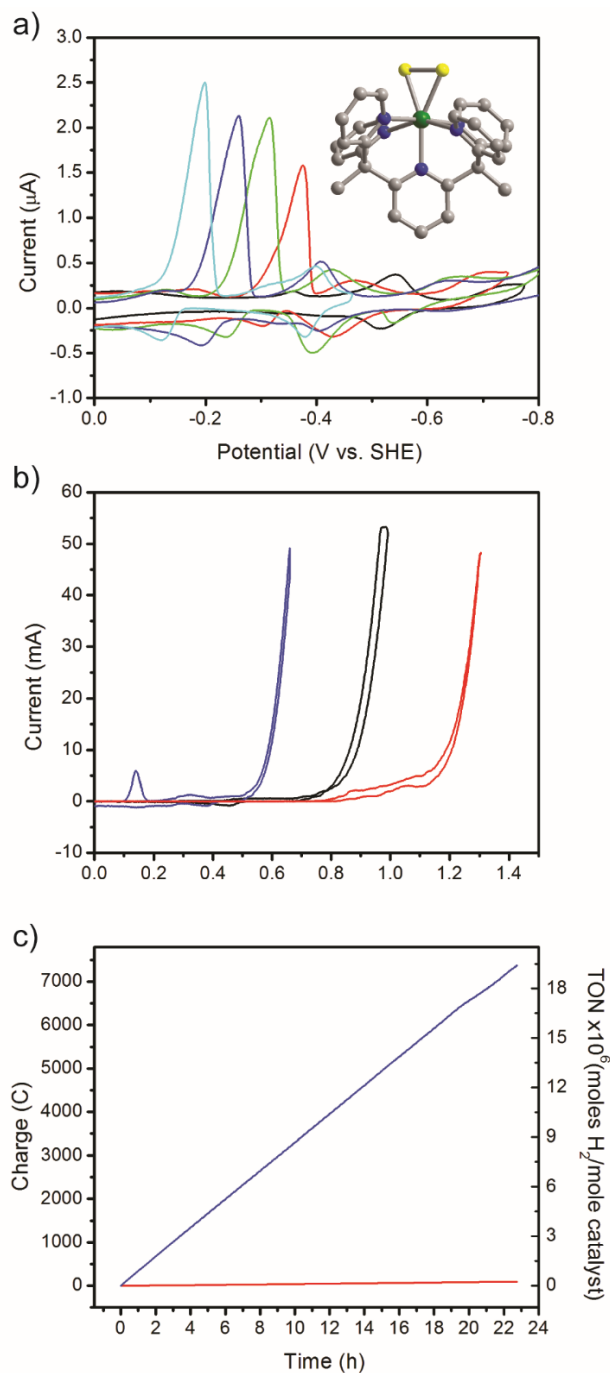


Figure 1.6. a) CVs of 3 in 0.05 M phosphate buffered to pH ranging from 3 to 7. The first reductive wave shifts by *ca.* 60 mV per unit change in pH, suggesting that the reduction is proton-coupled. Inset shows the crystal structure of 3, R_1 (wR_2) = 2.85% (6.08%). b) CVs of 1 M acetate buffer at pH 3 at a mercury pool electrode (red) with 2 (130 μ M, black) and 3 (130 μ M, blue). c) CPE of 3 (66 μ M) in 3 M aqueous acetate buffer (blue) versus the buffer alone (red) at -0.96 V vs SHE ($\eta = 0.78$ V).

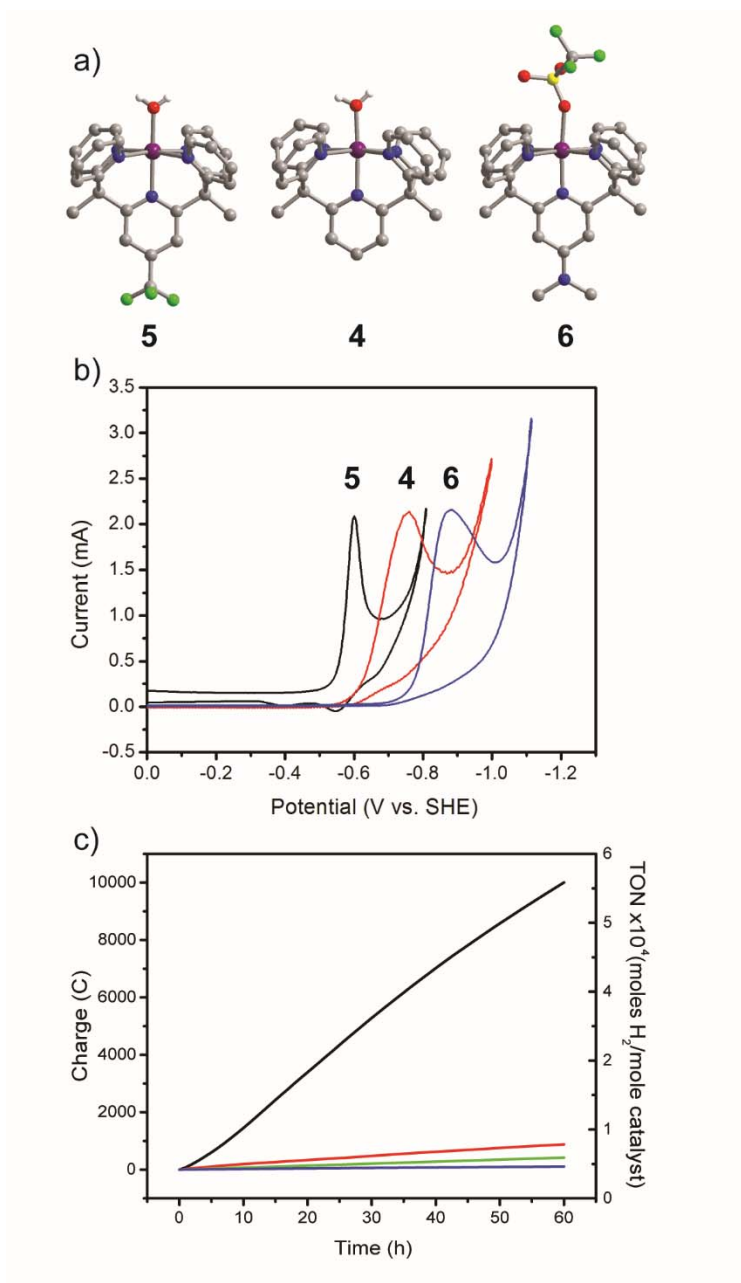


Figure 1.7. a) Crystal structures of 4, 5, and 6, R_1 (wR_2) = 3.04% (8.19%), 2.62% (6.67%), and 6.11% (18.9%). b) Normalized CVs of 4 (red), 5 (black) and 6 (blue) in 1 M phosphate buffer at pH 7 at a Hg pool electrode. c) CPE at -1.30 V vs SHE of 4 (black), $[(PY5Me_2)Zn(H_2O)]^{2+}$ (green), PY5Me₂ ligand (red) and without additives (blue). Control experiments show that the ligand or metal alone or an isostructural PY5Me₂ complex with Zn(II) are inactive for catalysis. Only the CoPY5Me₂ unit shows competent reactivity. All electrolyses were performed in 2 M phosphate buffer at pH 7.

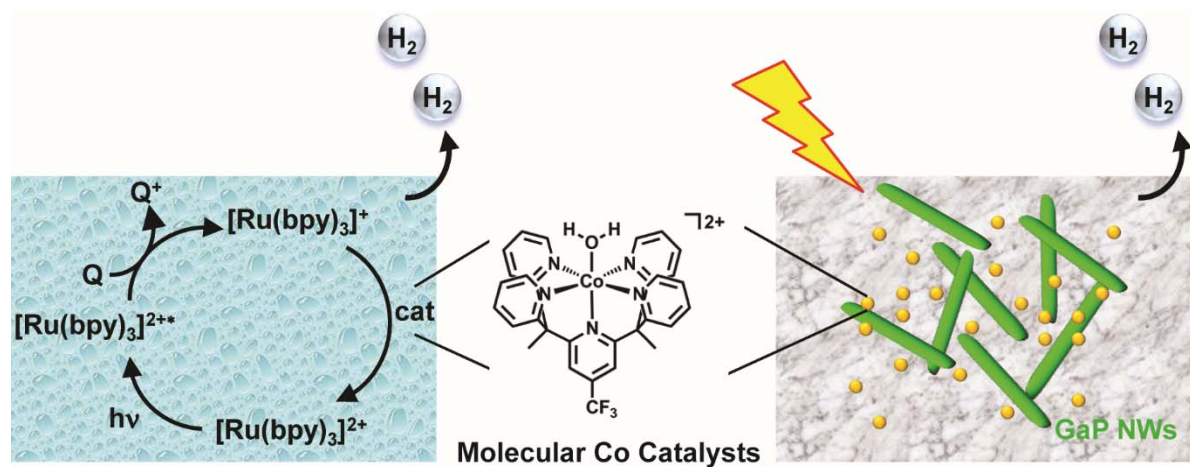


Figure 1.8. Photochemical generation of H_2 by 5 photosensitized with either $[\text{Ru}(\text{bpy})_3]^{2+}$ (left) or GaP nanowires (right), with ascorbate as a sacrificial reductant.

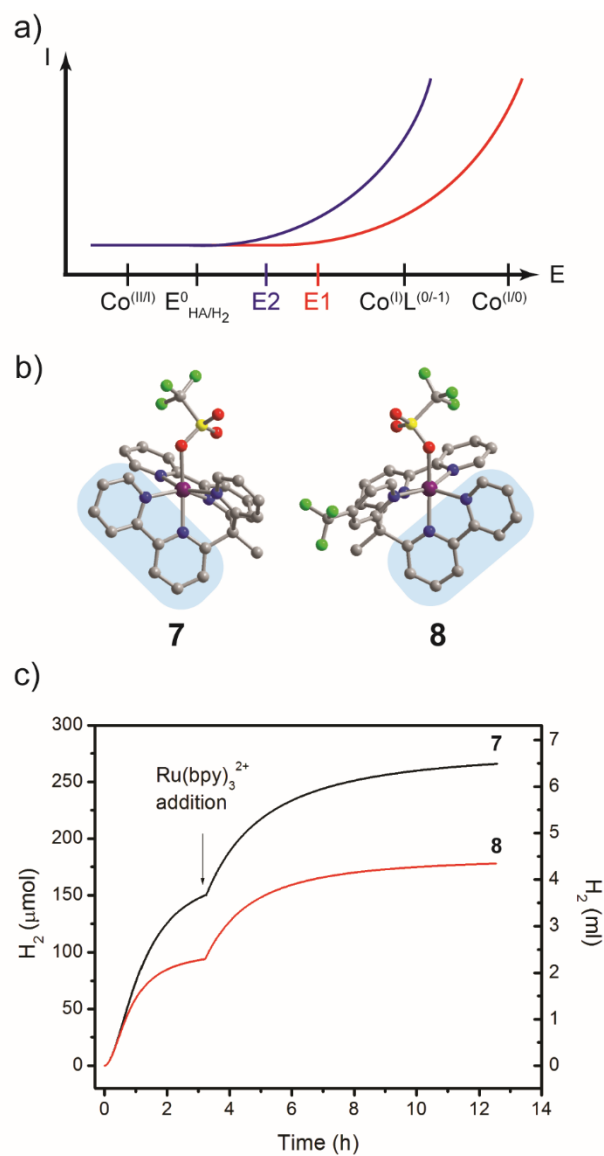


Figure 1.9. a) To reduce a weak acid such as water, catalysis may involve a Co(II/0) process, with a driving force of E1 (red). Introduction of a ligand-based redox state gives a new driving force E2 that can afford catalysis at less extreme potentials (blue). b) Crystal structures of 7 and 8, R_1 (wR_2) = 3.61% (9.25%) and 3.32% (7.83%). Blue areas highlight one of the redox-active bpy moieties. c) Photocatalytic H_2 evolution in water by 7 and 8. Once catalysis levels off, addition of $[\text{Ru}(\text{bpy})_3]^{2+}$ regenerates activity.

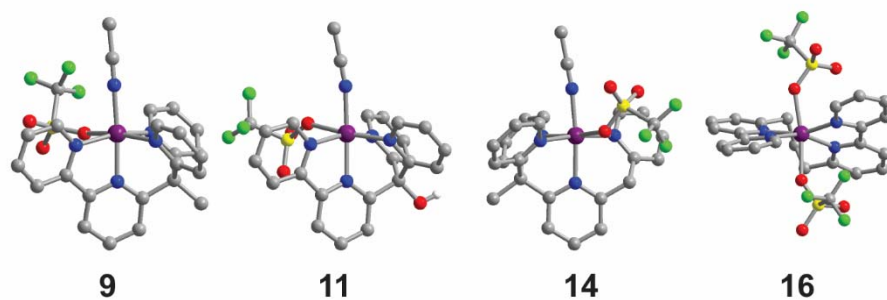


Figure 1.10. Crystal structures of 9, 11, 14, and 15, R_1 (wR_2) = 2.53% (6.58%), 2.75% (11.3%), 2.77% (6.60%), and 2.96% (7.01%). 9, 11 and 14 contain two *cis* open sites while 16 has two *trans* open sites.

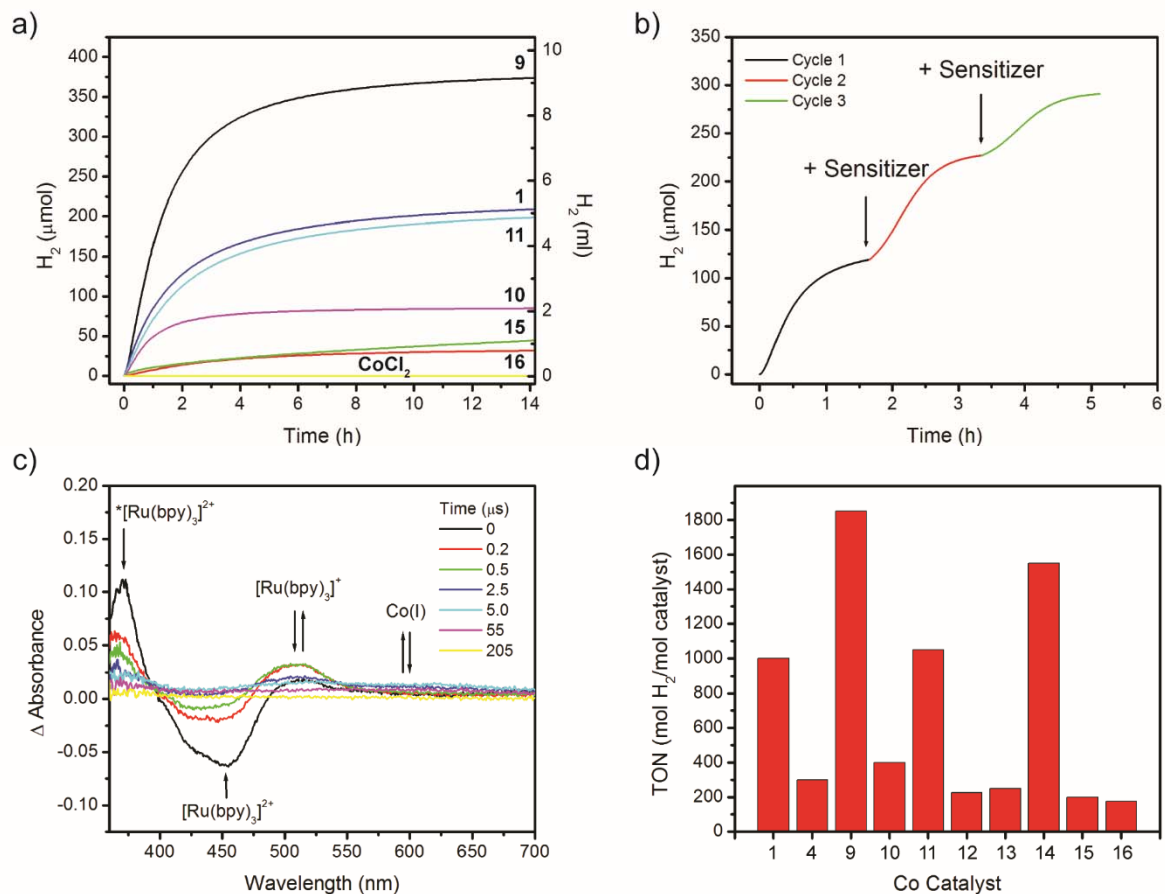


Figure 1.11. a) Photocatalytic hydrogen production versus time of different Co catalysts. b) Catalysis is limited by photosensitizer stability. c) Transient absorption difference spectra shows formation of a Co(I) species of 9 coinciding with disappearance of $[\text{Ru}(\text{bpy})_3]^+$. d) TONs of different Co catalysts at their respective optimal pH.

Table 1.1. CPE Data of Hydrogen-Producing Catalysts.

	Applied Potential (η^a)	Faradaic Efficiency (%)	TON (reaction time) (mol H ₂ (mol cat) ⁻¹)	TOF (mol H ₂ (mol cat h) ⁻¹)	Electrode ^b	Electrolyte	Ref
1	-1.40 V vs Fc ⁺⁰ (0.62 V)	99	–	40 ^c	GC	65 mM TFA ^d in CH ₃ CN ^e	16
2	-1.40 V vs SHE (0.99 V)	100	610,000 (72 h)	8,500 ^f	Hg	3.0 M pH 7 phosphate in H ₂ O	26
2	-2.24 V vs Fc ⁺⁰ (0.90 V)	99	3.7 (1 h)	3.7 ^f	GC	170 eq AcOH ^g in CH ₃ CN ^e	27
3	-0.96V vs SHE (0.78 V)	100	19,000,000 (23 h) ^h	830,000 ^{h,i}	Hg	3.0 M pH 3 acetate in H ₂ O	35
3	-1.73 V vs Fc ⁺⁰ (0.39 V)	100	5.7 (2.75 h)	2.1 ^f	GC	160 eq AcOH ^g in CH ₃ CN ^e	35
4	-1.30 V vs SHE (0.89 V)	100	55,000 (60 h)	920 ^f	Hg	2.0 M pH 7 phosphate in H ₂ O	36
5	-0.96 V vs SHE (0.55 V)	95	–	–	GC	0.1 M pH 7 phosphate in H ₂ O	41
7	-1.80 V vs Fc ⁺⁰ (0.46 V)	90	–	–	GC	AcOH ^g in CH ₃ CN ^e	64

^a η = overpotential = applied potential – (0.059 V x pH) in water. η = applied potential – [($E^{\circ}_{H^+/H_2}$) – (0.059 V x pK_a)] for nonaqueous systems.⁷¹

^bGC = glassy carbon

^cEstimated from CV data.

^d E° = –0.78 V vs Fc⁺⁰.

^eWith 0.1 M NBu₄PF₆ as supporting electrolyte.

^fThese numbers are estimated from the CPE data assuming all catalyst molecules in solution participate in the reaction at any given time. Thus they represent a *lower bound* of the true TOF.

^g E° = –1.34 V vs Fc⁺⁰.

^hCalculated based on the estimated surface coverage of the catalyst on the Hg pool.

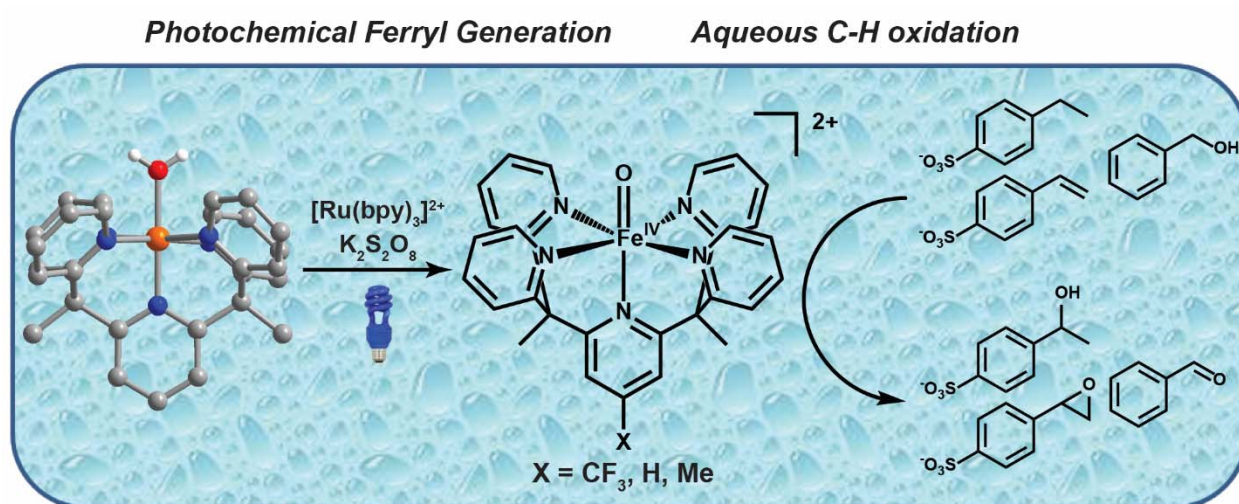
ⁱIn an optimized medium, the TOF reaches 480 moles H₂ per mole catalyst per second.³⁵
– no published data available.

Table 1.2. Photolytic Hydrogen Production by Molecular Cobalt Catalysts.**Photolysis conditions: 330 μM $[\text{Ru}(\text{bpy})_3]^{2+}$, 0.3 M ascorbate buffer, and 20 μM catalyst in

	TON (mol H ₂ (mol cat) ⁻¹)	TOF (mol H ₂ (mol cat h) ⁻¹)	pH with highest activity	Reaction time (h)	Ref
1	1015	73	4.5	14	65
4	290	22	6.0	13	64
5	300	23	6.0	13	64
7	1625	125	4.0	13	64
8	1375	106	4.5	13	64
9	1875	134	4.0	14	65
10	425	30	4.5	14	65
11	1065	76	4.0	14	65
12	235	13	5.0	18	65
13	260	14	5.5	18	65
14	1565	87	5.0	18	65
15	225	16	5.5	14	65
16	150	11	5.0	14	65

water, irradiated at 452 nm with 540 mW output.

Chapter 2. Water-Soluble Iron(IV)-Oxo Complexes Supported by Pentapyridine Ligands: Axial Ligand Effects on Hydrogen Atom and Oxygen Atom Transfer Reactivity



This chapter includes work published in: [Chantarojsiri, T., Sun, Y. S., Long, J. R., Chang, C. J. *Inorg. Chem.*, 2015, 54, 5879–5887.](#)

2.1 Abstract

We report the photochemical generation and study of a family of water-soluble iron(IV)-oxo complexes supported by pentapyridine PY5Me₂-X ligands (PY5Me₂ = 2,6-bis(1,1-bis(2-pyridyl)ethyl)pyridine; X = CF₃, H, Me, or NMe₂), in which the oxidative reactivity of these ferryl species correlates with the electronic properties of the axial pyridine ligand. Synthesis of a systematic series of [Fe^{II}(L)(PY5Me₂-X)]²⁺ complexes, where L = CH₃CN or H₂O, and characterizations by several methods, including X-ray crystallography, cyclic voltammetry, and Mössbauer spectroscopy, show that increasing the electron-donating ability of the axial pyridine ligand tracks with less positive Fe(III)/Fe(II) reduction potentials and quadrupole splitting parameters. The Fe^{II} precursors are readily oxidized to their Fe(IV)-oxo counterparts using either chemical outer-sphere oxidants such as CAN (ceric ammonium nitrate) or flash-quench photochemical oxidation with [Ru(bpy)₃]²⁺ as a photosensitizer and K₂S₂O₈ as a quencher. The Fe(IV)-oxo complexes are capable of oxidizing the C-H bonds of alkane (4-ethylbenzenesulfonate) and alcohol (benzylalcohol) substrates via hydrogen atom transfer (HAT) and an olefin (4-styrenesulfonate) substrate by oxygen atom transfer (OAT). The [Fe^{IV}(O)(PY5Me₂-X)]²⁺ derivatives with electron-poor axial ligands show faster rates of HAT and OAT compared to their counterparts supported by electron-rich axial donors, but the magnitudes of these differences are relatively modest.

2.2 Introduction

High-valent iron-oxo intermediates play important roles in chemical and biological oxidations.¹⁻¹⁵ Iron coordinated within heme- and non-heme-dependent enzyme active sites are capable of a diverse array of oxidative transformations, including hydrogen atom transfer (HAT) from and O-atom transfer (OAT) to hydrocarbon substrates, as well as oxidation of phosphines, sulfides, and amines.¹⁵⁻²² This rich reactivity continues to inspire the development of synthetic analogs, particularly Fe(IV)-oxo moieties with $S = 1$ ²³⁻³⁶ or $S = 2$ spin states.³⁷⁻⁴³ In contrast to their enzymatic counterparts, however, the vast majority of biomimetic Fe(IV)-oxo complexes have been prepared and studied in organic solution. Inspired by the wealth of elegant synthetic chemistry using amine- and pyridine-based ligands for supporting ferryl intermediates, for example, cyclam,^{23,24,31,36,44} N4PY,²⁶ BnTPEN,⁴⁵ Me₂TACN-Py₂,⁴⁶ BP1 and BP2,^{28,47,48} as well as our laboratories' work on the development of water-soluble molecular catalysts for reduction of protons to hydrogen,⁴⁹⁻⁵² we sought to expand the palette of this synthetic chemistry to aqueous media.

In this report, we present the chemical and photochemical generation, spectroscopy, and reactivity of water-soluble Fe(IV)-oxo complexes supported by an isostructural family of pentapyridine ligands where the electronic properties of the axial pyridine *trans*- to the oxo moiety can be tuned in a systematic fashion. This series of compounds allows us to probe axial ligand effects on ferryl reactivity in water, which is of fundamental interest with regard to both heme and non-heme systems.^{4,27,31,32,53-58} Indeed, in one notable study from the bioinorganic model literature, evaluation of [FeTMC(MeCN)₂]²⁺ (TMC = tetramethylcyclam) complexes with a variety of anionic axial ligands (OH⁻, CF₃CO⁻, N₃⁻, NCS⁻, NCO⁻) in organic solution show that the rates of OAT reactions decrease with increasing electronic density, whereas HAT reactivity increases with more electron-rich ligands.^{4,27,30,31} Here, we provide a complementary set of data

on axial ligand effects of neutral pyridine donors on ferryl reactivity in aqueous solution, focusing on OAT and HAT reactivity with hydrocarbon substrates.

2.3 Results and Discussion

2.3.1 Fe(II)-PY5Me₂ Complexes with Varying Electronic Properties

We reasoned that varying substituents on the *para* position of the axial pyridine in a PY5Me₂ scaffold would directly tune electron density in the d_z^2 orbital and hence allow us to evaluate the influence of these electronic changes on Fe-oxo bonding and reactivity. As a first step toward this goal, we synthesized a series of Fe(II)-PY5Me₂-X complexes (where X = CF₃, H, Me, or NMe₂) with a span of electron-donating and electron-withdrawing groups (Scheme 2.1). Mixing equimolar amounts of Fe(OTf)₂ and ligand in MeCN at room temperature yields the compounds [Fe^{II}(MeCN)(PY5Me₂-X)](OTf)₂ (**1-X**, X = CF₃, H, Me, NMe₂). As expected, the complexes are low-spin d^6 and diamagnetic ($S = 0$) and can be readily characterized by NMR spectroscopy. Crystal structures show that the **1-X** series of complexes show high structural similarity, as evidenced by their Fe-N bond lengths and N-Fe-N bond angles (Figure 2.1). Upon dissolution of the compounds **1-X** in water or when [Fe^{II}(OH₂)₆](BF₄)₂ was used as a starting material, the corresponding [Fe^{II}(OH₂)(PY5Me₂)]²⁺ complexes (**2-X**, X = CF₃, H, Me, NMe₂) were obtained (Scheme 2.1). Similar to what is observed for their Fe(II)-acetonitrile counterparts, crystal structures of the Fe(II)-aqua complexes show comparable Fe-N bond lengths within the series (Figure 2.1). During the preparation of this manuscript, **2-NMe₂** was reported as a potential MRI contrast agent.⁵⁹

Despite structural similarities between the different derivatives, cyclic voltammetry measurements on complexes **1-X** reveal that the Fe(III/II) redox potentials in MeCN solution can vary by up to 300 mV between the most electron-withdrawing (**1-CF₃**, +0.86 V vs Ag/AgCl) and electron-donating (**1-NMe₂**, +0.56 V vs Ag/AgCl) congeners. Overall, the Fe(III/II) redox potentials correlate well with the Hammett parameter (σ_p)⁶⁰ of the added substituents (Figure 2.2, 2.3 and Table 2.1), where electron-rich derivatives are more easily oxidized from Fe(II) to Fe(III).

The Fe(II)-aqua series, **2-X**, exhibit a similar trend, with the Fe(III/II) redox potential of the NMe₂ derivative being 200 mV more negative than that of the CF₃ derivative (Figure 2.4, top). Moreover, the Fe^{III/II} redox potentials of these aqua complexes show a linear dependence on pH with a slope of 59 mV/pH within the pH 3-6 range, establishing that the redox process is proton-coupled and likely involves conversion of the Fe(II)-OH₂ to an Fe(III)-OH species (Figure 2.4, bottom), akin to what Stack observed in related FePY5 models for lipoxygenases.^{61,62} In the case of the NMe₂ derivative, the Fe(III/II) potential is negative enough to allow oxidation of **2-NMe₂** by molecular oxygen, consistent with a previous study reporting that **2-NMe₂** has a spin-crossover transition at room temperature, which enables its reactivity with oxygen.⁵⁹

We also evaluated the effects of varying the electronics of the axial pyridine ligand in the **1-X** and **2-X** series using Mössbauer spectroscopy. Although the isomer shifts of all Fe(II) complexes are similar, the quadrupole splitting values ($|\Delta E_q|$) rise with increasing the electron-donating ability of the ligand platform, establishing the influence of the ancillary ligand on the nuclear quadrupole moments at the iron centers (Table 2.2).⁶³

2.3.2 Chemical Oxidation of Fe(II)-Aquo PY5Me₂ Complexes to Fe(IV)-Oxo Species.

Initial attempts to generate [Fe^{IV}(O)(PY5Me₂)]²⁺ species centered on oxidation of **1-X** complexes in MeCN by traditional OAT reagents such as PhIO and mCPBA, based on the reported formation of an Fe(IV)-oxo species at low temperature with the related ligand PY5 (Table 2.3).^{6,26,61} However, use of these agents, as well as other oxidants, such as persulfate or Oxone®, did not yield Fe(IV)-oxo species for any of the PY5Me₂ derivatives. Likewise, hydrogen peroxide and O₂ did not react appreciably with these complexes in MeCN solution, as the Fe(III/II) redox couples of the **1-X** derivatives are significantly more positive than those of other related amine-supported Fe complexes that can be oxidized readily by PhIO (Table 2.3).

As such, we turned our attention to the Fe(II)-OH₂ congeners **2-X**, as their Fe(III/II) redox couples are ~700 mV less positive relative to the MeCN-ligated **1-X** species. Cyclic voltammograms at high scan rate of **2-X** also revealed second redox couple which could be attributed to Fe(IV)/(III) redox couple (Figure 2.5-2.9). Specifically, we were encouraged by examples of Fe(IV)-oxo formation by oxidation of Fe(II)-OH₂ complexes in a proton-coupled electron transfer process, which has been achieved by chemical,^{20,64} electrochemical,²⁹ and photochemical^{46,65} means. Notably, only a few of the reported ferryl species produced in this manner have been shown to be competent for substrate oxidations in water using water itself as an OAT source, and most of these examples still require acetonitrile as an organic co-solvent.^{46,65}

We were pleased to observe that the Fe(II)-OH₂ complexes **2-X** can be oxidized rapidly with CAN (ceric ammonium nitrate) in water or a water/MeCN mixture, producing the corresponding pale-green Fe(IV)-oxo species (**3-X**). Oxidation of **1-X** in aqueous media also yielded the same results as the apical ligand is labile. These complexes could be observed and characterized at room temperature (Scheme 2.2), with the exception of the **3-NMe₂** derivative, which was only fleetingly observed at low temperature and quickly decomposed (Figure 2.27). We speculate that autoxidation and decomposition of the ligand contributes to the instability of this intermediate. Nevertheless, the Fe(IV)-oxo species **3-CF₃**, **3-H**, and **3-Me** exhibit good stability in water in the absence of competent substrates, with half-lives of ~2 h in aqueous solution at room temperature, as determined by the decay of the characteristic weak d-d band for Fe(IV)-oxo intermediates in UV-vis spectrum centered at ~710 nm. Interestingly, the related [Fe^{IV}(O)(PY5)]²⁺ species, which contains methoxy instead of methyl groups at the methine positions supporting the pentapyridine scaffold, exhibits a reported half-life of 90 min at -65°C in MeCN solution.^{61,62}

The Fe(IV)-oxo-containing compounds, **3-CF₃**, **3-H**, and **3-Me**, could also be isolated in solid form when CAN oxidations were performed in 3:1 MeCN:H₂O solvent mixtures at higher concentrations. The isolable green-colored solid samples were characterized by Mössbauer spectroscopy, and the presence of a single Fe species confirmed complete oxidation of the Fe center (Figure 2.10). The observations of isomer shift values near zero mm/s are consistent with assignment to an Fe(IV) species with O- and N-donors in an octahedral ligand field. Moreover, the measured quadrupole splitting values at approximately 0.8 mm/s suggest a low-spin Fe(IV) (*S* = 1) configuration for all complexes. Unlike the corresponding Fe^{II}-PY5Me₂ species, we observe only small differences in the quadrupole splitting parameters across the [Fe^{IV}(O)(PY5Me₂-X)]²⁺ series. Interestingly, this situation is in contrast to the axial ligand substitution studies performed on related [Fe^{IV}(O)(TMC)(X)]²⁺ complexes with a wider range of anionic and neutral donors (X = MeCN, CF₃CO₂⁻, and N₃⁻), which result in relatively large differences in quadrupole splitting parameters. We rationalize the smaller magnitudes of

alterations in the fitted quadrupole splitting parameters in complexes **3-X** compared to the TMC system by the more subtle fine-tuning of pyridine donor strengths on the Fe(IV)-oxo unit.^{27,30,31} A summary of spectroscopic characterization parameters for Fe(IV)-oxo complexes **3-X** are listed in Table 2.4.

To help establish that the source of oxo ligand is derived from water, H₂¹⁸O was used in the oxidation reaction to synthesize the [Fe^{IV}(O)(PY5Me₂-X)]²⁺ species. Infrared spectra of solid Fe(IV)-oxo samples generated using ¹⁸O-labeled water show expected peak shifts in the Fe-O vibrations in agreement with a harmonic oscillator model (Table 2.3, Figure 2.19-2.24). Across this homologous series, the Fe-O bond for the **3-CF₃** derivative is the strongest among the three derivatives. In addition, the ¹⁸O-labeled [Fe^{IV}(O)(PY5Me₂-X)]²⁺ species generated was subjected to mass spectrometric analysis. As the oxygen in the ferryl moiety is susceptible to facile exchange with oxygen from trace H₂¹⁶O in the solvent, H₂¹⁸O was employed as a solvent during the oxidation reaction and subsequent spectroscopic characterization. High resolution ESI-MS data show the expected shift in m/z of 1 Da for the [Fe^{IV}(O)(PY5Me₂-X)]²⁺ dication fragment (Figure 2.25).

2.3.3 Photochemical Oxidation of Fe(II)-Aqua PY5Me₂ Complexes to Fe(IV)-Oxo Species.

The Fe(II)-aqua complexes in **2-X** can also be oxidized to the corresponding Fe(IV)-oxo complexes (as present in **3-X**) by photochemical means. These experiments were performed using a simple 13-W blue fluorescence light bulb as an energy source and water as the solvent and oxygen-atom source, with [Ru(bpy)₃]²⁺ as a photosensitizer and K₂S₂O₈ as a terminal electron acceptor. As shown in Figure 2.28, the same UV-vis spectrum, indicative of Fe(IV)-oxo formation, with the characteristic d-d band centered at ~710 nm, is produced under photochemical conditions as is observed for chemical oxidation by CAN (Figure 2.29). Complete conversion to the ferryl species proceeded within 25 min of irradiation. Reaction mixtures after photolysis were subjected to mass spectrometry, and [Fe^{IV}(O)(PY5Me₂-X)]²⁺ intermediates where X = CF₃, H and Me were detected directly (Table 2.8). Moreover, in control experiments performed in the absence of light, photosensitizer, and/or terminal electron acceptor, no evidence for Fe(IV)-oxo formation was apparent.

We speculate that initial oxidation of the Fe(II)-OH₂ starting material to Fe(III)-OH and subsequent oxidation to Fe(IV)-oxo is a logical pathway, as direct generation of Fe(IV)-oxo in the presence of Fe^{II} starting material can undergo an intermolecular reaction to produce a μ-oxo Fe^{III} sink that cannot be oxidized to Fe(IV)-oxo. A similar pathway for the generation of Fe^{IV}(O)(^{Me}2Py₂tacn) has been proposed.⁴⁶ We suggest that the initial oxidation of Fe(II)-OH₂ to Fe(III)-OH proceeds via K₂S₂O₈, which is in excess under these photochemical conditions, and subsequent oxidation of Fe(III)-OH to Fe(IV)-oxo occurs by [Ru(bpy)₃]²⁺-initiated photochemistry. Indeed, **2-X** can react with K₂S₂O₈ (Figure 2.31), as shown by UV-vis spectroscopy, and Mössbauer spectroscopy of the resulting species reveals an isomer shift of 0.23 mm/s, consistent with an Fe^{III} species (Figure 2.18). Given the facile proton-coupled oxidation of the complexes in **2-X**, as shown by cyclic voltammetry, we tentatively propose that K₂S₂O₈ oxidation of the Fe(II)-aqua complexes generates their putative Fe(III)-hydroxide counterparts.

2.3.4 Oxidative Reactivity of Photochemically Generated Fe(IV)-Oxo PY5Me₂ Species: Electron-Withdrawing Axial Pyridines Increase Rates of Both HAT and OAT Reactions.

With a systematic series of $[\text{Fe}^{\text{IV}}(\text{O})(\text{PY5Me}_2\text{-X})]^{2+}$ species in hand, we surveyed their oxidative reactivity for HAT and OAT reactions with hydrocarbons and alcohols, to benchmark their properties compared to other synthetic $S = 1$ Fe(IV)-oxo complexes reported in the literature. Stoichiometric reactivity studies of the Fe(IV)-oxo complexes in **3-CF₃**, **3-H**, and **3-Me** in MeCN solution, isolated from chemical oxidation, show rapid reaction with hydrocarbon substrates containing weak C-H bonds, including 9,10-dihydroanthracene (BDE = 77 kcal/mol) and ethylbenzene (87 kcal/mol).^{2,42} The ferryl species are also competent for oxidation of benzyl alcohol to benzaldehyde, as well as oxidation of *N,N*-dimethylaminobenzene; the latter result provides a rationale for the relative instability of **3-NMe₂**, suggesting that ligand oxidation can lead to formation of an Fe^{III} byproduct.

We also observe that the $[\text{Fe}^{\text{IV}}(\text{O})(\text{PY5Me}_2\text{-X})]^{2+}$ species are capable of hydrocarbon oxidations in aqueous solution at pH 5.5 (non-buffered water), expanding their use beyond organic media. Specifically, we evaluated three water-soluble substrates to represent different modes of reactivity:²⁵ benzyl alcohol for HAT-mediated alcohol oxidation, 4-ethylbenzene sulfonate sodium salt for HAT-mediated hydrocarbon oxidation, and 4-styrenesulfonate sodium salt for olefin oxidation via OAT. Fe(IV)-oxo generated photochemically reacted with one equivalent of substrate. After 5 min, d₄-sodium trimethylsilylpropanoate was added as an internal standard. The products of the oxidation reaction were identified using NMR spectroscopy, and the results showed oxidation of benzyl alcohol to benzaldehyde, ethylbenzenesulfonate to 1-phenylethanol sulfonate and acetophenonesulfonate, and styrenesulfonate to styreneoxidesulfonate and the corresponding diol products.

Second-order rate constants were measured by observing decay of the characteristic Fe(IV)-oxo signature centered at 710 nm in the UV-vis spectra upon substrate oxidation. The Fe(IV)-oxo species were generated under photochemical conditions before addition of 5, 10, 20, 30, 40 equiv of substrate (Figure 2.34-2.36). Among this systematic series, we observe that the $[\text{Fe}^{\text{IV}}(\text{O})(\text{PY5Me}_2\text{-X})]^{2+}$ derivative containing the most electron-withdrawing group, the **3-CF₃** congener, shows the fastest rates of oxidation for both HAT and OAT reactions with the substrates tested (Table 2.5).

Reaction rate differences also correlate to the Hammett parameters (σ_p) of the ligand substituents, as shown in Figure 2.33, with slope (ρ) of 0.79 (benzylalcohol), 1.06 (ethylbenzenesulfonate), and 0.49 (styrenesulfonate). The oxidation rate enhancement by electron-withdrawing substituent is moderate compared to axial ligand effect of anionic ligand demonstrated in the non-heme model complex, $\text{Fe}^{\text{IV}}(\text{O})(\text{TMC})$ ^{30,31}, and to the $\text{Fe}^{\text{IV}}(\text{O})(\text{TMP}^+)$ ⁵⁸ and $\text{Mn}^{\text{V}}(\text{O})(\text{TBP}_8\text{Cz})$ ⁵⁵⁻⁵⁷ system. While those systems reported orders-of-magnitude increase in reaction rate, the change in substituents serve as a fine tuning to the electronic properties and vary the reaction rate by less than 10-fold. Small variations in Mössbauer parameters (Table 2.4) and redox potentials measured by voltammetry (Figure 2.6-2.9, Table 2.7)) also support this finding. DFT calculation study is currently employed to better understand structure-reactivity relationships.

2.4 Concluding Remarks

Through the synthesis, characterization, and evaluation of a family of Fe-PY5Me₂-X complexes, we have probed the effect of systematic changes on the axial pyridine ligand toward the electronic properties and reactivity of water-soluble Fe(IV)-oxo species supported by this pentapyridine platform. Substitutions at the *para* position of the axial pyridine with an array of electron-donating and electron-withdrawing functionalities results in a predictable and significant 200-300 mV shift in the Fe^{III/II} redox potentials, with concomitant changes in the quadrupole splitting parameters observed in the Mössbauer spectra. Oxidations of Fe(II)-aqua precursors by chemical or photochemical means proceed smoothly to generate water-soluble Fe(IV)-oxo complexes with competent lifetimes at room temperature; as expected across the series, electron-rich derivatives are more readily oxidized to the Fe(IV)-oxo species. Identification and characterization of the ferryl species was probed by multiple techniques, including *in-situ* UV-vis, Mössbauer, and infrared spectroscopies, as well as analysis of ¹⁸O-labeled products. The data reveal a correlation between axial ligand donor strength and ferryl reactivity within a structurally homologous series, but the effect is small in magnitude. The Fe(IV)-oxo complex **3-CF₃**, which contains the most electron-poor axial ligand synthesized in this series, showed the weakest Fe-O bond and the fastest rate with a variety of HAT and OAT substrates. Taken together, this study provides a unique family of synthetic, water-soluble Fe(IV)-oxo complexes with systematic electronic tuning of axial ligands with high structural similarity. Current and future efforts will further exploit the versatility of PY5Me₂ and related polypyridine platforms for catalytic oxidation and reduction reactions in green, aqueous media.

2.5 Experimental Section

General Synthetic and Physical Methods. All manipulations were performed under ambient conditions, unless otherwise noted. Pyrophoric reagents were handled using standard glovebox and Schlenk-line techniques. MilliQ H₂O was used in all experiments. All commercially available reagents were used without further purification, unless otherwise noted. PY5Me₂ (2,6-bis(1,1-bis(2-pyridyl)ethyl)pyridine), PY5Me₂-CF₃, and PY5Me₂-NMe₂ were synthesized according to literature procedures⁵¹ with slight modification. UV-vis spectra were recorded using a Varian Cary 50 BIO and an Agilent 8453 UV-visible spectrometer both equipped with a Unisoku cryostat. Infrared spectra were recorded using a Bruker FT-IR Alpha-P ATR Instrument. Measurements of pH were conducted using a Thermo Orion 420 A+. NMR experiments were conducted using Bruker AVB-400 and AV-600 spectrometers. ESI-MS experiments were performed by the QB3 Proteomics/Mass Spectrometry facility at University of California, Berkeley. X-ray crystallography was performed in the Chexray facility at the University of California, Berkeley. Elemental analyses were conducted at the Microanalytical Laboratory of the University of California, Berkeley.

Synthesis of PY5Me₂-Me: An *n*-BuLi solution (4 mL, 2.5 M, 10 mmol, 3 equiv) was added slowly to a solution of 1,1-dipyridylethane (1.86 g, 10 mmol, 3 equiv) in 40 mL of dry and degassed 1,4-dioxane at 0 °C. The solution was stirred for 30 min before 2,6-dichloro-4-picoline (0.545 g, 3.36 mmol, 1 equiv) was added as a solid. The reaction mixture was allowed to warm to room temperature and then heated to reflux for 2 days. After the solution was allowed to cool to room temperature, water was added to quench the reaction. The product was extracted with dichloromethane (3 × 20 mL). The organic layer was separated, washed with brine (2 × 15 mL), and dried with Na₂SO₄. The solvent was removed *in vacuo*. Methanol was added followed by

rotary evaporation to remove residual 1,4-dioxane. Et₂O was then added to precipitate a light yellow solid. The solid was washed with Et₂O and dried in air. A yellow solid (1.37 g, 87.3 % yield) was obtained. ¹H NMR (600 MHz, CDCl₃) δ 8.51 (d, J = 4.7 Hz, 4H), 7.38 (td, J = 7.8, 1.7 Hz, 4H), 7.04 (dd, J = 7.4, 5.0 Hz, 4H), 6.91 (s, 2H), 6.81 (d, J = 8.0 Hz, 4H), 2.24 (s, 3H), 2.19 (s, 6H). ESI-MS: m/z calcd for C₃₅H₃₂N₆ 536.27, found 537.3 (M+1). Calc. C₃₅H₃₂N₆ (536.67 g/mol): C, 78.33; H, 6.01; N, 15.66. Found: C, 78.06; H, 6.20; N, 15.49.

General Procedure for Synthesis of [Fe(MeCN)(PY5Me₂-X)](OTf)₂ Complexes (1-X). PY5Me₂-X ligand (100 mg, 0.186 mmol) was mixed with Fe(OTf)₂ (60.7 mg, 0.186 mmol) in 4 mL of MeCN. The solution color turned red upon mixing. The resulting solution was concentrated, filtered, and recrystallized by diffusing Et₂O into MeCN solution, yielding red needles suitable for single-crystal X-ray crystallography.

[Fe(MeCN)(PY5Me₂-CF₃)](OTf)₂ (1-CF₃): Yield: 58.9% ¹H NMR (600 MHz, CD₃CN) δ 9.60 (d, J = 6.1 Hz, 4H), 7.97 (s, 2H), 7.76 – 7.70 (m, 8H), 7.36 (tt, J = 5.4, 2.3 Hz, 4H), 2.60 (s, 6H). ESI-MS: m/z calcd for C₃₂H₂₇F₃FeN₆²⁺ 304.0794, found 304.0795 for C₃₁H₂₄F₆FeN₅O₃S⁺ 716.0859, found 716.0828 for Calc. C₃₄H₂₇F₆FeN₆O₆S₂ (906.58 g.mol⁻¹): C, 45.05; H, 3.00; N, 9.27. Found: C, 45.16; H, 2.78; N, 9.53.

[Fe(MeCN)(PY5Me₂-H)](OTf)₂ (1-H): Yield: 77.8% ¹H NMR (600 MHz, CD₃CN) δ 9.60 (d, J = 5.7 Hz, 4H), 7.81 (s, 2H), 7.72 (d, J = 4.6 Hz, 8H), 7.68 (s, 1H), 7.33 (p, J = 5.1 Hz, 4H), 2.52 (s, br, 6H). ESI-MS: m/z calcd for C₃₁H₂₈FeN₆²⁺ 270.0857, found 270.0857; for C₃₀H₂₅F₃FeN₅O₃S⁺ 648.0974, found 648.0952. Calc. C₃₃H₂₈F₆FeN₆O₆S₂ (838.58 g.mol⁻¹): C, 47.27; H, 3.37; N, 10.02. Found: C, 47.12; H, 3.37; N, 9.94.

[Fe(MeCN)(PY5Me₂-Me)](OTf)₂ (1-Me): Yield: 86.7% ¹H NMR (600 MHz, CD₃CN) δ 9.62 – 9.57 (d, 4H), 7.74 – 7.69 (m, 8H), 7.68 (s, 2H), 7.33 (dq, J = 6.5, 4.2, 3.5 Hz, 4H), 2.52 (s, 6H), 2.29 (s, 3H). ESI-MS: m/z calcd for C₃₂H₃₆FeN₆²⁺ 277.0942, found 277.0935; for C₃₁H₂₇F₃FeN₅O₃S⁺ 662.1132, found 662.1110. Calc. C₃₄H₃₀F₆FeN₆O₆S₂ (852.61 g.mol⁻¹): C, 47.90; H, 3.55; N, 9.86. Found: C, 47.97; H, 3.55; N, 9.88.

[Fe(MeCN)(PY5Me₂-NMe₂)](OTf)₂ (1-NMe₂): Yield: 98.0% ¹H NMR (600 MHz, CD₃CN) δ 9.58 (d, J = 5.8 Hz, 4H), 7.69 (dd, J = 17.9, 7.8 Hz, 8H), 7.32 (t, J = 6.7 Hz, 4H), 6.93 (s, 2H), 2.91 (s, 6H), 2.48 (s, 6H). ESI-MS: m/z calcd for C₃₃H₃₃FeN₇²⁺ 291.6065 found 291.6068; for C₃₂H₃₀F₃FeN₆O₃S⁺ 691.1382, found 691.1375. Calc. C₃₅H₃₄F₆FeN₇O₆S₂ (881.65 g.mol⁻¹): C, 47.68; H, 3.77; N, 11.12. Found: C, 48.00; H, 3.78; N, 11.34.

General Procedure for Synthesis of [Fe(OH₂)(PY5Me₂-X)](BF₄)₂ Complexes (2-X). A slurry of PY5Me₂-X ligand (100 mg, 0.186 mmol) in 4 mL of acetone was mixed with Fe(OH₂)₆(BF₄)₂ (60.7 mg, 0.186 mmol) in 0.5 mL of water. The solution color turned red immediately upon addition of the iron salt. The resulting solution was concentrated, filtered, and recrystallized by diffusing Et₂O into the resulting solution, yielding X-ray diffraction-quality red needles.

[Fe(OH₂)(PY5Me₂-CF₃)](BF₄)₂ (2-CF₃): Yield: 78.4% Calc. C₃₀H₃₄B₂F₁₁FeN₅O₅ (831.079 g.mol⁻¹): C, 43.36; H, 4.12; N, 8.43. Found: C, 43.75; H, 4.25; N, 8.42.

[Fe(OH₂)(PY5Me₂-H)](BF₄)₂ (2-H): Yield: 89.7% Calc. C₂₉H₂₇B₂F₈FeN₅O (691.02 g.mol⁻¹): C, 50.41; H, 3.94; N, 10.13. Found: C, 50.24; H, 3.80; N, 10.22.

[Fe(OH₂)(PY5Me₂-Me)](BF₄)₂ (2-Me): Yield: 83.5% Calc. C₃₀H₃₇B₂F₈FeN₅O₅ (777.11 g.mol⁻¹): C, 46.37; H, 4.80; N, 9.01. Found: C, 46.86; H, 4.85; N, 9.01.

General Procedure for Chemical Formation of [Fe^{IV}(O)(PY5Me₂-X)]²⁺ Complexes (3-X). 1-X or 2-X complex (40 mg, 0.047 mmol) was dissolved in 0.6 ml of 3:1 MeCN:H₂O.

(NH₄)₂Ce(NO₃)₆ (137 mg, 0.25 mmol) was added as a solid. The mixture was sonicated for 30 seconds and placed in an ice bath as green precipitate formed. The solid was collected on a sintered glass frit and washed with ice cold 3:1 MeCN:H₂O mixed solvent. The products were stored at -20 °C or used directly used as samples for Mössbauer, IR spectroscopy and Mass Spectrometry. For UV-vis experiments, 1 mM solution of **1-X** or **2-X** in 4 ml H₂O were prepared. 5 eq of (NH₄)₂Ce(NO₃)₆ were added as a solid into a quartz cuvette equipped with a stir bar for rapid stirring. Absorption at 710 nm was monitored as the reaction progressed to completion. For O-18 labeling experiments, H₂¹⁸O was used a solvent during the formation of **3-X-¹⁸O** only.

Synthesis of 2,6-dichloro-4-(2',5'-dimethyl-1H-pyrrol-1-yl)pyridine (S1): 4-amino-2,6-dichloropyridine (4.7 g, 29 mmol) was mixed with of 2,5-hexanedione (4 mL, 34 mmol) in 20 mL toluene; *p*-toluenesulfonic acid (48 mg, 0.25 mmol) was added before the solution was brought to reflux with a Dean-Stark trap for 2 h. The reaction mixture was allowed to cool to 40°C before the reaction flask was put in an ice bath. Pink-orange solid crashed out of the solution immediately. The solid (4.0 g, 58% yield) was washed with Et₂O and left to dry in air. ¹H NMR (400 MHz, CDCl₃): δ 7.142 (s, 2H), 5.947 (s, 2H), 2.121 (s, 6H) ppm. GC-MS: *m/z* calcd for C₁₁H₁₀Cl₂N₂ 240.0, found 240.0. Calc. C₁₁H₁₀Cl₂N₂ (241.12 g.mol⁻¹): C, 54.79; H, 4.18; N, 11.62. Found: C, 54.77; H, 4.44; N, 11.55.

Synthesis of PY5Me₂-pyr (S2): *n*BuLi solution (16 mL, 1.6 M, 25 mmol, 2.5 eq) was added slowly to 1,1-dipyridylethane (4.61 g, 25 mmol, 2.5 eq) in 50 mL dry THF solution at -70°C. The solution was stirred for 25 minutes before a 20 mL THF solution of **9** (2.41 g, 10 mmol) was added slowly. The reaction mixture was warmed up to room temperature and then refluxed overnight. After the refluxed solution was cooled to room temperature, ice was added to quench the reaction. The organic layer was separated, washed with brine (2 × 20 mL), and dried with Na₂SO₄. The solvent was removed *in vacuo*. Et₂O was added and a tan-colored solid crashed out. The solid was washed with more Et₂O and dried in air. Tan solid (4.315 g, 80.4% yield) was obtained. ¹H NMR (400 MHz, CDCl₃): δ 8.523 (dd, 4H), 7.464 (td, 4H), 7.073 (dd, 4H), 6.933 (d, 4H), 6.818 (s, 2H), 5.835 (s, 2H), 2.144 (s, 6H), 1.986 (s, 6H) ppm. EI-MS: *m/z* calcd for C₃₅H₃₂N₆ 536.27, found 537.3 (M+1). Calc. C₃₅H₃₂N₆ (536.67 g.mol⁻¹): C, 78.33; H, 6.01; N, 15.66. Found: C, 78.06; H, 6.20; N, 15.49.

Synthesis of PY5Me₂-NH₂ (S3): **6** (1.127 g, 2.1 mmol) was dissolved in 20 mL EtOH, 5 mL H₂O and 1 mL Et₃N before NH₂OH (2.94 g, 42 mmol, 20 eq) was added to the solution. The reaction mixture was brought to reflux for 16 h before being cooled to room temperature. The reaction mixture was added to an ice-cold 10 mL of 1 M HCl. The solution was washed with Et₂O (2 × 15 mL) before the separated aqueous layer was basified to pH 10-11 using 6 M NaOH. DCM was used to extract the amine products (2 × 20 mL). The organic layer was washed with NaCl brine solution then dried with Na₂SO₄ and evaporated to dryness. A white solid was obtained (0.8903 g, 92% yield). ¹H NMR (400 MHz, CDCl₃): δ 8.493 (d, 4H), 7.373 (td, 4H), 7.030 (td, 4H), 6.840 (d, 4H), 6.323 (s, 2H), 3.995 (s, 2H), 2.139 (s, 6H) ppm. EI-MS: *m/z* calcd for C₂₉H₂₆N₆ 458.22, found 459.3 (M+1). Calc. C₂₉H₂₆N₆ (458.56 g.mol⁻¹): C, 75.96; H, 5.71; N, 18.33. Found: C, 74.87; H, 5.89; N, 18.00.

Synthesis of PY5Me₂-Cl (S4): An ice-cold saturated solution of NaNO₂ (0.552 g, 8 mmol, 4 eq) was added to an ice-cold solution of PY5Me₂-NH₂, **7**, (0.9172 g, 2 mmol, 1 eq) in 8 mL of 7.5 M H₂SO₄. The solution was stirred for one minute before an ice-cold saturated solution of CuCl (2.5 g, excess) was added as a slurry in 1 M HCl. Solution immediately turned

blue. Upon completion of the addition, the mixture was removed from ice and allowed to warm to room temperature and stir for 2 h. The pH of the solution was adjusted to 7-8 using saturated solutions of NaOH and NaHCO₃. The product was extracted using DCM (6 × 20 mL). The DCM solution was then extracted with saturated solution of NaEDTA to remove residual copper and dried with Na₂SO₄ and evaporated to dryness. Yellow solid (0.4523 g, 79% yield) was obtained. Purified yield: 0.844 g, 88.3% ¹H NMR (400 MHz, CDCl₃): δ 8.449 (s, 4H), 7.370 (t, 4H), 7.002 (m, 6H), 6.785 (d, 4H), 2.256 (s, 6H) ppm.

Synthesis of [Fe(PY5Me₂-pyr)(MeCN)](OTf)₂ (1-pyr): PY5Me₂-pyr (100 mg, 0.186 mmol) was mixed with Fe(OTf)₂ (60.7 mg, 0.186 mmol) in MeCN. The solution turned red upon mixing. The resulting solution was filtered and recrystallized by diffusing Et₂O into MeCN solution, yielding X-ray crystallography quality red needles. Yield: 83.5% ¹H NMR (400 MHz, CD₃CN): δ 9.789 (dd, 4H), 7.942 (m, 8H), 7.834 (s, 2H), 7.548 (m, 4H), 5.927 (s, 2H), 2.144 (s, 6H), 2.019 (s, 6H) ppm. ESI-MS: *m/z* calcd for C₃₅H₃₂FeN₆ 296.1, found 296.1; for C₃₇H₃₅FeN₇ 316.6, found 316.6. for C₃₆H₃₂FeN₆F₃O₃S₁ 741.2, found 741.2. Calc. C₃₉H₃₅F₆FeN₇O₆S₂ (931.71 g.mol⁻¹): C, 50.28; H, 3.79; N, 10.52. Found: C, 49.44; H, 3.58; N, 10.27.

Synthesis of [Fe(PY5Me₂-NH₂)](OTf)₂ (1-NH₂): PY5Me₂-NH₂ (20 mg, 0.037 mmol) was mixed with Fe(OTf)₂ (15.5 mg, 0.037 mmol) in MeCN. The solution turned red upon mixing. The resulting solution was filtered and recrystallized using MeCN/Et₂O, yielding X-ray crystallography quality red needles. Yield: 71.4% ¹H NMR (400 MHz, CD₃CN): δ 9.756 (dd, 4H), 7.889 (m, 8H), 7.505 (t, 4H), 7.245 (s, 2H), 5.537 (s, 2H), 2.597 (s, 6H) ppm. EI-MS: *m/z* calcd for C₂₉H₂₆FeN₆ 257.1, found 257.1; for C₃₁H₂₉FeN₇ 277.6, found 277.6 for C₃₀H₂₆F₃FeN₆O₃S 663.1, found 663.1. Calc. C₃₃H₂₉F₆FeN₇O₆S₂ (853.59 g.mol⁻¹): C, 46.43; H, 3.42; N, 11.49. Found: C, 46.13; H, 3.31; N, 11.39.

Synthesis of [FePY5Me₂-Cl](OTf)₂ (1-Cl): PY5Me₂-Cl (20 mg, 0.034 mmol) was mixed with 14.4 mg (0.034 mmol) of Fe(OTf)₂ in MeCN. The solution turned red upon mixing. The resulting solution was filtered and recrystallized using MeCN/Et₂O, yielding X-ray crystallography quality red needles. Yield 88.4%. EI-MS: *m/z* calcd for C₃₀H₂₄FeF₃N₅O₃SCl 683.1, found 683.1. ¹H NMR (400 MHz, CD₃CN): δ 9.804 (d, 4H), 8.077 (s, 2H), 7.937 (m, 8H), 7.558 (td, 4H), 3.423 (s, 6H) ppm.

Electrochemical Methods. Nonaqueous electrochemical experiments were conducted under an Ar atmosphere in 0.1 M NBu₄PF₆ in CH₃CN. Cyclic voltammetry experiments were carried out using a BASI Epsilon potentiostat with a C-3 cell stand. The working electrode was a glassy carbon disk (3.0 mm diameter), and the counter electrode was a platinum wire. A silver wire in a porous Vycor tip glass tube filled with 0.1 M NBu₄PF₆ in CH₃CN was used as a pseudo-reference electrode. The scan rate for all cyclic voltammograms was 100 mV/s unless otherwise noted. All potentials were referenced against ferrocenium/ferrocene as an external standard and converted to SCE by adding 0.40 V to the measured potentials. Aqueous electrochemical experiments were conducted in a similar set-up except that a Ag/AgCl electrode (CH Instruments) was used as a reference electrode with no external standard.

Photochemical Studies. All photochemical studies were performed under ambient conditions with either a 13-W blue fluorescence light bulb (GE, ACE hardware) or small blue LED (VWR International). General conditions are as follows: 0.5 mM [Fe^{II}(MeCN)(PY5Me₂-X)]²⁺, 0.1 mM [Ru(bpy)₃]Cl₂, and 5 mM K₂S₂O₈. Kinetic studies were conducted with 0.5 mM [Fe^{II}(MeCN)(PY5Me₂-X)]²⁺, 0.1 mM [Ru(bpy)₃]Cl₂, and 10 mM K₂S₂O₈. Solutions were

photolyzed for 10 minutes before 5, 10, 20, 30 and 40 equivalents of substrate were added. Decay rates of absorbance at 710 nm were measured in at least triplicate.

NMR Studies. Stoichiometric reactions of Fe(IV)-oxo species and substrate were performed in 5% d₆-DMSO and 95% D₂O. Delay time was adjusted to 10 seconds. General conditions were as follows: 2 mM Fe complexes, 2 mM substrate and 1 mM of 3-(Trimethylsilyl)propionic-2,2,3,3-d₄ acid sodium salt (NaTSP) as an internal standard.⁶⁷

General Methods for X-ray Crystallography. Single-crystal X-ray diffraction was conducted at University of California, Berkeley, College of Chemistry, X-ray Crystallography Facility. Crystals were mounted on nylon loops in paratone-N hydrocarbon oil. All data collections were performed on either a Bruker Quazar or APEX diffractometer equipped with a CCD area detector and a low temperature apparatus. Data integration was performed using SAINT. Preliminary data analysis and absorption correction were performed using XPREP and SADABS. Structure solution and refinement was performed using SHELX software package.

General Methods for Mössbauer Spectroscopy. Zero-field, ⁵⁷Fe Mössbauer spectra were recorded in constant acceleration spectrometer (SEE Co Edina, MN) between room temperature and 5 K in a Janis Research Co. cryostat (Willington, MA). Collected spectra were analyzed using the WMOSS software package (See Co, Edina, MN). Isomer shifts are reported relative to α -iron (27 μ m foil) at room temperature. Samples were prepared by mixing Boron Nitride (BN) with finely ground crystalline samples of Fe complexes. Powder mixture was placed in nylon washer wrapped in Kapton® tape under inert atmosphere prior to introducing into the spectrometer in air. Solution samples were prepared by freezing Teflon sample holder containing 0.5 mL of sample in liquid nitrogen before introducing into the previously cooled spectrometer in air.

2.6 References

- (1) Costas, M.; Mehn, M. P.; Jensen, M. P.; Que, Jr., L. *Chem. Rev.* **2004**, 104, 939–986.
- (2) Que, Jr., L. *Acc. Chem. Res.* **2007**, 40, 493–500.
- (3) Nam, W. *Acc. Chem. Res.* **2007**, 40, 522–531.
- (4) Nam, W.; Lee, Y.; Fukuzumi, S. *Acc. Chem. Res.* **2014**, 47, 1146–1154.
- (5) Stone, K. L.; Borovik, A. S. *Curr. Opin. Chem. Biol.* **2009**, 13, 114–118.
- (6) Wang, D.; Ray, K.; Collins, M. J.; Farquhar, E. R.; Frisch, J. R.; Gomez, L.; Jackson, T. a.; Kerscher, M.; Waleska, A.; Comba, P.; Costas, M.; Que Jr., L. *Chem. Sci.* **2012**, 4, 282–291.
- (7) Groves, J. T. J. *Inorg. Biochem.* **2006**, 100, 434–447.
- (8) Shaik, S.; Cohen, S.; Wang, Y.; Chen, H.; Kumar, D.; Thiel, W. *Chem. Rev.* **2010**, 110, 949–1017.
- (9) Krebs, C.; Galonić Fujimori, D.; Walsh, C. T.; Bollinger, J. M. *Acc. Chem. Res.* **2007**, 40, 484–492.
- (10) Holm, R. H.; Kennepohl, P.; Solomon, E. I. *Chem. Rev.* **1996**, 96, 2239–2314.
- (11) Feig, A. L.; Lippard, S. J. *Chem. Rev.* **1994**, 94, 759–805.
- (12) Wallar, B. J.; Lipscomb, J. D. *Chem. Rev.* **1996**, 96, 2625–2658.
- (13) McGown, A. J.; Kerber, W. D.; Fujii, H.; Goldberg, D. P. *J. Am. Chem. Soc.* **2009**, 131, 8040–8048.
- (14) Krishnamurthy, D.; Kasper, G. D.; Namuswe, F.; Kerber, W. D.; Narducci Sarjeant, A. A.; Moënné-Loccoz, P.; Goldberg, D. P. *J. Am. Chem. Soc.* **2006**, 128, 14222–14223.

- (15) Sahu, S.; Quesne, M. G.; Davies, C. G.; Dürr, M.; Ivanović-Burmazović, I.; Siegler, M. A.; Jameson, G. N. L.; de Visser, S. P.; Goldberg, D. P. *J. Am. Chem. Soc.* **2014**, 136, 13542–13545.
- (16) Vaillancourt, F. H.; Yeh, E.; Vosburg, D. A.; Garneau-Tsodikova, S.; Walsh, C. T. *Chem. Rev.* **2006**, 106, 3364–3378.
- (17) Baik, M.-H.; Newcomb, M.; Friesner, R. A.; Lippard, S. J. *Chem. Rev.* **2003**, 103, 2385–2419.
- (18) Gunay, A.; Theopold, K. H. *Chem. Rev.* **2010**, 110, 1060–1081.
- (19) Abouelatta, A. I.; Campanali, A. A.; Ekkati, A. R.; Shamoun, M.; Kalapugama, S.; Kodanko, J. J. *Inorg. Chem.* **2009**, 48, 7729–7739.
- (20) Ekkati, A. R.; Kodanko, J. J. *J. Am. Chem. Soc.* **2007**, 129, 12390–12391.
- (21) Cho, K.; Leeladee, P.; McGown, A. J.; DeBeer, S.; Goldberg, D. P. *J. Am. Chem. Soc.* **2012**, 134, 7392–7399.
- (22) Mandal, D.; Ramanan, R.; Usharani, D.; Janardanan, D.; Wang, B.; Shaik, S. *J. Am. Chem. Soc.* **2014**, 137, 722–733.
- (23) Bukowski, M. R.; Koehntop, K. D.; Stubna, A.; Bominaar, E. L.; Halfen, J. A.; Münck, E.; Nam, W.; Que, Jr., L. *Science* **2005**, 310, 1000–1002.
- (24) Rohde, J.-U.; In, J.-H.; Lim, M. H.; Brennessel, W. W.; Bukowski, M. R.; Stubna, A.; Münck, E.; Nam, W.; Que, Jr., L. *Science* **2003**, 299, 1037–1039.
- (25) Lim, M. H.; Rohde, J.-U.; Stubna, A.; Bukowski, M. R.; Costas, M.; Ho, R. Y. N.; Münck, E.; Nam, W.; Que, Jr., L. *Proc. Natl. Acad. Sci.* **2003**, 100, 3665–3670.
- (26) Klinker, E. J.; Kaizer, J.; Brennessel, W. W.; Woodrum, N. L.; Cramer, C. J.; Que, Jr., L. *Angew. Chem. Int. Ed. Engl.* **2005**, 44, 3690–3694.
- (27) Sastri, C. V.; Park, M. J.; Ohta, T.; Jackson, T. A.; Stubna, A.; Seo, M. S.; Lee, J.; Kim, J.; Kitagawa, T.; Münck, E.; Que, Jr., L.; Nam, W. *J. Am. Chem. Soc.* **2005**, 127, 12494–12495.
- (28) Bautz, J.; Bukowski, M. R.; Kerscher, M.; Stubna, A.; Comba, P.; Lienke, A.; Münck, E.; Que, Jr., L. *Angew. Chem. Int. Ed. Engl.* **2006**, 45, 5681–5684.
- (29) Collins, M. J.; Ray, K.; Que, Jr., L. *Inorg. Chem.* **2006**, 45, 8009–8011.
- (30) Sastri, C. V.; Lee, J. J.; Oh, K.; Lee, Y. J.; Lee, J. J.; Jackson, T. a; Ray, K.; Hirao, H.; Shin, W.; Halfen, J. a; Kim, J.; Que, Jr., L.; Shaik, S.; Nam, W. *Proc. Natl. Acad. Sci. U. S. A.* **2007**, 104, 19181–19186.
- (31) Jackson, T. A.; Rohde, J. U.; Mi, S. S.; Sastri, C. V.; DeHont, R.; Stubna, A.; Ohta, T.; Kitagawa, T.; Münck, E.; Nam, W.; Que, Jr., L. *J. Am. Chem. Soc.* **2008**, 130, 12394–12407.
- (32) Chanda, A.; Shan, X.; Chakrabarti, M.; Ellis, W. C.; Popescu, D. L.; Tiago de Oliveira, F.; Wang, D.; Que, Jr., L.; Collins, T. J.; Münck, E.; Bominaar, E. L. *Inorg. Chem.* **2008**, 47, 3669–3678.
- (33) Mukherjee, A.; Martinho, M.; Bominaar, E. L.; Münck, E.; Que, Jr., L. *Angew. Chem. Int. Ed. Engl.* **2009**, 48, 1780–1783.
- (34) Kim, S. O.; Sastri, C. V.; Seo, M. S.; Kim, J.; Nam, W. *J. Am. Chem. Soc.* **2005**, 127, 4178–4179.
- (35) Ray, K.; Pfaff, F. F.; Wang, B.; Nam, W. *J. Am. Chem. Soc.* **2014**, 136, 13942–13958.
- (36) Wilson, S. A.; Chen, J.; Hong, S.; Lee, Y.-M.; Clémancey, M.; Garcia-Serres, R.; Nomura, T.; Ogura, T.; Latour, J.-M.; Hedman, B.; Hodgson, K. O.; Nam, W.; Solomon, E. I. *J. Am. Chem. Soc.* **2012**, 134, 11791–11806.

- (37) Pestovsky, O.; Stoian, S.; Bominaar, E. L.; Shan, X.; Münck, E.; Que, Jr., L.; Bakac, A. *Angew. Chem. Int. Ed. Engl.* **2005**, 44, 6871–6874.
- (38) England, J.; Guo, Y.; Farquhar, E. R.; Young, V. G.; Münck, E.; Que, Jr., L. *J. Am. Chem. Soc.* **2010**, 132, 8635–8644.
- (39) Lacy, D. C.; Gupta, R.; Stone, K. L.; Greaves, J.; Ziller, J. W.; Hendrich, M. P.; Borovik, A. S. *J. Am. Chem. Soc.* **2010**, 132, 12188–12190.
- (40) MacBeth, C. E.; Golombek, A. P.; Young, V. G., Jr.; Yang, C.; Kuczera, K.; Hendrich, M. P.; Borovik, A. S. *Science* **2000**, 289, 938–941.
- (41) England, J.; Guo, Y.; Van Heuvelen, K. M.; Cranswick, M. A.; Rohde, G. T.; Bominaar, E. L.; Münck, E.; Que, Jr., L. *J. Am. Chem. Soc.* **2011**, 133, 11880–11883.
- (42) Seo, M. S.; Kim, N. H.; Cho, K.-B.; So, J. E.; Park, S. K.; Clémancey, M.; Garcia-Serres, R.; Latour, J.-M.; Shaik, S.; Nam, W. *Chem. Sci.* **2011**, 2, 1039–1045.
- (43) Bigi, J. P.; Harman, W. H.; Lassalle-Kaiser, B.; Robles, D. M.; Stich, T. A.; Yano, J.; Britt, R. D.; Chang, C. J. *J. Am. Chem. Soc.* **2012**, 134, 1536–1542.
- (44) Grapperhaus, C. A.; Mienert, B.; Bill, E.; Weyhermuller, T.; Wieghardt, K. *Inorg. Chem.* **2000**, 39, 5306–5317.
- (45) Company, A.; Prat, I.; Frisch, J. R.; Mas-Ballesté, R.; Güell, M.; Juhász, G.; Ribas, X.; Münck, E.; Luis, J. M.; Que, Jr., L.; Costas, M. *Chem. Eur. J.* **2011**, 17, 1622–1634.
- (46) Company, A.; Sabenya, G.; González-Béjar, M.; Gómez, L.; Clémancey, M.; Blondin, G.; Jasniewski, A. J.; Puri, M.; Browne, W. R.; Latour, J.-M.; Que, Jr., L.; Costas, M.; Pérez-Prieto, J.; Lloret-Fillol, J. *J. Am. Chem. Soc.* **2014**, 136, 4624–4633.
- (47) Bukowski, M. R.; Comba, P.; Lienke, A.; Limberg, C.; Lopez de Laorden, C.; Mas-Ballesté, R.; Merz, M.; Que, Jr., L. *Angew. Chem. Int. Ed. Engl.* **2006**, 45, 3446–3449.
- (48) Comba, P.; Fukuzumi, S.; Kotani, H.; Wunderlich, S. *Angew. Chem. Int. Ed. Engl.* **2010**, 49, 2622–2625.
- (49) Bigi, J. P.; Hanna, T. E.; Harman, W. H.; Chang, A.; Chang, C. J. *Chem. Commun.* **2010**, 46, 958–960.
- (50) Karunadasa, H. I.; Chang, C. J.; Long, J. R. *Nature* **2010**, 464, 1329–1333.
- (51) Sun, Y.; Bigi, J. P.; Piro, N. A.; Tang, M. L.; Long, J. R.; Chang, C. J. *J. Am. Chem. Soc.* **2011**, 2, 9212–9215.
- (52) Karunadasa, H. I.; Montalvo, E.; Sun, Y.; Majda, M.; Long, J. R.; Chang, C. J. *Science* **2012**, 335, 698–702.
- (53) Korendovych, I. V.; Kryatov, S. V.; Rybak-Akimova, E. V. *Acc. Chem. Res.* **2007**, 40, 510–521.
- (54) Widger, L. R.; Davies, C. G.; Siegler, M. A.; Troeppner, O.; Jameson, G. N. L.; Ivanoić-Burmazović, I.; Goldberg, D. P. *J. Am. Chem. Soc.* **2013**, 136, 2699–2702.
- (55) Prokop, K. A.; de Visser, S. P.; Goldberg, D. P. *Angew. Chem. Int. Ed. Engl.* **2010**, 49, 5091–5095.
- (56) Neu, H. M.; Quesne, M. G.; Yang, T.; Prokop-Prigge, K. A.; Lancaster, K. M.; Donohoe, J.; DeBeer, S.; de Visser, S. P.; Goldberg, D. P. *Chem. A Eur. J.* **2014**, 20, 14584–14588.
- (57) Neu, H. M.; Yang, T.; Baglia, R. A.; Yosca, T. H.; Green, M. T.; Quesne, M. G.; de Visser, S. P.; Goldberg, D. P. *J. Am. Chem. Soc.* **2014**, 136, 13845–13852.
- (58) Takahashi, A.; Yamaki, D.; Ikemura, K.; Kurahashi, T.; Ogura, T.; Hada, M.; Fujii, H. *Inorg. Chem.* **2012**, 51, 7296–7305.
- (59) Jeon, I.-R.; Park, J. G.; Haney, C. R.; Harris, T. D. *Chem. Sci.* **2014**, 5, 2461–2465.

- (60) Hansch, C.; Leo, A.; Taft, R. W. *Chem. Rev.* **1991**, 91, 165–195.
- (61) Goldsmith, C. R.; Stack, T. D. P. *Inorg. Chem.* **2006**, 45, 6048–6055.
- (62) Jonas, R. T.; Stack, T. D. P.; *J. Am. Chem. Soc.*, **1997**, 119, 8566–8567
- (63) Gütllich, Philipp, Bill, Eckhard, Trautwein, A. X.; Gütllich, P.; Link, R.; Trautwein, A. *Mössbauer Spectroscopy and Transition Metal Chemistry*; Springer, 2011.
- (64) Fillol, J. L.; Codolà, Z.; Garcia-Bosch, I.; Gómez, L.; Pla, J. J.; Costas, M. *Nat. Chem.* **2011**, 3, 807–813.
- (65) Kotani, H.; Suenobu, T.; Lee, Y.-M.; Nam, W.; Fukuzumi, S. *J. Am. Chem. Soc.* **2011**, 133, 3249–3251.
- (66) Hirai, Y.; Kojima, T.; Mizutani, Y.; Shiota, Y.; Yoshizawa, K.; Fukuzumi, S. *Angew. Chem. Int. Ed. Engl.* **2008**, 47, 5772–5776.

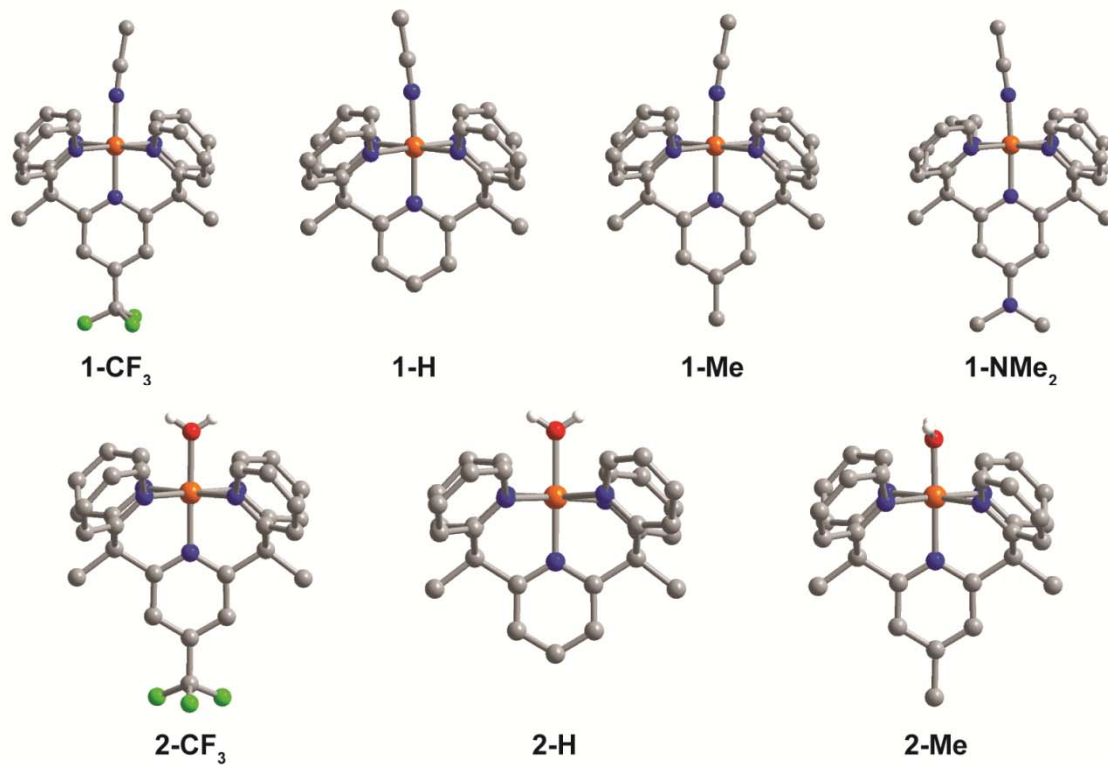


Figure 2.1. Crystal structures of **1-X** and **2-X**. Anions and hydrogen atoms are omitted for clarity, except for OH groups. Orange, blue, red, grey, green and white represent Fe, N, O, C, F and H respectively. Structure of **2-NMe₂** was reported previously.

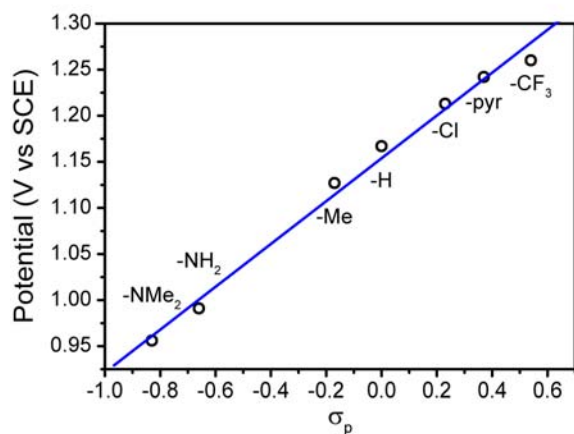


Figure 2.2. Linear free energy relationship of Fe(III/II) redox couples of **1-X** and Hammett Parameters (σ_p) with ρ 2.24×10^{-1} , $R^2 = 0.99$. Fe(III/II) redox couples were measured with 1 mM of **1-X** in 0.1 M NBu₄PF₆ MeCN using glassy carbon as a working electrode, Ag/AgCl as a reference electrode and Pt wire as a counter electrode. Ferrocene was used as an external standard and the potential was corrected to vs SCE by addition of 0.4 V. Experimental details on the synthesis of **1-pyr**, **1-Cl**, and **1-NH₂** can be found in the Supplementary Information. Pyr = 2,5-dimethylpyrrole.

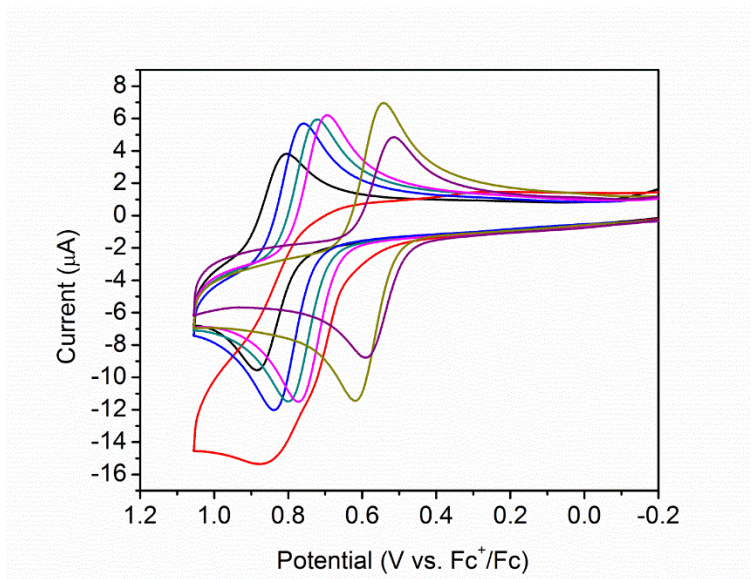


Figure 2.3. Cyclic voltammograms of **1-CF₃** (black), **1-pyr** (red), **1-Cl** (blue), **1-H** (green), **1-Me** (magenta), **1-NH₂** (dark yellow), and **1-NMe₂** (purple) in 0.1 M NBu₄PF₆ MeCN solution using glassy carbon as a working electrode, 1 mM Ag/AgNO₃ as a reference electrode and Pt wire as a counter electrode. Ferrocene was added as an external standard. **1-pyr** redox couple showed slight irreversibility due to oxidation of the ligand.

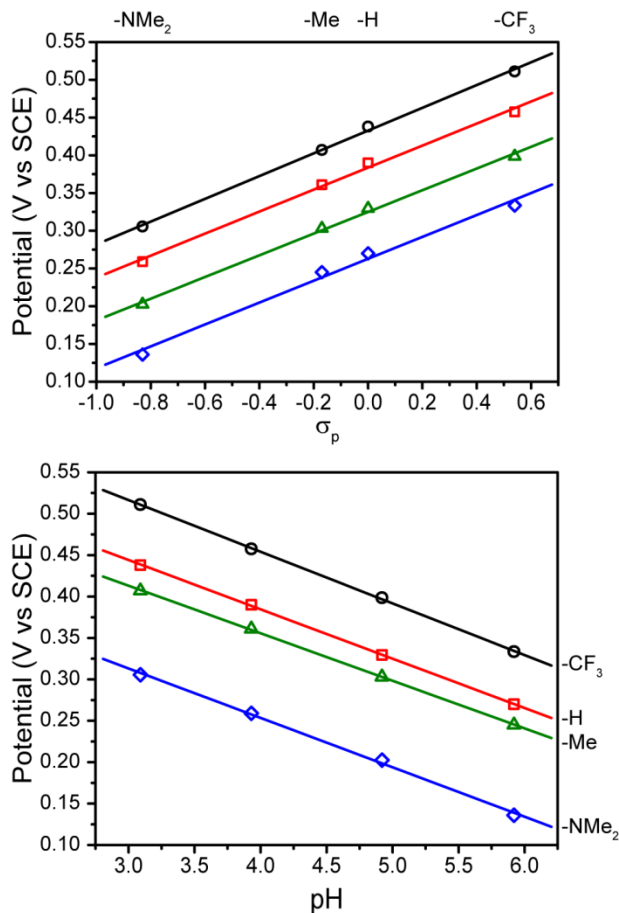


Figure 2.4. Linear free energy relationship of Fe(III/II) redox couples of **2-X** in water with p of 1.51×10^{-1} , $R^2 = 0.99$ (pH 3), 1.46×10^{-1} , $R^2 = 0.99$ (pH 4), 1.48×10^{-1} , $R^2 = 0.99$ (pH 5), 1.45×10^{-1} , $R^2 = 0.99$ (pH 6). The Fe(III/II) redox couples were measured with 1 mM of **2-X** in 0.1 M Potassium Acetate (KOAc) buffer at pH 3-6, using glassy carbon as a working electrode, Ag/AgCl as a reference electrode and Pt wire as a counter electrode. Black circle, red square, green triangle and blue diamond represent redox potential measured at pH 3, 4, 5, and 6 respectively (top). Pourbaix diagram of **2-X** at pH 3 to 6 (bottom). The slopes of all lines match the theoretical value of 59 mV/pH, $R^2 = 0.99$. Black circle, red square, green triangle and blue diamond represent redox potential of **2-CF₃**, **2-H**, **2-Me**, and **2-NMe₂** respectively.

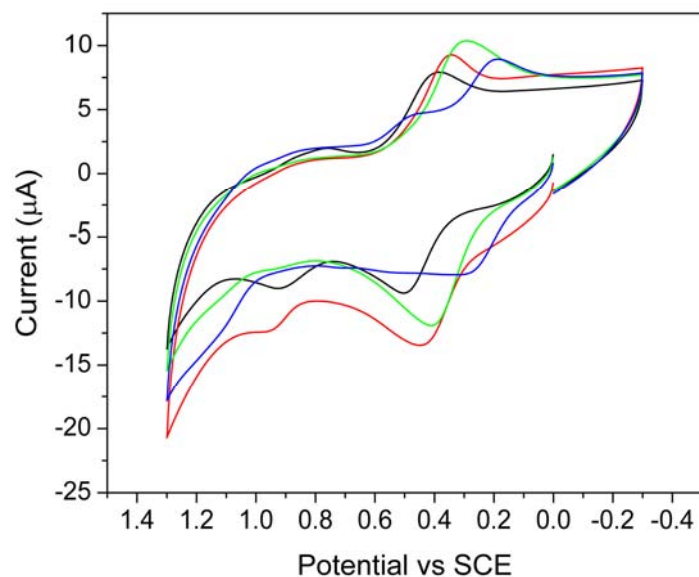


Figure 2.5. Cyclic voltammograms of **2-CF₃** (black), **2-H** (red), **2-Me** (green), and **2-NMe₂** (blue) in 0.1 M KNO₃ aqueous solution (non-buffered) using glassy carbon as a working electrode, Ag/AgCl as a reference electrode and Pt wire as a counter electrode. **2-CF₃** and **2-H** showed second oxidation event around 0.9 V.

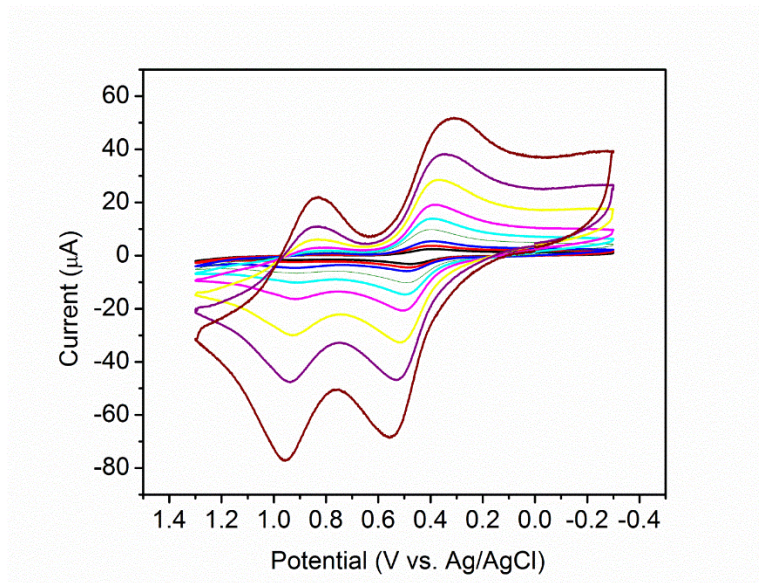


Figure 2.6. Cyclic voltammograms of **2-CF₃** with increasing scan rate from 25 mV/s (black), 50 mV/s (red), 100 mV/s (blue), 250 mV/s (green), 500 mV/s (cyan), 1000 mV/s (magenta), 2500 mV/s (yellow), 5000 mV/s (purple), to 10000 mV/s (wine), in 0.1 M KNO₃ aqueous solution (non-buffered) using glassy carbon as a working electrode, Ag/AgCl as a reference electrode and Pt wire as a counter electrode. Background currents were subtracted from the voltammogram.

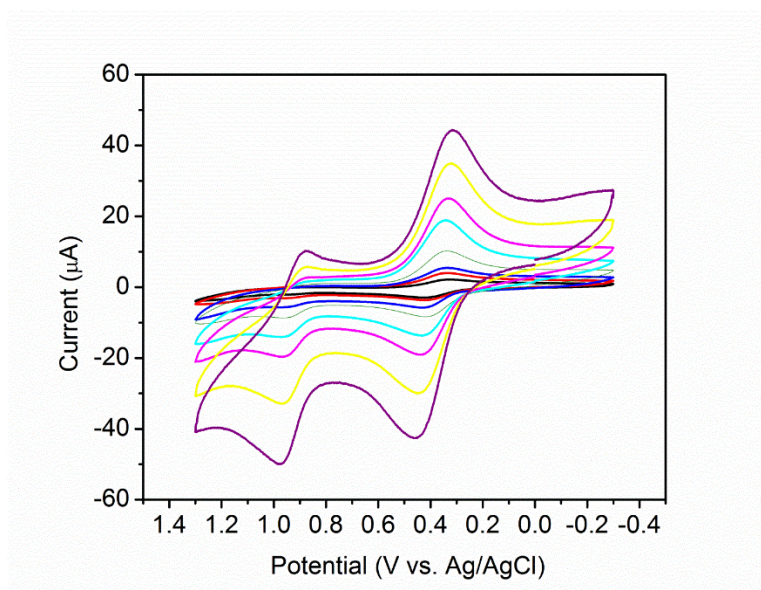


Figure 2.7. Cyclic voltammograms of **2-H** with increasing scan rate from 25 mV/s (black), 50 mV/s (red), 100 mV/s (blue), 250 mV/s (green), 500 mV/s (cyan), 1000 mV/s (magenta), 2500 mV/s (yellow), to 5000 mV/s (purple), in 0.1 M KNO₃ aqueous solution (non-buffered) using glassy carbon as a working electrode, Ag/AgCl as a reference electrode and Pt wire as a counter electrode. Background currents were subtracted from the voltammogram.

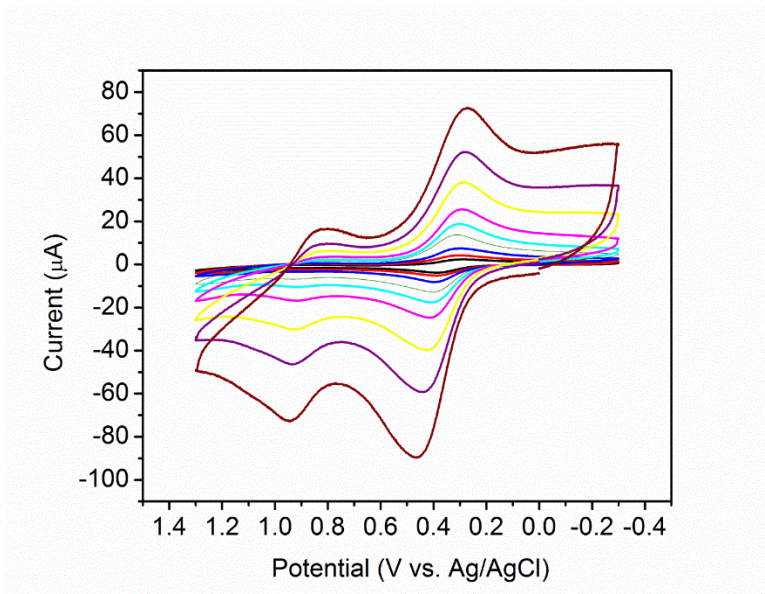


Figure 2.8. Cyclic voltammograms of **2-Me** with increasing scan rate from 25 mV/s (black), 50 mV/s (red), 100 mV/s (blue), 250 mV/s (green), 500 mV/s (cyan), 1000 mV/s (magenta), 2500 mV/s (yellow), 5000 mV/s (purple), to 10000 mV/s (wine), in 0.1 M KNO₃ aqueous solution (non-buffered) using glassy carbon as a working electrode, Ag/AgCl as a reference electrode and Pt wire as a counter electrode. Background currents were subtracted from the voltammogram.

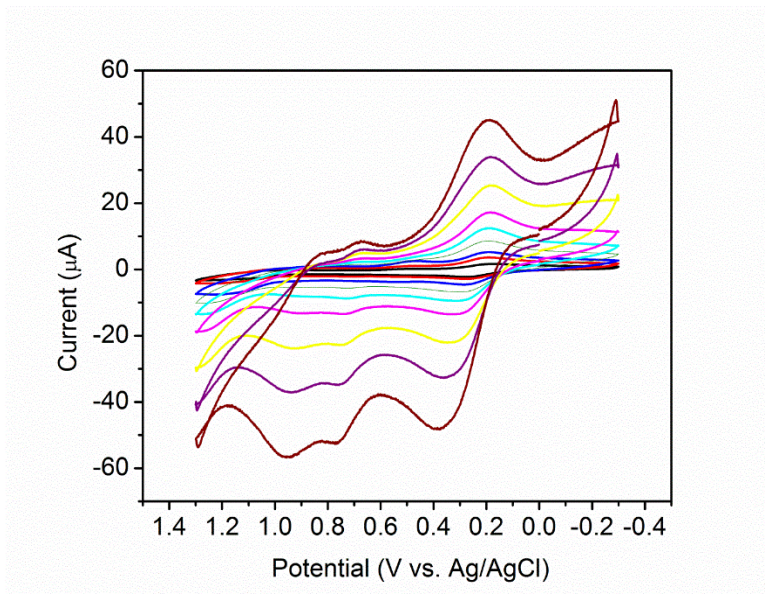


Figure 2.9. Cyclic voltammograms of **2-NMe₂** with increasing scan rate from 25 mV/s (black), 50 mV/s (red), 100 mV/s (blue), 250 mV/s (green), 500 mV/s (cyan), 1000 mV/s (magenta), 2500 mV/s (yellow), 5000 mV/s (purple), to 10000 mV/s (wine), in 0.1 M KNO₃ aqueous solution (non-buffered) using glassy carbon as a working electrode, Ag/AgCl as a reference electrode and Pt wire as a counter electrode. Background currents were subtracted from the voltammogram. A redox couple around 0.76 V indicates ligand oxidation that occurs before the oxidation at the Fe center.

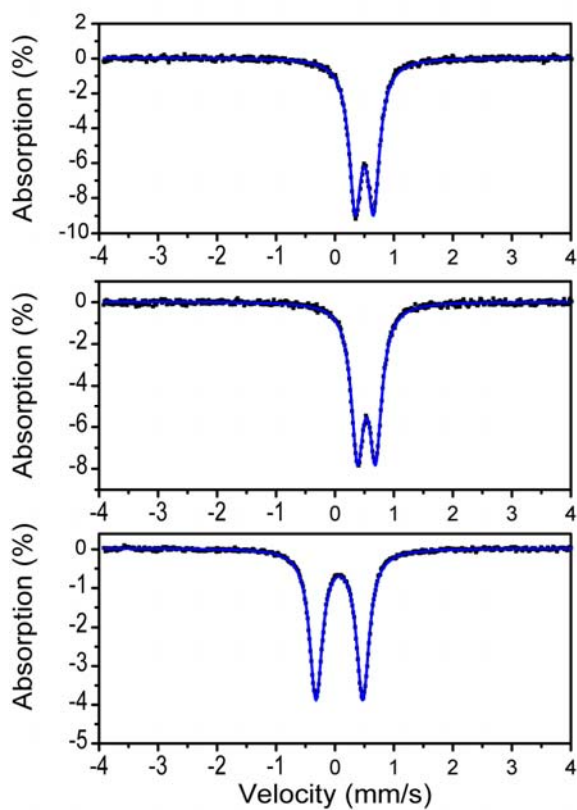


Figure 2.10. Zero-field Mössbauer spectra of solid **1-CF₃** (top), **2-CF₃** (middle), and **3-CF₃** (bottom) (black squares) acquired at 5 K. A least-square fit (blue line) provided the parameters listed in Tables 2.2 and 2.4.

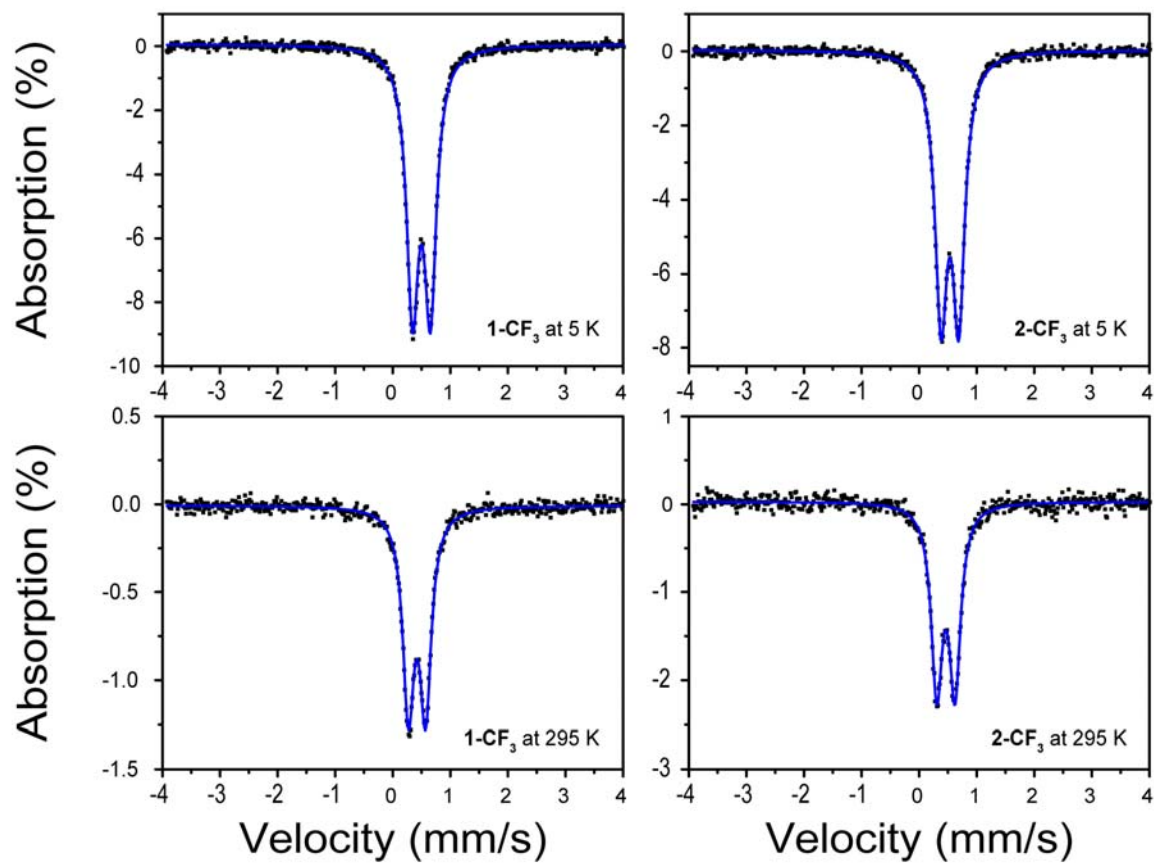


Figure 2.11. Mössbauer spectra of **1-CF₃** and **2-CF₃** at 5 K and 295 K. Black square represents the collected spectra and blue line represents a least square fit.

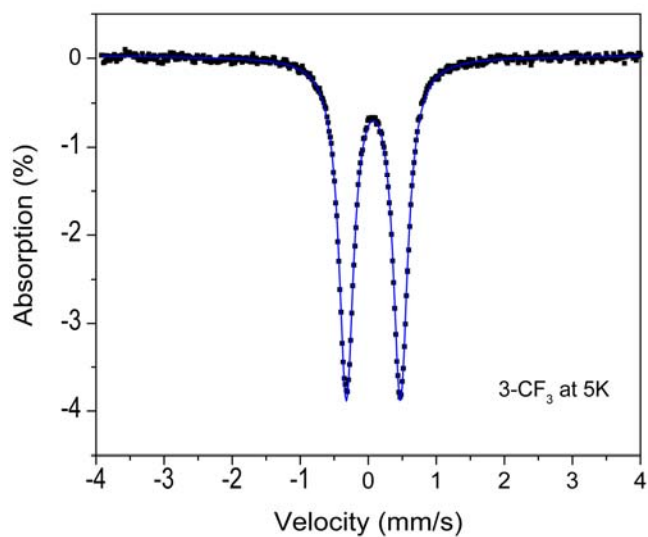


Figure 2.12. A Mössbauer spectrum of **3-CF₃** at 5 K. Black square represents the collected spectra and blue line represents a least square fit.

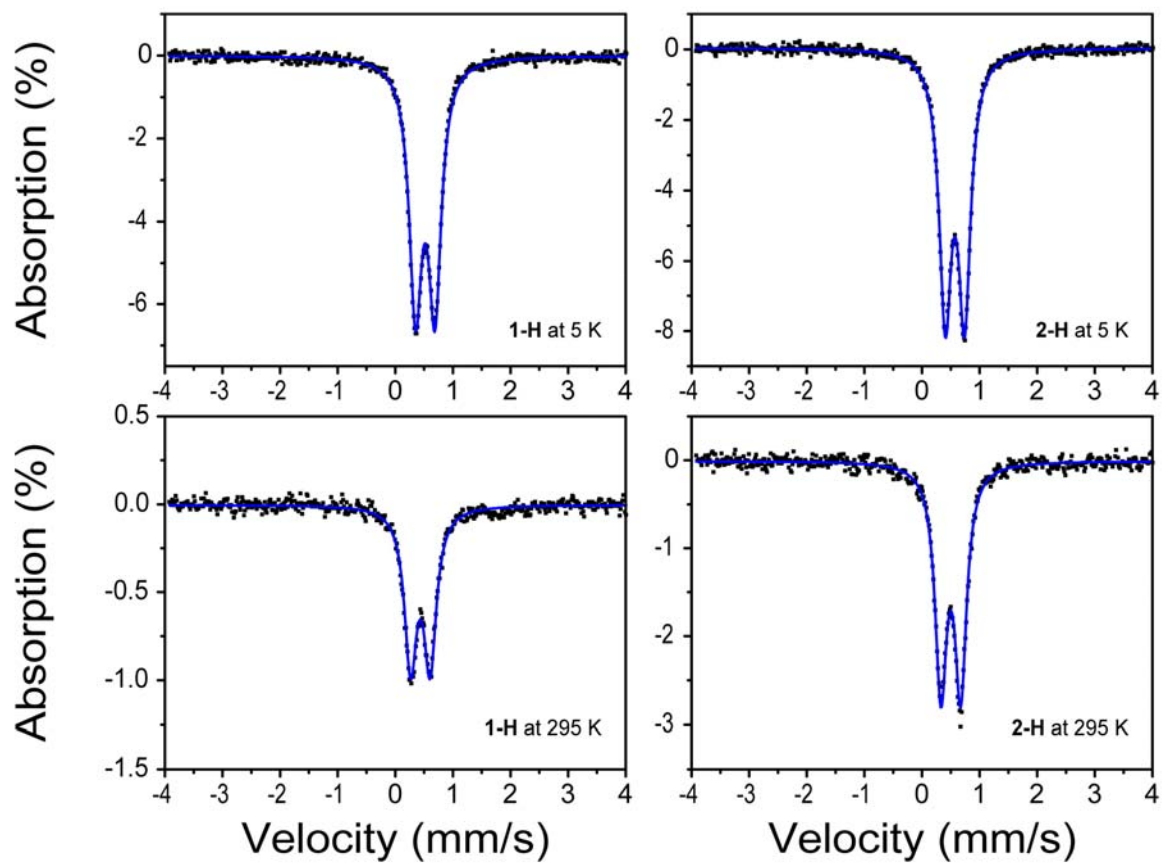


Figure 2.13. Mössbauer spectra of **1-H** and **2-H** at 5 K and 295 K. Black square represents the collected spectra and blue line represents a least square fit.

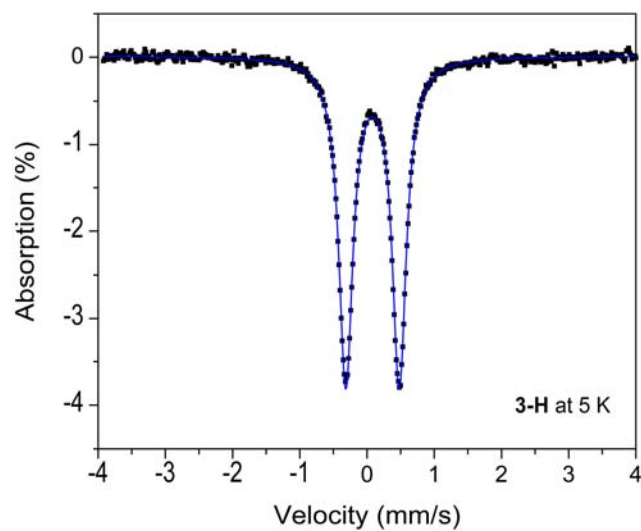


Figure 2.14. A Mössbauer spectrum of 3-H at 5 K. Black square represents the collected spectra and blue line represents a least square fit.

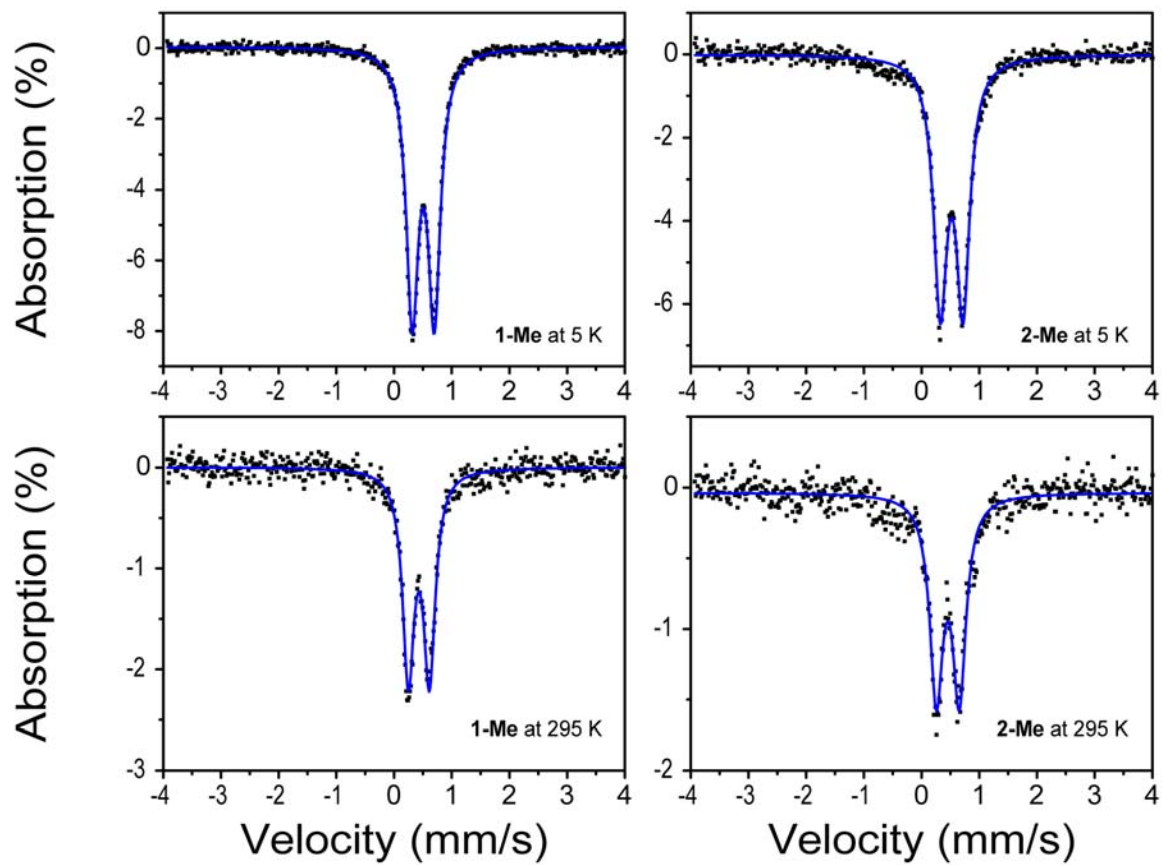


Figure 2.15. Mössbauer spectra of **1-Me** and **2-Me** at 5 K and 295 K. Black square represents the collected spectra and blue line represents a least square fit.

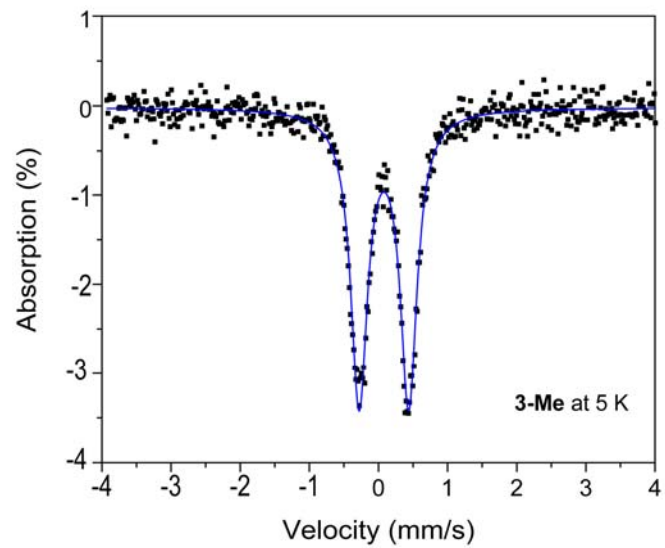


Figure 2.16. A Mössbauer spectrum of **3-Me** at 5 K. Black square represents the collected spectra and blue line represents a least square fit.

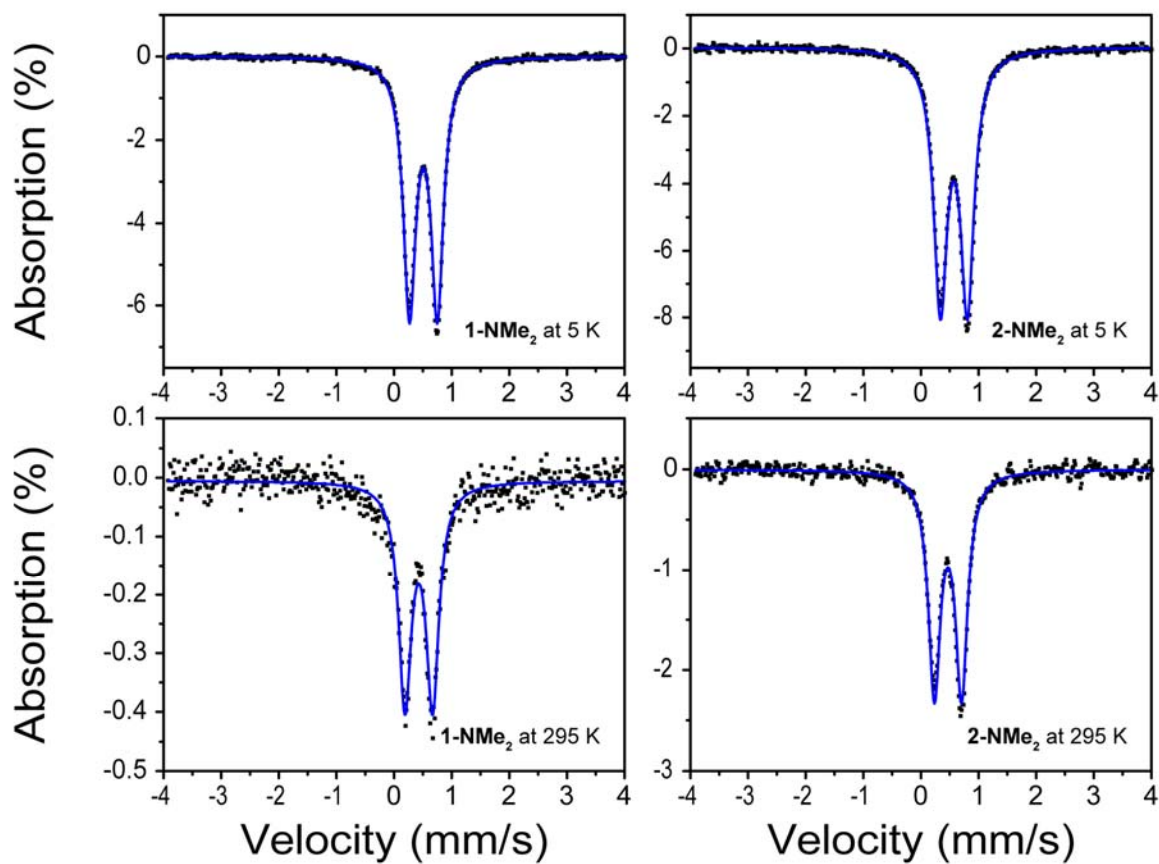


Figure 2.17. Mössbauer spectra of 1-NMe₂ and 2-NMe₂ at 5 K and 295 K. Black square represents the collected spectra and blue line represents a least square fit.

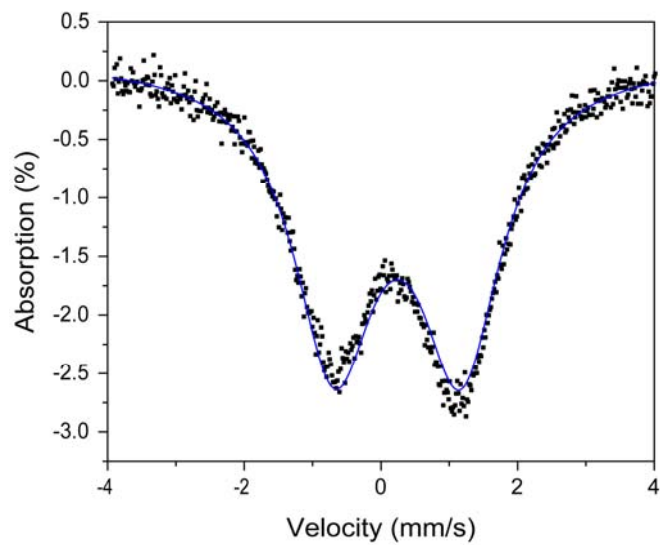


Figure 2.18. Mössbauer spectra of 1-CF_3 and $\text{K}_2\text{S}_2\text{O}_8$ at 5 K. Line broadening is caused by thickness of frozen solution sample. Black square represents the collected spectra and blue line represents a least square fit. $\delta = 0.242$ mm/s, $|\Delta E_q| = 1.852$ mm/s.

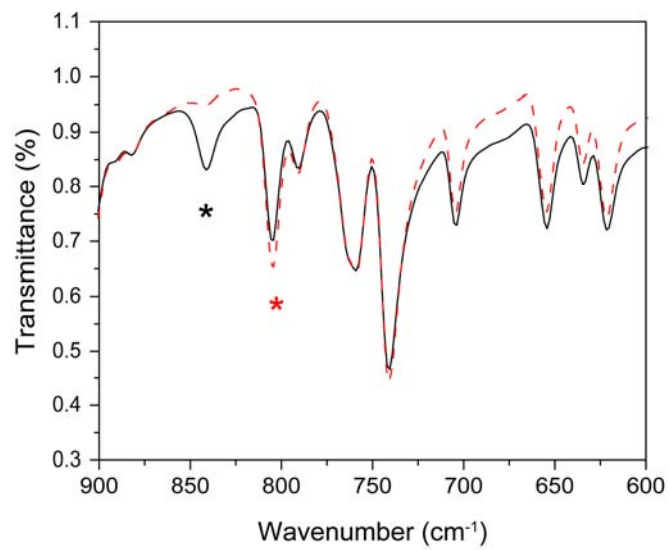


Figure 2.19. Infrared spectra of **3-CF₃**. Solid traces: Fe^{IV}(¹⁶O), dotted traces: Fe^{IV}(¹⁸O). Asterisks denote assignments to ν(Fe-O) stretches.

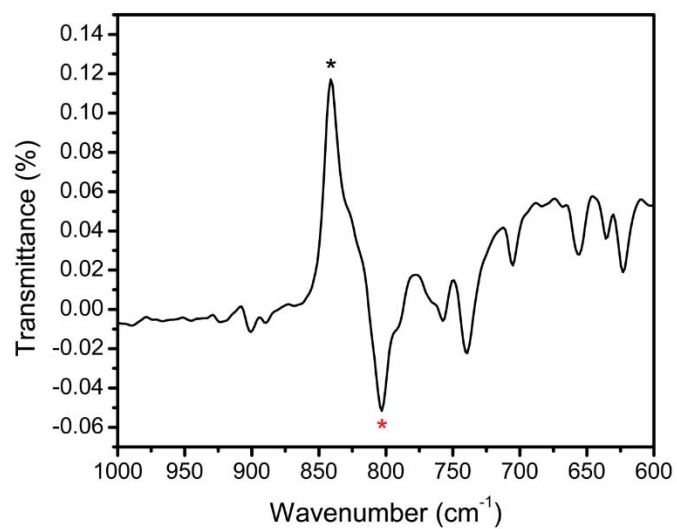


Figure 2.20. Difference Infrared spectra of **3-CF₃**. Asterisks denote assignments to $\nu(\text{Fe-O})$ stretches, $\text{Fe}^{\text{IV}}(^{16}\text{O})$ (black), $\text{Fe}^{\text{IV}}(^{18}\text{O})$ (red).

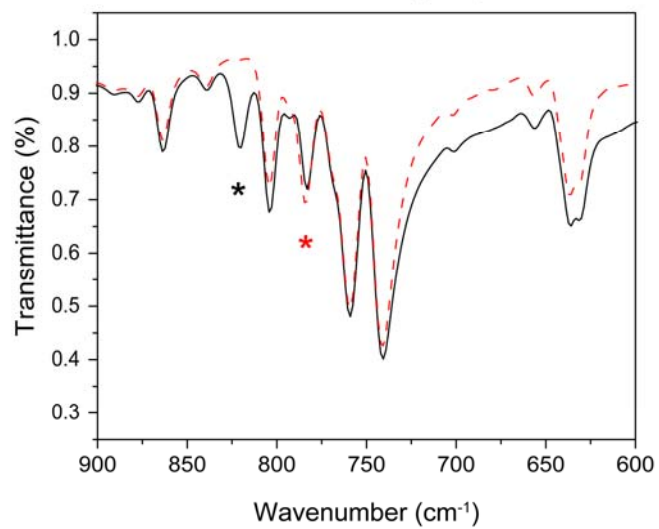


Figure 2.21. Infrared spectra of **3-H**. Solid traces: Fe^{IV}(¹⁶O), dotted traces: Fe^{IV}(¹⁸O). Asterisks denote assignments to $\nu(\text{Fe-O})$ stretches

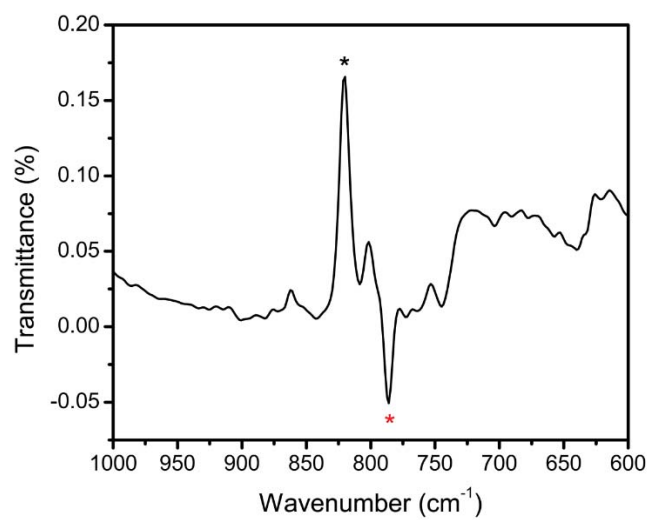


Figure 2.22. Difference Infrared spectra of **3-H**. Asterisks denote assignments to $\nu(\text{Fe-O})$ stretches, $\text{Fe}^{\text{IV}}(^{16}\text{O})$ (black), $\text{Fe}^{\text{IV}}(^{18}\text{O})$ (red).

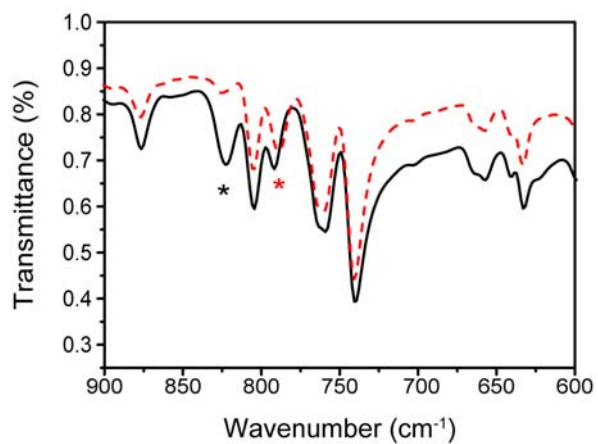


Figure 2.23. Infrared absorption spectra of the Fe(IV)-oxo PY5Me₂ complex **3-Me** synthesized from H₂¹⁶O (black) and H₂¹⁸O (red). Asterisks denote the Fe-oxo vibration $\nu(\text{Fe-O})$. Difference Spectra are shown in **Figure 2.24**.

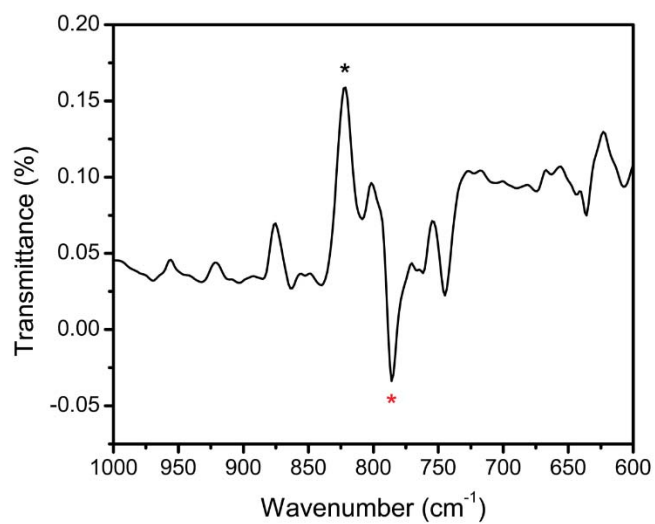


Figure 2.24. Difference Infrared spectra of **3-Me**. Asterisks denote assignments to $\nu(\text{Fe-O})$ stretches, $\text{Fe}^{\text{IV}}(^{16}\text{O})$ (black), $\text{Fe}^{\text{IV}}(^{18}\text{O})$ (red).

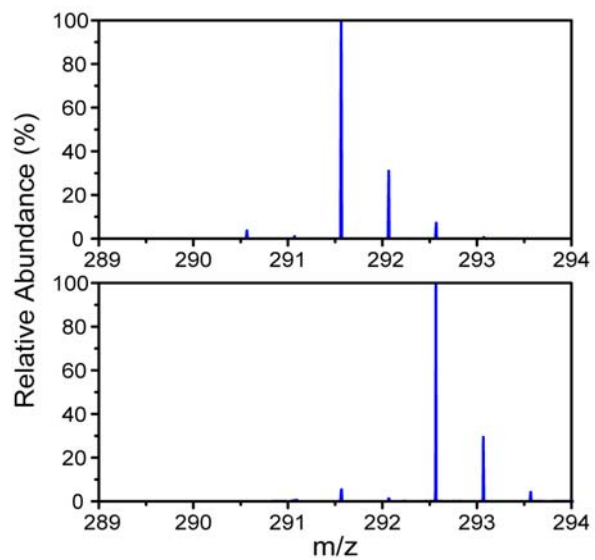


Figure 2.25. Mass spectra of **3-CF₃-¹⁶O** and **3-CF₃-¹⁸O**. A mass shift of $m/z = 1$ Da was observed when H₂¹⁸O is employed, consistent with water as the source of the oxo ligand.

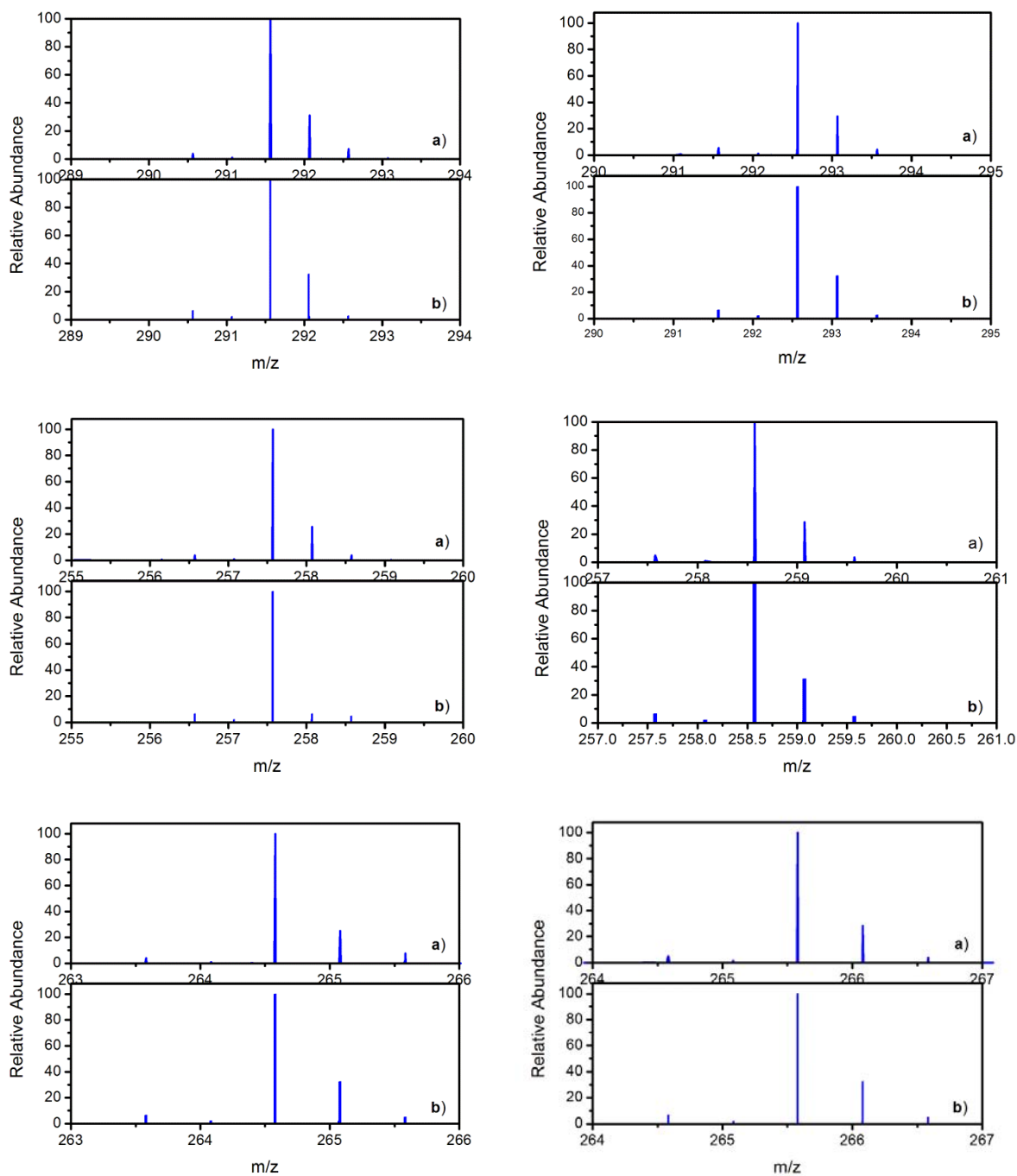


Figure 2.26. Mass spectra (a) and simulated mass spectra (b) of **3-CF₃-¹⁶O** (top left), **3-CF₃-¹⁸O** (top right), **3-H-¹⁶O** (middle left), **3-H-¹⁸O** (middle right), **3-Me-¹⁶O** (bottom left), and **3-Me-¹⁸O** (bottom right).

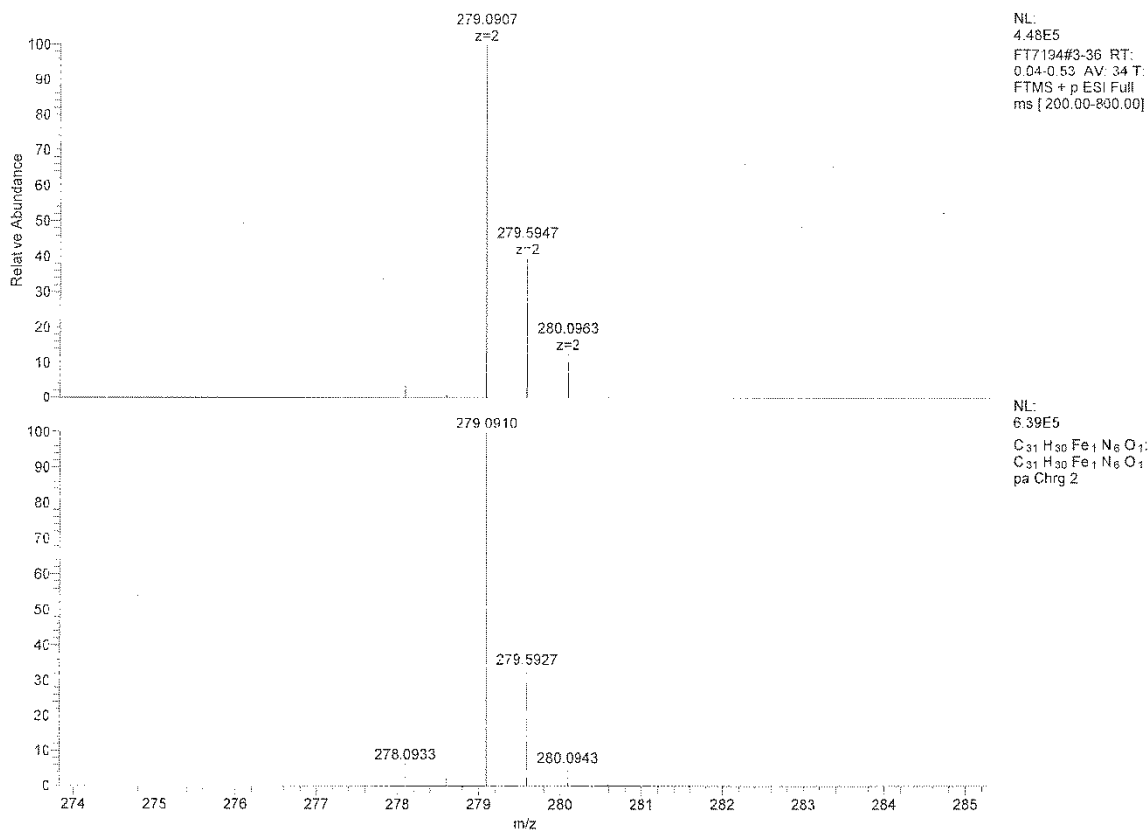


Figure 2.27. Mass spectra (top) and simulated mass spectra (bottom) of **3-NMe₂** that formed and decomposed quickly at 0°C.

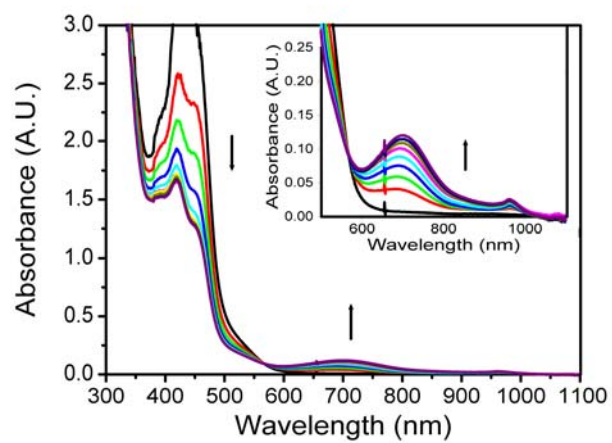


Figure 2.28. Photochemical oxidation of Fe(II)-aqua **2-CF₃** to Fe(IV)-oxo **3-CF₃** in water using a flash-quench $[\text{Ru}(\text{bpy})_3]^{2+}/\text{K}_2\text{S}_2\text{O}_8$ system.

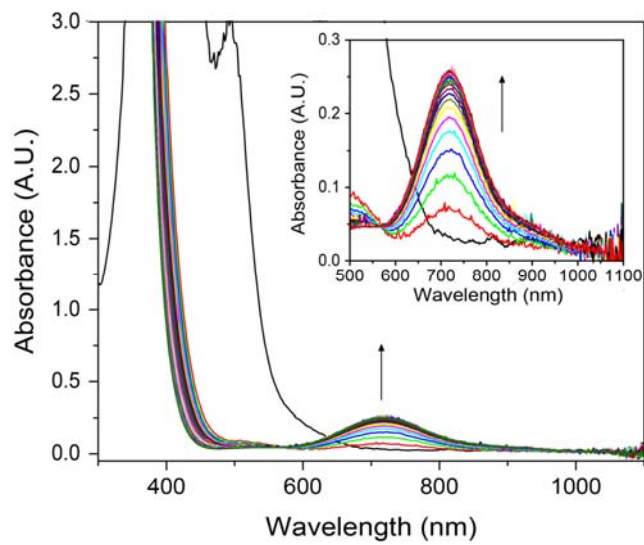


Figure 2.29. UV-visible spectra of formation of 3-CF_3 by CAN in water at room temperature.

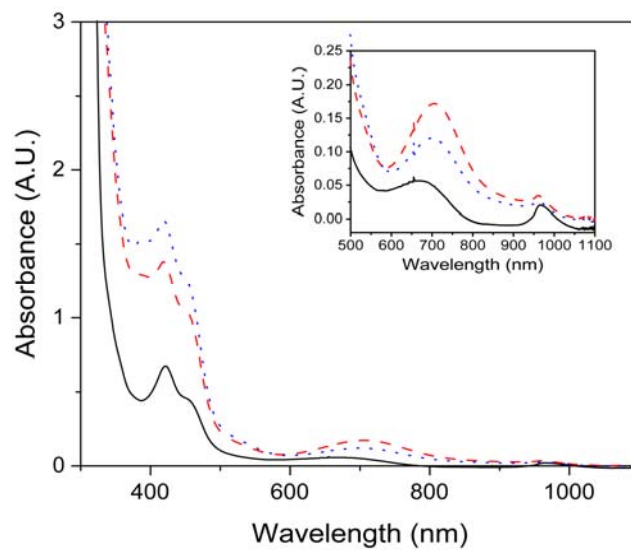


Figure 2.30. UV-visible spectra of **3-CF₃** (dotted blue trace) and **3-H** (dashed red trace) in comparison to Ru(bpy)₃³⁺ background (solid black trace) during photolysis. The inset shows the characteristic weak band of Fe^{IV}(O) at 710 nm, which does not overlap with Ru³⁺ absorption at 680 nm.

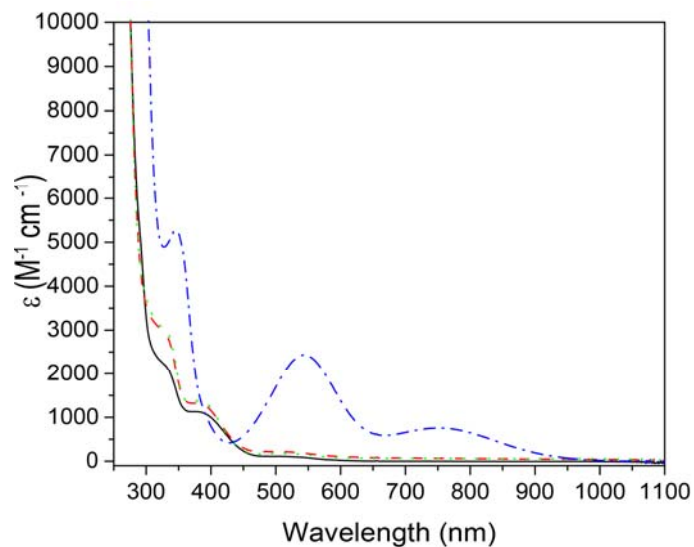


Figure 2.31. UV-visible spectra of **2-CF₃** (black solid trace), **2-H** (red dashed trace), **2-Me** (dotted green trace), and **2-NMe₂** (blue dotted-dashed trace) and excess $K_2S_2O_8$ in water at room temperature, showing the absence of features around 300-500 nm which is characteristic of Fe^{II} species.

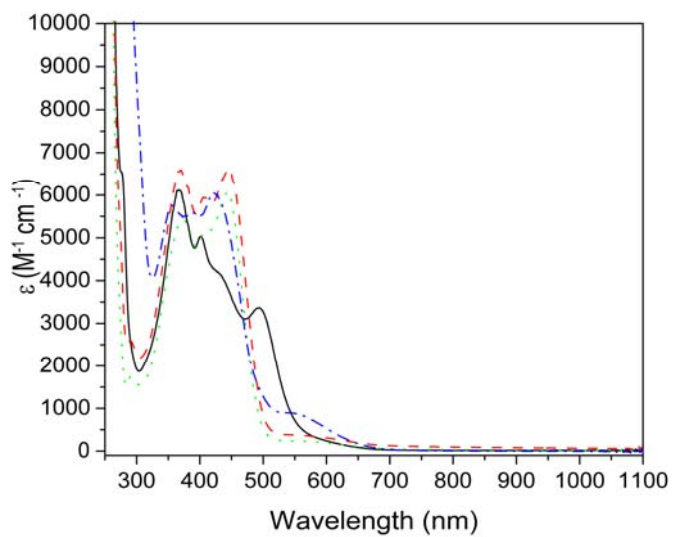


Figure 2.32. UV-visible spectra of **2-CF₃** (black solid trace), **2-H** (red dashed trace), **2-Me** (green dotted trace), and **2-NMe₂** (blue dotted-dashed trace) in water at room temperature.

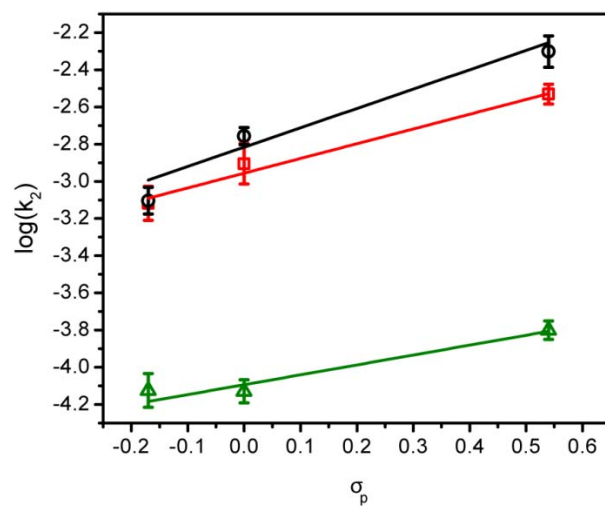


Figure 2.33. Linear free energy relationship of oxidation reaction rate constants (pseudo first-order) of hydrocarbon substrates by **3-X** and Hammett Parameters (σ_p). Black squares, red circles, green triangles represent oxidation rate of benzyl alcohol (ρ 0.79, $R^2 = 0.98$), 4-ethylbenzene sulfonate (ρ 1.06, $R^2 = 0.95$) and 4-styrene sulfonate (ρ 0.49, $R^2 = 0.94$) respectively.

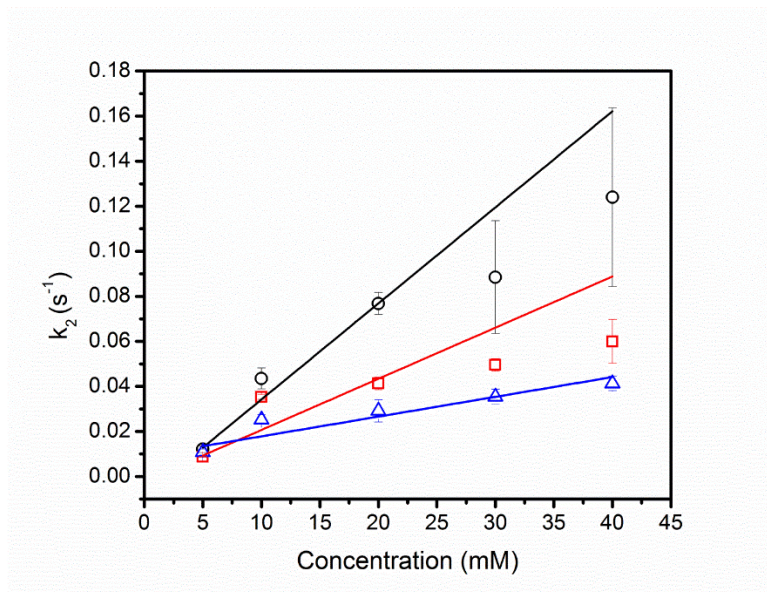


Figure 2.34. Concentration dependent of apparent rate (k_{obs}) of oxidation of Benzylalcohol with **3-CF₃** (black circle), **3-H** (red square), and **3-Me** (blue triangle).

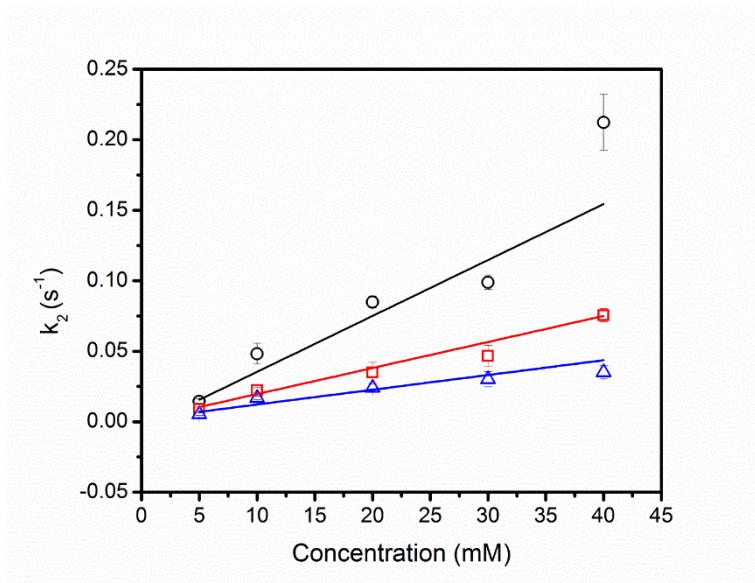


Figure 2.35. Concentration dependent of apparent rate (k_{obs}) of oxidation of 4-Ethylbenzene Sulfonate with **3-CF₃** (black circle), **3-H** (red square), and **3-Me** (blue triangle).

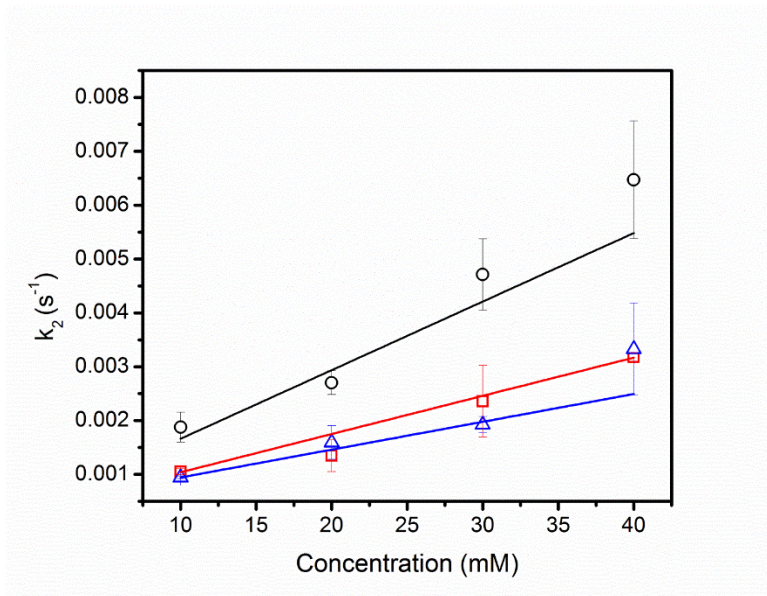
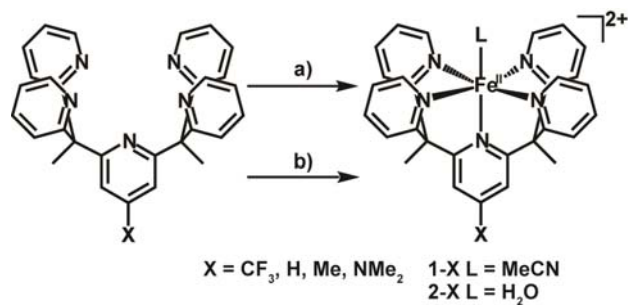
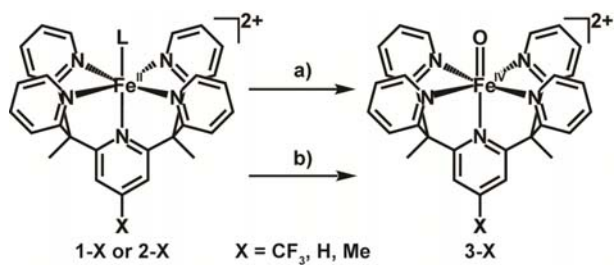


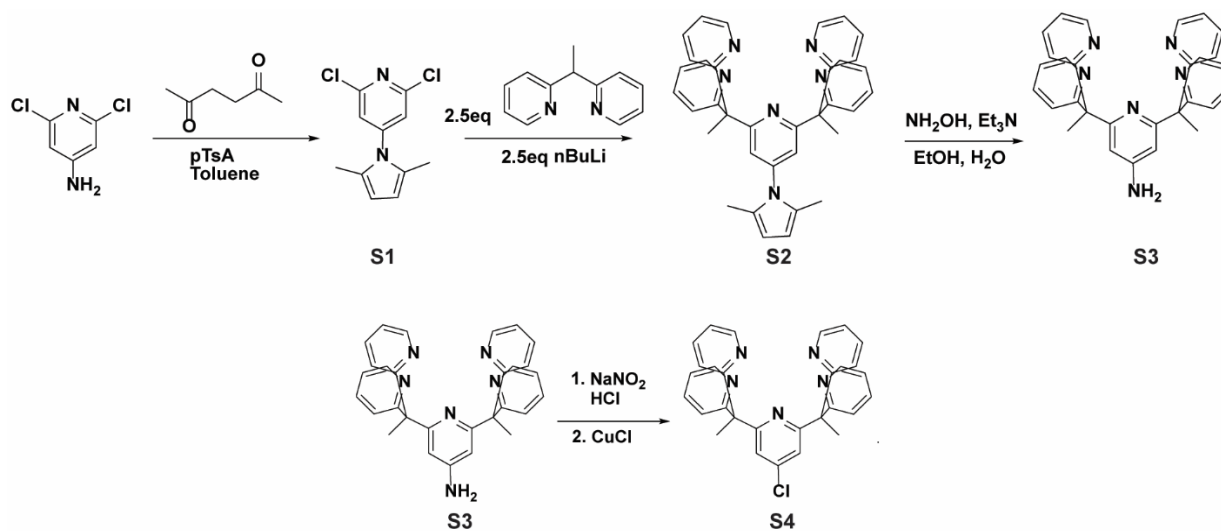
Figure 2.36. Concentration dependent of apparent rate (k_{obs}) of oxidation of 4-Styrene Sulfonate with **3-CF₃** (black circle), **3-H** (red square), and **3-Me** (blue triangle).



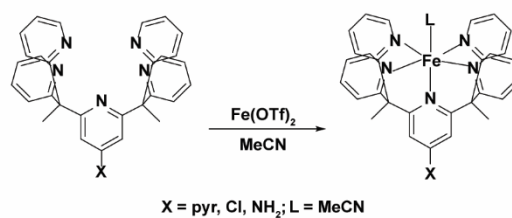
Scheme 2.1. Synthesis of $[\text{Fe}^{\text{II}}(\text{L})(\text{PY5Me}_2\text{-X})]^{2+}$, **1-X** and **2-X**. a) $\text{Fe}(\text{OTf})_2$ in MeCN yielded $[\text{Fe}^{\text{II}}(\text{MeCN})(\text{PY5Me}_2\text{-X})](\text{OTf})_2$ (**1-X**), b) $\text{Fe}(\text{OH}_2)_6(\text{BF}_4)_2$ in acetone/water mixture yielded $[\text{Fe}^{\text{II}}(\text{OH}_2)(\text{PY5Me}_2\text{-X})](\text{BF}_4)_2$ (**2-X**)



Scheme 2.1. Oxidation of Fe(II)-PY5Me₂ complexes to their Fe(IV)-oxo counterparts by chemical or photochemical routes. a) CAN in H₂O, b) Ru(bpy)₃²⁺, K₂S₂O₈ and hv (blue light). L = H₂O or MeCN.



Scheme 2.3. Ligand synthesis for PY5Me₂-X (X = pyr, Cl, and NH₂).



Scheme 2.4. Synthesis Procedure for 1-pyr, 1-Cl, and 1-NH₂

Table 2.1. Fe(III)/Fe(II) reduction potentials of **1-X** and **2-X** in MeCN and water, respectively.

X	Fe(III/II) Potential (V vs SCE) of 1-X in MeCN	Fe(III/II) Potential (V vs SCE) of 2-X at different pH values in water			
		3	4	5	6
CF₃	1.260	0.511	0.458	0.399	0.334
H	1.167	0.438	0.390	0.330	0.270
Me	1.127	0.407	0.361	0.303	0.245
NMe₂	0.956	0.306	0.259	0.203	0.136

Table 2.2. Mössbauer parameters of Fe(II)-PY5Me₂ complexes of the **1-X** and **2-X** series at 295 and 5 K. The quadrupole splitting ($|\Delta E_q|$) values increase with the electron-donating ability.

T(K)	X	1-X		2-X	
		δ	$ \Delta E_q $	δ	$ \Delta E_q $
295	CF ₃	0.4208	0.298	0.4650	0.316
	H	0.4344	0.339	0.5003	0.344
	Me	0.4339	0.367	0.4582	0.399
	NMe ₂	0.4286	0.480	0.4692	0.472
5	CF ₃	0.4987	0.311	0.5346	0.307
	H	0.5189	0.336	0.5717	0.335
	Me	0.5062	0.382	0.5208	0.394
	NMe ₂	0.5092	0.482	0.5723	0.468

Table 2.3. Comparison of Fe(III/II) reduction potentials of various Fe complexes supported by pyridine-amine ligands. All but **1-H**, which exhibits the most positive potential, can be oxidized to Fe(IV)-oxo species using OAT reagents.

	Fe(III/II) Redox Couple (V vs Fc ⁺⁰)	Reference
Fe ^{II} (MeCN)(^{Me} 2TACN-Py2)	0.55	6
Fe ^{II} (MeCN)(N4PY)	0.61	26
Fe ^{II} (MeCN)(PY5)	0.40	61
1-H	0.767	This work

Table 2.4. Mössbauer, UV-visible, and infrared spectroscopic parameters for Fe(IV)-oxo

	δ ($ \Delta E_Q $) (mm/s) at 5K	λ_{\max} (nm) (ϵ , $M^{-1}cm^{-1}$)	$\nu(Fe=^{16}O)$, $\nu(Fe=^{18}O)$ (cm^{-1})
3-CF₃	0.0782 (0.800)	710 (300)	841, 807
3-H	0.0820 (0.795)	712 (310)	821, 785
3-Me	0.0785 (0.718)	713 (300)	822, 786

PY5Me₂ complexes 3-X.

Table 2.5. Second-order rate constants of substrate oxidation by Fe^{IV}(O) PY5Me₂ species **3-X** at 25°C in aqueous solution at pH 5.5 (non-buffered water)

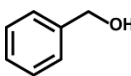
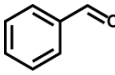
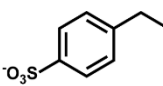
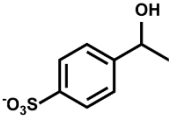
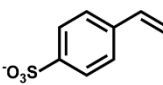
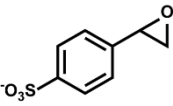
Substrate	Major Product	k ₂ (mM ⁻¹ s ⁻¹) (x 10 ⁻⁴)		
		3-CF ₃	3-H	3-Me
		29.4 ± 3.5	12.4 ± 3.0	7.60 ± 1.57
		49.7 ± 9.5	17.5 ± 1.8	7.86 ± 1.29
		1.58 ± 0.18	0.740 ± 0.105	0.750 ± 0.150

Table 2.6. Fe^{III/II} Reduction potentials of **1-X**. Fe(III/II) redox couples were measured with 1 mM of **1-X** in 0.1 M NBu₄PF₆ MeCN using glassy carbon as a working electrode, Ag/AgCl as a reference electrode and Pt wire as a counter electrode. Ferrocene was used as an external standard.

^a2,5-dimethylpyrrole

1-X	Fe^{III/II} vs Fc⁺/Fc (V)
CF ₃	0.860
Py ^a	0.842
Cl	0.813
H	0.767
Me	0.727
NH ₂	0.591
NMe ₂	0.556

Table 2.7. Fe^{III}(OH)/Fe^{II}(OH₂) Reduction potentials of **2-X**. Fe(III/II) redox couples were measured with 1 mM of **2-X** in 0.1 M KNO₃ H₂O using glassy carbon as a working electrode, Ag/AgCl as a reference electrode and Pt wire as a counter electrode.

2-X	Fe^{III}(OH)/Fe^{II}(OH₂) vs SCE (V)	2nd redox couple vs SCE (V)
CF₃	0.441	0.892
H	0.389	0.893
Me	0.348	0.880
NMe₂	0.242	0.891

Table 2.8. Mass spectrometry of reaction mixtures after photolysis confirming that all **3-X** complexes are successfully generated.

	m/z calc	m/z observed
3-CF₃	291.5636	291.5639
3-H	257.5699	257.5702
3-Me	264.5781	264.5779

Table 2.9 Crystal Structure Tables

Identification code	1-CF₃	
Empirical formula	C ₃₄ H ₂₇ F ₉ Fe N ₆ O ₆ S ₂	
Formula weight	906.58	
Temperature	100(2) K	
Wavelength	0.71073 Å	
Crystal system	Monoclinic	
Space group	P 21/n	
Unit cell dimensions	a = 9.255 Å	α = 90°.
	b = 16.4150(10) Å	β = 92.8870(10)°.
	c = 23.0480(10) Å	γ = 90°.
Volume	3497.0(3) Å ³	
Z	4	
Density (calculated)	1.722 Mg/m ³	
Absorption coefficient	0.656 mm ⁻¹	
F(000)	1840	
Crystal size	0.200 x 0.200 x 0.140 mm ³	
Theta range for data collection	1.524 to 25.362°.	
Index ranges	-10 ≤ h ≤ 11, -19 ≤ k ≤ 19, -27 ≤ l ≤ 27	
Reflections collected	52414	
Independent reflections	6410 [R(int) = 0.0482]	
Completeness to theta = 25.000°	100.0 %	
Absorption correction	None	
Refinement method	Full-matrix least-squares on F ²	
Data / restraints / parameters	6410 / 0 / 542	
Goodness-of-fit on F ²	1.044	
Final R indices [I > 2σ(I)]	R1 = 0.0319, wR2 = 0.0781	
R indices (all data)	R1 = 0.0382, wR2 = 0.0829	
Extinction coefficient	n/a	
Largest diff. peak and hole	0.402 and -0.401 e.Å ⁻³	

Identification code	1-H
Empirical formula	C37 H34 F6 Fe N8 O6 S2
Formula weight	920.69
Temperature	100(2) K
Wavelength	0.71073 Å
Crystal system	Monoclinic
Space group	P 21/n
Unit cell dimensions	a = 12.4770(10) Å α = 90°. b = 15.8020(10) Å β = 90.8980(10)°. c = 19.9400(10) Å γ = 90°.
Volume	3930.9(4) Å ³
Z	4
Density (calculated)	1.556 Mg/m ³
Absorption coefficient	0.576 mm ⁻¹
F(000)	1888
Crystal size	0.400 x 0.220 x 0.100 mm ³
Theta range for data collection	1.644 to 25.355°.
Index ranges	-15<=h<=15, -19<=k<=19, -24<=l<=24
Reflections collected	85415
Independent reflections	7182 [R(int) = 0.0346]
Completeness to theta = 25.000°	99.9 %
Absorption correction	Semi-empirical from equivalents
Max. and min. transmission	0.7452 and 0.6655
Refinement method	Full-matrix least-squares on F ²
Data / restraints / parameters	7182 / 0 / 544
Goodness-of-fit on F ²	1.054
Final R indices [I>2sigma(I)]	R1 = 0.0363, wR2 = 0.0895
R indices (all data)	R1 = 0.0422, wR2 = 0.0944
Extinction coefficient	n/a
Largest diff. peak and hole	0.508 and -0.481 e.Å ⁻³

Identification code	1-Me
Empirical formula	C34 H30 F6 Fe N6 O6 S2
Formula weight	852.61
Temperature	100(2) K
Wavelength	0.71073 Å
Crystal system	Monoclinic
Space group	P 21/n
Unit cell dimensions	a = 9.1512(3) Å $\alpha = 90^\circ$. b = 16.8978(5) Å $\beta = 91.7320(10)^\circ$. c = 22.2872(6) Å $\gamma = 90^\circ$.
Volume	3444.81(18) Å ³
Z	4
Density (calculated)	1.644 Mg/m ³
Absorption coefficient	0.649 mm ⁻¹
F(000)	1744
Crystal size	0.030 x 0.040 x 0.100 mm ³
Theta range for data collection	1.513 to 25.436°.
Index ranges	-11 ≤ h ≤ 11, 0 ≤ k ≤ 20, 0 ≤ l ≤ 26
Reflections collected	6734
Independent reflections	6734 [R(int) = ?]
Completeness to theta = 25.000°	99.0 %
Absorption correction	None
Refinement method	Full-matrix least-squares on F ²
Data / restraints / parameters	6734 / 0 / 498
Goodness-of-fit on F ²	1.071
Final R indices [I > 2σ(I)]	R1 = 0.0471, wR2 = 0.1341
R indices (all data)	R1 = 0.0545, wR2 = 0.1411
Extinction coefficient	n/a
Largest diff. peak and hole	0.518 and -0.452 e.Å ⁻³

Identification code	1-NMe₂
Empirical formula	C76 H80 F12 Fe2 N16 O12.50 S4
Formula weight	1885.50
Temperature	100(2) K
Wavelength	0.71073 Å
Crystal system	Triclinic
Space group	P -1
Unit cell dimensions	a = 11.7950(10) Å α = 78.7160(10)°. b = 19.0780(10) Å β = 88.0480(10)°. c = 20.3130(10) Å γ = 74.8080(10)°.
Volume	4325.2(5) Å ³
Z	2
Density (calculated)	1.448 Mg/m ³
Absorption coefficient	0.526 mm ⁻¹
F(000)	1944
Crystal size	0.740 x 0.160 x 0.120 mm ³
Theta range for data collection	1.662 to 25.348°.
Index ranges	-14 ≤ h ≤ 14, -22 ≤ k ≤ 22, -24 ≤ l ≤ 24
Reflections collected	56384
Independent reflections	15757 [R(int) = 0.0403]
Completeness to theta = 25.000°	99.7 %
Absorption correction	Semi-empirical from equivalents
Max. and min. transmission	0.7452 and 0.6614
Refinement method	Full-matrix least-squares on F ²
Data / restraints / parameters	15757 / 0 / 1133
Goodness-of-fit on F ²	1.056
Final R indices [I > 2σ(I)]	R1 = 0.0461, wR2 = 0.1148
R indices (all data)	R1 = 0.0580, wR2 = 0.1244
Extinction coefficient	n/a
Largest diff. peak and hole	1.257 and -1.089 e.Å ⁻³

Identification code	2-CF₃	
Empirical formula	C30 H34 B2 F11 Fe N5 O5	
Formula weight	831.09	
Temperature	100(2) K	
Wavelength	0.71073 Å	
Crystal system	Triclinic	
Space group	P -1	
Unit cell dimensions	a = 11.9538(12) Å	α = 110.228(2)°.
	b = 12.0106(12) Å	β = 105.795(2)°.
	c = 13.8708(14) Å	γ = 104.259(2)°.
Volume	1665.4(3) Å ³	
Z	2	
Density (calculated)	1.657 Mg/m ³	
Absorption coefficient	0.564 mm ⁻¹	
F(000)	848	
Crystal size	0.600 x 0.100 x 0.100 mm ³	
Theta range for data collection	1.912 to 25.680°.	
Index ranges	-14 ≤ h ≤ 14, -14 ≤ k ≤ 14, -16 ≤ l ≤ 16	
Reflections collected	54287	
Independent reflections	6306 [R(int) = 0.0368]	
Completeness to theta = 25.000°	99.9 %	
Absorption correction	Semi-empirical from equivalents	
Max. and min. transmission	0.7453 and 0.6470	
Refinement method	Full-matrix least-squares on F ²	
Data / restraints / parameters	6306 / 0 / 517	
Goodness-of-fit on F ²	1.071	
Final R indices [I > 2σ(I)]	R1 = 0.0339, wR2 = 0.0835	
R indices (all data)	R1 = 0.0377, wR2 = 0.0872	
Extinction coefficient	n/a	
Largest diff. peak and hole	0.655 and -0.544 e.Å ⁻³	

Identification code	2-H
Empirical formula	C ₂₉ H ₂₇ B ₂ F ₈ Fe N ₅ O S ₀
Formula weight	691.03
Temperature	100(2) K
Wavelength	0.71073 Å
Crystal system	Monoclinic
Space group	C2/c
Unit cell dimensions	a = 20.930(11) Å α = 90°. b = 12.259(3) Å β = 119.82(2)°. c = 12.759(2) Å γ = 90°.
Volume	2840.2(16) Å ³
Z	4
Density (calculated)	1.616 Mg/m ³
Absorption coefficient	0.619 mm ⁻¹
F(000)	1408
Crystal size	0.26 x 0.16 x 0.08 mm ³
Theta range for data collection	2.00 to 25.70°.
Index ranges	-25 ≤ h ≤ 25, -14 ≤ k ≤ 14, -15 ≤ l ≤ 15
Reflections collected	29258
Independent reflections	2699 [R(int) = 0.0306]
Completeness to theta = 25.00°	100.0 %
Absorption correction	Semi-empirical from equivalents
Max. and min. transmission	0.9521 and 0.8556
Refinement method	Full-matrix least-squares on F ²
Data / restraints / parameters	2699 / 0 / 213
Goodness-of-fit on F ²	1.064
Final R indices [I > 2σ(I)]	R1 = 0.0274, wR2 = 0.0710
R indices (all data)	R1 = 0.0297, wR2 = 0.0729
Largest diff. peak and hole	0.366 and -0.450 e.Å ⁻³

Identification code	2-Me	
Empirical formula	C15 H17.50 B F4 Fe0.50 N2.50 O2	
Formula weight	379.55	
Temperature	100(2) K	
Wavelength	0.71073 Å	
Crystal system	Monoclinic	
Space group	P 21/m	
Unit cell dimensions	a = 9.187 Å	$\alpha = 90^\circ$.
	b = 13.5440(10) Å	$\beta = 95.747(2)^\circ$.
	c = 12.4320(10) Å	$\gamma = 90^\circ$.
Volume	1539.12(17) Å ³	
Z	4	
Density (calculated)	1.638 Mg/m ³	
Absorption coefficient	0.586 mm ⁻¹	
F(000)	780	
Crystal size	0.180 x 0.160 x 0.040 mm ³	
Theta range for data collection	1.646 to 25.424°.	
Index ranges	-11 ≤ h ≤ 11, -15 ≤ k ≤ 16, -14 ≤ l ≤ 14	
Reflections collected	19789	
Independent reflections	2952 [R(int) = 0.0615]	
Completeness to theta = 25.000°	100.0 %	
Absorption correction	Semi-empirical from equivalents	
Max. and min. transmission	0.7452 and 0.6616	
Refinement method	Full-matrix least-squares on F ²	
Data / restraints / parameters	2952 / 0 / 241	
Goodness-of-fit on F ²	1.027	
Final R indices [I > 2σ(I)]	R1 = 0.0486, wR2 = 0.1140	
R indices (all data)	R1 = 0.0661, wR2 = 0.1245	
Extinction coefficient	n/a	
Largest diff. peak and hole	0.719 and -0.766 e.Å ⁻³	

Chapter 3 Reactivity of Fe Salen Complexes in Electrocatalytic CO₂

Reduction

3.1 Abstract

We report electrocatalytic reactivity of Fe supported by salen (N,N'-ethylenebis(salicylimine) ligand and derivatives toward carbon dioxide with high selectivity for carbon monoxide over proton reduction. Low selectivity is observed as CO can be trapped and inhibits the catalyst. A CO scavenger molecule [Ni(TMC)](PF₆)₂ was shown to increase catalytic current and CO production.

3.2 Introduction

The rising level of carbon dioxide (CO₂) in the atmosphere contributes to global climate change. One attractive solution is to use CO₂ as C₁ building blocks for fine and commodity chemicals.¹ However, the high molecular stability of CO₂ has proven a challenge to the development catalysts for CO₂ reduction as the process is energy-intensive and potentially has selectivity problems.²⁻⁴ Several homogeneous metal-based catalysts have been reported for CO₂ reduction electrochemically and photochemically.^{2,5,6} Fe complexes supported by porphyrin ligands have been shown to electrochemically transform CO₂ selectively to CO.^{3,7-10} Although porphyrin ligand can be functionalized to incorporate electron-withdrawing groups and proton relay moieties, the syntheses of porphyrins are fairly challenging (Scheme 3.1).

As a result, we turned our attention to metal complexes that can perform similar chemical transformations to iron porphyrin complexes. We found that Fe with salen can be a good candidate as these complexes have been reported as oxygenases mimics,¹¹ similar to Fe(porphyrin), and some reactivity toward carbon dioxide in polycarbonate formation has been reported^{12,13}. Salen ligand is also reported to be redox-active, similar to porphyrins and derivatives.¹⁴⁻¹⁶ Facile syntheses of salen ligand and Fe(salen) complex allow scalability and derivatization of the complex.

3.3 Results and Discussions

To test our hypothesis, we synthesized salen ligand, according to the reported procedures, via Schiff base formation of ethylene diamine and salicylaldehyde. Metallation with FeCl₃ yielded the Fe(salen) complex. Cyclic voltammetry of Fe(salen)Cl complex, **1**, under Ar and CO₂ atmospheres was conducted. To our delight, **1** showed current enhancement under a CO₂ atmosphere at the second reduction process, which is the Fe(II/I) redox couple. Addition of water further increased the catalytic current under CO₂ while it seems to have less effect under Ar, indicating some selectivity toward CO₂ reduction over H⁺ reduction (Figure 3.1).

Due to the high overpotential of the catalyst, we sought to tune the electronic properties of the complexes by varying substituents on the ligands. This approach have been demonstrated in our previously published pentapyridine ligand system^{17,18} and in tuning the Fe(III/II) redox couple of Fe salen complexes for aerobic hydrocarbon oxidation.^{14,19} We investigate the electronic effect on lower valent metal complexes, specifically the Fe(II/I) redox couple. Substitution of electron withdrawing groups, chloro and nitro groups, shifts the reduction potential cathodically by 150 mV for **2** and 500 mV for **3** (Figure 2, left). Complex **2** and **3** also showed current enhancement under an atmosphere of CO₂, indicating some electrocatalytic processes (Figure 3.2, right).

Preliminary controlled potential electrolysis experiments were performed on **1**, **2**, and **3**. Under a CO₂ atmosphere, **1** and **2** produced carbon monoxide (CO) as a product, while **3** did not. Although **3** seems to give rise to catalytic current at the most positive potential, we postulate that due to highly electron-withdrawing nitro groups, the iron center might not be nucleophilic enough to reduce CO₂. Low solubility of **3** also makes it difficult to study. Comparing the 3 derivatives in hand, **2** has the highest catalytic current while having moderately less overpotential compared to **1**, therefore we further modified the ligand framework based on derivatives of **2**.

Head groups of salen ligand can be modified by using different diamines as starting materials. *Trans*-Cyclohexane diamine, meso-diphenylethylene diamine and *S,S*-diphenylethylene diamine head groups were used to further tune the electronics of the ligand (Scheme 3.2). Complex **4**, **5** and **6** showed moderate differences in redox potentials compared to **2** under an Ar atmosphere (Figure 3.3, left); complex **5** and **6** have marginally more positive potential with **5** with displaying the highest catalytic current under a CO₂ atmosphere (Figure 3.3, right). Solid state structures of **5** and **6** are also reported here (Figure 3.4). Thus, complex **5** was selected for further studies by controlled potential electrolysis.

Electrolysis of **5** at -2.35 V vs Fc⁺⁰ produced CO in 40% faradaic efficiency with less than 1% H₂ produced even when 0.1 M of water is present in the solution. The high selectivity despite low faradaic yield is remarkable considering the ease of synthesis of the complex. Attempts to detect other C1 products, using NMR spectroscopy and formate enzymatic assay, have been unsuccessful.

We hypothesize that low faradaic efficiency arises from the fact that some CO product was trapped at the Fe center, resulting in lower amount of CO in the headspace to be detected by GC. The effects of several Lewis acids, including Li⁺, Na⁺, and Mg²⁺, have been studied with cyclic voltammetry experiments. Although the current seems to rise in the first scan, there is no current in the second scan, indicative of decomposition processes.

Inspired by work from the Kubiak group with [Ni(cyclam)](PF₆)₂ (cyclam = 1,4,8,11-tetraazacyclotetradecane), we attempted to trap CO using a CO scavenger molecule, [Ni(TMC)](PF₆)₂ (TMC = 1,4,8,11-tetramethyl-1,4,8,11-tetraazacyclotetradecane).²⁰ Addition of 1 to 5 equivalents of [Ni(TMC)](PF₆)₂ to **5** increases the catalytic current under a CO₂ atmosphere (Figure 3.5), similar to the case of [Ni(cyclam)](PF₆)₂ previously reported (citation). This result supports our hypothesis as [Ni(TMC)]²⁺ has been shown to scavenge CO and prevent CO from deactivating the catalyst.

To study the direct effect of CO on the reduced species of **5**, cyclic voltammetry was conducted under a CO atmosphere. After the first reduction of **5**, new peaks around -1.2 V were observed (Figure 3.6), which are similar to the new peak that appears after electrolysis under a CO₂ atmosphere. We hypothesize that these new features arise from Fe carbonyl species. Attempts to synthesize Fe(salen)(CO) are underway. We also attempted to detect the metal carbonyl species by infrared spectroscopy, however, only some broad peaks appeared in the regions for metal carbonyls around 2000 cm⁻¹ (Figure 3.8) Controlled potential electrolysis experiment of **5** in the presence of [Ni(TMC)](PF₆)₂ showed enhanced reactivity as the amount of CO produced is nearly doubled, from 264 μL to 532 μL with the same catalyst loading. Increased amount of H₂ are detected as a result of H⁺ reduction reactivity of [Ni(TMC)](PF₆)₂ which was verified by electrolysis of the Ni complex alone at the same potential. While more CO was produced, Faradaic efficiency is lower due to the reduction of the CO scavenger to Ni(0) carbonyl species as previously reported.²⁰ Table 1 summarized the electrolysis results.

Analysis of the solution reveals changes in **5** after electrolysis. UV-visible spectra of the solution before and after electrolysis show that different species are presented in the solution after electrolysis (Figure 3.10). Addition of CO scavenger still causes the decay of a shoulder at 500 nm but to a lesser degree (Figure 3.11). Isolation of metal complex in solution after electrolysis yields a dinuclear μ -oxo species, **7**, (Figure 3.12) which could also be another deactivation pathway of **5**.

3.4 Conclusions

In closing, we have presented an example of square planar Fe complexes, Fe(salen)Cl and its derivatives, which can perform electrocatalytic CO₂ reduction. While product inhibition makes the system non-ideal for use, we demonstrated tunability of the system which can be further utilized to design catalysts with improved reactivity and the use of CO scavenger molecule to increase CO evolution.

3.5 Experimental

General Synthetic and Physical Methods

All manipulations were performed under ambient conditions, unless otherwise noted. Milli-Q H₂O and HPLC grade acetonitrile were used in all experiments. All commercially available reagents were used without further purification, unless otherwise noted. All salen ligands and Fe(salen) complexes were synthesized according to literature procedures.¹⁹ Synthesis of **1** and **3** were reported previously. UV-vis spectra were recorded using a Varian Cary 50 BIO UV-visible spectrometer, equipped with a Unisoku cryostat. Infrared spectra were recorded using a Bruker FT-IR Instrument. NMR experiments were conducted using Bruker AVB-400 and AV-600 spectrometers. X-ray crystallography was performed in the Chexray facility at the University of California, Berkeley. Glassy carbon was obtained from Tokai Carbon and carbon cloth was obtained from Fuel Cell Earth.

Electrochemical Methods

Nonaqueous electrochemical experiments were conducted under Ar or CO₂ atmosphere in 0.1 M NBu₄PF₆ in CH₃CN. Cyclic voltammetry experiments were carried out using a BASI Epsilon potentiostat with a C-3 cell stand. The working electrode was a glassy carbon disk (3.0 mm diameter), and the counter electrode was a platinum wire. A silver wire in a porous Vycor tip glass tube filled with 1 mM of Ag/NO₃ in 0.1 M NBu₄PF₆ in CH₃CN was used as a reference electrode. The scan rate for all cyclic voltammograms was 100 mV/s unless otherwise noted. All potentials were referenced against ferrocenium/ferrocene as an external standard.

Controlled potential electrolysis were performed in a 2-compartment PEEK cell with a ultra-fine glass frit separator, with 1 cm² glassy carbon plate as a working electrode, Ag wire/1 mM AgNO₃ reference electrode and carbon cloth as counter electrode. Both compartments were saturated with CO₂ before electrolysis experiments. All electrolyses were carried out using a BASI Epsilon potentiostat.

Gas Chromatographic Analysis

An Agilent 490-GC Micro-gas chromatograph with a 5A Mol Sieve column and an in-line injector was used for product detection. The column was heated to 80°C under Ar flow. A

calibration curves were made for CO and H₂, using CH₄ as an internal standard. The solution was electrolyzed at -2.35 V vs Fc⁺⁰ for 3 hours before injection for analysis.

General Methods for X-ray Crystallography

Single-crystal X-ray diffraction was conducted at the University of California, Berkeley, College of Chemistry, X-ray Crystallography Facility. Crystals were mounted on nylon loops in paratone-N hydrocarbon oil. All data collections were performed on either a Bruker Quazar or an APEX diffractometer equipped with a CCD area detector and a low-temperature apparatus. Data integration was performed using SAINT. Preliminary data analysis and absorption correction were performed using XPREP and SADABS. Structure solution and refinement was performed using the SHELX software package.

General Methods for Salen Ligand Synthesis

Salicylaldehyde derivatives (2 mmol, 2 equiv) was dissolved in 100 mL of EtOH and heated to reflux. Ethylenediamine derivatives (1 mmol, 1 equiv) was added to the refluxing solution which immediately turned bright yellow. The solution was heated at reflux for another 2 hours before cooling down to room temperature. Half of the solvent was then removed *in vacuo* before the precipitates were collected via vacuum filtration. The yellow precipitates were washed with cold EtOH. The ligand was used for the next step without further purification.

Ligand of **2**: 92.3%, ¹H NMR (400 MHz, CDCl₃) δ 13.97 (s, 2H), 8.28 (s, 2H), 7.40 (d, *J* = 2.5 Hz, 2H), 7.15 (d, *J* = 2.5 Hz, 2H), 4.01 (s, 4H). ESI-MS: *m/z* calc [MH]⁺ C₁₆H₁₃O₂N₂Cl₄ 404.9726, found 404.9721.

Ligand of **4**: 92.6%:, ¹H NMR (400 MHz, CDCl₃) δ 14.20 (s, 2H), 8.18 (s, 2H), 7.36 (d, *J* = 2.5 Hz, 2H), 7.08 (d, *J* = 2.5 Hz, 2H), 3.42 – 3.30 (m, 2H), 1.92 (ddt, *J* = 15.0, 5.0, 2.6 Hz, 4H), 1.82 – 1.56 (m, 2H), 1.58 – 1.43 (m, 2H). ESI-MS: *m/z* calc [MH]⁺ C₂₀H₁₉O₂N₂Cl₄ 459.0195, found 459.0189.

Ligand of **5**: 95.0%, ¹H NMR (400 MHz, CDCl₃) δ 13.97 (s, 2H), 7.92 (s, 2H), 7.37 (d, *J* = 2.5 Hz, 2H), 7.33 (d, *J* = 4.3 Hz, 10H), 6.95 (d, *J* = 2.5 Hz, 2H), 4.74 (s, 2H). ESI-MS: *m/z* calc [MH]⁺ C₂₈H₂₁O₂N₂Cl₄ 557.0357, found 557.0358.

Ligand of **6**: 53.2%, ¹H NMR (400 MHz, CDCl₃) δ 14.06 (s, 2H), 8.27 (s, 2H), 7.39 (p, *J* = 2.5 Hz, 2H), 7.21 (td, *J* = 4.8, 1.7 Hz, 6H), 7.17 – 7.11 (m, 4H), 7.09 (d, *J* = 2.5 Hz, 2H), 4.76 (s, 2H). ESI-MS: *m/z* calc [MH]⁺ C₂₈H₂₁O₂N₂Cl₄ 557.0357, found 557.0358.

General Methods for Fe(Salen) Synthesis

Salen ligand (0.5 mmol, 1 equiv) was dissolved in 100 mL hot EtOH. The solution was heated to reflux when anhydrous FeCl₃ (0.6 mmol, 1.2 equiv) was added. The solution immediately turned dark brown and was refluxed overnight. Half of the solvent was then removed *in vacuo* before the precipitates were collected via vacuum filtration. The brown precipitates were washed with cold EtOH and Et₂O. X-ray crystallography-quality crystal were obtained by recrystallization in MeCN with Et₂O diffusion.

2: 82.0%, ESI-MS: *m/z* calc [M-MeCN]⁺ C₁₈H₁₃O₂N₃Cl₄Fe 500.9076, found 500.9071.

4: 87.8%, ESI-MS: *m/z* calc [M]⁺ C₂₀H₁₆O₂N₂Cl₄Fe 513.9280, found 513.9282.

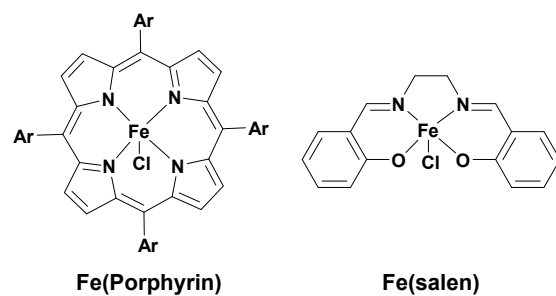
5: 44.6%, ESI-MS: *m/z* calc [M]⁺ C₂₈H₁₈O₂N₂Cl₄Fe 611.9437, found 611.9436. *m/z* calc [M-MeCN]⁺ C₃₀H₂₁O₂N₃Cl₄Fe 652.9702, found 652.9691.

6: 53.2%, ESI-MS: m/z calc $[M]^+$ C₂₈H₁₈O₂N₂Cl₄Fe 611.9437, found 611.9436. m/z calc $[M\text{-MeCN}]^+$ C₃₀H₂₁O₂N₃Cl₄Fe 652.9702, found 652.9687.

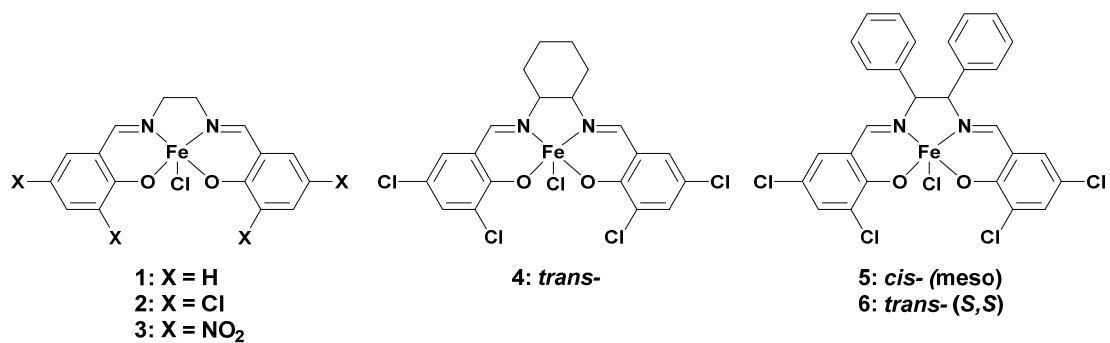
3.6 References

- 1 E. E. Benson, C. P. Kubiak, A. J. Sathrum and J. M. Smieja, *Chem. Soc. Rev.*, 2009, **38**, 89–99.
- 2 B. Kumar, M. Llorente, J. Froehlich, T. Dang, A. Sathrum and C. P. Kubiak, *Annu. Rev. Phys. Chem.*, 2012, **63**, 541–69.
- 3 C. Costentin, M. Robert and J.-M. Savéant, *Chem. Soc. Rev.*, 2013, **42**, 2423–36.
- 4 A. M. Appel, J. E. Bercaw, A. B. Bocarsly, H. Dobbek, D. L. Dubois, M. Dupuis, J. G. Ferry, E. Fujita, R. Hille, P. J. a Kenis, C. a. Kerfeld, R. H. Morris, C. H. F. Peden, A. R. Portis, S. W. Ragsdale, T. B. Rauchfuss, J. N. H. Reek, L. C. Seefeldt, R. K. Thauer and G. L. Waldrop, *Chem. Rev.*, 2013, **113**, 6621–6658.
- 5 J. Bonin, M. Robert and M. Routier, *J. Am. Chem. Soc.*, 2014.
- 6 C. a Craig, L. Spreer, J. W. Otvos and M. Calvin, *J. Phys. Chem. C*, 1990, **94**, 7957–7960.
- 7 J.-M. Savéant, *Chem. Rev.*, 2008, **108**, 2348–2378.
- 8 C. Costentin, S. Drouet, M. Robert and J.-M. Saveant, *Science (80-.)*, 2012, **338**, 90–94.
- 9 C. Costentin, M. Robert, J. M. Savéant and C. Tard, *Acc. Chem. Res.*, 2014, **47**, 271–280.
- 10 C. Costentin, S. Drouet, G. Passard, M. Robert and J. M. Savéant, *J. Am. Chem. Soc.*, 2013, **135**, 9023–9031.
- 11 C. T. Lyons and T. D. P. Stack, *Coord. Chem. Rev.*, 2013, **257**, 528–540.
- 12 D. J. Darensbourg, *Chem. Rev.*, 2007, **107**, 2388–410.
- 13 P. G. Cozzi, *Chem. Soc. Rev.*, 2004, **33**, 410.
- 14 L. Chiang, L. E. N. Allan, J. Alcantara, M. C. P. Wang, T. Storr and M. P. Shaver, *Dalton Trans.*, 2014, **43**, 4295–304.
- 15 S.-N. Pun, W.-H. Chung, K.-M. Lam, P. Guo, P.-H. Chan, K.-Y. Wong, C.-M. Che, T.-Y. Chen and S.-M. Peng, *J. Chem. Soc. Dalt. Trans.*, 2002, 575.
- 16 A. Kochem, L. Chiang, B. Baptiste, C. Philouze, N. Leconte, O. Jarjayes, T. Storr and F. Thomas, *Chem. - A Eur. J.*, 2012, **18**, 14590–14593.

- 17 Y. Sun, J. P. Bigi, N. A. Piro, M. L. Tang, J. R. Long and C. J. Chang, 2011, **2**, 9212–9215.
- 18 T. Chantarojsiri, Y. Sun, J. R. Long and C. J. Chang, *Inorg. Chem.*, 2015, **54**, 5879–5887.
- 19 A. Böttcher, M. W. Grinstaff, J. A. Labinger and H. B. Gray, *J. Mol. Catal. A Chem.*, 1996, **113**, 191–200.
- 20 J. D. Froehlich and C. P. Kubiak, *J. Am. Chem. Soc.*, 2015, **137**, 3565–73.



Scheme 3.1. Fe supported by porphyrin ligand reported as electrocatalyst for CO₂ reduction (left) and Fe supported by salen ligand complex



Scheme 3.2. Fe(salen)Cl complex and its derivatives were studied as electrochemical CO₂ reduction catalyst in this report.

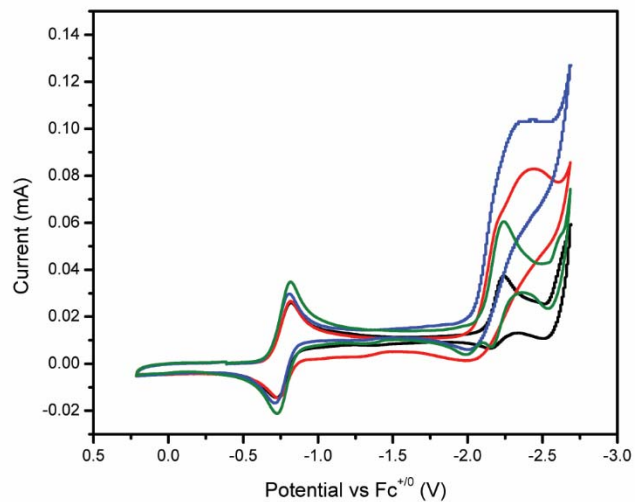


Figure 3.1. Cyclic voltammogram (CV) of 0.5 mM of **1** under Ar atmosphere (black), CO₂ atmosphere (red), CO₂ atmosphere with water added (blue) and Ar atmosphere with water added (green).

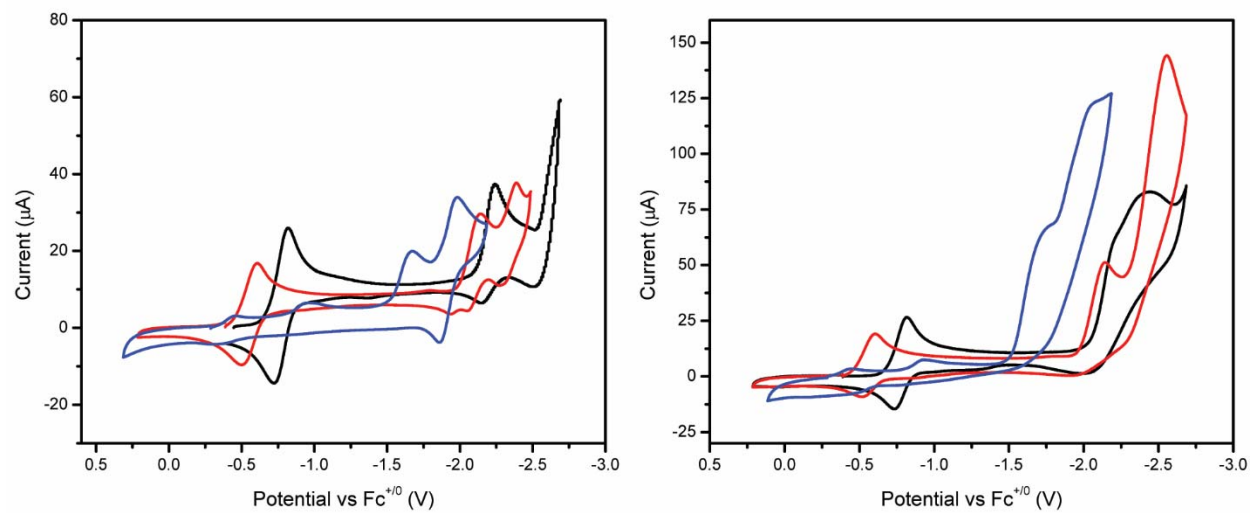


Figure 3.2. CVs of **1** (black), **2** (red), and **3** (blue) in MeCN under Ar atmosphere (left) and CO₂ atmosphere (right). The most electron withdrawing group (NO₂) shifts the Fe(II/I) redox couple to the most positive potential.

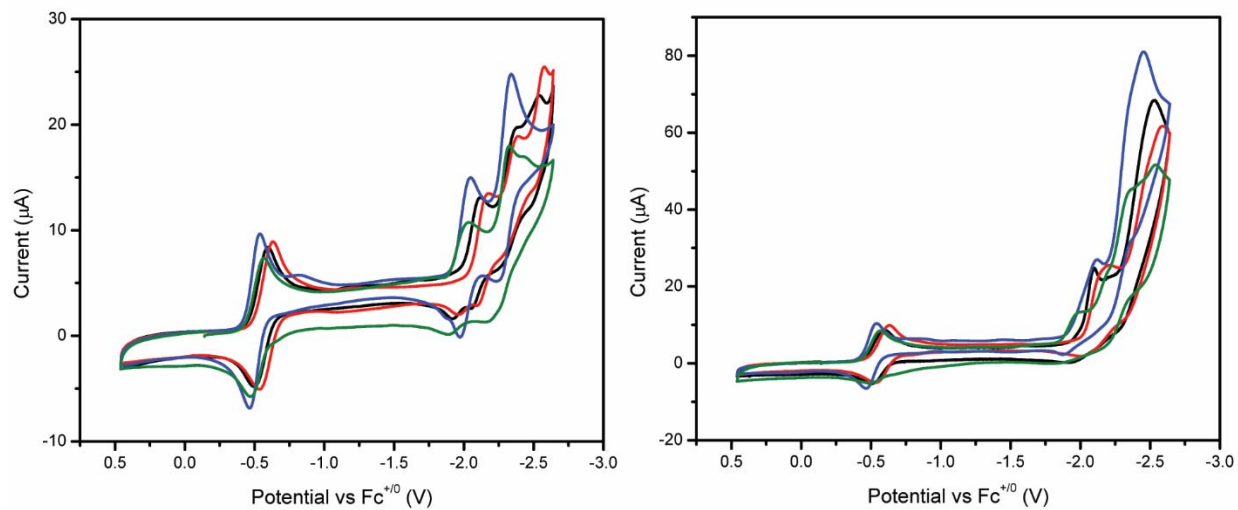


Figure 3.3. CVs of **2** (black), **4** (red), **5** (blue), and **6** (green) in MeCN under Ar atmosphere (left) and CO₂ atmosphere (right). **5** with the most electron-deficient head group shows the most positive Fe(II/I), Fe(I/0) redox potentials and gave rise to the highest catalytic current.

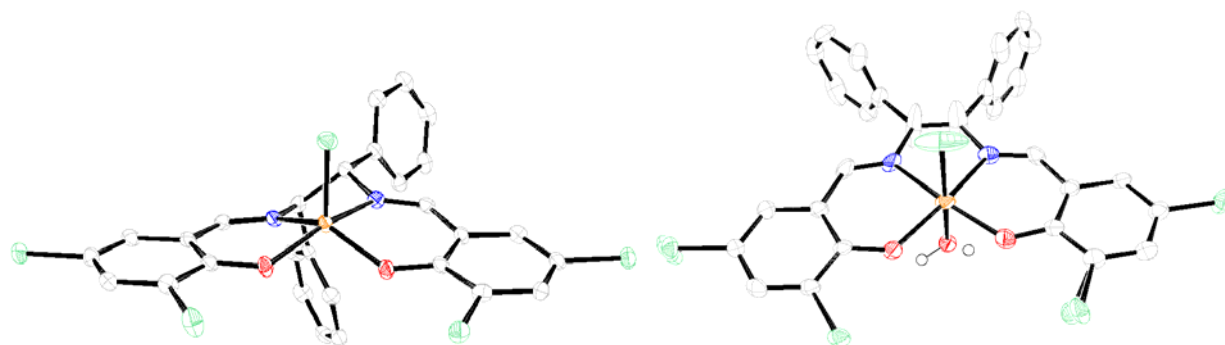


Figure 3.4. Solid state structure of **5** (left) and **6** (right).

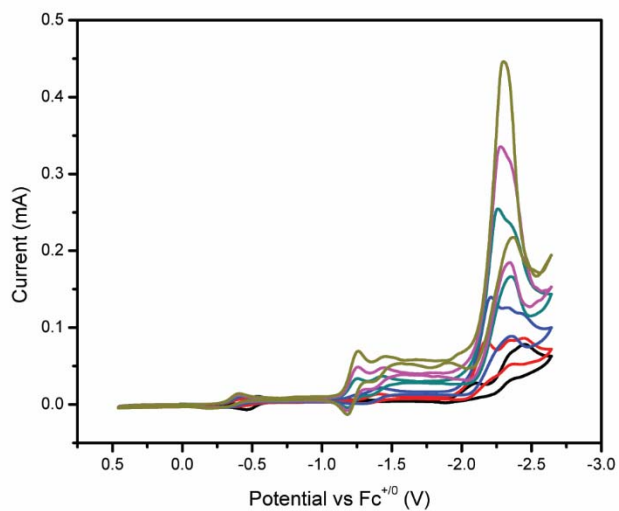


Figure 3.5. CVs of **5** with 0 eq (black), 1 eq (red), 2 eq (blue), 3 eq (cyan), 4 eq (pink) and 5 eq (yellow) of [Ni(TMC)](PF₆)₂ in MeCN under CO₂ atmosphere. Catalytic current increases with the increasing amount of [Ni(TMC)](PF₆)₂ which serves as a CO scavenger.

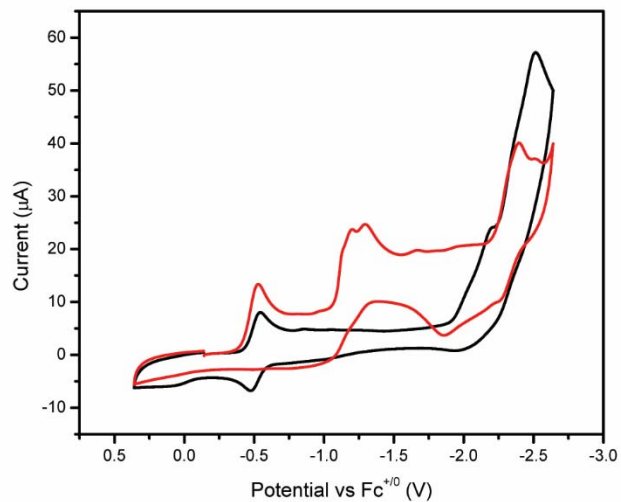


Figure 3.6. CVs of **5** under CO₂ (black) and CO (red) atmosphere. New features around -1.2 V developed under CO atmosphere matched the peaks that appeared after controlled potential electrolysis, suggesting some Fe complex trapped CO as metal carbonyl species.

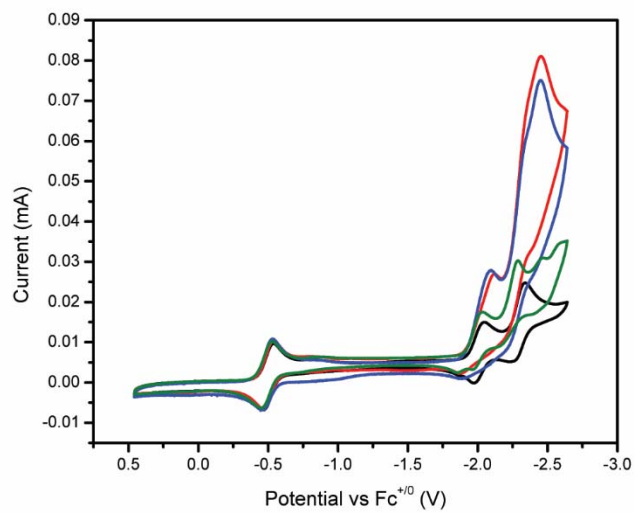


Figure 3.7. CV of 0.5 mM of **5** under Ar atmosphere (black), CO₂ atmosphere (red), CO₂ atmosphere with water added (blue) and Ar atmosphere with 0.1 M water added (green).

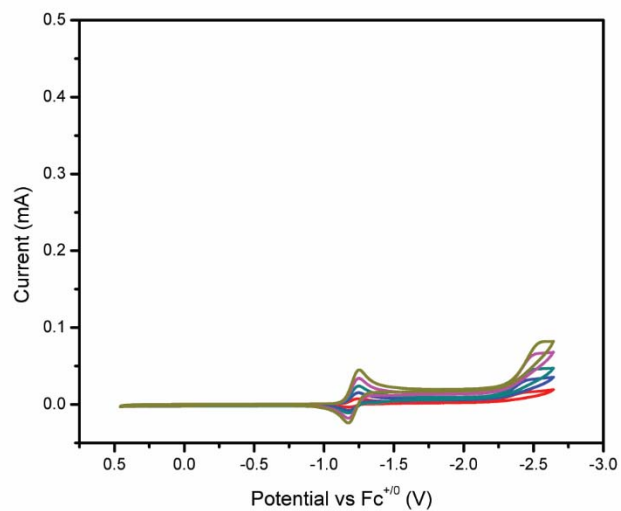


Figure 3.8. CV of 0.5 mM (red), 1.0 mM (blue), 1.5 mM (cyan), 2.0 mM (pink), and 2.5 mM (dark yellow) [Ni(TMC)](PF₆)₂ in MeCN under CO₂ atmosphere, showing no background current when it is added to the solution of **5**.

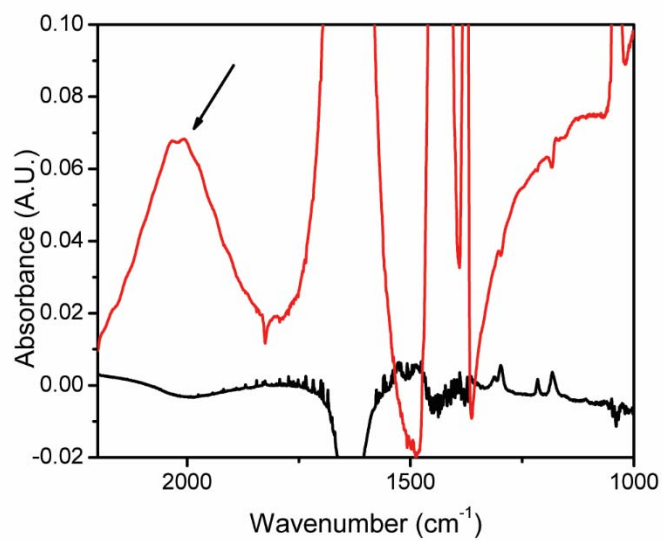


Figure 3.9. IR spectra of MeCN of **5** before (black) and after (red) controlled potential electrolysis experiment.

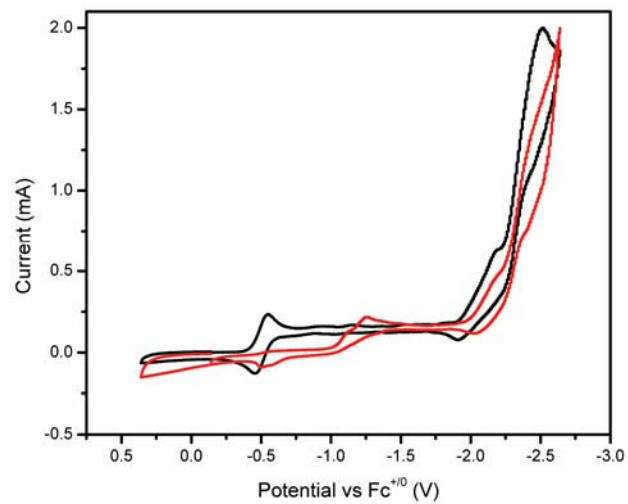


Figure 3.10. CV of **5** before (black) and after (red) controlled potential electrolysis experiment.

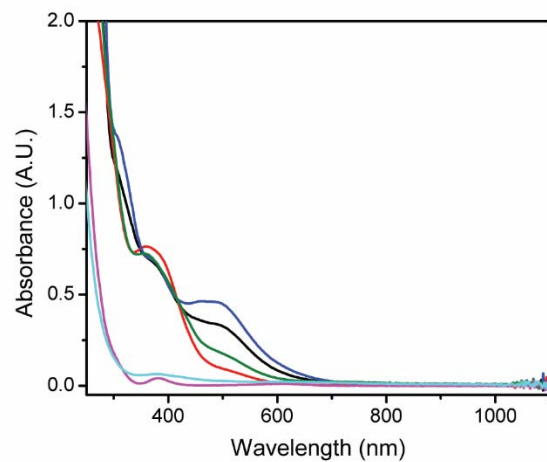


Figure 3.11. UV-visible spectra of MeCN of **5** before (black) and after (red) and **5** with 5 eq before (blue) and after (green) controlled potential electrolysis experiment. Spectra of $[\text{Ni}(\text{TMC})](\text{PF}_6)_2$ before (pink) and after (cyan) controlled potential electrolysis experiment.

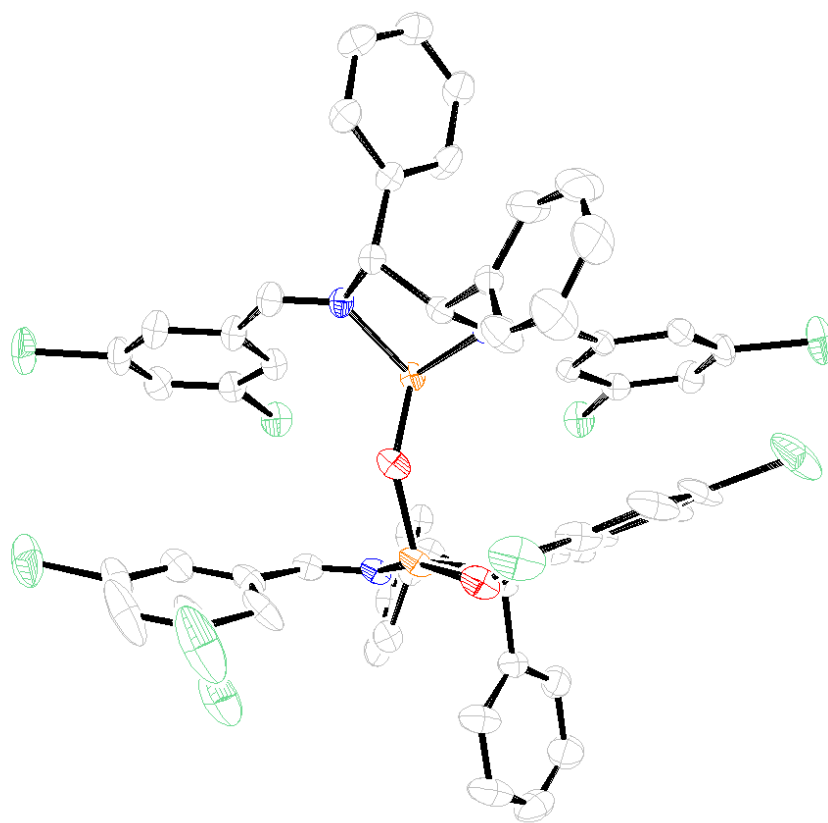


Figure 3.12. solid state structure of dinuclear μ -oxo species of **5** isolated after the electrolysis.

Table 3.1. Summary of electrolysis results of **5** in the absence and presence of CO scavenger molecule.

	5	5 + [Ni(TMC)](PF ₆) ₂	[Ni(TMC)](PF ₆) ₂
Charge (C)	4.42	13.67	5.28
CO (μL)	264	532	0
H ₂ (μL)	1.7	25	77

Table 3.2. Crystal data and structure refinement for **5**.

Identification code	5	
Empirical formula	C ₃₀ H ₂₁ Cl ₅ Fe N ₃ O ₂	
Formula weight	688.60	
Temperature	100(2) K	
Wavelength	0.71073 Å	
Crystal system	Monoclinic	
Space group	P 21/c	
Unit cell dimensions	a = 13.6305(6) Å	α = 90°.
	b = 11.6666(5) Å	β = 109.702(2)°.
	c = 19.2489(8) Å	γ = 90°.
Volume	2881.8(2) Å ³	
Z	4	
Density (calculated)	1.587 Mg/m ³	
Absorption coefficient	1.022 mm ⁻¹	
F(000)	1396	
Crystal size	0.150 x 0.040 x 0.010 mm ³	
Theta range for data collection	1.587 to 25.406°.	
Index ranges	-16 ≤ h ≤ 13, -14 ≤ k ≤ 13, -18 ≤ l ≤ 23	
Reflections collected	21430	
Independent reflections	5138 [R(int) = 0.0476]	
Completeness to theta = 25.000°	97.2 %	
Absorption correction	Semi-empirical from equivalents	
Max. and min. transmission	0.7452 and 0.6106	
Refinement method	Full-matrix least-squares on F ²	
Data / restraints / parameters	5138 / 0 / 371	
Goodness-of-fit on F ²	1.125	
Final R indices [I > 2σ(I)]	R1 = 0.0464, wR2 = 0.0977	
R indices (all data)	R1 = 0.0640, wR2 = 0.1055	
Extinction coefficient	n/a	
Largest diff. peak and hole	0.417 and -0.507 e.Å ⁻³	

Table 3.3. Crystal data and structure refinement for 7.

Identification code	7
Empirical formula	C ₅₈ H ₃₉ Cl ₈ Fe ₂ N ₅ O ₅
Formula weight	1281.24
Temperature	100(2) K
Wavelength	0.71073 Å
Crystal system	Monoclinic
Space group	P 21/n
Unit cell dimensions	a = 21.0350(5) Å α = 90°. b = 12.7478(3) Å β = 110.5350(10)°. c = 22.4197(6) Å γ = 90°.
Volume	5629.8(2) Å ³
Z	4
Density (calculated)	1.512 Mg/m ³
Absorption coefficient	0.949 mm ⁻¹
F(000)	2600
Crystal size	0.080 x 0.040 x 0.010 mm ³
Theta range for data collection	1.143 to 25.442°.
Index ranges	-25 ≤ h ≤ 25, -15 ≤ k ≤ 15, -27 ≤ l ≤ 26
Reflections collected	99931
Independent reflections	10333 [R(int) = 0.0532]
Completeness to theta = 25.000°	100.0 %
Absorption correction	Semi-empirical from equivalents
Max. and min. transmission	0.7452 and 0.7024
Refinement method	Full-matrix least-squares on F ²
Data / restraints / parameters	10333 / 0 / 713
Goodness-of-fit on F ²	1.054
Final R indices [I > 2σ(I)]	R1 = 0.0468, wR2 = 0.1171
R indices (all data)	R1 = 0.0666, wR2 = 0.1291
Extinction coefficient	n/a
Largest diff. peak and hole	0.944 and -0.679 e.Å ⁻³

Appendix A Toward the Synthesis of Mo and V Imido Complexes

Supported by PY5Me₂ Ligand

A.1. Synopsis

This chapter summarized the attempts toward synthesis of Mo and V imido or nitrido complexes supported by PY5Me₂ ligand.

A.2. Motivation and Design

We reported a proton reduction electrocatalyst, [MoO(PY5Me₂)]²⁺, that can generate hydrogen gas from neutral water at a remarkable rate and can operate in buffered water and sea water.¹⁸ Unfortunately, the overpotential at which proton reduction occurs is large. Extensive studies of the metal complexes showed that the electronic properties of such catalysts can be tuned by substitution at the *para* position of the axial pyridine with electron-donating and withdrawing groups. Preliminary experiments conducted by the Chang and Long groups on the *para*-CF₃ functionalized ligand showed that this complex is easier to reduce while the *para*-NMe₂ functionalized PY5Me₂ is more difficult to reduce in acetonitrile solution for the first reductive process, but further reductions are largely unaltered.¹⁶ These results led us to examine the effects of modifying the axial ligand directly bonded to the metal. According to literature precedent, the modification of an oxo ligand to an imido ligand can shift the reduction potential of the molecule to more positive values, which would be useful for a proton reduction catalyst.¹⁷ Using the same platform of Mo(PY5Me₂), isoelectronic [MoN(PY5Me₂)]⁺ or [MoNR(PY5Me₂)]²⁺, could potentially possess the same reactivity and potentially shift the reduction potential of proton reduction. We therefore propose the synthesis of nitrido and imido complexes Mo(PY5Me₂) as potential hydrogen evolution catalysts (Scheme 1). Vanadium complexes supported by similar ligand platform, [V^{IV}(O)(PY5Me₂)]²⁺ and [V^{III}(O)(PY5Me₂)]⁺, have also been synthesized. Derivatives of [V^{IV}(O)(PY5Me₂)]²⁺ is synthesized and studied the electronic property electrochemically. Despite lack of rich Oxygen atom transfer and Hydrogen atom abstraction reactivity, summarized here are the attempts to synthesize [V^{IV}(NH)PY5Me₂]²⁺ complexes to further explore their reactivities.

A.3. Results and Discussion

A.3.1. Toward the synthesis of imido and nitrido complexes of the Mo(PY5Me₂) platform

Attempts to synthesize imido and nitrido complexes of MoPY5Me₂ started from the low-valent precursor [Mo(PY5Me₂)(OTf)](OTf) (**1**) or [Mo(PY5Me₂)(OTf)](OTf)₂ (**2**). The syntheses of **1** and **2** were adapted from the literature.¹⁸ The PY5Me₂ ligand was synthesized in 3 steps and subsequent metal compounds were synthesized in 4 to 5 additional steps. Three strategies were employed to prepare imido and nitrido complexes of Mo(PY5Me₂) based on: i) reactions with azides ii) reactions with amines and iii) reactions with nitrene transfer agents.

Reactions with Azides

The first attempt to synthesize imido and nitrido complexes of Mo(PY5Me₂) involved the two-electron oxidation by azides.²⁵ Both **1** and **2** were subjected to a variety of alkyl and aryl azides in different solvents: 1,2-difluorobenzene (DFB), 1,2-dimethoxyethane (DME), acetonitrile (MeCN) and tetrahydrofuran (THF). Typical reaction conditions are described in the experimental section. Reaction of **1** with sodium azide, adamantylazide (AdN₃) and *p*-methoxyphenylazide in DFB resulted in a color change from dark green to dark purple. Different

green and orange mixtures were produced as the solvent was removed, and the solid residue was extracted with THF and MeCN. Unfortunately, none of the reaction mixtures proved tractable. The same reactions were repeated in DME, THF and MeCN. While similar results were obtained in DME and THF, no color change occurred when MeCN was used as a solvent. These results can be rationalized on the basis of the coordinating ability of each solvent. While DFB, DME and THF are either weakly coordinating or non-coordinating, MeCN is a strongly coordinating solvent. As a result, it is more difficult for azides to replace MeCN, which is expected to be a necessary step prior to imido or nitrido formation.

Thermolysis of the above reactions typically led to decomposition of the metal complex under an N₂ atmosphere, yielding yellow or orange solutions of the azides, which was characterized by ¹H NMR spectroscopy.

The reaction of **2** and NaN₃ in MeCN proceeded differently from that observed for **1**. The light green color of **2** in MeCN solution became dark green after 12 h. An X-ray diffraction study revealed the product to be the result of the cycloaddition of the metal-azide complex with MeCN (**3**). Similar reactivity was previously reported for a separate Mo-containing system.²⁶ The unexpected cycloaddition product suggests that azides can indeed bind to the metal center prior to cycloaddition, although MeCN is not a suitable solvent for subsequent nitrido formation. An ORTEP representation of the cycloaddition product (**3**) is shown in Figure 1.

Reaction with Amines

Since the molybdenum oxo complex, [MoO(PY5Me₂)](OTf)₂ (**4**) can be synthesized by adding water to **1**, an imido complex was targeted by the reaction of **1** with ammonia to generate the isoelectronic imido complex, MoNH(PY5Me₂)(OTf)₂. In order to do this, ammonia gas passed into a drying tube containing NaOH was condensed into a frozen solution of **1** in DFB. Upon warming to room temperature, the solution of **1** immediately changed color from dark green to orange. An infrared (IR) spectrum of the product showed a weak absorbance at 3455 cm⁻¹, which is indicative of the presence of an N-H bond. Solids obtained from the reaction changed color to bright green upon contact with air and were readily converted to **4** during an electrospray ionization mass spectrometry (ESI-MS), suggesting that the products were unstable. Hence, we selected 1-adamantylamine as the next reagent in the hope that the bulky adamantyl group would sterically protect the metal center. Reaction of **1** with adamantylamine produced the same color change as the ammonia reaction. While no single product could be isolated, a significant color change indicated the transformation of starting material. Interestingly, the products from the reaction of **1** with adamantylamine gave an IR spectrum very similar to the products from the reaction of **1** with adamantylazide, except for an absorbance at 2085 cm⁻¹ in the latter case. It can be implied that a similar set of products was formed, with residual azido complex observed for the reaction with AdN₃ (Figure 2). NMR spectra of diamagnetic products from different reactions were obtained; however, none of them showed clean well-defined compounds.

Reaction with Nitrene and Nitride Transfer Reagents

The third approach to the synthesis of nitrido or imido complexes was to use a nitrene or nitride transfer reagent. Reagents in the family of [N-phenylsulfonyl]imino]phenyliodinane were used to transfer a nitrogen atom to complex **1**.²⁷ Among the reagents available, we used [N-(p-nitrophenylsulfonyl)imino] phenyliodinane (PhINNs), as the electron-withdrawing nature of the

nosyl group makes it a good leaving group and would allow for cleavage of the sulfonyl group to yield a parent imido functionality. Reactions were performed in various solvents, including DFB, DME and MeCN. While reactions with azides and amines were slow, reaction with PhINNs occurred within 15 minutes, as indicated by a change in color of the solution from dark green to brown/dark yellow. UV-vis spectroscopy showed the transition around 492 nm, which is not present in the pure sample of **4**, which often appeared as a by-product due to the high sensitivity of **1** towards water (Figure 3). An NMR spectrum of the crude product showed spectrum of **4**, which could be the result of the product's high sensitivity to water, and additional peaks which could possibly be the desired precursor, [MoNNs(PY5Me₂)](OTf)₂ (**5**).

To determine the identity of this new product, a brown precipitate from the reaction above was isolated and subjected to mass spectrometry. While there were some impurities, the major product exhibited an *m/z* of 370.553, which matched the calculated mass of [MoNNs(PY5Me₂)]²⁺ (*m/z* = 370.552), suggesting successful nitrene transfer (Figure 4). Unfortunately, the intensity of the product peak, [MoNNs(PY5Me₂)]²⁺, decreased as the mass spectrometry experiment progressed and, was accompanied by growth of **4**, indicating that the product is unstable relative to the formation of **4** under ESI-MS conditions. The dark yellow solution was recrystallized from MeCN and benzene, yielding dark yellow needle-shaped crystals suitable for single-crystal X-ray crystallography. The appearance of dark yellow crystals was noticeably different from **4**, which are typically appeared as bright green crystals. The solid-state structure of the product showed a single atom bound to the Mo center, with the PY5Me₂ ligand intact. Surprisingly, no sulfonyl group was found in the unit cell. Despite various attempts to refine the structure, the identity of the atom attached to Mo center is ambiguous. The Mo-X bond length is 1.689(3) Å, which is similar to the Mo-O bond length of **4**, but is also close to the expected distance for the parent imido (Figure 5). As solvents and anions contained in the unit cell were highly disordered, they were excluded using Squeeze function. After final refinement, *R*₁ of Mo-O appeared to be 0.0905 and *R*₁ of Mo-N appeared to be 0.0916.³² The current data set only preferred **4** as a product by 0.11%. Successive fractional recrystallizations are currently ongoing to obtain better crystals suitable for determining the identity of X.

The UV-vis absorbance spectrum of the yellow crystals of **5** is different from that of **4**, with a distinct absorption at around 492 nm, which we ascribe to the yellow imido-nosyl complex (Figure 6). The ¹H NMR spectrum of the crystals, however, is consistent with the presence of **4**; upon addition of **4** to the same NMR tube, the peaks appeared at the same chemical shifts. Nevertheless, the immensely different colors of the yellow crystals relative to bright green **4** and the distinct absorption spectrum suggest a product different from **4** was obtained. It is possible that the desired product, **5**, decomposes quickly to **4** upon exposure to moisture, resulting in the prevailing presence of **4**. Cyclic voltammogram of **5** also suggested that it is possible that this reaction generates a mixture of **5** and **4** as products as it showed reduction and oxidation peaks at the same potentials as **4** overlapping with other peaks in the spectrum (Figure 8).

Other group transfer reagents were also tested. CrN(OtBu)₃, a nitride transfer reagent, was added to **2** after a 2-electron reduction with magnesium anthracene (MgA) to intermediate Mo(I) specie.²⁷ The color of the reaction changed from dark purple to green. The product was subjected to mass spectrometry and cyclic voltammetry, both of which suggested that the green solid obtained was **4**. Lithium 2,3:5,6-dibenzo-7-aza-bicyclo[2.2.1]hepta-2,5-diene (Lidbabh) was also used as a nitrogen transfer agent. Although the color changed to dark purple, the

reaction mixture was intractable. Exposing the reaction mixture to air resulted in a color change to orange.

A.3.2. *The synthesis of derivatives of $[V(O)PY5Me_2-X]^{2+}$ and imido/nitrido complexes of the $V(PY5Me_2)$ platform*

The low valent precursor, $[V(PY5Me_2-CF_3)(MeCN)](OTf)_2$ (**6**) and $[V(PY5Me_2-NMe_2)(MeCN)](OTf)_2$ (**7**) can be synthesized by metallation of $PY5Me_2$ ligand derivatives with V(II) precursor, $V(MeCN)_6(OTf)_2$, in acetonitrile. Upon recrystallization by Et_2O diffusion yielded red crystals. The isolated products were used to synthesize $[V(O)PY5Me_2-CF_3](OTf)_2$ (**8**) and $[V(O)PY5Me_2-NMe_2](OTf)_2$ (**9**) by oxidation with Iodosobenzene (PhIO) to yield light green solution.³³ The products can be isolated by Et_2O diffusion producing single crystal with x-ray diffraction quality, Figure 9. Cyclic voltammetry of **8** and **9** showed cathodic and anodic shifts of $V^{IV}(O)/V^{III}(O)$ redox couples respectively, Figure 10.

Attempts to synthesize imido and nitrido complexes of $VPY5Me_2$ started from the low-valent precursor $[V(PY5Me_2)(MeCN)](OTf)_2$ (**10**) with various azide precursors. Upon mixing **10** with NaN_3 , the solution changed color from deep red to dark blue. Recrystallization by Et_2O diffusion gave single crystal x-ray diffraction quality crystal of $[V(PY5Me_2)(N_3)](OTf)$ (**11**). IR spectrum of **11** showed N-N stretches at 2050 cm^{-1} . Oxidation of **11** by $AgOTf$ gave a mixture of $[V^{III}(N_3)(PY5Me_2)]^{2+}$ and $[V^{IV}(NH)(PY5Me_2)]^{2+}$ which were verified by high resolution ESI-MS. On the other hand, $[V(PY5Me_2)(ArN_3)]^{2+}$ complex did not form when aryl azide was used as a reagent. Cyclic voltammogram of oxidation product **12** shows difference in reduction potentials (CV) and modest difference in bond length between V-N and V-O, Figure 11 and 12. Oxidation of **11** by $NOBF_4$ yielded yellow crystal of $[V^{III}(F)(PY5Me_2)](BF_4)_2$ by squid magnetometry and X-ray crystallography (Figure 13).

A.4. Conclusion and Future Directions

A.4.1. *Imido and nitrido complexes of the $Mo(PY5Me_2)$ platform*

Although our current methods have yet to yield the desired products, a variety of techniques remain to be tested for the generation of nitrido and imido complexes. For example, different nitrene/nitrido transfer reagents can be used. Alternatively, a Mo starting material that already contains a terminal nitride can be used to install this functionality. Elemental analysis can be used to analyze the percentage of N atom present in the product, to distinguish between **4** and the parent imido complex. In terms of reactivity, the newly-synthesized imido/nitrido complexes will be explored electrochemically to determine the relationship between the axial ligand (nitride, imide or oxo) and the electronic properties of these molecules. Furthermore, modifications to the ligand platform may stabilize nitride and imido metal complexes. A series of imido ligands with different aryl substitutions will be synthesized and studied to further understand the effect of the axial ligand on the reduction potentials of the molecules.

A.4.2. Derivatives of $[V(O)PY5Me_2-X]^{2+}$ and imido/nitrido complexes of the $V(PY5Me_2)$ platform

Electronic tuning of axial ligand in V-oxo complexes by substitution of ligand affect $V^{IV/III}$ redox couple; electron-withdrawing group shifts the potential cathodically while electron-donating group shifts the potential anodically. V-imido can be synthesized from V-azide precursor **11**. Similar to Mo-imido and Mo-oxo system, V-oxo and V-imido are also difficult to synthesize and purify as trace oxygen in glovebox atmosphere will also oxidize **10** and **11** to V-oxo which is an undesired side product.

A.5. Experimental

General Information: All manipulations were performed under air- and water- free conditions using standard glovebox and Schlenk-line techniques, unless otherwise noted. All commercially available reagents were used without further purification, unless otherwise noted. Toluene, acetonitrile (MeCN), tetrahydrofuran (THF) and diethylether (Et₂O) were dried and degassed using the VAC 103991 solvent system and stored over 3-Å molecular sieves under a nitrogen atmosphere, and 1,2-difluorobenzene (DFB) was distilled over calcium hydride and stored over 3-Å molecular sieves prior to use. $[Mo(PY5Me_2)(OTf)](OTf)_2$ and $PY5Me_2$ ((2,6-bis(1,1-bis(2-pyridyl)ethyl)pyridine)), were synthesized according to literature procedures.¹⁴ Synthesis of $[Mo(PY5Me_2)(OTf)](OTf)$ (**1**) was adapted from the published procedure.¹⁴ UV-vis spectra were recorded on a VARIAN CARY 50 BIO UV-Visible Spectrophotometer. Infrared spectra were recorded on a Bruker FT-IR Alpha-P ATR Instrument. NMR experiments were conducted on a Bruker AVB-400 spectrometer. ESI-MS experiments were performed by the Proteomics/Mass Spectrometry facility at University of California-Berkeley. X-ray crystallography was performed in the Chexray facility.

$[Mo(PY5Me_2)(OTf)](OTf)$ (1**)** : A 2 mL THF solution of $Mg(Anthracene)(THF)_3$ (32 mg, 0.077 mmol, 1 eq) was added slowly to a cold 8 mL THF solution of $Mo(PY5Me_2)(OTf)_3$ (150 mg, 0.152 mmol, 2 eq). The solution turned dark purple after the addition and turned dark green after 2 days at room temperature. The solvent was removed *in vacuo*, and the resulting solid was washed with pentane and THF. The remaining solid was recrystallized from DFB/Et₂O. After 2 days, a dark green solid (120 mg, 98%) was collected and washed with Et₂O. IR (neat): 1600(w), 1506(w), 1450(m), 1392(w), 1326(w), 1269(s), 1233(m), 1223(m), 1202 (m), 1145(s), 1100(m), 1028(s), 991(m), 864(w), 841(w), 778(w), 750(s), 726(m), 696(w), 633(s), 586(m), 571(m), 515(m), 493(m), 439(m) cm^{-1} .

Typical reaction with Organic Azides: An equimolar amount of azide in 1 mL of solvent was added to a 5 mL solution of 20 mg (0.024 mmol) of **1**. The solution was left to stir at room temperature over the period of 1-2 days. The solid from the reaction mixture was then attempted to fractional recrystallize from MeCN/Et₂O diffusion. AdN₃ IR(neat): 2912(w), 2852(w), 2085(m), 1599(w), 1505(w), 1495(w), 1481(w), 1468(w), 1453(w), 1439(w), 1256(s), 1224(m), 1149(m), 1100(w), 1058(w), 1027(s), 966(s), 883(w), 863(w), 841(w), 755(s), 677(w), 634(s), 572(m), 516(m), 496(w), 441(w), 401(w) cm^{-1} .

Typical reaction with NaN₃: An equimolar amount of sodium azide in 1 mL of solvent was added to 5 mL solution of 20 mg (0.024 mmol) of **1**. The solution was left to stir at room

temperature over the period of 1-2 days. Solvent was removed *in vacuo* and the solid was washed with THF to remove NaOTf. The remaining solid was then attempted to fractional recrystallize from MeCN/Et₂O diffusion.

Reaction of 1 with Ammonia: Anhydrous ammonia gas was passed through NaOH pellets before condensation at -78°C in a Schlenk tube with a DFB solution of **1**, equipped with a stir bar. After exposure to ammonia for 20 minutes, the reaction mixture changed color from a dark green solution to an orange solution with a green solid. The solid was washed with DFB until the filtrate was clear. IR (of the green solid) (neat): 3455(w), 3115(w), 3077(w), 3045(w), 1597(s), 1462(s), 1433(m), 1383(m), 1308(w), 1260(w), 1168(w), 1152(w), 1088(m), 1062(m), 1026(s), 972(w), 900(w), 863(w), 842(m), 785(w), 773(s), 759(s), 700(w), 647(m), 632(s), 678(w), 515(w), 494(w), 473(w), 437(w), 428(m), 414(w) cm⁻¹.

Reaction of 1 with 1-aminoadamantane: A DFB solution (1 mL) of (5.6 mg, 0.037 mmol) 1-adamantylamine was added to a 4 mL DFB solution of 30 mg (0.036 mmol) of **1**. The reaction was left to stir overnight at room temperature and its color changed from dark green to reddish purple. The solvent was removed *in vacuo* and the remaining solid was attempted to fractional recrystallize from DFB/Et₂O. IR(neat): 2907(w), 2849(w), 1597(w), 1505(w), 1482(w), 1453(w), 1438(w), 1267(s), 1224(m), 1151(m), 1096(m), 1062(m), 1027(s), 965(s), 855(w), 787(w), 755(s), 634(s), 572(m), 515(m), 498(w), 453(w), 406(w) cm⁻¹.

MoNNs(PY5Me₂)(OTf)₂ (5): PhINNs (9.7 mg, 0.024 mmol) was made into slurry in 1 mL DFB before being added to 20 mg (0.024 mmol) of **1** in 5 mL DFB. Brown solid started to precipitate after 15 minutes. The solution was stirred at room temperature overnight. The solid from the reaction was collected, washed with toluene, and then extracted into MeCN. The MeCN solution was then attempted to fractional crystallize by layering with benzene. Dark yellow needle crystals were collected and examined by X-ray crystallography. Crude yield: 80.2% UV-Vis (MeCN): λ_{max} 486 (s), 788 (w) nm. ESI-MS calc *m/z* 370.552, found *m/z* 370.553. Calc. C₃₇H₂₉F₆MoN₇O₁₀S₃ (1037.81 g.mol⁻¹): C, 42.82; H, 2.82; N, 9.45. Found: C, 39.31; H, 2.80; N, 8.00.

Synthesis of [V(N₃)PY5Me₂](OTf): [V(MeCN)PY5Me₂](OTf)₂ (50 mg, 60 μmol, 1 eq) was dissolved in 3 ml MeCN before NaN₃ in 1 ml MeCN solution (4 mg, 60 μmol, 1 eq) was added. The red solution turned purple upon stirring at room temperature overnight. The MeCN solution was then concentrated and recrystallized by Et₂O diffusion to yield X-ray crystallography quality purple needles (36.8mg, 76.1%). ESI-MS *m/z* calcd for C₂₉H₂₅N₈V 536.1643, found 536.1636. Calc. C₃₀H₂₅F₃VN₈O₃S₁ (685.57 g.mol⁻¹): C, 52.56; H, 3.68; N, 16.34. Found: C, 52.57; H, 3.71; N, 16.70.

Synthesis of [V(NH)PY5Me₂](OTf)₂: [V(N₃)PY5Me₂](OTf) (20 mg, 29 μmol, 1 eq) was dissolved in 1 ml MeCN before 0.5 ml solution of AgOTf (7.5 mg, 29 μmol, 1 eq) was added. The red solution turned yellow upon mixing and was left stirring at room temperature overnight. The MeCN solution was then concentrated and recrystallized by Et₂O diffusion to yield X-ray crystallography quality crystals (yield). ESI-MS *m/z* calcd for C₂₉H₂₅N₆V (254.5834), found (254.5823). Calc. C₃₁H₂₅F₆VN₆O₆S₂ (806.63 g.mol⁻¹): C, 46.16; H, 3.12; N, 10.42. Found: C, 46.31; H, 3.36; N, 10.27.

SQUID Magnetometry. Direct-current (dc) magnetic susceptibility data for all compounds were collected using a Quantum Design MPMS-XL SQUID magnetometer from 2 to 300 K under a constant applied field of 1000 Oe. Measurements for all compounds were obtained on a polycrystalline sample sealed in a polycarbonate gelcap. Dc magnetic susceptibility data were corrected for diamagnetic contributions from the sample holder as well as the core diamagnetism of the sample (estimated using Pascal's constants).

A.6. References

- (1) Lewis, N. S.; Nocera, D. G. *Proc. Natl. Acad. Sci. U.S.A.* **2006**, *103*, 15729-35.
- (2) Vincent, K.A.; Parkin, A.; Armstrong, F. A. *Chem. Rev.* **2007**, *107*, 4366-413.
- (3) Vignais, P. M.; Billoud, B. *Chem. Rev.* **2007**, *107*, 4206-72.
- (4) Yachandra, V. K.; Sauer, K.; Klein, M. P. *Chem. Rev.* **1996**, *96*, 2927-50.
- (5) Sono, M.; Roach, M. P.; Coulter, E. D.; Dawson, J. H. *Chem. Rev.* **1996**, *96*, 2841-88.
- (6) Wallar, B. J.; Lipscomb, J. D. *Chem. Rev.* **1996**, *96*, 2625-58.
- (7) Magnuson, A.; Anderlund, M.; Johansson, O.; Lindblad, P.; Lomoth, R.; Polivka, T.; Ott, S.; Stensjö, K.; Styring, S.; Sundström, V.; Hammarström, L. *Acc. Chem. Res.* **2009**, *42*, 1899-909.
- (8) Holm, R. H.; Solomon, E. I. *Chem. Rev.* **2004**, *104*, 347-8.
- (9) Breslow, R. *Acc. Chem. Res.* **1995**, *28*, 146-53.
- (10) Dempsey, J. L.; Brunschwig, B. S.; Winkler, J. R.; Gray, H. B. *Acc. Chem. Res.* **2009**, *42*, 1995-2004.
- (11) Dismukes, G. C.; Brimblecombe, R.; Felton, G. a N.; Pryadun, R. S.; Sheats, J. E.; Spiccia, L.; Swiegers, G. F. *Acc. Chem. Res.* **2009**, *42*, 1935-43.
- (12) Que, L.; Dong, Y. *Acc. Chem. Res.* **1996**, *29*, 190-6.
- (13) Yoshizawa, K. *Acc. Chem. Res.* **2006**, *39*, 375-82.
- (14) (a) Laplaza, C. E.; Cummins, C. C. *Science* **1995**, *268*, 861-3. (b) Yandulov, D. V., Schrock, R. R. *Science* **2003**, *301*, 76-8.
- (15) Stone, K. L.; Borovik, a S. *Curr. Opin. Chem. Biol.* **2009**, *13*, 114-8.
- (16) Esswein, A. J.; Nocera, D. G. *Chem. Rev.* **2007**, *107*, 4022-47.
- (17) Kubas, G. J.; Ryan, R. R. *Polyhedron* **1986**, *5*, 473-85.
- (18) Karunadasa, H. I.; Chang, C. J.; Long, J. R. *Nature* **2010**, *464*, 1329-33.
- (19) Jonas, R.T. and, T. D. P. Stack, *J. Am. Chem. Soc.* **1997** *119* (36), 8566-67
- (20) Bigi, J. P. *Unpublished results*
- (21) Mösch-Zanetti, N. C.; Wurm, D.; Volpe, M.; Lyashenko, G.; Harum, B.; Belaj, F.; Baumgartner, J. *Inorg. Chem.* **2010**, *49*, 8914-21.
- (22) Gunay, A.; Theopold, K. H. *Chem. Rev.* **2010**, *110*, 1060-81.
- (23) Harman, W. H.; Chang, C. J. *J. Am. Chem. Soc.* **2007**, *129*, 15128-29.
- (24) Nam, W. *Acc. Chem. Res.* **2007**, *40*, 522-31.
- (25) Eikey, R. *Coord. Chem. Rev.* **2003**, *243*, 83-124.
- (26) Liu, F.-C.; Lin, Y.-L.; Yang, P.-S.; Lee, G.-H.; Peng, S.-M. *Organometallics* **2010**, *29*, 4282-90.
- (27) Watson, I. D. G.; Yu, L.; Yudin, A. K. *Acc. Chem. Res.* **2006**, *39*, 194-206.

- (28) Chiu, H.-T.; Chen, Y.-P.; Chuang, S.-H.; Jen, J.-S.; Lee, G.-H.; Peng, S.-M. *Chem. Commun.* **1996**, 139-40.
- (29) DiPasquale, A. *Personal Communication*.
- (30) Hapke, M.; Staats, H.; Wallmann, I.; Lützen, A. *Synthesis* **2007**, 2007, 2711-19.
- (31) Sun, Y.; Bigi, J. P.; Piro, N. A.; Tang, M. L.; Long, J. R.; Chang, C. J., *J. Am. Chem. Soc.* **2011**, *133*, 9212-15.
- (32) Chantarojsiri, T.; Sun, Y.; Long, J. R.; Chang, C. J., *Inorg. Chem.* **2015**, *54*, 5879–87
- (33) King, A. E.; Nippe, M.; Atanasov, M.; Chantarojsiri, T.; Wray, C.; Bill, E.; Neese, f.; Long, J. R.; Chang, C. J., *Inorg. Chem.* **2014**, *53*, 11388-11395.

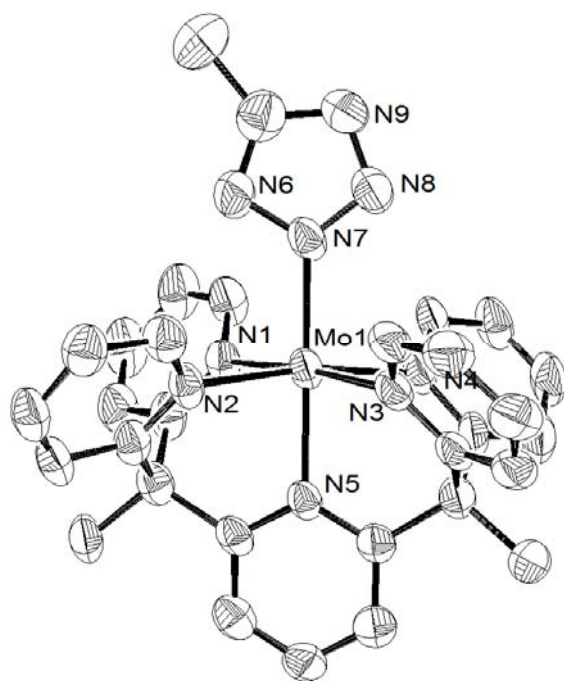


Figure A.1. Cycloaddition product of MoPY5Me₂(N₃)(OTf)₂ with MeCN (**3**). Hydrogen atoms and counter ions are omitted for clarity.

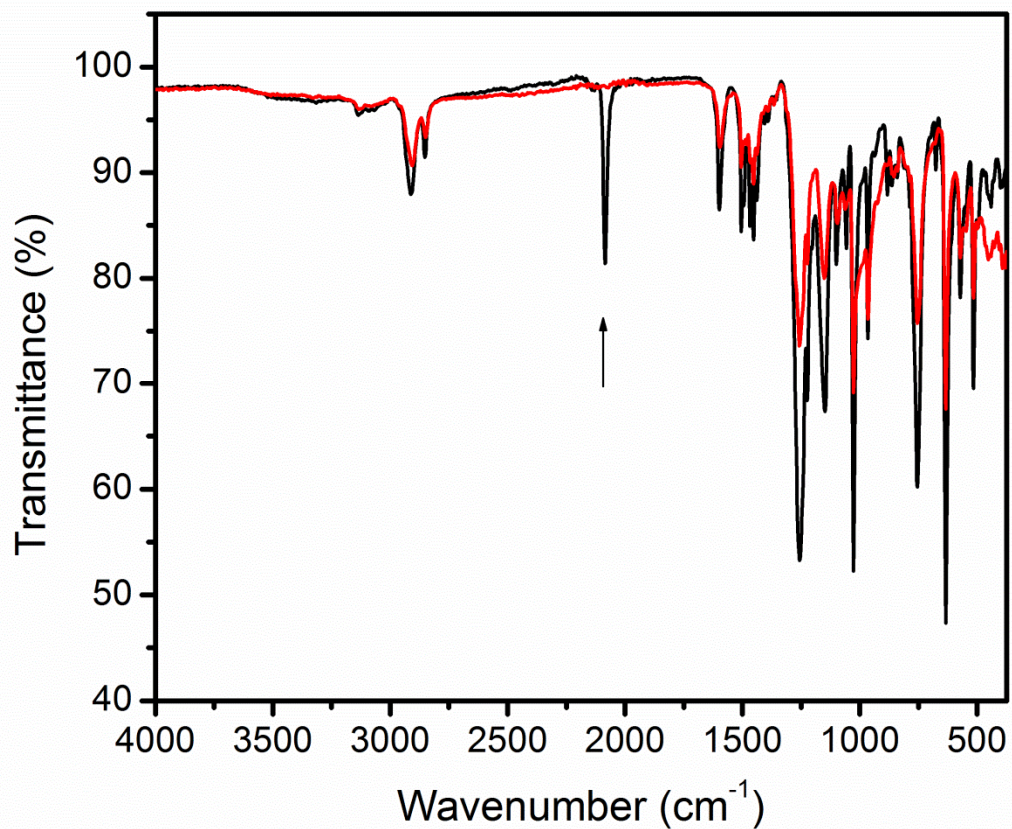


Figure A.2. IR spectra for the reaction of **1** with adamantylazide (black) and with adamantylamine (red) reaction. The two spectra show the same fingerprint pattern with the exception of the azide N=N stretching peak, 2085 cm⁻¹ (arrow), indicating similarity of products from both reactions.

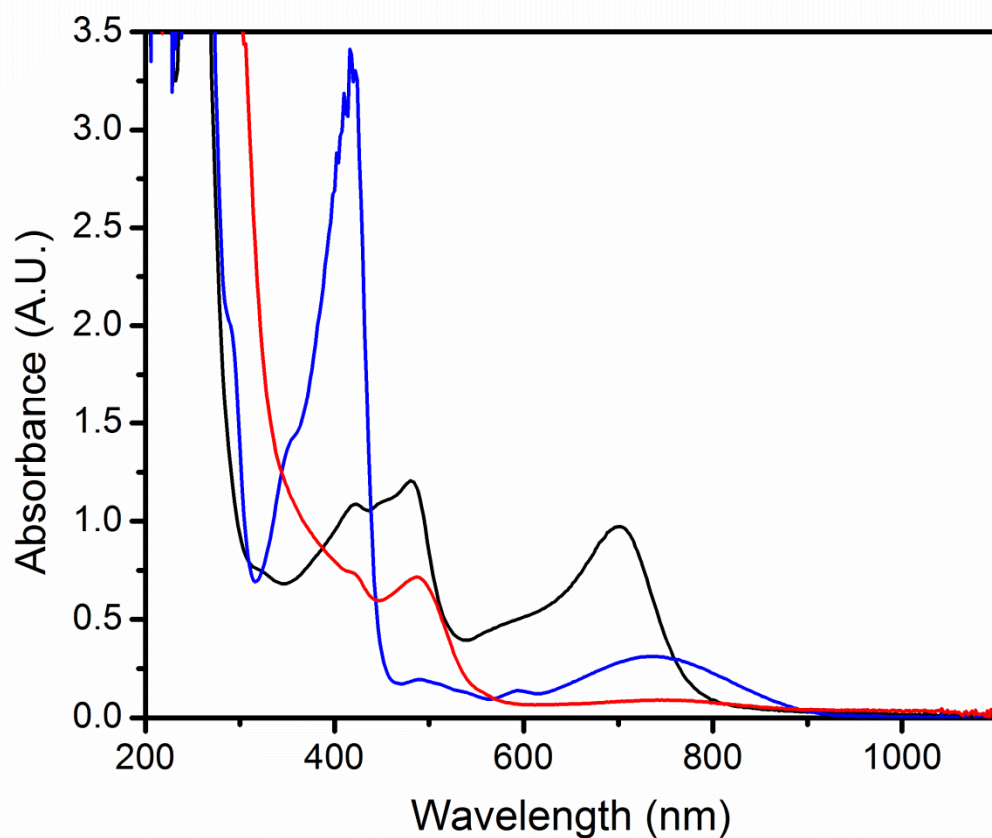


Figure A.3. UV-vis spectra of MoPY5Me₂(OTf)₂ (**1**) (black), MoO(PY5Me₂)(OTf)₂ (**3**) (blue), product from reaction of **1** with PhINNs (red). These spectra indicate that the product from reaction of **1** with PhINNs is not the same as **3**.

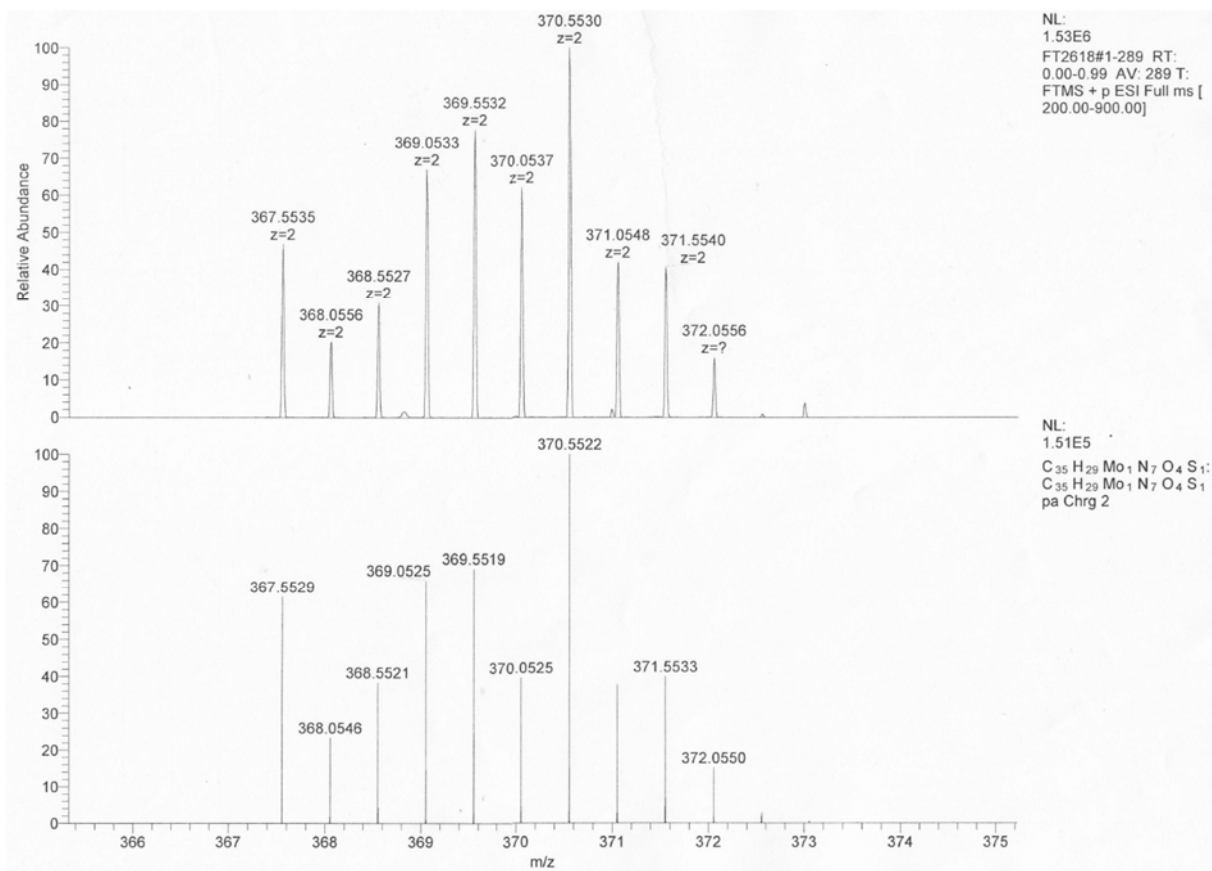


Figure A.4. Mass spectrum of MoPY5Me₂NNs²⁺ (m/z of 370.553) and the isotopic simulation of MoPY5Me₂NNs²⁺ showing (m/z of 370.552)

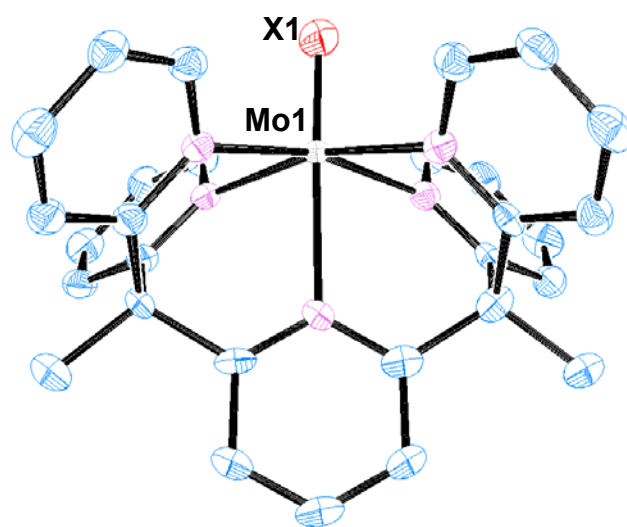


Figure A.5. Solid state structure showing atom connectivities of product from reaction of **1** with PhINNs. The ambiguous atom (X1) is shown on top. Hydrogen atoms and counter ions are omitted for clarity. Mo-X bond length is 1.689(3) Å.

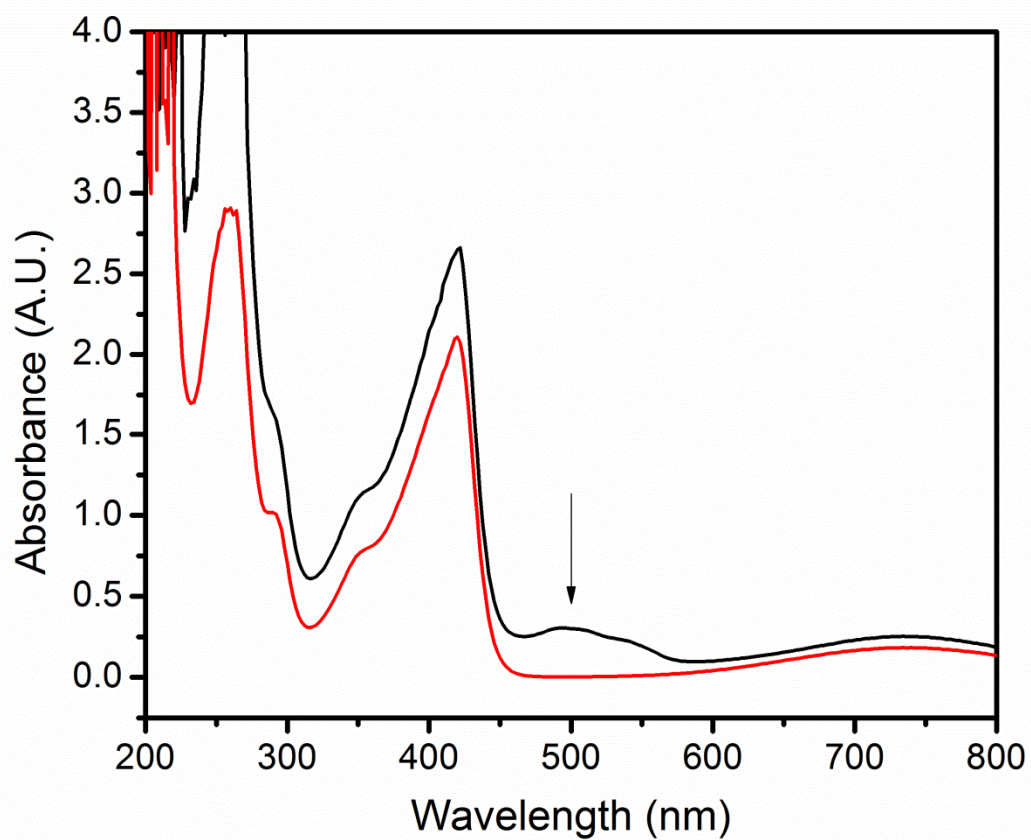


Figure A.6. UV-vis spectra of MeCN solution of dark brown crystal from reaction of **1** with PhINNs (solid line) and MoO(PY5Me₂)(OTf)₂ (**4**) (dashed line). Absorption at 492 nm (arrow) is indicative of the yellow product.

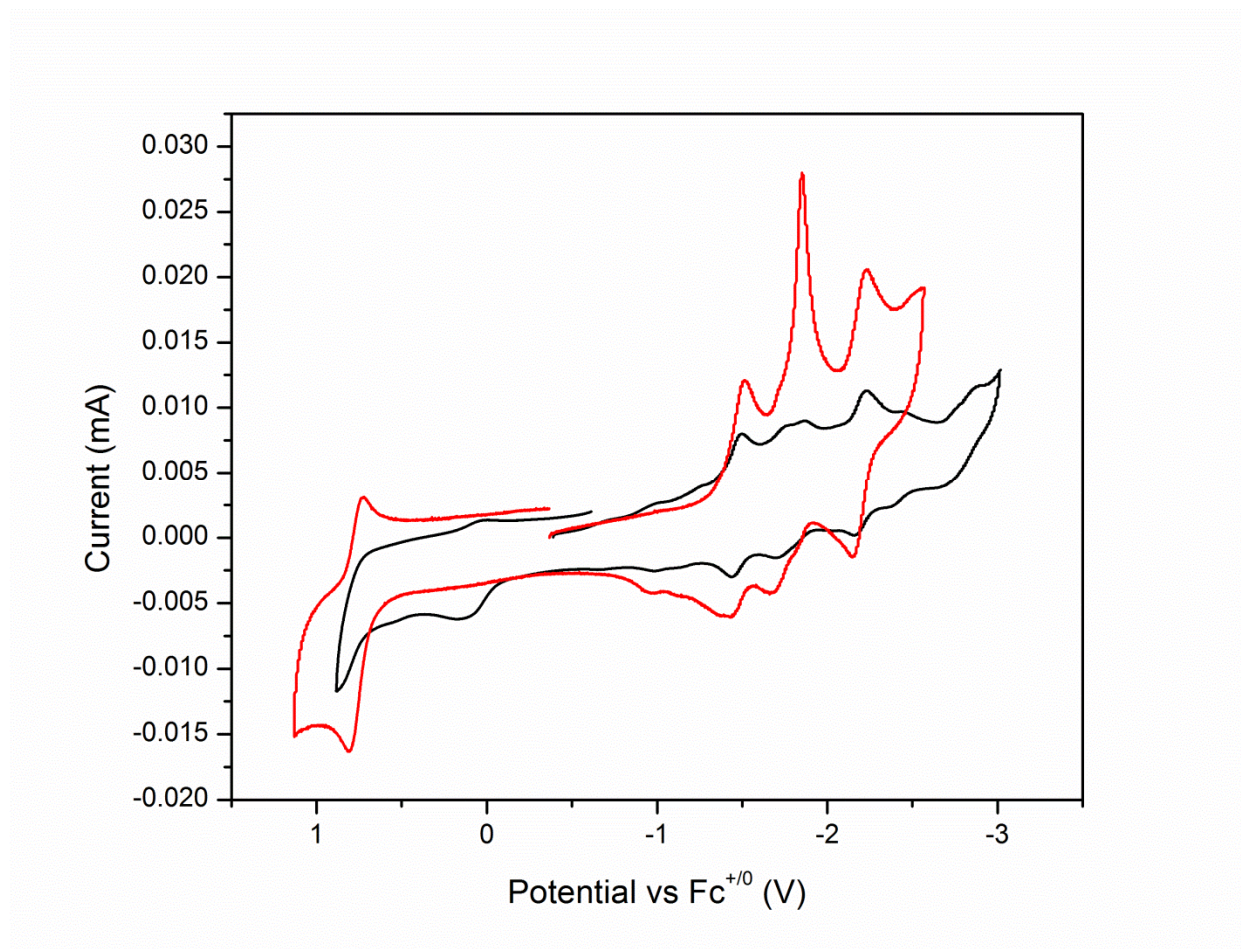


Figure A.7. CV of $[\text{MoNNs}(\text{PY5Me}_2)](\text{OTf})_2$ (**4**, black) and $[\text{MoO}(\text{PY5Me}_2)](\text{OTf})_2$ (**5**, red) in 0.1 M $(^t\text{Bu})_4\text{NPF}_6$ in MeCN on glassy carbon electrode at 100 mV/s, showing that the **5** is not a clean product and suggested that it contained **4** as impurities.

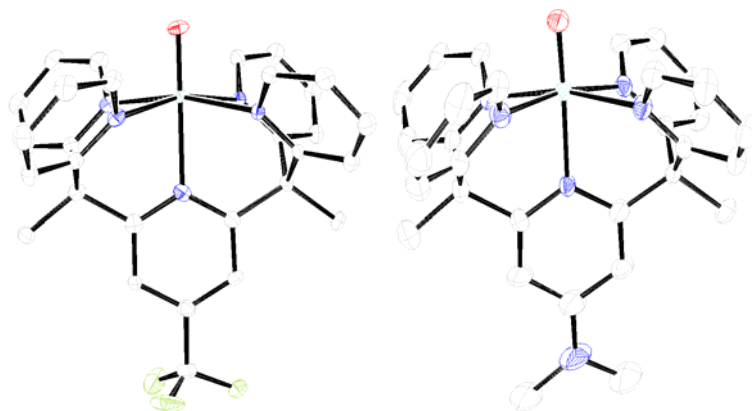


Figure A.8. Solid State structure of **7** (left) and **9** (right). Hydrogen atoms and counter ions are omitted for clarity. V-O bond length is 1.588(5) Å in **7** and 1.597(6) Å in **9**, compared to 1.595(2) Å in $[V^{IV}(O)(PY5Me_2)](OTf)_2$. Ellipsoid in **9** is 20% probability.

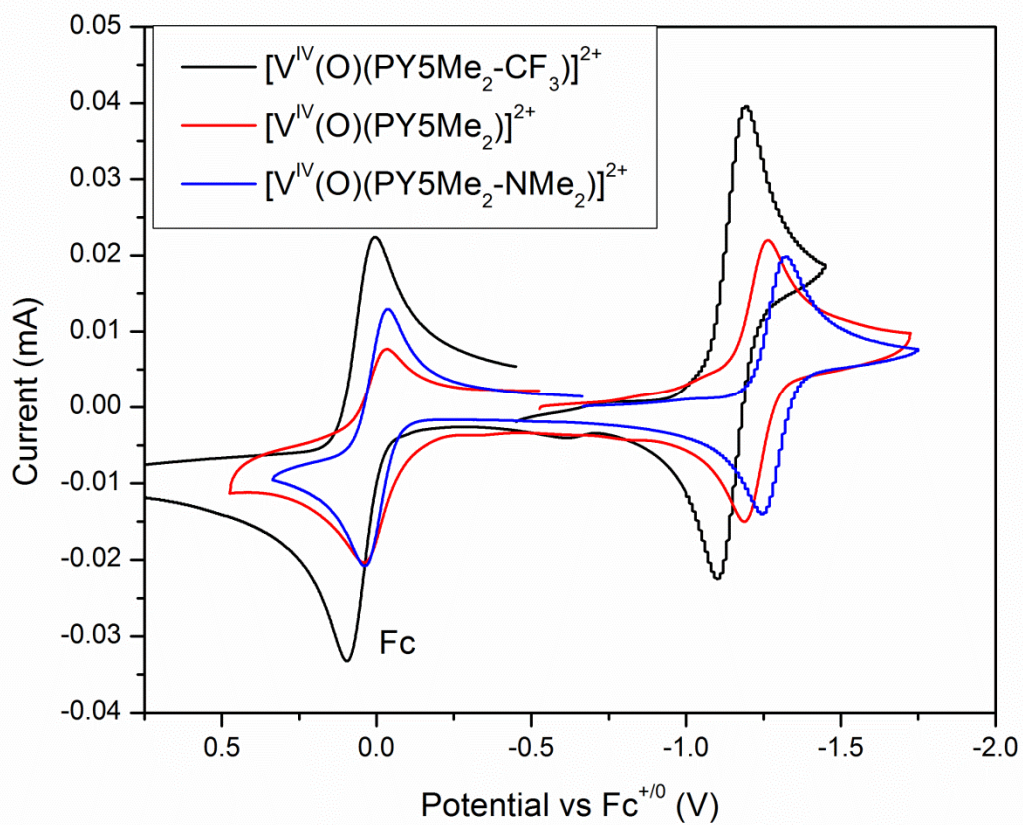


Figure A.9. Cyclic voltammogram of $[V^{IV}(O)(PY5Me_2-X)]^{2+}$ derivatives. When $X = CF_3$, $V^{IV}(O)/V^{III}(O)$ redox couple is the most positive and the most negative when $X = NMe_2$. The redox couple around 0 V is ferrocene which is an external standard.

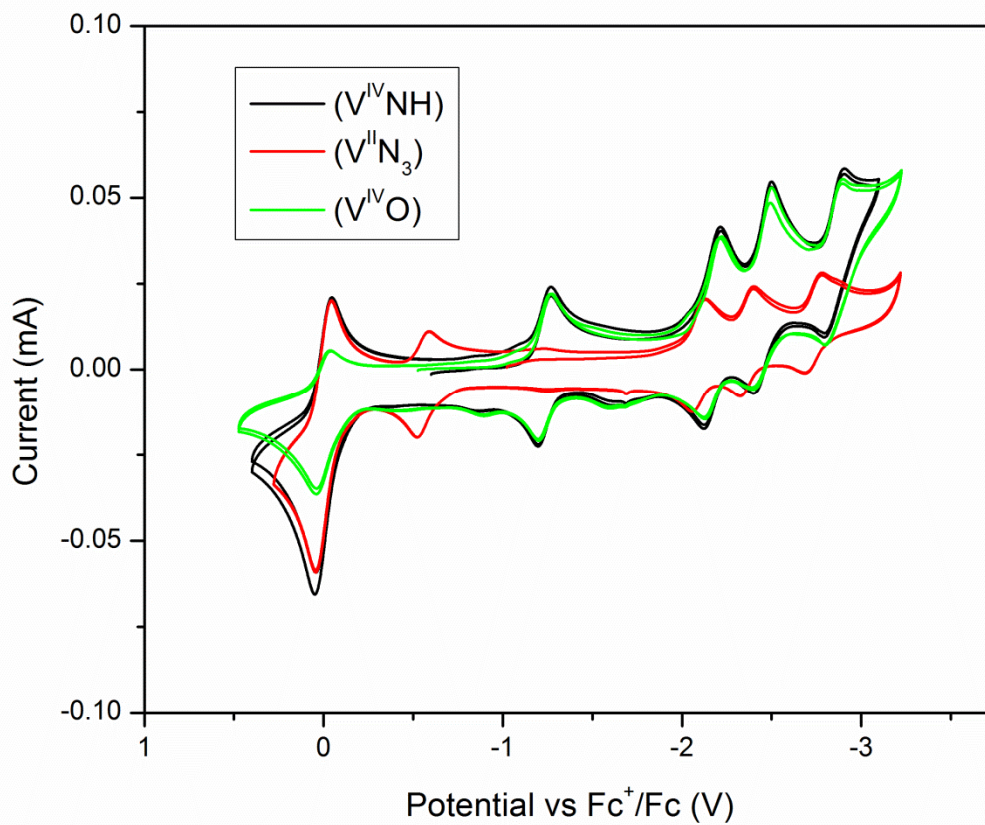


Figure A.10. Cyclic voltammograms of VII(N₃), 11 (red) and VIV(NH) 12 (black) in comparison to [VIV(O)(PY5Me₂)]²⁺ (green). The redox couple at 0 V is an external standard, ferrocene.

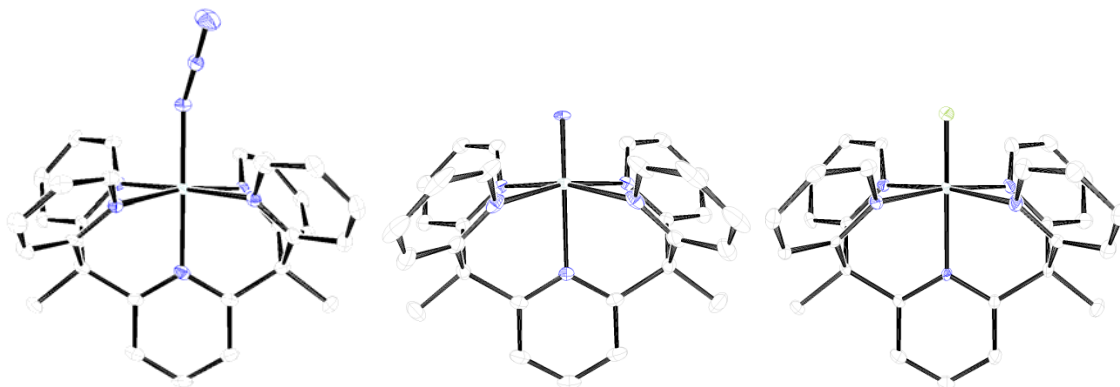


Figure A.11. Solid state structure of **11** (left), **12** (middle) and **13** (right). Hydrogen atoms and counter ions are omitted for clarity. V-N bond length is 1.618(8) Å in **12** and V-F bond length is 1.789(4) Å in **13**

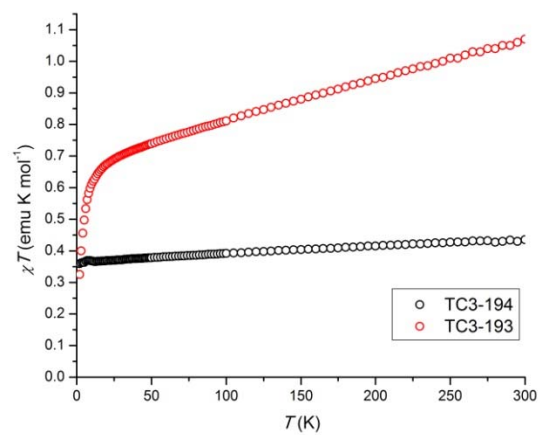
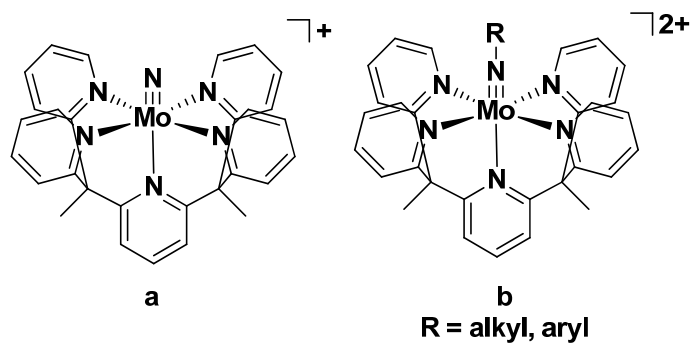
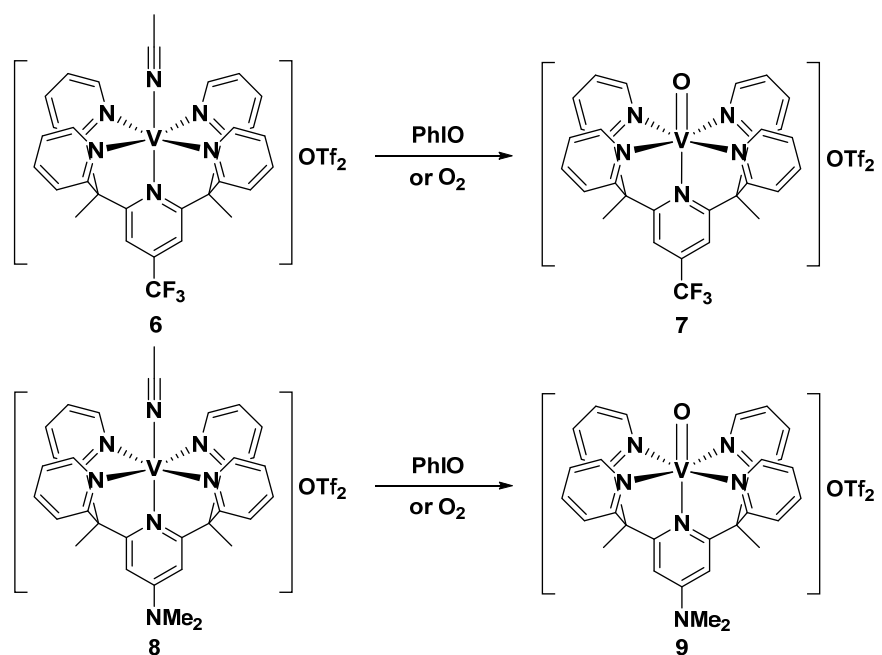


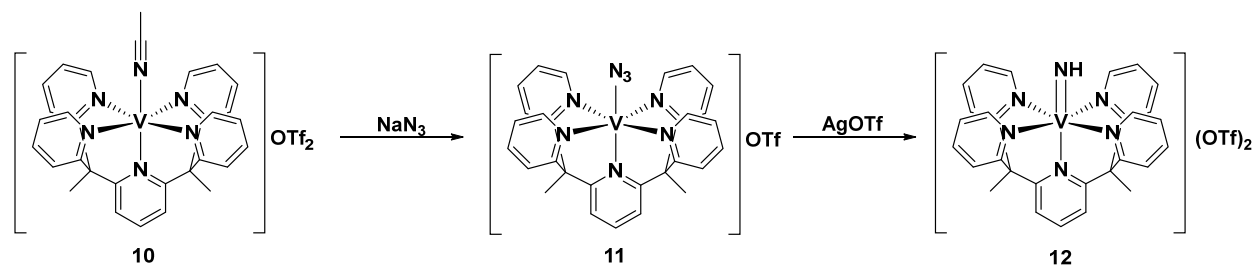
Figure A.12. Squid Magnetometry of $V^{IV}(O)$ (TC3-194, black) and $V^{III}(F)$ (TC3-193, red, **13**), showing $S = 1/2$ and $S = 1$ spin state.



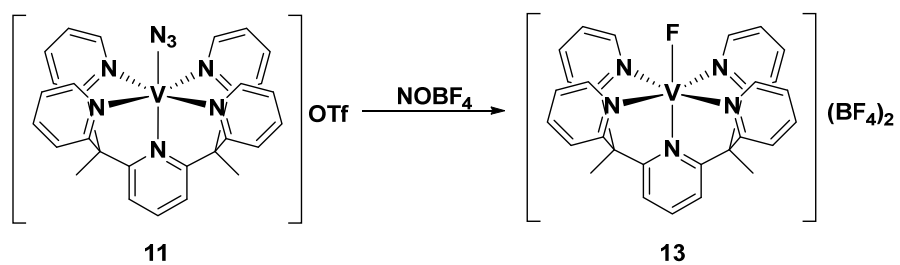
Scheme A.1. Nitrido complex (a) and imido complex (b) of Mo(PY5Me₂)



Scheme A.2. Syntheses of **7** and **9**.



Scheme A.3. Synthesis of **11** and **12**.



Scheme A.4. Synthesis of **13** by oxidation of **11** with NOBF_4 .

Table A.1. Crystallographic Data of Mo(2-methyltetrazole) (PY5Me₂)(OTf)₂ (**3**)

Empirical Formula	C ₃₃ H ₂₈ F ₆ MoN ₁₀ O ₅ S ₂
Formula Weight	890.49
Crystal System	Triclinic
Space Group	<i>P</i> -1
<i>a</i>	11.9117(18)
<i>b</i>	12.803(2)
<i>c</i>	13.154(2)
α (°)	75.905(2)
β (°)	85.418(2)
γ (°)	89.810(2)
<i>V</i> (Å ³)	1939.2(5)
<i>Z</i>	2
ρ_{calc} (g/cm ³)	1.525
μ (mm ⁻¹)	0.527
2 θ_{max} (°)	51.00
Reflections Collected	33482
Independent Reflections	7154
Refl/Param	12.25
<i>RI</i> , <i>wR2</i> (<i>I</i> > 2 σ)	0.1073, 0.3322
<i>RI</i> , <i>wR2</i> (<i>all data</i>)	0.1201, 0.3550

Table A.2. Crystallographic Data of V(O) (PY5Me₂-CF₃)(OTf)₂ (7)

Identification code	7	
Empirical formula	C ₃₂ H ₂₄ F ₉ N ₅ O ₇ S ₂ V	
Formula weight	876.62	
Temperature	100(2) K	
Wavelength	0.71073 Å	
Crystal system	Monoclinic	
Space group	P 21/c	
Unit cell dimensions	a = 9.458 Å	α = 90°.
	b = 19.522 Å	β = 100.24°.
	c = 18.843 Å	γ = 90°.
Volume	3423.7 Å ³	
Z	4	
Density (calculated)	1.701 Mg/m ³	
Absorption coefficient	0.518 mm ⁻¹	
F(000)	1772	
Crystal size	0.800 x 0.300 x 0.240 mm ³	
Theta range for data collection	1.515 to 25.335°.	
Index ranges	-11 ≤ h ≤ 11, -23 ≤ k ≤ 23, -22 ≤ l ≤ 22	
Reflections collected	52996	
Independent reflections	6239 [R(int) = 0.0323]	
Completeness to theta = 25.000°	100.0 %	
Absorption correction	Semi-empirical from equivalents	
Max. and min. transmission	0.7452 and 0.5793	
Refinement method	Full-matrix least-squares on F ²	
Data / restraints / parameters	6239 / 0 / 505	
Goodness-of-fit on F ²	1.140	
Final R indices [I > 2σ(I)]	R1 = 0.0875, wR2 = 0.2317	
R indices (all data)	R1 = 0.0906, wR2 = 0.2330	
Extinction coefficient	n/a	
Largest diff. peak and hole	1.039 and -0.727 e.Å ⁻³	

Table A.3. Crystallographic Data of V(O) (PY5Me₂-NMe₂)(OTf)₂ (**9**)

Identification code	9	
Empirical formula	C ₃₃ H ₃₀ F ₆ N ₆ O ₇ S ₂ V	
Formula weight	851.69	
Temperature	100(2) K	
Wavelength	0.71073 Å	
Crystal system	Trigonal	
Space group	R -3 :R	
Unit cell dimensions	a = 20.361 Å	α = 112.31°.
	b = 20.361 Å	β = 112.31°.
	c = 20.361 Å	γ = 112.31°.
Volume	5714.1 Å ³	
Z	6	
Density (calculated)	1.485 Mg/m ³	
Absorption coefficient	0.453 mm ⁻¹	
F(000)	2610	
Crystal size	0.250 x 0.200 x 0.100 mm ³	
Theta range for data collection	1.367 to 25.556°.	
Index ranges	-20 ≤ h ≤ 24, -24 ≤ k ≤ 21, -24 ≤ l ≤ 24	
Reflections collected	71577	
Independent reflections	7110 [R(int) = 0.0439]	
Completeness to theta = 25.000°	100.0 %	
Absorption correction	Semi-empirical from equivalents	
Max. and min. transmission	0.7452 and 0.6648	
Refinement method	Full-matrix least-squares on F ²	
Data / restraints / parameters	7110 / 0 / 496	
Goodness-of-fit on F ²	2.469	
Final R indices [I > 2σ(I)]	R1 = 0.1904, wR2 = 0.5142	
R indices (all data)	R1 = 0.2170, wR2 = 0.5452	
Extinction coefficient	n/a	
Largest diff. peak and hole	3.087 and -1.705 e.Å ⁻³	

Table A.4. Crystallographic Data of V(N₃)(PY5Me₂)(OTf)₂ (**11**)

Identification code	11	
Empirical formula	C ₆₂ H ₅₃ F ₆ N ₁₇ O ₆ S ₂ V ₂	
Formula weight	1412.21	
Temperature	100(2) K	
Wavelength	0.71069 Å	
Crystal system	Monoclinic	
Space group	C 2/c	
Unit cell dimensions	a = 23.837(5) Å	α = 90.000(5)°.
	b = 12.445(5) Å	β = 118.702(5)°.
	c = 23.271(5) Å	γ = 90.000(5)°.
Volume	6055(3) Å ³	
Z	4	
Density (calculated)	1.549 Mg/m ³	
Absorption coefficient	0.466 mm ⁻¹	
F(000)	2896	
Crystal size	0.300 x 0.080 x 0.050 mm ³	
Theta range for data collection	1.710 to 25.427°.	
Index ranges	-27<=h<=28, -15<=k<=14, -27<=l<=28	
Reflections collected	21452	
Independent reflections	5568 [R(int) = 0.0283]	
Completeness to theta = 25.000°	100.0 %	
Absorption correction	None	
Max. and min. transmission	0.8620 and 0.7965	
Refinement method	Full-matrix least-squares on F ²	
Data / restraints / parameters	5568 / 0 / 446	
Goodness-of-fit on F ²	1.337	
Final R indices [I>2sigma(I)]	R1 = 0.0754, wR2 = 0.1828	
R indices (all data)	R1 = 0.0784, wR2 = 0.1838	
Extinction coefficient	n/a	
Largest diff. peak and hole	0.546 and -0.670 e.Å ⁻³	

Table A.5. Crystallographic Data of V(NH) (PY5Me2)(OTf)2 (12)

Identification code	12
Empirical formula	C ₃₄ H _{29.50} F _{6.50} N _{7.50} O _{6.50} S ₂ V
Formula weight	885.71
Temperature	100(2) K
Wavelength	0.71073 Å
Crystal system	Orthorhombic
Space group	C m c 21
Unit cell dimensions	a = 14.8896(11) Å α = 90°. b = 22.0140(16) Å β = 90°. c = 21.9823(16) Å γ = 90°.
Volume	7205.4(9) Å ³
Z	8
Density (calculated)	1.633 Mg/m ³
Absorption coefficient	0.485 mm ⁻¹
F(000)	3612
Crystal size	0.400 x 0.280 x 0.160 mm ³
Theta range for data collection	1.651 to 25.721°.
Index ranges	-18 ≤ h ≤ 18, -26 ≤ k ≤ 26, -26 ≤ l ≤ 26
Reflections collected	100778
Independent reflections	7165 [R(int) = 0.0248]
Completeness to theta = 25.000°	100.0 %
Absorption correction	Semi-empirical from equivalents
Max. and min. transmission	0.7453 and 0.6755
Refinement method	Full-matrix least-squares on F ²
Data / restraints / parameters	7165 / 1 / 606
Goodness-of-fit on F ²	1.068
Final R indices [I > 2σ(I)]	R1 = 0.0316, wR2 = 0.0919
R indices (all data)	R1 = 0.0318, wR2 = 0.0926
Absolute structure parameter	0.001(3)
Extinction coefficient	n/a
Largest diff. peak and hole	0.576 and -0.678 e.Å ⁻³

Table A.6. Crystallographic Data of V(F) (PY5Me₂)(OTf)₂ (**13**)

Identification code	13	
Empirical formula	C ₃₁ H ₂₈ B ₂ F ₉ N ₆ V	
Formula weight	728.15	
Temperature	100(2) K	
Wavelength	0.71073 Å	
Crystal system	Triclinic	
Space group	P -1	
Unit cell dimensions	a = 8.841 Å	α = 67.92°.
	b = 12.189 Å	β = 89.70°.
	c = 15.240 Å	γ = 88.96°.
Volume	1521.6 Å ³	
Z	2	
Density (calculated)	1.589 Mg/m ³	
Absorption coefficient	0.416 mm ⁻¹	
F(000)	740	
Crystal size	0.200 x 0.170 x 0.120 mm ³	
Theta range for data collection	1.442 to 25.420°.	
Index ranges	?<=h<=?, ?<=k<=?, ?<=l<=?	
Reflections collected	5564	
Independent reflections	5564 [R(int) = ?]	
Completeness to theta = 25.000°	99.3 %	
Absorption correction	Semi-empirical from equivalents	
Max. and min. transmission	0.745211 and 0.558912	
Refinement method	Full-matrix least-squares on F ²	
Data / restraints / parameters	5564 / 0 / 443	
Goodness-of-fit on F ²	1.013	
Final R indices [I>2sigma(I)]	R1 = 0.0577, wR2 = 0.1657	
R indices (all data)	R1 = 0.0618, wR2 = 0.1681	
Extinction coefficient	n/a	
Largest diff. peak and hole	1.842 and -0.389 e.Å ⁻³	

Appendix B Assorted Synthesis of Ligand for Fe Complexes

B.1. Synopsis

This appendix describes syntheses of ligand based on PY5Me₂, bis-sulfonamide and dipyrin platforms

B.2. Motivation and design

Ligand based on PY5Me₂ platform has been studied extensively for both reductive and oxidative transformations. The pre-organized octahedral geometry and pyridine donor provides a strong field ligand which can also be tuned by varying substituents at the ligands. Previously examples includes the use of [Mo(O)PY5Me₂](OTf)₂¹, [Mo(S₂)PY5Me₂](OTf)₂² and [Co(OH₂)PY5Me₂](OTf)₃³ for proton reduction from water. Fe complexes of PY5Me₂ ligand system can also be oxidized to Fe(IV)-Oxo which is also stable in water.⁴ Electronic tuning of ligand includes substitution at 4-position of axial pyridine by electron withdrawing group, trifluoromethyl (-CF₃), and electron donating group, dimethylamino (-NMe₂), resulted in more positive and more negative reduction potential respectively.^{3,4} Herein, we reported the syntheses of PY5Me₂-BF₃⁻ (**3**), an anionic ligand which could potentially stabilized high-valent metal center, DMAP5 (**7**), a derivative of PY5Me₂ with NMe₂ moiety at 4-position of every pyridines, and NMe₂-PY5Me₂ (**9**), a substitution of NMe₂ at 6-position of one equatorial pyridine to provide potential proton relay group.

Unlike PY5Me₂ ligand, phenylenebissulfonamide (**11** and **12**) are dianionic ligands, which can support a Fe center with 2 open *cis*- sites, rendering the ability to various small-molecule activation.^{5,6} The charged -ligand should also provide electron density which can stabilize high-valent species. There are some reports on Cu complexes supported by similar ligands⁷ and their influence on diastereomic interactions.

On the other hand, Dipyrinphenolate ligands, **23**, can provide 2 open *trans*- sites as it coordinates Fe in a square planar geometry. The dipyrin moiety provides strong ligand field and mimic a part of the porphyrin ring, while the phenolate functional group, an X-type donor, provides aromaticity to the ligand, enabling the delocalization similar to the porphyrin systems.⁸ Multiple complexes of this ligand family have been synthesized. Their Mn complexes have been reported as a oxidation catalysts.⁹ While early metal such as Ge and Ti complexes have been reported to catalyze polycarbonate polymerization with CO₂ and epoxides.^{10,11} Given their similarity to porphyrins and reactivity with CO₂ in polymerization reaction, dipyrinphenolate ligands can potentially be used to support Fe center as an electrocatalyst for CO₂ reduction.

B.3. Results and Discussions

B.3.1. PY5Me₂-BF₃⁻ (**3**)

Synthesis of **3** involves installing borate functional group on PY5Me₂ ligand. Sandmeyer reaction of PY5Me₂-NH₂ generates PY5Me₂-Cl, PY5Me₂-Br, and PY5Me₂-I. All 3 derivatives were tested their reactivity with Turbo Grignard reaction, iPrMgCl-LiCl and trimethylborate; PY5Me₂-Br yielded the desired product while the other 2 derivatives yielded protonated product, PY5Me₂, or did not proceed at a desirable rate. The resulting methyl borate ligand was hydrolyzed to **2**, which is less soluble and can be precipitated out from the reaction mixture. The borate ligand **2** was then fluorinated with KHF₂ which also enables the product to precipitate out of the reaction. Metallation of **3** by Fe(OTf)₂ gave an orange crystal suitable for x-ray crystallography. The crystal structure is shown in Figure 1. Cyclic voltammogram of Fe complex

showed a Fe^{III/II} redox couple at 0.659 V vs Fc⁺⁰. The redox potential is less negative than the Fe complexes supports by PY5Me₂-NH₂ and PY5Me₂-NH₂⁴ but more positive than complex with PY5Me₂ ligand.

B.3.2. DMAP5 (7)

Synthesis of DMAP5 proceeds similarly to PY5Me₂ synthesis but all pyridine starting materials possess –NMe₂ moiety at the 4-position. Substitution of Cl group by NMe₂ group in 2,4-dichloropyridine yielded **4** which can undergo cross coupling with EtMgBr and Ni(dppp)Cl₂ as a catalyst to form 2-ethyl-4-dimethylaminopyridine **5**. Deprotonation of **5** followed by S_N^{Ar} reaction with **4** yielded **6** which can undergo another deprotonation and S_N^{Ar} with 2,6-difluoro-4-dimethylaminopyridine to yield the ligand. Metallation with Fe^{II} starting material yielded Fe(II) complex with a redox potential around 0 V vs Fc⁺⁰.¹² Oxidation by ferrocenium triflate gave Fe(III) complex supported by **7**.¹²

B.3.3. NMe₂-PY5Me₂ (9)

Similar synthesis procedures to other PY5Me₂ derivatives are employed. PY3-F, **8**, was synthesized through a one-pot synthesis with good yields of 80%. The reaction can also be easily scaled up. Dipyrindylethane with –NMe₂ was obtained from Yujie Sun (YS2-49) as a yellow oil. Deprotonation by nBuLi followed by S_N^{Ar} reaction with PY3-F yielded the desired product. The ligand can be metallated by divalent metal, Fe^{II}, Mn^{II}, and Co^{II}. Fe complex of **9** is high-spin and crystal structure showed that only 4 pyridines are coordinated to the Fe center while the steric bulk of the pyridine with NMe₂ prevented the **9** to be pentadentate ligand. The Fe complex has one vacant site as shown in crystal structure, Figure 2. (Eva Nichols)

B.3.4. Bis-sulfonamide (11 and 12)

Phenylenebissulfonamide ligands can be synthesized by microwave reaction of 2-pyridine sulfonyl chloride and phenylenediamine. 2-pyridine sulfonyl chloride can be synthesized from a reaction with 2-pyridine sulfonic acid and SOCl₂ or purchased as a HCl salt. The ligand can be deprotonated easily with a variety of base, NaOMe, NaH and NaHMDS. While sodium salt of the ligand can be isolated, the deprotonated ligand can be used without further purification. Different Fe^{II} sources had been used for metallation, however, the reaction usually produced insoluble yellow precipitates. When FeCl₂ was used as a Fe source, the yellow precipitates show Mössbauer parameters of δ=1.010, ΔE_q= 3.870, indicating a high spin Fe(II) species. Reaction in pyridine with FeOTf₂ yielded dinuclear product that can be crystallized out from Et₂O diffusion, Figure 3. When the ligand is deprotonated by excess NaOMe, a dinuclear bis-μ-methoxo compounds can be obtained.

B.3.5. Dipyrin-phenoxide

Dipyrin ligand can be synthesized by condensation of functionalized pyrroles with an aldehyde. Cross coupling of N-pyrrole and bromoanisole derivatives yielded a building block for condensation (**17**, **18**, and **19**). Bromoanisole with CF₃ and tBu groups are utilized to tune the electronics of the ligand. Condensation reactions proceeds slowly in DCM, therefore, DCE should be used while the reaction should be heated slightly. All the reactions should be performed in the dark. Deprotection of phenol from an anisole can be tricky as CF₃ derivative is quite electron-poor and did not proceed well with BBr₃ standard deprotection procedure. Therefore, sodium salt of long chain thiol was used instead.¹⁰

B.4. Experimental

General information: All manipulations were performed under air- and water- free conditions using standard glovebox and Schlenk-line techniques, unless otherwise noted. All commercially available reagents were used without further purification, unless otherwise noted. Toluene, acetonitrile (MeCN), tetrahydrofuran (THF) and diethylether (Et₂O) were dried and degassed using the VAC 103991 solvent system and stored over 3-Å molecular sieves under a nitrogen atmosphere, and 1,4-dioxane was distilled over sodium ketyl and stored over 3-Å molecular sieves prior to use. PY5Me₂-NH₂ and dipyriddyethane were synthesized according to literature procedures.⁴ N,N-dimethyl-6-(1-(pyridin-2-yl)ethyl)pyridin-2-amine¹² and sodium pyrrole were synthesized according to the literature procedure. Pyridine sulfonylchloride HCl was purchased from combi-blocks. NMR experiments were conducted on a Bruker AVB-400, AVQ-400 and AV-600 spectrometer. ESI-MS experiments were performed by the Proteomics/Mass Spectrometry facility at University of California-Berkeley. X-ray crystallography was performed in the Chexray facility.

Synthesis of PY5Me₂-Br (1): An ice-cold saturated solution of NaNO₂ (0.276 g, 4 mmol, 4 eq) was added very slowly to an ice-cold solution of PY5Me₂-NH₂ (0.4586 g, 1 mmol, 1 eq) in 4 mL of HBr. The solution was stirred for one minute before CuBr (2 eq, excess) was added slowly. Some bromine will form. Upon completion of the addition, the mixture was removed from ice and allowed to warm to room temperature. The pH of the solution was adjusted to 9-10 using saturated solutions of NaOH and NaHCO₃. Saturated aqueous solution of Na₂EDTA was added. The product was extracted using DCM. The pink DCM solution was dried with Na₂SO₄ and evaporated to dryness. The solid was then recrystallized in acetone/Et₂O yielding light pink solid. ¹H NMR (400 MHz, CDCl₃) δ 8.52 (ddd, *J* = 4.9, 1.9, 0.9 Hz, 4H), 7.42 (td, *J* = 7.8, 1.9 Hz, 4H), 7.24 (s, 2H), 7.07 (ddd, *J* = 7.5, 4.8, 1.1 Hz, 4H), 6.84 (dt, *J* = 8.0, 1.1 Hz, 4H), 2.17 (s, 6H).

Synthesis of PY5Me₂-B(OH)₂ (2): In 50 ml dry THF, a slurry of 0.522 g, (1 mmol, 1 eq), PY5Me₂-Br (1) was stirred under N₂ atmosphere. the solution was cooled down to -78°C and 1.3 ml (1.3 M, 1.69 mmol) of iPrMgCl-LiCl was slowly added. The light pink slurry will change color to light orange. Stir at -78°C for 45 minutes. Warm it up slightly for 15 minutes and put it back in the cold bath before adding 0.23 ml of B(OMe)₃. Stir at -78°C for another 15 minutes before slowly warm it up to room temperature. Reflux the reaction overnight. Quench the reaction by adding 5 ml of water. The light yellow slurry will become more soluble. Remove the solvent until yellow solid crashed out. Filter the solid out and keep the filtrate. Remove the solvent from the filtrate to yield white solid.

Synthesis of PY5Me₂-BF₃K (3): PY5Me₂-B(OH)₂ (2) is used without further purification. Dissolve all 129.5 mg in 2 ml water and 2.5 ml EtOH. (Or start with 1:1 mixture and slowly add EtOH until all dissolve). Saturated aqueous solution of 3 eq KHF₂ was added into the mixture. Precipitated will slowly form after 1 hour but the mixture was stirred overnight. The white precipitate was filtered and characterize by ESI-MS (ESI-pos 492.2, ESI-neg 510.2). ¹H NMR (400 MHz, DMSO-*d*₆) δ 8.25 – 8.19 (m, 4H), 7.82 (t, *J* = 7.9 Hz, 4H), 7.49 (d, *J* = 7.9 Hz, 2H), 7.31 (dd, *J* = 7.5, 4.8 Hz, 4H), 7.19 (d, *J* = 8.0 Hz, 4H), 2.19 (s, 6H).

Synthesis of 2-chloro-4-dimethylaminopyridine (4): To a 250 ml round bottom flask charged with 2,4-dichloropyridine (14.8 g, 0.1 mol, 1 eq) and a stir bar, added 100 ml of 40% dimethylamine solution in water. Heat the solution at 50°C under N₂ for 20 h. After cooling down to room temperature, the solution was extracted with Et₂O (3x100 ml). The organic layer was combined and dried with Na₂SO₄. The solvent was removed *in vacuo* to yield light yellow oil. Addition of Et₂O yields white solid. (10.73 g, 68.5%) ¹H NMR (400 MHz, CDCl₃) δ 7.97 (d, *J* = 6.1 Hz, 1H), 6.51 – 6.37 (m, 2H), 3.00 (s, 6H).

Synthesis of 2-ethyl-4-dimethylaminopyridine (5): To a 500 ml schlenk flask charged with 200 ml dry THF, add 2-chloro-4-dimethylaminopyridine (4) (7 g, 44.7 mmol, 1 eq) and Ni(dppp)Cl₂ (4 mol%). Cool down the mixture to -78°C and slowly add 3.0 M EtMgBr solution (22.3 ml, 67 mmol, 1.5 eq) in Et₂O over the course of 10 minutes. Color of the reaction slowly changed from red to orange. Stir for 30 minutes at -78°C and warm up the slurry to room temperature, at which point the slurry disappear. The color of the reaction became darker, from brown to black. Heat the reaction at reflux for 20 h. Cool down the reaction to room temperature and quench the reaction with H₂O, yielding yellow solution with green solid which was filtered out. The reaction was extracted with H₂O and EtOAc. The organic layer was combined and dried with Na₂SO₄. Solvents were removed *in vacuo*, yielding light yellow oil, which underwent vacuum distillation to yield clear oil at 60°C under vacuum. ¹H NMR (400 MHz, CDCl₃) δ 8.15 (dd, *J* = 5.8, 0.7 Hz, 1H), 6.35 (dt, *J* = 8.4, 2.5 Hz, 2H), 2.98 (s, 6H), 2.70 (q, *J* = 7.6 Hz, 2H), 1.28 (t, *J* = 7.6 Hz, 3H).

Synthesis of di(6-dimethylamino)pyridyl)ethane (6): 2-ethyl-4-dimethylaminopyridine (4 g, 26.6 mmol, 2eq) in 100 ml of dry THF is degassed under N₂ for 10 minutes. The solution was cooled down to -78°C before 2.5 M nBuLi in hexane (10.6 ml, 26.6 mmol, 2eq) was slowly added. The reaction was stirred for 30 minutes before 2-chloro-4-dimethylaminopyridine was added as a solid. The reaction was stirred for another 30 minutes before warming up to room temperature and being heated to reflux overnight. The reaction was quenched with H₂O and extract with EtOAc. The organic layer was combined and dried with Na₂SO₄ before the solvent was removed *in vacuo*. The resulting oil was then recrystallized from DCM/Et₂O to yield yellow solid. ¹H NMR (400 MHz, CDCl₃) δ 8.17 (d, *J* = 6.0 Hz, 2H), 6.57 (d, *J* = 2.6 Hz, 2H), 6.33 (dd, *J* = 6.0, 2.6 Hz, 2H), 4.20 (q, *J* = 7.2 Hz, 1H), 2.95 (s, 12H), 1.70 (d, *J* = 7.2 Hz, 3H).

Synthesis of DMAP5 (7):

In 20 ml of dry Dioxane, di(6-dimethylamino)pyridyl)ethane (1.216 g, 4.5 mmol, 3 eq) was added and degassed. The flask was cooled down to 0°C by an ice-bath before 2.5 M of nBuLi (1.8 ml, 4.5 mmol, 3 eq) was added slowly. The reaction turned orange and then became darker red while it was stirred at 0°C for 45 minutes. In one portion, 2,6-difluoro-4-dimethylaminopyridine (0.2372 g, 1.5 mmol, 1eq) was added as a solid. The reaction was warmed up to room temperature and then heated to reflux for 3 days. The reaction was cooled down to room temperature and quenched with water. The reaction mixture was extracted with EtOAc (3x50 ml). The organic layers were combined and dried with Na₂SO₄ before the solvent was removed under reduced pressure, yielding foamy yellow solid. The solid was recrystallized

from EtOAc by sonication. Yield 0.901 g, 91.2% ¹H NMR (400 MHz, CDCl₃) δ 8.15 (d, *J* = 5.6 Hz, 4H), 6.38 (s, 2H), 6.25 (d, *J* = 5.8 Hz, 8H), 2.83 (s, 6H), 2.70 (s, 24H), 2.17 (s, 6H).

Synthesis of PY3-F (8): In 500 ml schlenk flask, 2-ethylpyridine (6 g, 6.4 ml, 56 mmol, 2.125 eq) was degassed in 200 ml dry THF. The solution was cooled down to -78°C before 2.5 M nBuLi (19.2 ml, 48 mmol, 2 eq) was added slowly through addition funnel. The reaction was stirred at this temperature for 30 minutes, before 2-fluoropyridine (2.33 g, 2 ml, 24 mmol, 1 eq) was added. The reaction was warmed up to -20°C for 30 minutes and heated to reflux for 1 h. The reaction was cooled down to room temperature for 30 minutes and 2,6-difluoropyridine (2.76 g, 2.2 ml, 24 mmol, 1 eq) was added. The solution was heated to reflux for another hour before cooling down to room temperature and quenched with 20 ml of H₂O. The organic layer was separated out and the aqueous layer was extracted with DCM (3x50 ml). The organic layer was combined and dried with Na₂SO₄. The solvent was removed *in vacuo* before hexanes and Et₂O was added to the oil until white precipitate appeared. Yield (5.10 g, 76.2 %) ¹H NMR (400 MHz, CDCl₃) δ 8.58 (dd, *J* = 4.9, 2.1 Hz, 2H), 7.73 – 7.55 (m, 3H), 7.18 – 7.05 (m, 4H), 6.96 (dd, *J* = 7.6, 2.5 Hz, 1H), 6.77 (dd, *J* = 8.1, 3.1 Hz, 1H), 2.30 (s, 3H).

Synthesis of NMe₂-PY5Me₂ (9): In 30 ml dry THF, N,N-dimethyl-6-(1-(pyridin-2-yl)ethyl)pyridin-2-amine (0.568 g, 2.5 mmol, 1.25 eq) was stirred and degassed. The solution was cooled down to -78°C before 2.5 M nBuLi (1 ml, 2.5 mmol, 1.25 eq) was added slowly. The reaction mixture was stirred at low temperature for 30 minutes before PY3-F (0.704 g, 2 mmol, 1 eq) was added as a solid in one portion. The reaction mixture was then warmed up to room temperature and heated to reflux overnight. Color of the reaction changed from red to yellow. The reaction was cooled down to room temperature before 5 ml of water was added to quench the reaction. The reaction was extracted with Et₂O (2x30 ml) and DCM (2x30 ml). The organic layers were combined and dried with Na₂SO₄. The solvent of the reaction was removed under reduced pressure, yielded light yellow oil which was subjected to alumina column chromatography (30% EtOAc in hexanes, R_f = 0.2 for NMe₂-PY5Me₂, 0.4 for PY3-F and 0.8 for PY2NMe₂). Combined yield 0.96 g, 98% ¹H NMR (400 MHz, CDCl₃) δ 8.50 (td, *J* = 4.9, 2.1 Hz, 3H), 7.50 (t, *J* = 7.9 Hz, 1H), 7.45 – 7.31 (m, 3H), 7.26 (d, *J* = 15.9 Hz, 1H), 7.08 – 6.95 (m, 5H), 6.88 (dd, *J* = 8.2, 4.6 Hz, 3H), 6.29 (d, *J* = 8.4 Hz, 1H), 6.17 (d, *J* = 7.5 Hz, 1H), 2.91 (s, 6H), 2.22 (s, 3H), 2.15 (s, 3H).

Synthesis of pyridine sulfonylchloride (10): Pyridine sulfonic acid (1.399 g, 4.4 mmol, 1 eq) was dissolved in SOCl₂ (3.07 ml, 42.24 mmol, 4.8 eq). A drop of dry DMF (34 μl, 0.22 mmol, 0.05 eq) was added to the solution before it was heated to 80°C for 4 hours. SOCl₂ was removed by distillation. The light yellow oil was used without further purification.

Synthesis of PhenylenebisSulfonamide ligand (11): Pyridine sulfonylchloride HCl, synthesized or commercially available, (428 g, 2 mmol, 4 eq) were added to a microwave tube containing 3 ml of dry pyridine and o-phenylenediamine (54 mg, 0.5 mmol, 1 eq). Repeat the same process for 3 other tubes. The tubes were subjected to a microwave reactor at 300 W, 130°C and 300 psi for 25 minutes. The mixtures from 4 tubes were combined and water was added to the solution until precipitated appeared. The tubes were placed in an ice bath for 10 minutes. The precipitate was filtered, washed with water and dried in air. White solid (0.48 g,

41.2 %) ^1H NMR (400 MHz, CDCl_3) δ 10.37 (s, 2H), 8.74 (dt, $J = 4.8, 1.3$ Hz, 2H), 8.08 – 7.93 (m, 4H), 7.61 – 7.49 (m, 4H), 7.18 (dd, $J = 6.1, 3.5$ Hz, 2H).

Synthesis of dimethylphenylenebissulfonamide (12): Pyridine sulfonylchloride HCl, synthesized or commercially available through Combi-Blocks, (428 g, 2 mmol, 4 eq) were added to a microwave tube containing 3 ml of dry pyridine and 4,5 -dimethylphenylenediamine (68 mg, 0.5 mmol, 1 eq). Repeat the same process for 3 other tubes. The tubes were subjected to a microwave reactor at 300 W, 130°C and 300 psi for 25 minutes. The mixtures from 4 tubes were combined and water was added to the solution until precipitated appeared. The tubes were placed in an ice bath for 10 minutes. The precipitate was filtered, washed with water and dried in air. White solid (0.317 g, 37.9 %) ^1H NMR (400 MHz, CDCl_3) δ 10.22 (s, 2H), 8.73 (ddd, $J = 4.9, 1.7, 0.9$ Hz, 2H), 8.07 – 7.92 (m, 4H), 7.55 (ddd, $J = 7.6, 4.8, 1.3$ Hz, 2H), 7.29 (s, 2H), 2.15 (s, 6H).

Synthesis of 15: In 50 ml Acetone, 2-bromo-4-tert-butylphenol (4.58 g, 20 mmol, 1 eq) was stirred with K_2CO_3 (5.52 g, 40 mmol, 2 eq) while iodomethane (22.7 g, 160 mmol, 8 eq) was added to the solution. The reaction was heated to reflux for 18 h. After the reaction was cooled down, the suspension was filtered and the solvent was removed. 40 ml of H_2O and 40 ml of DCM were added to the concentrated filtrate which was extracted with more DCM. The organic layers were combined and dried with Na_2SO_4 . Organic solvent was removed under reduced pressure. The resulting oil was purified with silica column chromatography (hexanes, R_f 0.27). The yellow oil was purged with N_2 and it solidified into yellow solid. Yield 4.00 g, 82.3%. ^1H NMR (600 MHz, CDCl_3) δ 7.55 (d, $J = 2.3$ Hz, 1H), 7.28 (dd, $J = 8.6, 2.4$ Hz, 1H), 6.84 (d, $J = 8.6$ Hz, 1H), 3.88 (s, 3H), 1.29 (s, 9H).

Synthesis of 16: In 50 ml Acetone, 2-bromo-4,6-di-tert-butylphenol (2.86 g, 10 mmol, 1 eq) was stirred with K_2CO_3 (2.76 g, 20 mmol, 2 eq) while iodomethane (5.68 g, 80 mmol, 8 eq) was added to the solution. The reaction was heated to reflux for 18 h. After the reaction was cooled down, the suspension was filtered and the solvent was removed. 40 ml of H_2O and 40 ml of DCM were added to the concentrated filtrate which was extracted with more DCM. The organic layers were combined and dried with Na_2SO_4 . Organic solvent was removed under reduced pressure. The resulting oil was purified with silica column chromatography (hexanes, R_f 0.27). The yellow oil was purged with N_2 and it solidified into yellow solid. Yield 2.82 g, 94%. ^1H NMR (600 MHz, CDCl_3) δ 7.40 (d, $J = 2.3$ Hz, 1H), 7.27 (d, $J = 2.4$ Hz, 1H), 3.91 (s, 3H), 1.39 (s, 9H), 1.29 (s, 9H).

Synthesis of 17: In 30 ml dry dioxane under inert atmosphere, Napyrrole (**13**, 4.4 g, 50 mmol, 4 eq) was mixed with ZnCl_2 (6.8 g, 50 mmol, 4 eq). The slurry was stirred for 30 minutes. $\text{Pd}(\text{OAc})_2$ (45 mg, 0.2 mmol, 0.4 mol%) and Johnphos (60 mg, 0.2 mmol, 0.4 mol%) was added to the slurry. The flask was brought out of the glovebox. **14** (3.19 g, 12.5 mmol, 1 eq) was added to the slurry under the back flow of N_2 . The mixture was heated to 100°C for 48 h. The reaction was cooled down and 15 ml of Et_2O and 15 ml of H_2O were added to the reaction mixture. The slurry was filtered by Celite®. Organic layer of the filtrate was separated out. The aqueous layer was extracted with Et_2O (3x50 ml). The organic layers were combined and dried with Na_2SO_4 . Organic solvent was removed under reduced pressure, yielding oil which was subjected to a

silica plug (DCM). The product was purified again using silica column chromatography (15% EtOAc in Hexanes) to yield clear oil. Yield (1.36 g, 64.7%) ¹H NMR (400 MHz, CDCl₃) δ 9.76 (s, 1H), 7.88 (d, *J* = 2.3 Hz, 1H), 7.44 – 7.36 (m, 1H), 7.02 (d, *J* = 8.7 Hz, 1H), 6.90 (q, *J* = 2.3 Hz, 1H), 6.69 (dt, *J* = 3.9, 1.9 Hz, 1H), 6.31 (q, *J* = 3.0 Hz, 1H), 4.02 (s, 3H), 2.05 (s, 0H).

Synthesis of 19: The same procedure as **17** was employed with 6.06 g, 25 mmol of **16**. The product was purified with silica gel column chromatography (20% toluene in hexanes, *R_f* 0.27) to give color less solid, yield 2.877 g, 40.0%. ¹H NMR (600 MHz, CDCl₃) δ 9.18 (s, 1H), 7.36 (d, *J* = 2.5 Hz, 1H), 7.23 (d, *J* = 2.5 Hz, 1H), 6.89 (td, *J* = 2.7, 1.5 Hz, 1H), 6.45 (ddd, *J* = 3.8, 2.6, 1.5 Hz, 1H), 6.29 (dt, *J* = 3.5, 2.7 Hz, 1H), 3.43 (s, 3H), 1.43 (s, 9H), 1.32 (s, 9H).

Synthesis of 20: In a 250 ml schlenk flask equipped with a stir bar, **17** (0.72 g, 3 mmol, 2 eq) was stirred with mesitylaldehyde (0.222 g, 1.5 mmol, 1 eq) in 90 ml of dry DCM before 35 μl (0.45 mmol, 0.3 eq) of TFA was added. The solution changed color and was stirred in the dark at room temperature for 3 h. 2,3-dichloro-5,6-dicyano-*p*-benzoquinone (DDQ) (0.34 g, 1.5 mmol, 1 eq) was added and the resulting mixture was stirred for another 4 h in the dark. The reaction mixture was then washed with saturated Na₂CO₃ solution (3x50 ml). The organic layer was concentrated under reduced pressure before transferred to a short pad of basic Alumina with DCM as a running solvent. The filtrated was purified by silica column chromatography (check this and ¹H NMR (400 MHz, CDCl₃) δ 8.27 – 8.21 (m, 2H), 7.61 – 7.53 (m, 2H), 7.07 (d, *J* = 8.7 Hz, 2H), 6.95 (s, 2H), 6.86 (d, *J* = 4.3 Hz, 2H), 6.44 (d, *J* = 4.2 Hz, 2H), 3.88 (s, 6H), 2.37 (s, 3H), 2.16 (s, 6H). ¹⁹F NMR (376 MHz, CDCl₃) δ -60.71.

Synthesis of 22: In a 250 ml schlenk flask equipped with a stir bar, **19** (1.43 g, 5 mmol, 2 eq) was stirred with mesitylaldehyde (0.371 g, 2.5 mmol, 1 eq) in 90 ml of dry DCM before 80 μl (0.75 mmol, 0.3 eq) of TFA was added. The solution changed color and was stirred in the dark at room temperature for 3 h. 2,3-dichloro-5,6-dicyano-*p*-benzoquinone (DDQ) (0.57 g, 2.5 mmol, 1 eq) was added and the resulting mixture was stirred for another 4 h in the dark. The reaction mixture was then washed with saturated Na₂CO₃ solution (3x50 ml). The organic layer was concentrated under reduced pressure before transferred to a short pad of basic Alumina with DCM as a running solvent. The filtrated was purified by silica column chromatography (DCM to 20% EtOAc in DCM) to yield orange solid (0.6 g, 34.3%). ¹H NMR (600 MHz, CDCl₃) δ 7.53 (s, 2H), 7.37 – 7.31 (m, 2H), 6.95 (d, *J* = 2.4 Hz, 2H), 6.69 (t, *J* = 3.2 Hz, 2H), 6.40 (s, 2H), 3.63 – 3.60 (m, 6H), 2.40 – 2.36 (m, 3H), 2.21 – 2.17 (m, 6H), 1.42 – 1.37 (m, 18H), 1.34 – 1.30 (m, 18H).

Synthesis of 23: In 25 ml dried schlenk flask equipped with a stir bar, NaH (83 mg, 3.46 mmol, 4eq) and C₁₂H₂₅SH (0.7 g, 0.82 ml, 3.46 mmol, 4 eq) was stirred under inert atmosphere in 9 ml dry DMF for 1 h at room temperature. **22** (0.6 g, 0.86 mmol, 1 eq) was added before the reaction mixture was brought to 110°C for 4 h. The reaction was cooled down and 1.8 ml of saturated NH₄Cl, 3 ml of H₂O and 6 ml of EtOAc were added to the reaction. The aqueous layer was extracted with EtOAc (3x15 ml). Combined organic layers was washed with NaCl brine and dried with Na₂SO₄ before being concentrated at reduced pressure. The red oil was purified by silica column chromatography (5:1 hexanes: DCM, *R_f* 0.22), yielding red solid 0.121 g, 21%. ¹H

NMR (600 MHz, CDCl₃) δ 7.57 (d, J = 2.5 Hz, 2H), 7.34 (d, J = 2.4 Hz, 2H), 6.95 (s, 2H), 6.86 (d, J = 4.4 Hz, 2H), 6.45 (s, 2H), 2.38 (s, 3H), 2.13 (s, 6H), 1.54 (s, 18H), 1.34 (s, 18H).

B.5. References

- (1) Karunadasa, H. I.; Chang, C. J.; Long, J. R. *Nature* **2010**, *464*, 1329–1333.
- (2) Karunadasa, H. I.; Montalvo, E.; Sun, Y.; Majda, M.; Long, J. R.; Chang, C. J. *Science* **2012**, *335*, 698–702.
- (3) Sun, Y.; Bigi, J. P.; Piro, N. A.; Tang, M. L.; Long, J. R.; Chang, C. J. **2011**, *2*, 9212–9215.
- (4) Chantarojsiri, T.; Sun, Y.; Long, J. R.; Chang, C. J. *Inorg. Chem.* **2015**, *54*, 5879–5887.
- (5) Fillol, J. L.; Codolà, Z.; Garcia-Bosch, I.; Gómez, L.; Pla, J. J.; Costas, M. *Nat Chem* **2011**, *3*, 807–813.
- (6) Prat, I.; Mathieson, J. S.; Güell, M.; Ribas, X.; Luis, J. M.; Cronin, L.; Costas, M. **2011**, *3*.
- (7) Nanthakumar, A.; Miura, J.; Diltz, S.; Lee, C.-K.; Aguirre, G.; Ortega, F.; Ziller, J. W.; Walsh, P. J. *Inorg. Chem.* **1999**, *38*, 3010–3013.
- (8) Kochem, A.; Chiang, L.; Baptiste, B.; Philouze, C.; Leconte, N.; Jarjayes, O.; Storr, T.; Thomas, F. *Chem. - A Eur. J.* **2012**, *18*, 14590–14593.
- (9) El Ghachtouli, S.; Wójcik, K.; Copey, L.; Szydło, F.; Framery, E.; Goux-Henry, C.; Billon, L.; Charlot, M.-F.; Guillot, R.; Andrioletti, B.; Aukauloo, A. *Dalton Trans.* **2011**, *40*, 9090–9093.
- (10) Nakano, K.; Kobayashi, K.; Nozaki, K. *J. Am. Chem. Soc.* **2011**, *133*, 10720–10723.
- (11) Rausaria, S.; Kamadulski, A.; Rath, N. P.; Bryant, L.; Chen, Z.; Salvemini, D.; Neumann, W. L. *J. Am. Chem. Soc.* **2011**, *133*, 4200–4203.
- (12) Unpublished Results. Yujie Sun and Nick Piro

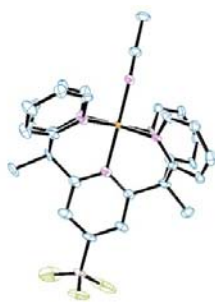


Figure B.1. Crystal Structure of Fe(PY5Me₂-BF₃⁻)

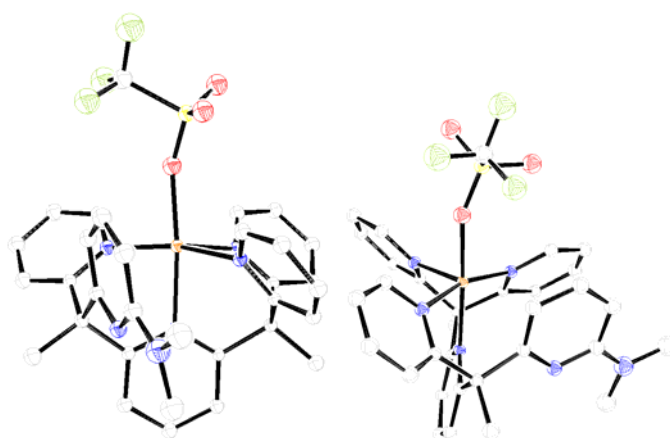


Figure B.2. Crystal Structure of Fe(NMe₂-PY5Me₂)

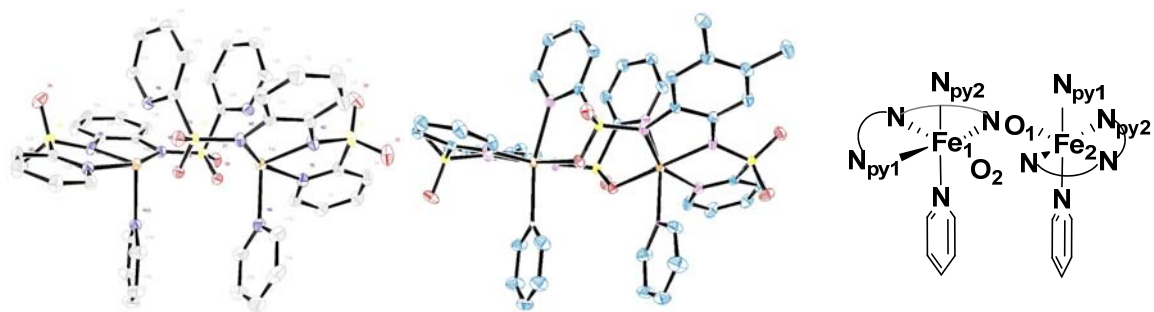
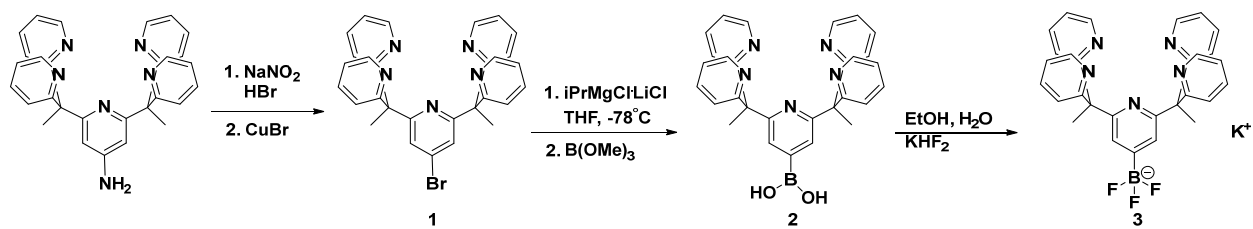
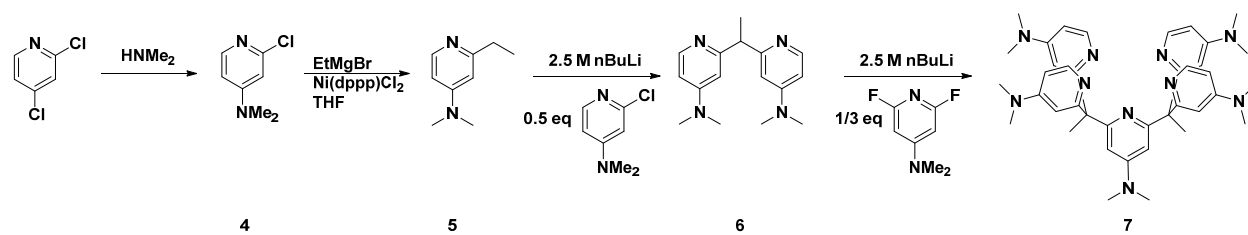


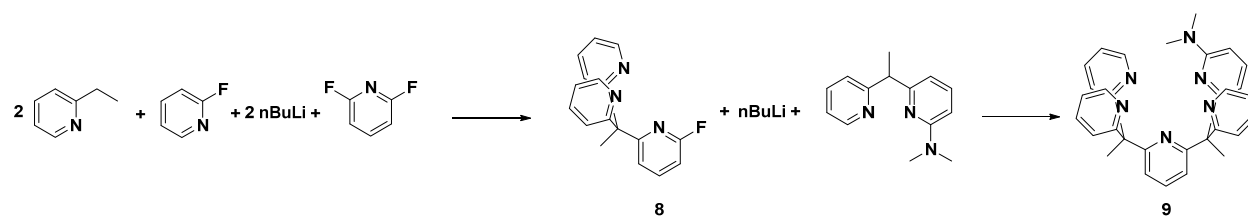
Figure B.3. Crystal Structure of [Fe(sulfonamide)]₂



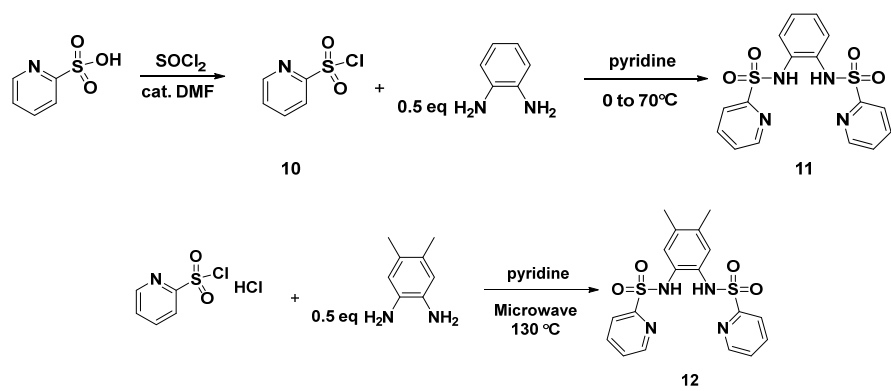
Scheme B.1. Synthesis of PY5Me₂-BF₃⁻



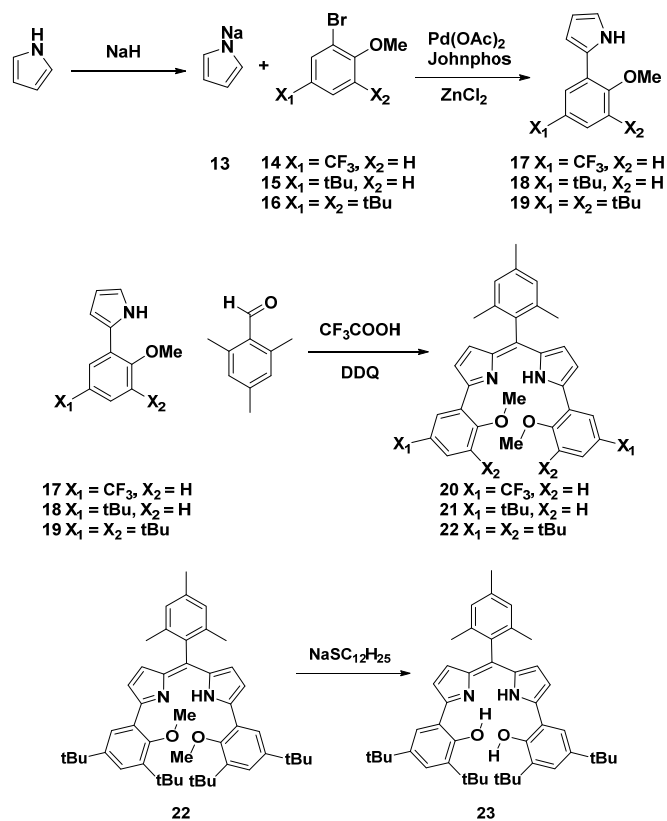
Scheme B.2. Synthesis of DMAP5



Scheme B.3. Synthesis of NMe₂-PY5Me₂



Scheme B.4. Synthesis of bis-sulfonamide ligand



Scheme B.5. Synthesis of Dipyrin-phenoxide platform

Appendix C Syntheses and Characterizations of Ir-Based Water-Soluble Photosensitizers

C.1. Synopsis

This appendix summarized the synthesis and characterizations of Ir-based photosensitizers which can be used in aqueous photolysis systems.

C.2. Motivation and Design

Increasing energy demands drive the developments of small-molecule-activation catalysts for proton reduction and carbon dioxide reduction. In order to drive these chemical transformations, solar energy which is ubiquitous and environmentally friendly can be utilized. Photosensitizers play an important role in this process as they can absorb light and transfer energy to the catalyst. However, most photosensitizers developed, including the commonly used Ir(ppy)₃ (**1**),¹ are incompatible with aqueous system due to hydrophobicity of the ligand. In this context, we seek to synthesize water-soluble photosensitizers with strong reductive power to drive the catalysts.

Our strategy involves incorporating functional group that is negatively charged and also easily coupled to other chemical moiety that will enhance water solubility. Carboxylic acid group is a good candidate as it can be easily incorporated into the phenylpyridine ligands and coupled to -OH or -NH₂ functionalized water-soluble moieties, amino acid or sugar, with modular synthesis.

C.3. Results and discussions

Target ligands are shown in Figure 1. Derivatized phenylpyridines can be synthesized by Pd cross-coupling of phenylboronic acid and bromopyridine. N-mppy is synthesized from phenylboronic acid and 6-bromonicotinamic acid with Pd(PPh₃)₄ as a catalyst. The carboxylic acid group is then protected as a methyl ester using MeOH and H₂SO₄ for subsequent metallation.² C-mppy is synthesized in a similar manner, starting from 4-methoxycarbonylbenzeneboronic acid and 2-bromopyridine with Pd(dppf)Cl₂ as a catalyst.³

The Ir complexes are synthesized in two steps to ensure correct stereoisomer, as *fac*-Ir(ppy)₃ is the desirable product. Heating IrCl₃ starting material at high temperature in ethoxyethanol yields bis- μ -chloro dinuclear Ir complexes as shown in Figure 3. Isolation of solid product by filtration and subsequent reaction with another equivalent of ligand in toluene at high temperature successfully generates *fac*- isomer. In order to synthesize Ir(N-cppy)₃ or Ir(C-cppy)₃, Ir(N-mppy)₃ or Ir(C-mppy)₃ respectively undergo ester hydrolysis to yield carboxylic acid groups on the phenylpyridine ligands.

All Ir complexes were characterized electrochemically to determine Ir^{IV/III} and Ir^{III/II} redox potentials. Together with E₀₋₀ value, which is 2.25 eV for Ir(ppy)₃ photosensitizer, and Rehm-weller equation⁴, Latimer diagrams can be generated to understand the redox properties of excited state Ir complexes. (Table 1).

C.4. Experimental

General Information: All manipulations were performed under air- and water- free conditions using standard glovebox and Schlenk-line techniques, unless otherwise noted. All commercially available reagents were used without further purification, unless otherwise noted. Toluene, acetonitrile (MeCN), tetrahydrofuran (THF) and diethylether (Et₂O) were dried and degassed using the VAC 103991 solvent system and stored over 3-Å molecular sieves under a nitrogen atmosphere, and ethoxyethanol was distilled over calcium hydride and stored over 3-Å

molecular sieves prior to use. UV-vis spectra and emission spectra were collected by Rony Khnayzer, Bowling Green State University. NMR experiments were conducted on Bruker AVB-400, AVQ-400 and AV-600 spectrometers. ESI-MS experiments were performed by the Proteomics/Mass Spectrometry facility at University of California-Berkeley. X-ray crystallography was performed in the Chexray facility. Nonaqueous electrochemical experiments were conducted under Ar atmosphere in 0.1 M NBu₄PF₆ in CH₃CN and DMF. Cyclic voltammetry experiments were carried out using BASI Epsilon potentiostat with a C-3 cell stand. The working electrode was a glassy carbon disk (3 mm diameter), the counter electrode is platinum wire with a Ag/AgCl as a reference electrode. Ferrocene was used as an external standard in all experiments. The scan rate was 0.1 V/s unless otherwise noted.

Synthesis of N-cppy: The solution of 50 ml 1 M Na₂CO₃ in water, 50 ml water and 50 ml THF was sparged for 15 minutes with N₂. Phenylboronic acid (1.6 g, 14 mmol, 1.4 eq) was added to the solution followed by 6-bromonicotinic acid (2.0 g, 10 mmol, 1 eq) under the counter flow of N₂. After stirring under N₂ for another 10 minutes, [Pd(Ph₃)₄] (250 mg, 0.25 mmol, 2.5 mol%) was added as a solid in one portion. The mixture was heated to reflux at 100°C for 24h. After the reaction cooled down to room temperature, THF was removed *in vacuo* to avoid emulsification during extraction. The aqueous layer was extracted with DCM (3x50 ml). The aqueous layer was then acidified to pH 1 with conc HCl. White solid precipitated out. The solid was filtered and washed with H₂O multiple times and dried with P₂O₅ in vacuum desiccators overnight. Yield 2.307 g, 99%. ¹H NMR (400 MHz, CD₃Cl) δ 9.38 – 9.32 (m, 1H), 8.41 (dd, *J* = 8.4, 2.2 Hz, 1H), 8.11 – 8.04 (m, 2H), 7.85 (d, *J* = 8.4 Hz, 1H), 7.51 (q, *J* = 7.7, 7.0 Hz, 3H).

Synthesis of N-mppy: N-cppy (2.25 g, 10 mmol) was dissolved in 70 ml of MeOH. Concentrated H₂SO₄ (4ml) was added and then the solution was heated to reflux overnight. The reaction was cooled down to room temperature and MeOH was removed *in vacuo*. 100 ml of water was added to the solution which was then acidified with saturated NaHCO₃ solution, followed by extraction with Et₂O (3x50 ml). The organic layer was combined, washed with NaCl brine, and dried with Na₂SO₄. Organic solvent was removed to yield light yellow solid (1.12 g, 50 %). ¹H NMR (400 MHz, CD₃Cl) δ 9.28 (d, *J* = 2.2 Hz, 1H), 8.35 (dd, *J* = 8.3, 2.2 Hz, 1H), 8.10 – 8.02 (m, 2H), 7.82 (d, *J* = 8.3 Hz, 1H), 7.56 – 7.43 (m, 3H), 3.98 (s, 3H).

Synthesis of C-mppy: In a flask charged with 100 ml THF and 90 ml saturated NaHCO₃, 4-methoxycarbonylbenzeneboronic acid (3.59 g, 20 mmol, 1 eq) and 2-bromopyridine (1.9 ml, 20 mmol, 1eq) were added. The solution was degassed under N₂ for 30 minutes before Pd(dppf)Cl₂ (100 mg, 0.6 mol%) was added in one portion. The solution was heated at 70°C for 2 days. After cooling down the solution, the organic layer was extracted with chloroform (3x50 ml). The combined organic layer was washed with NaCl brine, dried with Na₂SO₄, before solvent was removed *in vacuo*. The resulting pink solid was passed through a silica plug in DCM and EtOAc to yield white powder of C-mppy (1.883 g, 44%), ¹H NMR (400 MHz, CDCl₃) δ 8.73 (dddt, *J* = 857.9, 21.7, 4.8, 1.4 Hz, 1H), 8.19 – 8.02 (m, 4H), 7.85 – 7.75 (m, 2H), 7.29 (td, *J* = 4.8, 3.7 Hz, 1H), 3.95 (s, 4H).

Synthesis of 2: In a flask charged with magnetic stir bar, add $\text{IrCl}_3 \cdot x\text{H}_2\text{O}$ (0.298 g, 1 mmol, 1 eq) and N-mppy (0.469 g, 2.2 mmol, 2.2 eq) into 30 ml of Ethoxyethanol. The mixture was brought to reflux at 135°C for 24 h in the dark. After cooling down, 30 ml of H_2O was added to the solution, yielding orange precipitates of Tetrakis(2-phenyl-5-methoxycarbonylpyridine-C2,N')(μ -dichloro)diiridium(III) which was filtered and dried under vacuum overnight. Yield (0.517 mg, 79.3%) ^1H NMR (400 MHz, CDCl_3) δ 9.89 – 9.83 (m, 4H), 8.25 (dd, $J = 8.5$, 1.9 Hz, 4H), 7.93 (d, $J = 8.5$ Hz, 4H), 7.56 (d, $J = 7.7$ Hz, 4H), 6.80 (td, $J = 7.5$, 1.1 Hz, 4H), 6.63 (td, $J = 7.5$, 1.4 Hz, 4H), 5.89 – 5.82 (m, 4H), 3.84 (s, 12H).

$[(\text{N-mppy})_2\text{Ir}(\mu\text{-Cl})_2\text{Ir}(\text{N-mppy})_2]$ (200 mg, 0.15 mmol, 1 eq), N-mppy (147 mg, 0.69 mmol, 4.5 eq), AgOTf (79 mg, 0.3 mmol, 2 eq), and toluene (15 mL) were placed in a reaction vessel and degassed with N_2 . The reaction mixture was heated at 120°C while under N_2 and continuous stirring for 5 h. The resulting dark orange-red solution was cooled to room temperature and directly transferred to a silica column. The product was eluted with 20% DCM in acetone. *fac*- $\text{Ir}(\text{N-mppy})_3$ was obtained in a yield of 27% (67.2 mg). ^1H NMR (400 MHz, CDCl_3) δ 8.21 – 8.10 (m, 6H), 7.95 (d, $J = 8.6$ Hz, 3H), 7.76 – 7.69 (m, 3H), 6.98 – 6.77 (m, 9H), 3.78 (s, 9H).

Synthesis of 3: **2** (67.2 mg, 0.081 mmol) was dissolved in 4.8 ml of 6M NaOH combined with 8ml THF and 8 ml EtOH. The solution was heated to reflux overnight under N_2 . The solution was cooled to room temperature, acidified to a pH of 1 with HCl, and extracted with ethyl acetate/ H_2O . The organic layer was dried over Na_2SO_4 and the solvent was evaporated under reduced pressure to give a solid **3** (62.4 mg, 98%). ^1H NMR (400 MHz, $\text{DMSO-}d_6$) δ 8.31 (d, $J = 8.6$ Hz, 3H), 8.23 (dd, $J = 8.5$, 2.0 Hz, 3H), 7.98 (d, $J = 2.0$ Hz, 3H), 7.89 (d, $J = 8.0$ Hz, 3H), 6.88 (dd, $J = 8.1$, 6.8 Hz, 3H), 6.82 – 6.73 (m, 3H), 6.66 (d, $J = 7.4$ Hz, 3H), 5.76 (s, 3H).

Synthesis of 4: The same synthetic procedure of **2** was used to synthesize **4** with C-mppy ligand. $[(\text{N-mppy})_2\text{Ir}(\mu\text{-Cl})_2\text{Ir}(\text{N-mppy})_2]$: Yield 0.9279 g, 71.2%. ^1H NMR (400 MHz, CDCl_3) δ 9.25 (d, $J = 5.6$ Hz, 4H), 7.98 (d, $J = 7.9$ Hz, 4H), 7.86 (t, $J = 8.3$ Hz, 4H), 7.54 (d, $J = 8.1$ Hz, 4H), 7.42 (dd, $J = 8.0$, 1.7 Hz, 5H), 6.92 (t, $J = 6.9$ Hz, 5H), 6.56 (d, $J = 1.6$ Hz, 4H), 3.70 (s, 12H). **4** yield 120 mg, 18%. ^1H NMR (600 MHz, CDCl_3) δ 7.96 (d, $J = 8.2$ Hz, 3H), 7.73 – 7.62 (m, 6H), 7.58 (dd, $J = 8.3$, 1.8 Hz, 3H), 7.55 – 7.50 (m, 3H), 7.39 – 7.36 (m, 3H), 5.30 (s, 2H), 3.70 (s, 9H).

Synthesis of 5: The same synthetic procedure of **2** was used to synthesize **4** with C-mppy ligand. Yield 88.5 mg, 77.7%. ^1H NMR (600 MHz, CDCl_3) δ 7.44 (d, $J = 8.2$ Hz, 3H), 7.08 – 7.00 (m, 6H), 6.65 (d, $J = 5.4$ Hz, 3H), 6.57 (dd, $J = 8.1$, 1.9 Hz, 3H), 6.40 – 6.35 (m, 6H).

C.5. References

- (1) Kapturkiewicz, A.; Angulo, G. *Dalt. Trans.* **2003**, 3907.
- (2) Steunenbergh, P.; Ruggi, A.; van den Berg, N. S.; Buckle, T.; Kuil, J.; van Leeuwen, F. W. B.; Velders, A. H. *Inorg. Chem.* **2012**, *51*, 2105–2114.
- (3) Xie, Z.; Ma, L.; DeKrafft, K. E.; Jin, A.; Lin, W. *J. Am. Chem. Soc.* **2010**, *132*, 922–923.

(4) *Photochemistry and Photophysics of Coordination Compounds II*; Balzani, V.; Campagna, S., Eds.; Topics in Current Chemistry; Springer Berlin Heidelberg: Berlin, Heidelberg, 2007; Vol. 281.

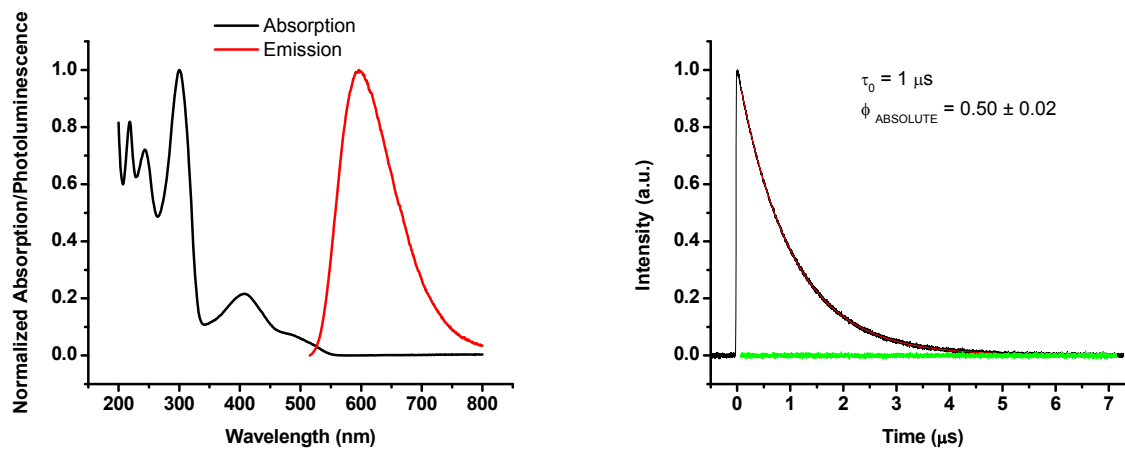


Figure C.1. Photophysics of Ir(N-ppy)₃ in CH₃CN

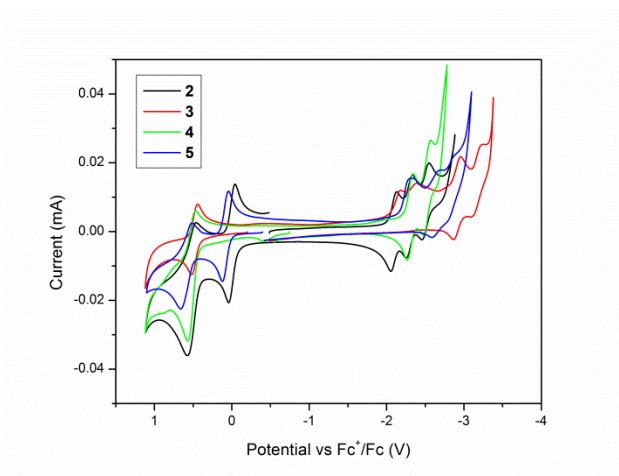
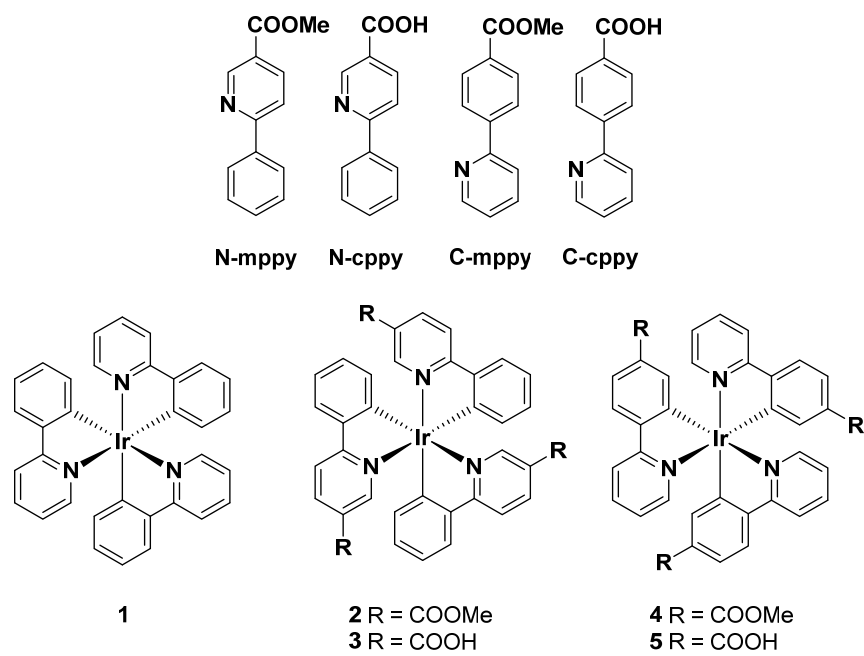
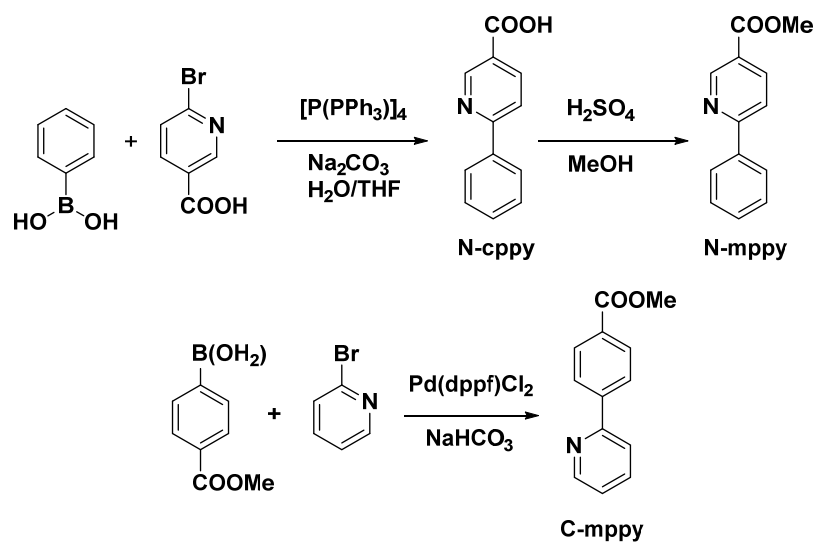


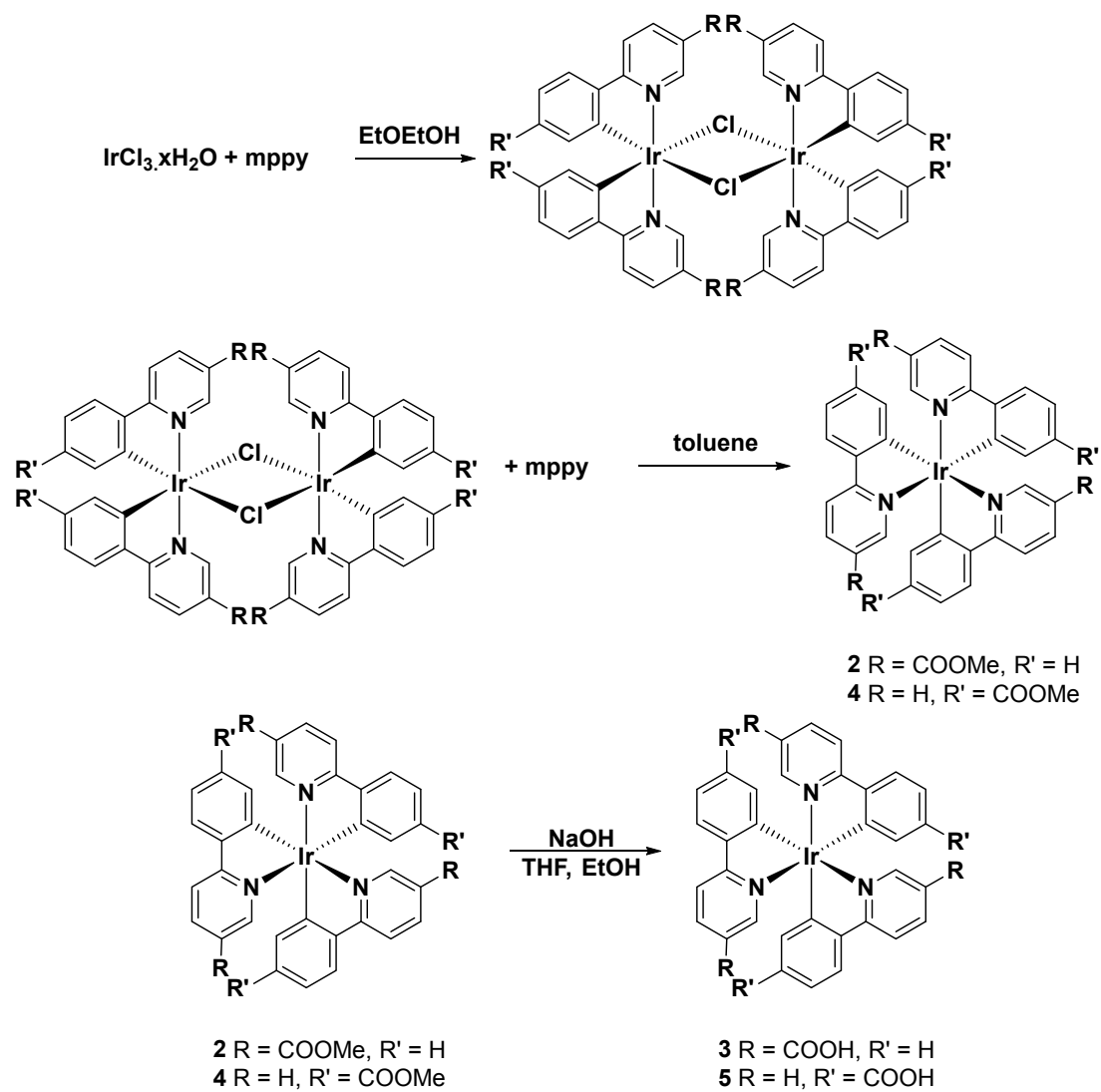
Figure C.2. Cyclic Voltammograms of complex **2-4**. Redox couple at 0 V is an external standard, ferrocene.



Scheme C.1. Derivatives of phenylpyridine which can be used to make water-soluble photosensitizer (top). $\text{Ir}(\text{ppy})_3$ (**1**) and target molecules, **2**, **3**, **4**, and **5**.

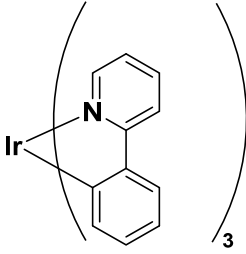
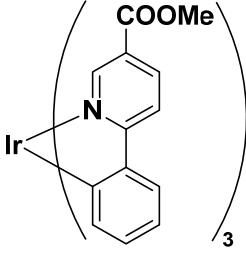
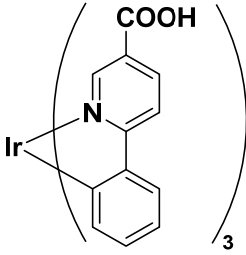
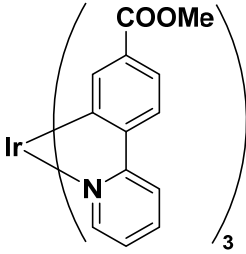
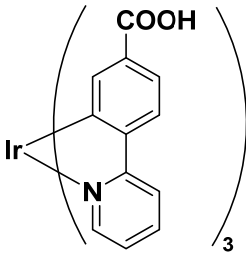


Scheme C.2. Synthesis of N-mppy and C-mppy



Scheme C.3. Two-step synthesis of *fac*-Ir(N/C-mppy)₃, methyl esters can then be hydrolyzed to give *fac*-Ir(N/C-cppy)₃

Table C.1. Latimer diagrams and solubility properties of complex 2-4.

Complex	Latimer Diagram	Solubility
	$ \begin{array}{c} \text{Ir(ppy)}_3 \\ \swarrow \quad \searrow \\ \text{[Ir]}^{\cdot-} \quad \text{[Ir]}^{\cdot+} \\ \leftarrow \quad \rightarrow \\ \text{[Ir]}^{\cdot-} \quad \text{[Ir]}^{\cdot+} \end{array} $ <p style="text-align: center;"> $\text{[Ir]}^{\cdot-} \xrightarrow{-0.94} \text{[Ir]}^{\cdot+}$ $\text{[Ir]}^{\cdot-} \xrightarrow{-3.19} \text{[Ir]}^{\cdot-}$ $\text{[Ir]}^{\cdot+} \xrightarrow{-1.93} \text{[Ir]}^{\cdot+}$ $\text{[Ir]}^{\cdot-} \xrightarrow{0.32} \text{[Ir]}^{\cdot+}$ $\text{[Ir]}^{\cdot-} \xrightarrow{2.25 \text{ eV}} \text{[Ir]}^{\cdot+}$ </p>	DCM, MeCN (0.2mM) *2 refs reported different numbers
	$ \begin{array}{c} \text{Ir(N-mppy)}_3 \\ \swarrow \quad \searrow \\ \text{[Ir]}^{\cdot-} \quad \text{[Ir]}^{\cdot+} \\ \leftarrow \quad \rightarrow \\ \text{[Ir]}^{\cdot-} \quad \text{[Ir]}^{\cdot+} \end{array} $ <p style="text-align: center;"> $\text{[Ir]}^{\cdot-} \xrightarrow{0.169} \text{[Ir]}^{\cdot+}$ $\text{[Ir]}^{\cdot-} \xrightarrow{-2.081} \text{[Ir]}^{\cdot-}$ $\text{[Ir]}^{\cdot+} \xrightarrow{-1.746} \text{[Ir]}^{\cdot+}$ $\text{[Ir]}^{\cdot-} \xrightarrow{0.504} \text{[Ir]}^{\cdot+}$ $\text{[Ir]}^{\cdot-} \xrightarrow{2.25 \text{ eV}} \text{[Ir]}^{\cdot+}$ </p>	DCM, MeCN, MeOH, Et ₂ O, EtOAc
	$ \begin{array}{c} \text{Ir(N-cppy)}_3 \\ \swarrow \quad \searrow \\ \text{[Ir]}^{\cdot-} \quad \text{[Ir]}^{\cdot+} \\ \leftarrow \quad \rightarrow \\ \text{[Ir]}^{\cdot-} \quad \text{[Ir]}^{\cdot+} \end{array} $ <p style="text-align: center;"> $\text{[Ir]}^{\cdot-} \xrightarrow{-0.647} \text{[Ir]}^{\cdot+}$ $\text{[Ir]}^{\cdot-} \xrightarrow{-2.897} \text{[Ir]}^{\cdot-}$ $\text{[Ir]}^{\cdot+} \xrightarrow{-1.770} \text{[Ir]}^{\cdot+}$ $\text{[Ir]}^{\cdot-} \xrightarrow{0.480} \text{[Ir]}^{\cdot+}$ $\text{[Ir]}^{\cdot-} \xrightarrow{2.25 \text{ eV}} \text{[Ir]}^{\cdot+}$ </p>	MeOH, MeCN, DMF, DMSO
	$ \begin{array}{c} \text{Ir(C-mppy)}_3 \\ \swarrow \quad \searrow \\ \text{[Ir]}^{\cdot-} \quad \text{[Ir]}^{\cdot+} \\ \leftarrow \quad \rightarrow \\ \text{[Ir]}^{\cdot-} \quad \text{[Ir]}^{\cdot+} \end{array} $ <p style="text-align: center;"> $\text{[Ir]}^{\cdot-} \xrightarrow{-0.277} \text{[Ir]}^{\cdot+}$ $\text{[Ir]}^{\cdot-} \xrightarrow{-2.527} \text{[Ir]}^{\cdot-}$ $\text{[Ir]}^{\cdot+} \xrightarrow{-1.729} \text{[Ir]}^{\cdot+}$ $\text{[Ir]}^{\cdot-} \xrightarrow{0.521} \text{[Ir]}^{\cdot+}$ $\text{[Ir]}^{\cdot-} \xrightarrow{2.25 \text{ eV}} \text{[Ir]}^{\cdot+}$ </p>	DCM, MeOH, MeCN
	$ \begin{array}{c} \text{Ir(C-cppy)}_3 \\ \swarrow \quad \searrow \\ \text{[Ir]}^{\cdot-} \quad \text{[Ir]}^{\cdot+} \\ \leftarrow \quad \rightarrow \\ \text{[Ir]}^{\cdot-} \quad \text{[Ir]}^{\cdot+} \end{array} $ <p style="text-align: center;"> $\text{[Ir]}^{\cdot-} \xrightarrow{-0.100} \text{[Ir]}^{\cdot+}$ $\text{[Ir]}^{\cdot-} \xrightarrow{(-2.350)} \text{[Ir]}^{\cdot-}$ $\text{[Ir]}^{\cdot+} \xrightarrow{-1.666} \text{[Ir]}^{\cdot+}$ $\text{[Ir]}^{\cdot-} \xrightarrow{0.584} \text{[Ir]}^{\cdot+}$ $\text{[Ir]}^{\cdot-} \xrightarrow{2.25 \text{ eV}} \text{[Ir]}^{\cdot+}$ irreversible reduction wave </p>	MeOH, MeCN, DMF (poor solubility in general)

Appendix D Mössbauer Spectroscopy of Linear Fe(I) complexes and Fe(0) complexes

This appendix includes work published in: Lipschutz, M. I., Chantarojsiri, T., Dong, Y., Tilley, T. D. *J. Am. Chem. Soc.*, 2015, 137 (19), pp 6366–6372.

D.1. Synopsis

This appendix summarized characterizations of a Linear Fe(I) complexes and its reduction product Fe(0) by Mössbauer Spectroscopy.

D.2. Motivation and Design

Complex **1** (Scheme D.1) is reported as alkyne trimerization catalyst for both internal and terminal alkynes at modest loading (2-6 mol%) and under mild conditions (room temperature). **1** is found to be redox active and can be reduced by KC_8 to form **5**.¹

D.3. Results and Discussion

Compound 1: At 5 K, Mössbauer spectrum of Fe(I) exhibited a sextet pattern with isomer shift, δ , of 0.387 mm/s and quadrupole splitting, ΔE_Q , of -2.253 mm/s with very large hyperfine field is 635.94 kG (Figure D.1). The non-ideal fit of the spectrum at 5 K may due to the non-linearity of the source motion outside the calibrated range. (Line 2 and 5 too wide and line 3 and 4 too narrow). The sextet pattern broadens at 50 K (figure D.1) and collapses into a doublet at 75 K with δ of 0.417 mm/s and ΔE_Q of 0.888 mm/s (figure D.2).

Mössbauer spectra of **1** closely resemble those of $[K(\text{crypt-222})]\{\text{Fe}[\text{C}(\text{SiMe}_3)_3]_2\}^2$. The sharp sextet in the Mossbauer spectrum at 5K indicates that the internal field is along the same molecular direction for almost all the iron in the sample, suggesting that the Fe center is an isolated paramagnet with an easy axis of magnetization which also supports by the lack of EPR spectrum.

Compound 5: The spectra of Fe(0) at variable temperature only show a doublet pattern. At 5 K, it has a δ of 0.812 mm/s and ΔE_Q of 2.364 mm/s. The increase in the value of isomer shift from 0.387 mm/s in **1** to 0.812 mm/s in **5** indicates reduction of the iron center. Comparing δ at 75 K (0.417 mm/s of **1** and 0.800 mm/s of **5**), the more positive isomer shift suggests reduction at the iron center.

Upon warming up to room temperature, **5** decomposes into another product. Mössbauer spectrum at 290 K is quite broad. Another measurement at 5 K conducted after a room temperature experiment showed that 50% of the iron center have become another species. (Figure D.4, Table D.4)

D.4. Experimental

Zero-field, ^{57}Fe Mössbauer spectra were recorded in constant acceleration spectrometer (See Co. Edina, MN) between room temperature and 5 K in a Janis Research Co. cryostat (Willmington, MA). Collected spectra were analyzed using the WMOSS software package (See Co. Edina, MN). Isomer shifts are reported relative to α -iron (27 μm foil) at room temperature. Samples were prepared by mixing Boron Nitride (BN) with finely ground crystalline samples of Fe complexes. Powder mixture was placed in nylon washer wrapped in Teflon tape and then Kapton® tape under inert atmosphere prior to introduction into the spectrometer in air. A layer of Teflon tape in between samples Kapton tape is crucial as the samples is not stable to Kapton tape adhesives materials.

The model used for fitting the sextet assumed that the principal component of the EFG (V_{zz}) is along the direction of H_{int} and $\theta=0$, therefore, V_{zz} was along the direction of H_{int} was assumed.

D.5. References

- (1) Lipschutz, M. I.; Chantarojsiri, T.; Dong, Y.; Tilley, T. D. *J. Am. Chem. Soc.* **2015**, *137*, 6366–6372.
- (2) Zadrozny, J. M.; Xiao, D. J.; Long, J. R.; Atanasov, M.; Neese, F.; Grandjean, F.; Long, G. J. *Inorg. Chem.* **2013**, *52*, 13123–13131.

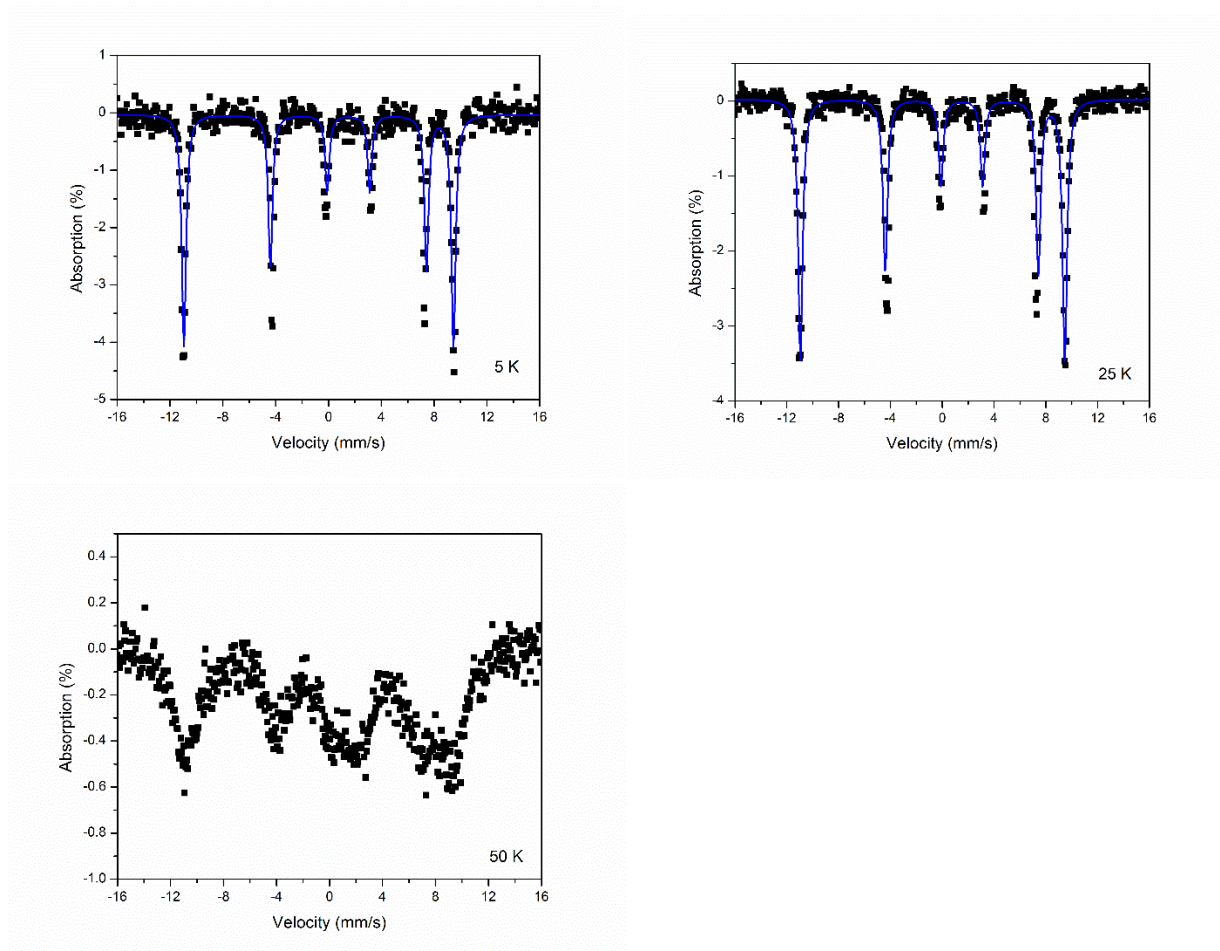


Figure D.1. Zero-field ^{57}Fe Mössbauer spectra of 1 at 5, 25 and 50 K respectively (black square). A least-squares fit (blue line) provided the parameters listed in Table D.1.

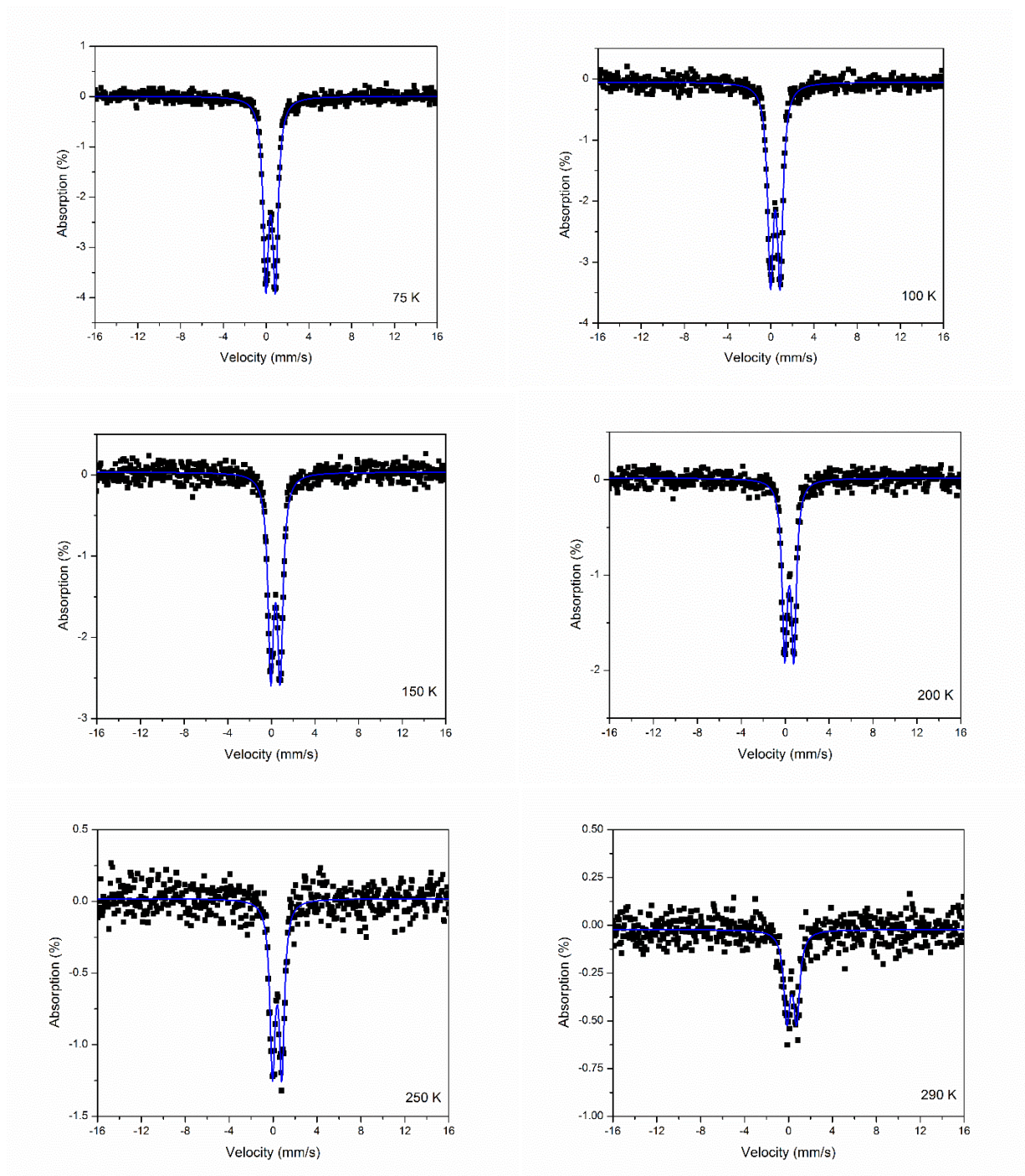


Figure D.2. Zero-field ^{57}Fe Mössbauer spectra of **1** acquired at 75, 100, 150, 200, 250 and 290 K (black squares). A least-squares fit (blue line) provided the parameters listed in Table D.2.

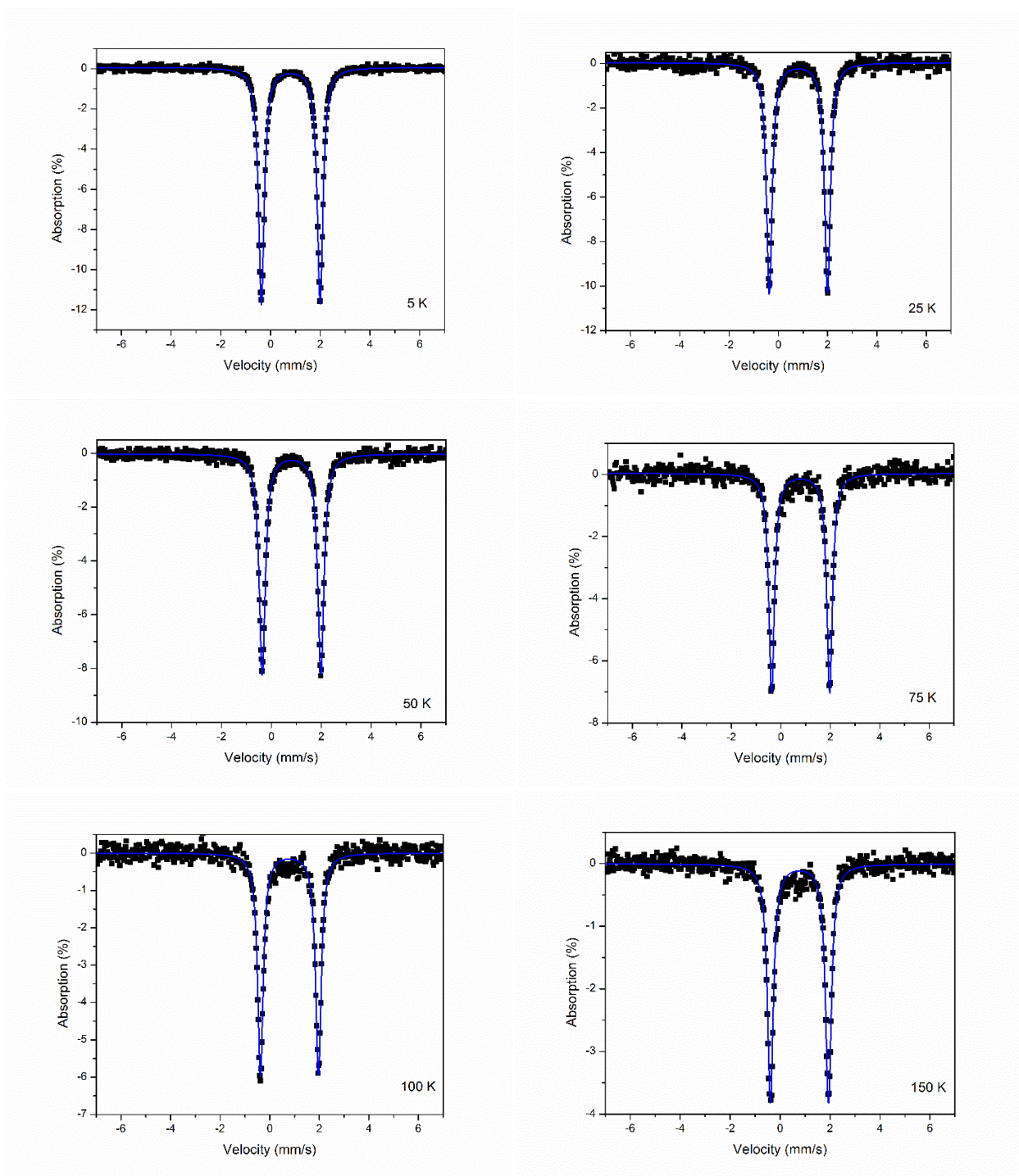


Figure D.3. Zero-field ^{57}Fe Mössbauer spectra of **5** acquired at 5, 25, 50, 75, 100, and 150 K (black squares). A least-squares fit (blue line) provided the parameters listed in Table D.3.

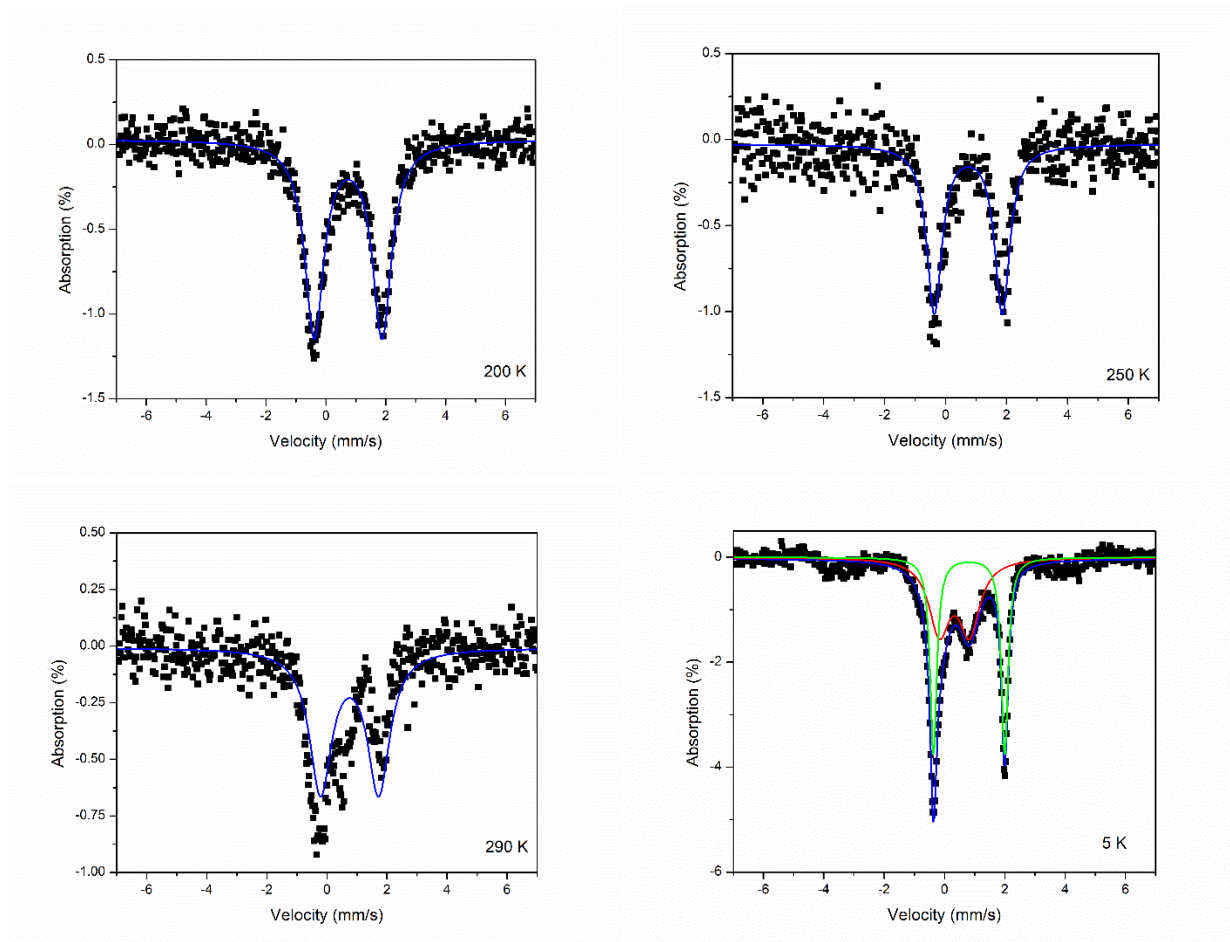


Figure D.4. Zero-field ^{57}Fe Mössbauer spectra of **5** acquired at 200, 250, and 290 K and at 5 K right after a room temperature experiments (black squares). A least-squares fit (blue line) provided the parameters listed in Table D.2. Green and red lines represent least-square fits of 2 iron species, **5** and decomposed product respectively.



Scheme D.1. Linear Fe(I) (**1**) and the reduction product Fe(0) (**5**)

Table D.1. Mössbauer parameters of **1** at 5, 25 and 50 K

	5 K	25 K	50 K
δ	0.387	0.384	N/A
ΔE_q	-2.253	-2.254	N/A
H_{int}	635.658	635.781	N/A

Table D.2. Mössbauer parameters of **1** at 75, 100, 150, 200, 250 and 290 K

	75 K	100 K	150 K	200 K	250 K	290 K
δ	0.417	0.416	0.379	0.370	0.367	0.290
ΔE_q	0.888	0.883	0.860	0.827	0.841	0.885
Γ	0.623	0.635	0.616	0.565	0.576	0.697

Table D.3. Mössbauer parameters of **5** at 5, 25, 50, 75, 100, 150, 200, 250, and 290 K

	5 K	25 K	50 K	75 K	100 K	150 K	200 K	250 K	290 K
δ	0.812	0.811	0.807	0.800	0.795	0.773	0.743	0.744	0.754
ΔE_q	2.364	2.357	2.353	2.345	2.339	2.324	2.262	2.231	1.943
Γ	0.277	0.279	0.294	0.271	0.274	0.284	0.767	0.602	0.900

Table D.4. Mössbauer parameters of **5** at 5 K after room temperature experiment, 50% of **5** decomposes into another product (specie 2)

	Species 1	Species 2
δ	0.813	0.327
ΔE_q	2.363	0.999
Γ	0.271	0.831
%	50	50

Appendix E Glovebox Guidelines and Basic Troubleshooting

E.1. Glovebox Guidelines

E.1.1. What should not be in the box:

The glovebox catalyst consists of copper particles and molecular sieves. Anything that binds to copper or destroys molecular sieves will lower the performance of the catalyst. In general, anything porous that has water and O₂ should **NOT** be in the box, for example paper, cork rings, liquid acids (acetic acid, TFA, HCl), liquid sulfides, liquid amines, volatile halogenated liquids (Br₂).

E.1.2. What solvents should be used only when the catalyst is turned off:

MeCN and all nitriles, DCM and all halogenated solvents, MeOH, DMF, DMSO. All solvents should be properly degassed and dried.

E.1.3. What reagents should be used only when the catalyst is turned off:

The rule of thumb is that if a particular reagent has a chance of destroying the catalyst, it should **ONLY** be used when the catalyst and the circulation is turned off (or should not be used in the box at all).

The following is not an exhaustive list--please use common sense and ask someone if you have questions:

Pyridine, nitromethane, liquid phosphines, I₂, nitromethane, nitrosonium salts, NBS, NCS, Haloboranes, methyl triflate, methyl triflate, isonitriles, volatile diazoalkanes, alkyl tin chlorides, TiCl₄, VOCl₃, MoCl₅. Haloboranes, Sure-Seal solvents from Aldrich (can still be wet, re-dry it before use).

E.1.4. What should be brought in overnight

Anything that is not glass or metal and could not be heated at 160°C for 8 hours should be brought in overnight.

Caps (teflon or all plastic caps only), syringes, needles, septa, paratone oil, tapes

Plastics should only be brought in overnight

Kimwipes should be dried in vacuum over at 130°C for at least 8 hours. The oven should be refilled with N₂ and purge with positive pressure of N₂ while it was quickly transferred into the glovebox antechamber. Normal cycle can be used. Note that the kimwipes will burn if it rests against the wall of the oven.

E.2. Policies Regarding N₂

E.2.1. How to change N₂ tank

Isolate the gloveboxes from the nitrogen tank by closing all the red valves at the manifold regulator. Turn off the empty tank and remove the adapter with the wrench. Screw in the adapter to a new tank at the outlet labelled "Gas Use". Turn on the tank and open the first valve after the regulator and check the pressure. It should be no higher than 80 psi. Purge the copper manifold by opening the yellow valve on the top and 2 other valves that are not connected to the box respectively. After 1 minute close all the valves and turn on the red valves that connect to both gloveboxes.

*****Place the order for new N₂ tank right away*****

E.2.2 How to order new N₂ tank online

- a. Go to express.praxair.com
- b. In the login box:
Username: chrischang
Password: oxidation or redox or reduction
- c. Click on “Enter Part Number” under Order Entry.
- d. Enter the part number in the dialog box
NI LC230-230
- e. Click “order” and then “check out”
- f. Check the P/O number and the room number in the shipping address (541 for the Gloveboxes and 401 for the LCMS), and then click “check out”
- g. If you want to check the status of the order online, go to “Open Orders” under “Account Inquiry” or check for an email by signing into changpraxair@gmail.com, password: oxidation.

E.3. Operation and Maintenance

E.3.1 How to turn off the catalyst

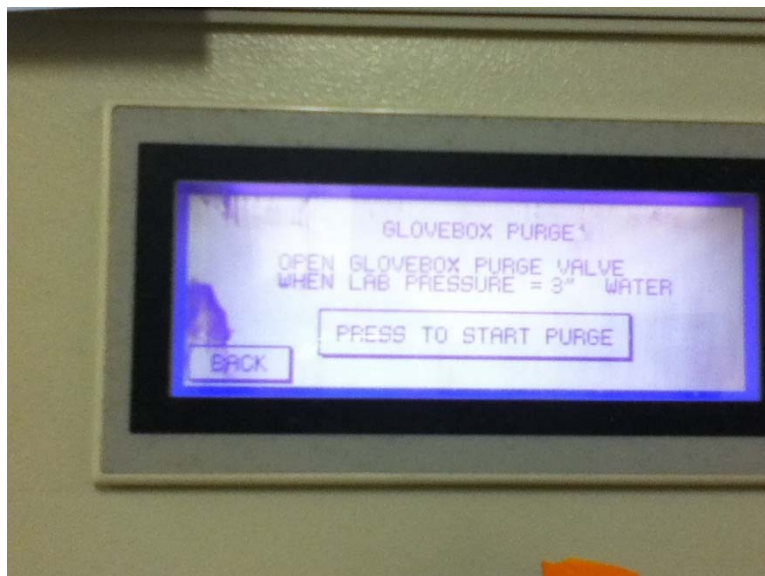
For the list of solvents and reagents that requires isolation of catalyst and purging, please see the Glovebox Guidelines section.

1. Close the two circulation valves that connect to the catalyst
2. Turn off the blower by pressing ‘Blower Control’ button, the ‘off’ should appear at the screen. At this point the O₂ reading is no longer accurate and it should go up with time

E.3.2 How to purge the box

After the catalyst and the blower is off, the purge should be performed for at least 15 minutes. Consider purging for a longer period of time if the catalyst was closed for many hours. Pictures of the screen can be found in the Glovebox manual.

1. Press ‘Purge Glove Box’ and the screen will pop up another purge button. Press ‘start purge’ and open the purge valve at the same time. The purge valve should only be open a quarter to half way, depending on the pressure of the nitrogen tank.



2. Monitor the pressure of the box at the screen, it should be around 1.8 to 2.0 sq ft of water. Modulate the pressure by adjusting the purge valve. If the box starts chugging, close the purge valve slightly and check the pressure on the nitrogen tank to make sure there is enough pressure (adjust pressure builder) and is not empty.
3. After the purge is done. Close the purge valve and press 'stop purge' button at the same time. Stop the purge completely by pressing 'stop purging' again.
4. Open the catalyst valves and turn on the blower. O₂ reading should go down to 0.99ppm (residual O₂ level of the N₂ tank). If it is higher than that, purge again. If O₂ level still stay above 0.99ppm, the catalyst might need to be regenerated.

E.3.3 How to bring anything into the box

See guidelines for what could be used in the gloveboxes and what could be brought in normally or overnight.

Make sure the big antechamber is isolated from the small antechamber by turning the big valve to a horizontal position.

*****The antechambers should be under vacuum at all time when not actively used for transferring items in or out. If you are doing something for 5 minutes, still evacuate the antechamber*****

1. Make sure both the interior and exterior antechamber doors are tightly closed (check that the door latches are in place)
2. Refill the N₂ by turning it to 'refill' and then turn it to 'off' position immediately after the pressure gauge stops increasing.
3. Open the outer door, place your item(s) in the antechamber and evacuate the antechamber by turning the valve to 'evacuation'.
4. Write in the logbook to inform others. Cycle the antechamber 3 times (5 mins each for small antechamber and 20 mins each for big antechamber)

5. After the last refill, the antechamber door can be opened and things can be brought in. Close the door tightly
6. Evacuate the empty antechamber

****Both antechamber should always be kept under vacuum****

During the day, the big antechamber should be isolated from the small antechamber

E.3.4 How to bring anything out of the box

In order to open the inner door of the antechamber, the antechamber should be under vacuum for at least 15 minutes (small) or 40 minutes (big) or was open to the box right before.

1. Refill the antechamber.
2. Place your item into the antechamber, close the inner door tightly.
3. Open the outer door and remove your item. **Quickly** close the door and evacuate the chamber.

E.3.5 How to bring things in overnight

For supplies that need overnight evacuation, please see the section above.

Similar to 3, let your items evacuate overnight. If it is a solid sample, place kimwipe and rubber band on the top of the vial to prevent spill. Write on the logbook that something is being evacuated overnight.

E.3.6 How to clean up solid spills

Load in a small weighing boat (overnight evacuation) and use the brush inside to scoop up the spill. If it is phosphines or amines, remove the spills from the box right after. Wipe the area clean using kimwipes in the box

E.3.7 How to bring in supplies-vials, pipettes, caps, septa, syringes, needles, kimwipes, stir bars, glass fiber filters, markers

Vials and Pipettes:

They should be placed in 1 L beaker before placing in the small oven for at least 8 hours. Make sure to replace the one in the oven right away. There should constantly be two sets of vials and pipettes in the oven at all times for the new two gloveboxes. Write which glovebox the supplies are for on the beaker.

Caps, septa and syringes:

Only teflons or all plastic caps could be in the box. Syringes and needles should be taken out of the wrapper. Everything should be brought in overnight.

Kimwipes:

Part of the box that contains glue should be cut out before placing it in the vacuum oven. Kimwipes should be heated at 150C overnight (level 5 on the heating gauge). The oven chamber should then be refilled with N₂. Kimwipes taken out of the vacuum oven should be placed in the antechamber as quickly as possible. It can be brought in after 15 minutes. Note that the kimwipes will be slightly colored so avoid contact between the oven wall and the kimwipes to minimize browning.

Stir bars and glass fiber filters:

Pack a vial with either stir bars or filters. Heat them up overnight in the oven before loading (while still hot) into the antechamber.

Markers:

Purge the cap with N₂ outside the box and quickly cap it. Bring it in after 15 minutes. After loading it in, purge the box and open the cap for 5 minutes to purge out residual air in the cap.

*E.3.8 How to bring in solvents, alumina, celite and mol sieves***Solvents:**

Most solvents can be collected from the solvent system. Collect each solvent according to the instruction. Degas the solvent on schlenk line for at least 3 hours. Bring solvent into the box using storage schlenk flask after 15 minutes. Take out 1 ml of the solvent and test the solvent with Na(benzophenone). If it is more than 1 drop, store the solvent under mol sieve. Note that MeCN and DCM cannot be tested with Na(benzophenone). For solvents that are not on the purifying system, distill over CaH₂ or Na(benzophenone) and degas before loading it into the box.

Alumina, 3A Molecular Sieve and Celite:

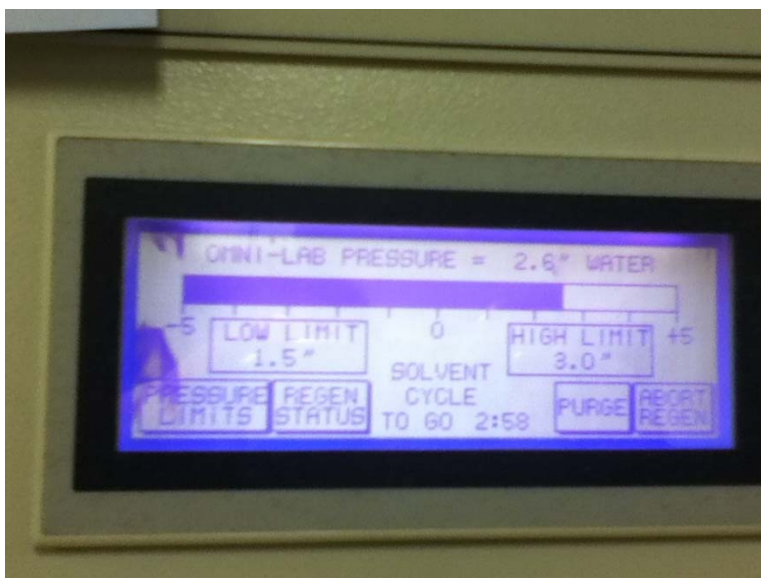
Activate Alumina, Molsieve or Celite by heating it under **vacuum** to 200-250°C, using the Variac transformer, overnight. Bring into the box after 15 mins and allow it to cool completely before transferring it into a container.

E.3.9 How to bring in NMR solvents

Distill each solvent over CaH₂, filter through activated alumina and store over mol sieve. For expensive solvents (d₂-DCM, d₈-THF) in low volumes, vacuum transfer the solvent over CaH₂.

E.3.10 How to regenerate the box

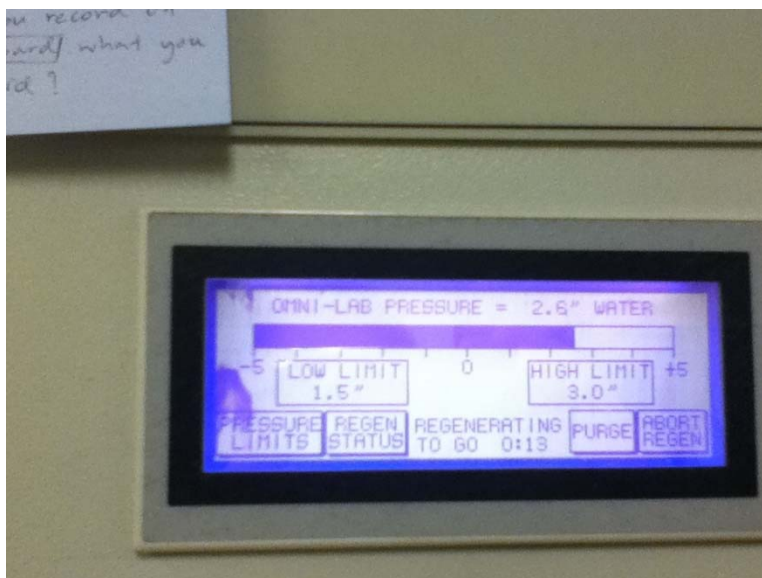
Tape all solvent bottles or any sensitive reagents. Turn off the evacuation valve of the antechambers. Turn off the catalyst and the blower. Make sure there is at least 400psi of regenerating gas remain in the tank. Monitor the pressure to make sure that it is around 35 psi. Press 'Regenerate purifier' button at the screen. See VAC manual for more information.



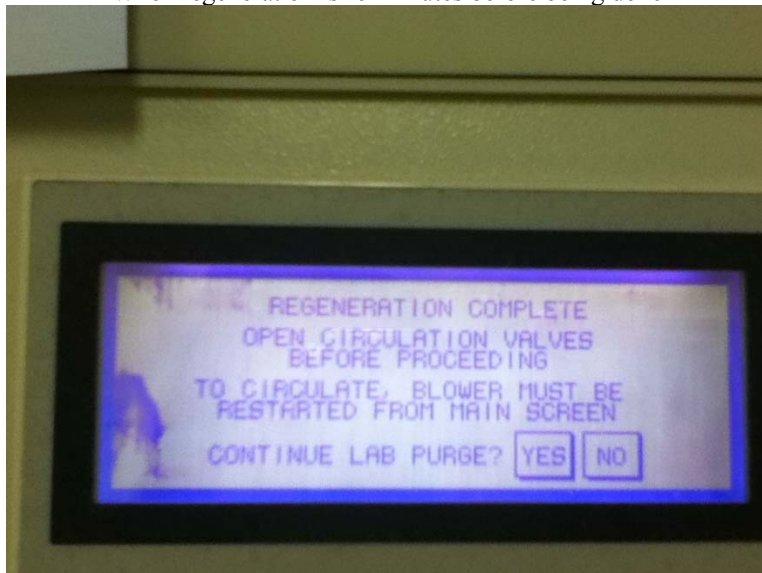
When regenerating with solvent removal cycle



Check the regen gas cylinder that it has at least 400 psi (cylinder NI HY10-K from praxair)



When regeneration is 19 minutes before being done



When regeneration is complete and purging is required

E.3.11 How to change the catalyst

See VAC manual for details. Shop Vac should be used to remove the catalyst. If possible, regenerate the catalyst beforehand to minimize gross stuff that will come out. Be sure to wear appropriate face mask. For one box, 10 lbs of catalyst and 20 lbs of molecular sieve is needed. Each side should be filled with 5 lbs of Molecular Sieve, 5 lbs Catalyst and then 5 lbs Molecular Sieve. Catalyst and mol sieve can be obtained from BASF or VAC.

E.3.12 How to set up a vacuum line

Evacuate the trap and set it up using LN2. Turn on the valve at the back of the box to open the line to the trap and the pump.

E.3.13 NMR solvents

Before usage of any NMR solvent, purge the box for 15 minutes to avoid contamination of non-deuterated solvent.

E.3.14 How to get to maintenance screen

Press the upper left corner until this screen appear

V6 is for evacuating the catalyst chamber

V5 is to refill the catalyst chamber

V1 is to refill the box

E.4. Troubleshootings

E.4.1 Oxygen level is unusually high.

1. Check if the blower is on. When the blower is off, the atmosphere is not being circulated through the catalyst bed and thus the oxygen detector is not “seeing” the real oxygen level. Please remember to turn the blower on only when the circulation valves are opened to the catalyst.
2. Begin purging the box to see if the oxygen level goes down. Please see purging instructions.
3. If the oxygen level still has not come down, check the pump to the antechamber. When this pump goes down, the pressure in the box cannot be regulated properly. Also check for leaks around the antechamber doors (interior and exterior) and the gloves.
4. Check the volatile chemicals to make sure “bad” chemicals are not the reason for the bad atmosphere.
5. Regenerate. See instructions for regeneration.
6. If all else fails, replace the catalyst. See instructions for changing the catalyst.

E.4.2 Nitrogen pressure is low (deflated gloves, gloves inside the box, can't purge properly, drastic pressure changes, etc).

1. Is the purge on in either boxes? Turn it off!
2. Turn off the catalyst before continuing troubleshooting.
3. Check the nitrogen tank to make sure it is not empty. Change out the tank if it is. See tank replacement instructions.
4. Check for leaks around the antechamber doors and gloves. Check both boxes as they are linked to the same nitrogen tank.

E.4.3 Nitrogen pressure is too high (drastic pressure changes, ballooning gloves, etc.)

1. Turn off the catalyst bed.
2. Check the regulator that is connected to the nitrogen tank. If the needle has spun 360 degrees and is on the wrong side of the pin, the pressure in the box is very high. Using the foot pedal and lowering the pressure maximum on the display screen, lower the pressure of the box.

3. Isolate the boxes from the nitrogen line and vent the copper tubing to bring the regulator pressure back down.
4. Document this incident and tell someone.

E.4.4 Strange gurgling noises and it's distracting me!

1. Check if the vacuum pumps are the cause. If the vacuum pump that is used for evaporating solvents in the box is the problem, there is likely a loose seal somewhere. Readjust the vacuum "suckers" if they are in use. Check the valves connecting to these "suckers" as well.
2. If the pumps are not the problem, find an inorganic person to help locate the source of the ruckus.

E.4.5 Problems with the gloves

1. Holes in the gloves are inevitable. Please repair small holes with the bicycle patches on the outside of the glove. These are located above the lights. For large holes or old gloves, replace with new glove. See glove replacement instructions.
2. If gloves pop off and the pressure is dropping, attempt to replace the displaced glove or cover the glove opening with the glove port located on the ceiling of the glovebox. Replace new gloves, if necessary. See glove replacement instructions

Appendix F Mössbauer Guidelines

F.1. Parts and Pieces

F.1.1 *Sample rod*

Sample rod must not be bended and kept straight at all time by either placing it straight in the chamber or hang straight at the holder bolted to the wall. Even at 0.5° bend will result in sample rod hitting the inner wall of the sample chamber and it will prevent vibrational isolation which is the principle of Mössbauer. Twisting the crown of the rod also strain the wire and can result in it breaking. Once the wire break, it is best to send the sample rod back to SEE Co., although the electrical shop can do simple fixing too.

F.1.1.1. Temperature probe wire

These are thermocouples with 4-color wire. Each pin on the B-side represent each wire. If the temperature reading became ??? when the sample rod is in the chamber, then the coating of the wires came off and short the circuit. Manny (Electrical shop) had covered the weak spot to prevent further shortage. See below for Tom's message.

You will need an ohm-meter to test the temperature sensor on the sample insert. The sensor is a Lakeshore Model DT670 silicon diode. The connections to the 10 pin connector are specified in the Janis manual for the cryostat. The pins on the ten pin connector on the sample insert are label with letters, A - K (I think "I" is omitted). The diode temperature sensor is connected via four wires: Pin A and Pin B are connected to the "+" side of the diode Pin C and Pin D are connected to the "-" side of the diode. The sensor lead wires are small and each has a resistance of approx. 5 to 10 ohms. If you measure with your ohm meter from A to B you should get 10 to 20 ohms. Same for C to D, 10 to 20 ohms. Resistance from any of A, B, C or D to sample rod or Heater should be several mega ohms at least. (Be careful not to touch the metal probes with your fingers when you make this measurement.) The resistance from A to C should be different from C to A because of the one way conductance of the diode. The Heater is connected to the last two pins, H and K (?). The heater resistance is 50 ohms, approx. The resistance between the heater and any of the diode connections and to the sample insert rod should be at least several mega ohms. Let me know the results. The most common problem is a broken wire between the ten pin connector and the diode. Inspect the full length of the wires carefully. Pay close attention to the connections on the back of the 10 pin connector. Excessive rotation of the sample rod will break the wires at that point.

F.1.1.2. Heater wire

Also connect to the pins on the crown of the sample rod H and K. The wire can break pretty easily so be careful when thawing the sample rod.

F.1.2. *Cryostat Chamber*

Should be kept straight up at all time. It is bolted on the top of the floating table and connect to the base plate that connect to the liquid He refrigerator. There is a knob that serves as a valve for the turbo pump to evacuate the cooling chamber. The height of the chamber has to be at the correct height for the gamma rays to pass through mylar windows. Use the ruler to measure exactly 202 cm from under the table to the seam under the metal bellow. The height should be measured when the chamber is not in vacuum. If it is too low (measure lower than 202 cm), put more air into the air pads. If it is too high (measure higher than 202 cm), release some more air out.

F.1.3.2. Mylar window

Mylar window seals well at a temperature below 150 K. At lower temperature, the chamber can be left at slight static vacuum. If your sample is air-sensitive, the chamber should be placed under dynamic vacuum above 150 K.

F.1.3. *Floating Table*

F.1.3.1. Rubber air patches

Air patches for the floating table should be around 2.5 inches. The top of the patches should be somewhat flat. It can be obtained from McMaster Carr part number 62075K22 Inflatable Vibration-Damping Mount, High-Deflection, 1/2"-13 Thread, 300 lb. Maximum Static Cap.

F.1.3.2. Metal bellow

Metal bellow should be straight if the cryostat chamber is straight.

F.1.4. *Liquid He Refrigerator*

Make sure the pressure reading is at least 1.5 of He in the unit. Otherwise refill is necessary. Water should be on while operating the refrigerator at the rate of 3.5L/min. to cool down the system. If the water flow is not high enough then the refrigerator will automatically shut down.

F.1.5. *Turbo Pump*

The pump should be able to lower the pressure to 10^{-3} very fast. If it doesn't, then it is likely a leak. You can take apart the connection, clean the o-ring and put them back together. Make sure that none of the connector or o-rings are placed directly on the ground as dust can really make it dirty or scratched. Vacuum grease can be lightly applied on the o-rings for better vacuum. If suspect that the pump is broken, the pump can be changed out for testing. Antonio at the CHEX-ray facility has a pump that has the same adapter and can be used to check whether the gauge or the pump is broken.

F.1.6. *Temperature Controller: W106*

Ch. 1 is the sample rod temperature

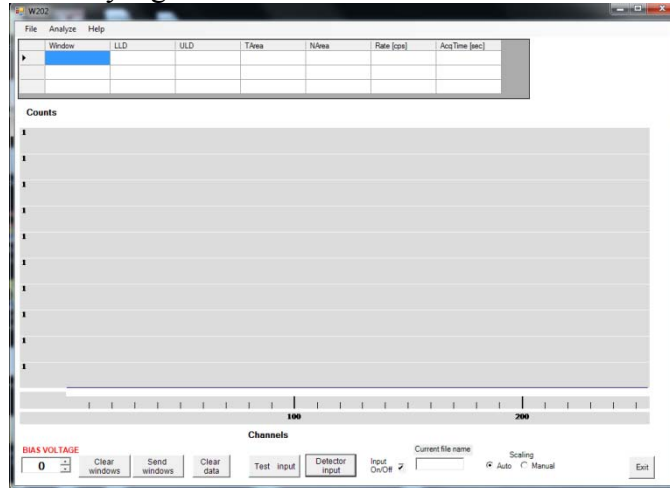
Ch. 2 is the cold head temperature

If the refrigerator is turned on, it will automatically cool to 5 K unless the heater is on and the temperature is set higher than 5 K. To set the temperature, hit 'menu' and keep pressing until Ch. 1 temperature showed up. It can be changed by pressing the number pad and press 'ok'. Repeat the same step with Ch. 2.

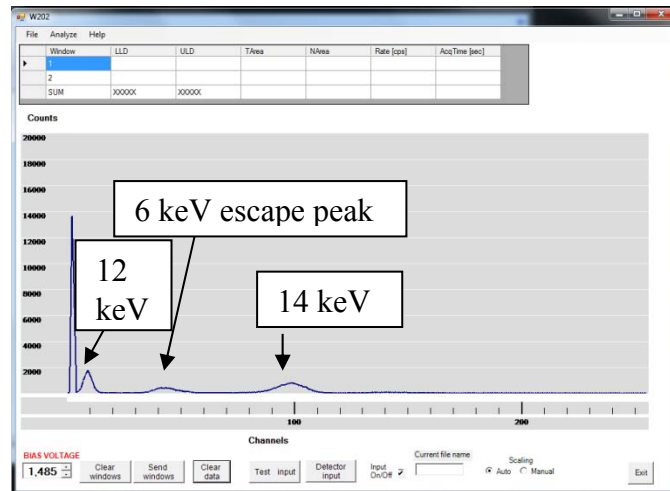
If temperature reading not accurate, i.e. reading 273K at room temperature, re-load the temperature calibration table by selection from the menu in the temperature controller box. The most accurate is DT670K which displays temperature in Kelvin and DT670C which displays T in C. Both of them use the same generic DT670 Curve.

F.1.7. Detector Controller: W202

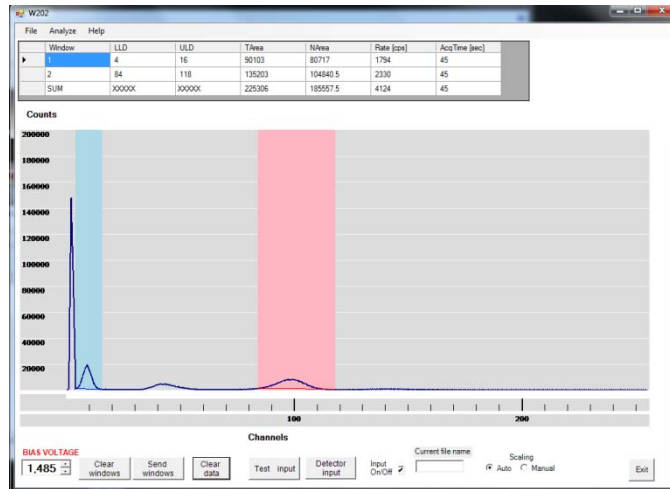
This control the energy range detected for the detector. Turning the instrument on requires adjusting the right energy range for the detector. Before setting any voltage, the instrument should not have any signal.



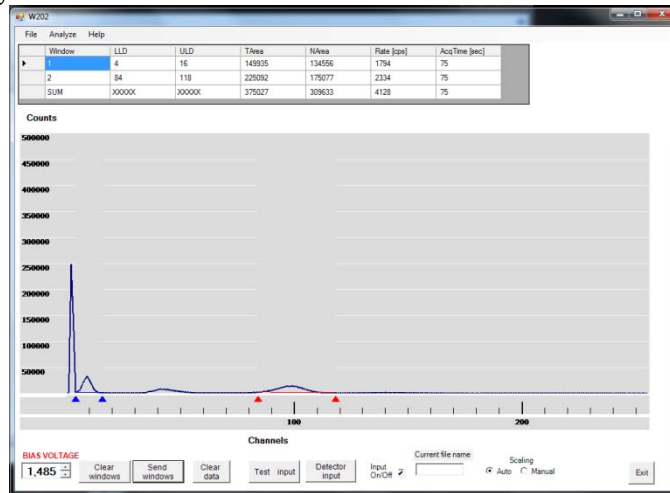
Bias voltage needs to be set for the detector to recognize the right energy range. The bias voltage should be adjusted so that the 14 keV bump is around 100 as shown in the picture. Always clear data after adjusting the bias voltage as the display shows the sum of signal over a period of time.



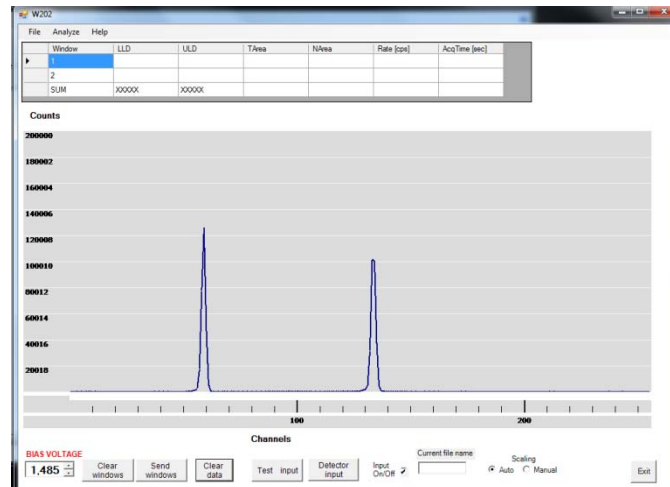
Select energy window by highlighting 12keV and 14 keV peak. The graphic is a little bit slow to respond.



After acquiring the desired energy window, click on 'send windows'. Now W302 will record the right energy window.

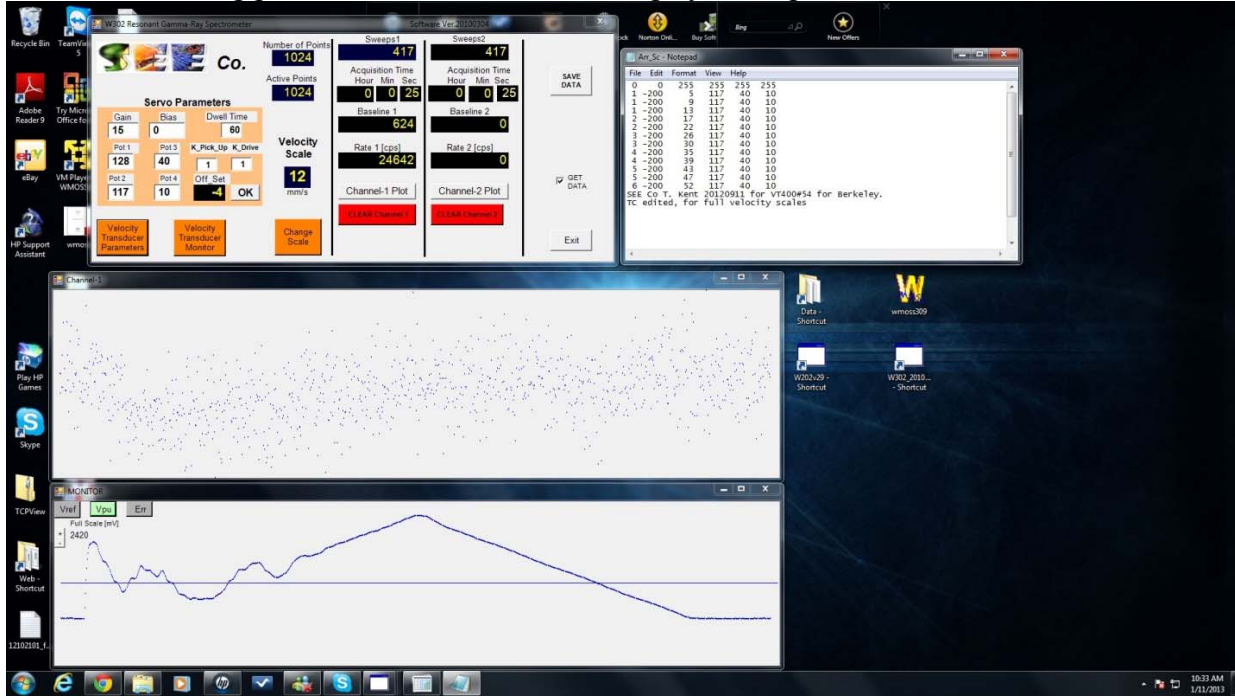


To check whether W202 is working properly, a test input can be used to check. Test input signal should look like the picture below. Make sure to clear signal before getting new detector inputs.



F.1.8. Controller for Co-57 source and data collection: W302

W302 receives energy window from W202 and also control velocity scale and detection. For V0-12, parameters are recorded in Arr_sc.txt. To change velocity scale, click 'change scale', change to the right scale and click 'ok.' Click on 'channel 1 plot' to see the spectra collected. Click on 'velocity transducer monitor' to check the error of the non-linearity of motor. Vref will always be a triangular shape. Vpu is the velocity of the motor. Err is the difference between Vref and Vpu. Err is higher at the end of the window and the middle. The rest of the error should fit in the -37mV window. Otherwise there is something really wrong. The picture shown below is when there is a big problem with the motor causing by servo parameters.



Software

The software is the part of the package. Before every experiment, W202 should be set to get the correct energy range.

F.2. How to align the instruments *See the blueprint from See Co. for dimensions and sizes.*

1. To align the floating table, the sample rod and the clamp at the bottom of the bellow must be removed.
2. Cryostat must be vertical
3. Air pads should have height 2.5". Pump air in using bicycle air pump until the distant from underneath the table to the seam should be 202 mm (+/- 1mm) which can be measured using pre-cut ruler in the tool box. Move table by nudging bottom of air pads to be centered on lower shelf semi-circle. Move each air only a couple of mm each time. Make sure that the gap of the semi-circle should be 0.5 inch which is the same size as the SEE Co. pen diameter.

4. Table must be level. Air can be removed from the air pad slowly while the levels on tops are checked repeatedly. Once the table is roughly level, the lead brick can be used to fine tune the alignment.
5. Adjust relative height of cryostat and table. (Hopefully, this is not necessary: the leveling screws on the base can be used to do this. If larger adjustment is required, change weight on table. Keep cryostat vertical and table level.)
6. Check alignment by looking at metal bellows and at sample chamber tube (must be concentric with inner tube of crown).

F.3. How to do iron metal calibration

After the instrument is well-aligned by eyes, iron calibration should be done. An α -Fe foil (thickness 25-27 μm) should come with the source (new source, new Fe foil) and it can be used to do calibration. The foil should be removed from ring and then taped to avoid surface oxidation. In general a good alignment should give a line width (peak width at half maximum of Lorentzian peak) less than 0.25 mm/s. If it is more than this number then the alignment should be conducted again until the number gets below 0.25 mm/s. The calibration should be done at room temperature with both ccr (He refrigerator) on and off. If the velocity is changed then it should be re-calibrated.

F.4. How to expand velocity scale and How to set up higher velocity data collection

Three parameters need to be changed to achieve different velocity scale, especially those higher than 12 mm/s. Click on “Velocity Transducer Parameters” and many boxes and number should appear. G represents the velocity scales divided by 2. The ratio of P1/P2 will govern the step size.

The desired step size for each velocity scale can be calculated from this equation

$$dV = (V \times 2) / 512$$

dV is step size, V is velocity scale, and there is 512 channel after folding. Current step size can be determined from iron calibration. If the step size is too small (either missing some part of the data or need higher velocity), increase P1 to increase P1/P2 ratio. For example, if 10% of the velocity scale is missing, P1 should be increased by 10%. Iron calibration should be done ****every time**** to verify the correct step size.

At a velocity higher than 12, it is better to decrease P2 to increase the ratio of P1/P2 instead. Here are the numbers for high velocity scale that has been set in the past. Always do iron calibrations should be done to check that the parameters yield correct step size.

V (mm/s)	G	P1	P2
12	6	52	117
16	8	26	44
30	15	51	46
40	20	65	44

*P3 = 40 and P4 =10

F.5. General Guidelines for data collection

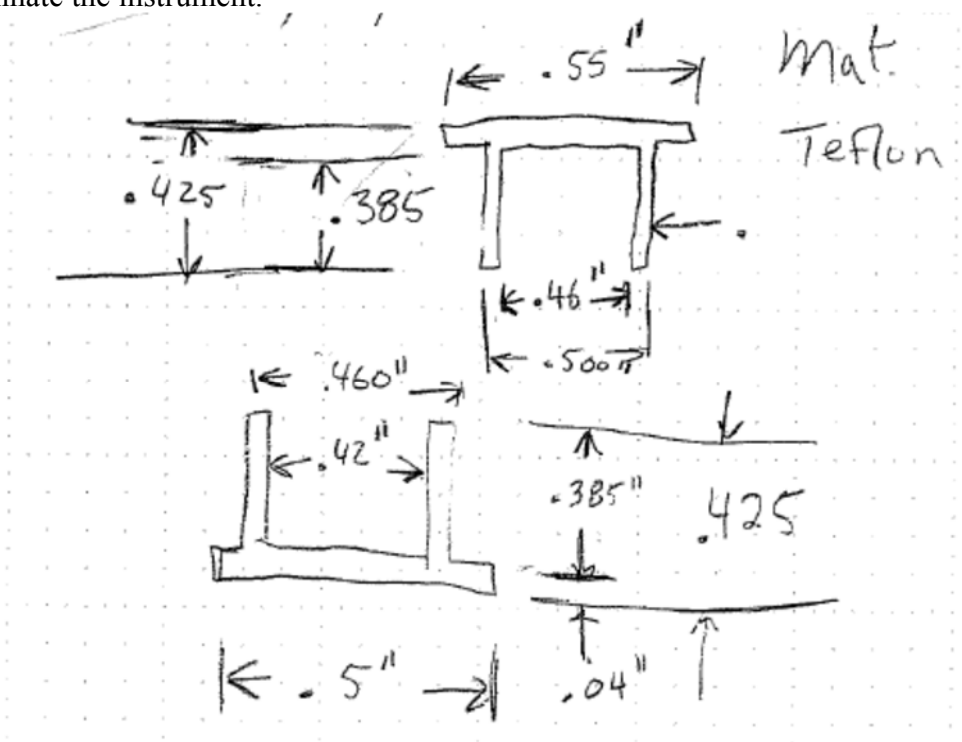
1. For a strong source: 10 mg of Fe in 1cm^3 will take 4 hours to collect data
2. Before data collection: error signal should fit into the window at -37
3. Low temperature samples take shorter time to collect data

F.6. How to prepare solid sample

Black Nylon washer (Ace Hardware) should be placed on a piece of Kapton tape. Sample mixed with BN should be loaded in the cavity. Wrap the tape around to secure the powder inside. Kapton tape can be obtained from VWR. If the sample is air-sensitive, the sample can be prepared in the glovebox and then transferred into a chamber of Ar while transporting or dropped into a bath of LN₂. If the sample react or decompose in the presence of the adhesive on the tape, place a small piece of Teflon tape to prevent direct contact and use Kapton tape to wrap the sample normally.

F.7. How to prepare frozen solution sample

Sample holder drawing is below. The full size sample holder (shown below) will hold 0.8 ml of liquid. The half-thickness holds 0.4 ml and might take less time to collect sample. The sample should be frozen in LN₂ before placing into the sample holder and it should fit snugly in the holder. Make sure the temperature in the sample chamber is below melting point of your solution before putting the sample in or taking it out to avoid sample thawing which could contaminate the instrument.



F.8. How to work up the data

F.8.1. Iron calibration

Collect both ccr on and off data at a room temperature (use heater for ccr on collection). Use WMoss_XP_v4c to get the parameters. The program is in WEB folder on the desktop. Change the directory to C:\Data before File-> Data Load. The program will ask for a filename. After loading the data normally in ASCII no header format (4), enter point in spectrum which is 1024.

Then hit 'y' for fold data

'n' to interchange first and second half of data

'n' to use previous calibration (unless you have saved calibration results)

'n' to remove linear or parabolic baseline

Choose 'Iron cal' option

'y' to use these lines for fittings of first half and second half (the lines can be manually picked as well, then select 'n' for this question)

'n' to add mask

The program will then show velocity linearity, make sure it is within 1% for both halves. The first half should be an upward curve and the second half should be a downward curve. Then all the number should appear. Make sure write fold point, V_0 and dV down as they will disappear later. When the parameter window appears, put in the fold point, V_0 and dV from the calibration.

Add mask to the spectra so that only the innermost doublet appears and fit those to get linewidth. If linewidth is higher than 0.25 mm/s, the instrument should be re-aligned.

F.8.2. *Sample spectra*

Similar to iron calibration, the data are loaded the same way. Instead of selecting 'Iron cal', pick 'manual fold' option instead. The program will ask for fold point, V_0 and dV . Enter the parameters from the latest Fe cal with the same ccr condition as your data collection.

Doublet: Use parameter file qp1v.pi

Sextet: Use parameter file hq.spi or V16.pi.

more on the software and different parameter files in WMOSS manual.

F.9. Experimental write-up for Mössbauer experiments

F.9.1. *Frozen Solution sample*

Mössbauer Spectroscopy. Zero-field, ^{57}Fe Mössbauer spectra were recorded in constant acceleration spectrometer (See Co. Edina, MN) between room temperature and 5 K in a Janis Research Co. cryostat (Willmington, MA). Collected spectra were analyzed using the WMOSS software package (See Co. Edina, MN). Isomer shifts are reported relative to α -iron (27 μm foil) at room temperature. Samples were prepared by freezing solution in a Teflon sample holder (thickness 0.2 inch) under an inert atmosphere. Sample holder was placed snugly in the sample rod holder and wrapped in Kapton® tape prior to introduction into the spectrometer in air.

F.9.2. *Solid sample*

Mössbauer Spectroscopy. Zero-field, ^{57}Fe Mössbauer spectra were recorded in constant acceleration spectrometer (See Co. Edina, MN) between room temperature and 5 K in a Janis Research Co. cryostat (Willmington, MA). Collected spectra were analyzed using the WMOSS software package (See Co. Edina, MN). Isomer shifts are reported relative to α -iron (27 μm foil) at room temperature. Samples were prepared by mixing Boron Nitride (BN) with finely ground crystalline samples of Fe complexes. Powder mixture was placed in nylon washer wrapped in Kapton® tape under inert atmosphere prior to introduction into the spectrometer in air.

How to Change the Source

F.10. Source Installation

EH&S must be contacted prior to any work on the lead enclosure, including source removal/replacement. The following procedure was written by Tom at See Co:

VT400 Velocity Transducer:

Installation and Removal of Ritverc Gamma Source in a Type 5 Holder Installation or removal of the gamma source on the SEE Co Model VT400 Velocity transducer requires removal of the primary source shield. In keeping with the As Low as Reasonably Achievable (ALARA) principle, the time the source is unshielded should be kept to a minimum and the distance from the source to the user should be maximized. With planning the source can be unshielded for less than 15 seconds. The time with the user's fingers are near the source can be as little as two seconds. Leak tests should be done on a regular schedule, e.g. biannually, to ensure the integrity of the sealed source.

F.10.1. Required items for source installation:

1. VT400 with source shield removed,
2. Gamma source stored in Pb pig,
3. Forceps with tips that fit into M4 female threaded hole.
4. 7/16 inch Hex Nut driver or similar tool,
5. Screwdriver (or Allen wrench) for 3-16 screws on VT400 source shield.

F.10.2. Source Removal Procedure

1. All required items should be at hand.
 2. Turn off the spectrometer electronics and remove the cable from the VT400.
 3. Place the VT400 in the vertical position on the workbench and place the lid of the Pb pig over the shield aperture.
 4. Remove the three 3-16 screws.
 5. Keeping the VT400 and source at arms length, remove the source shield.
 6. Place the 7/16 nut driver over the source and unscrew the source. If the source slips when the nut driver is turned try tilting the nut driver slightly.
 7. Using the forceps remove the source from the nut driver and place the source in the Pb pig. Grip the source by placing one tip of the forceps into the threaded hole in the source holder body. Be careful. Dropping the source will increase your exposure time and possibly damage the source.
 8. Place the lid on the Pb pig.
 9. Store in secure place.
- Survey the area to confirm no active material has leaked from source.

F.10.3. Installation Procedure

1. Place the VT400 in the vertical position on workbench and remove the source shield.
2. Keeping the source at arms length, remove the source from the Pb pig using the forceps. Grip the source by placing one tip of the forceps into the threaded hole in the source holder body. Be careful. Dropping the source will increase your exposure time and possibly damage the source.
3. Insert the source into the 7/16 nut driver.

4. Using the nut driver screw the source onto the VT400 motor drive shaft. Turn clockwise until the source slips in the driver.
5. Ensure the source is snug by quickly gripping the bottom of the source with your thumb and forefinger and giving the source a quick clockwise twist. Gripping the source at the bottom keeps the body of the Titanium holder between your finger and the active foil on the face of the source.
6. Place the source shield over the source and align the holes in the source shield base with the treaded 6-32 holes in the VT400 body.
7. Place the lid of the Pb pig over the source shield opening.
8. Secure the shield to the VT400 motor with the three 6-32 screws.
9. Place the VT400 in position, connect the control cable, and put any secondary shielding in place.

The entire installation procedure requires less than one minute. Survey the area around the spectrometer with a calibrated meter to confirm dose rates are acceptable.

F.11. Contacts

Thomas Kent, president of See Co, tkent@seeco.us,

Tel: 1-952-426-3678

Fax: 1-612-395-5558

Address: SEE Co. 5255 Edina Industrial Blvd. Edina, MN 55439 USA

---The sample rod, 202, 303, and Wmoss software are designed by Tom. We bought everything from him as a package deal though.

Compressor repairs: Aya Skica, askica@shicryogenics.com

Cryostat repairs: Dan Logan, dlogan@janis.com

Turbopump repairs: Andrea Tzannos, Andrea.TZANNOS@adixen-usa.com

EH&S: Jason Smith, tguncle@berkeley.edu, (510) 643-8529 direct (510) 643-7595 fax

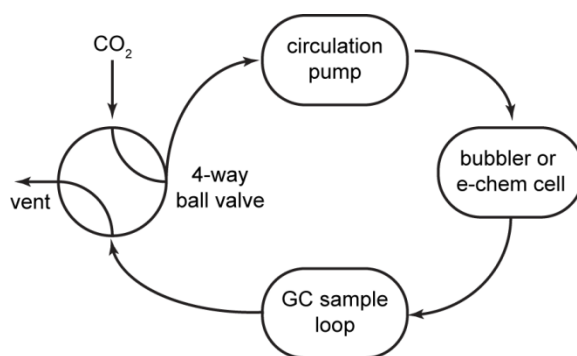
Appendix G Photolysis Setup

G.1. Parts and Pieces

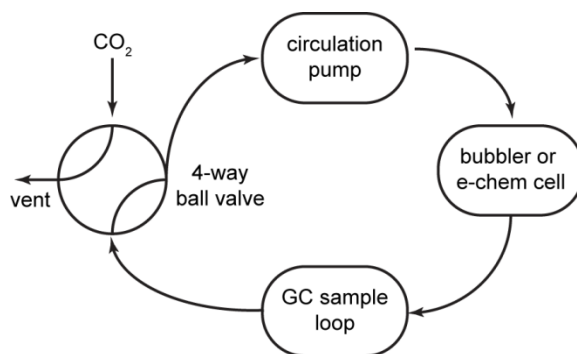
G.1.1. Circulation loop

1. CO₂ flow from a cylinder, the flow can be controlled by a mass flow controller (Omega)
2. 4-way ball valve (Swagelok part # SS43YFS2) fits to 1/8 inch tubing
3. Circulation pump (ADI part # B121-AP-AA1, Electrical shop designed the enclosure with the quick-connect inlet/outlet)
4. Bubbler for photochemical reaction (fits to Swagelok ultra torr with 1/4 inch, SS-4-UT=6-400 , change the o-ring frequently as those tends to swell and not seal well) or electrochemical cell (fit with quick-connect)
5. GC sample loop (quick-connect)

To sparge the cell, turn the valve so that CO₂ is going through the whole loop and vent out



The valve can be turned 90° to close the loop. At this point the circulation pump should be turned on to circulate the gas through the loop. CO₂ source should be turned off to not wasting the gas.



Swagelok quick-connect bodies and stems are used to connect each part as it is easily disconnected and reconnected. (Part numbers in parentheses are just an example; there are so many types of quick-connects).

G.1.2. Quick-connect Bodies

There are 2 types, normal body with o-ring (SS-QM2-B-200) and full-flow body without o-ring to seal (SS-QM2-B-200MB). Normal body will also shut-off when not connected to any stem. Full-flow body will always be opened. The o-ring in normal body will swell, causing clogging in the system. This will make the pump stops and the GC reading too high as the pump cannot circulate. Full-flow body can be used to avoid this problem.

G.1.3. *Quick-connect Stems*

There are also two types of quick-connect stems: one with shut-off valve when not connected (SS-QM2-D-100) and one without shut-off valve (SS-QM2-S-100). The shut-off valve stem cannot be used with the full-flow body but the one without the shut-off valve can be used with either type of body.

G.1.4. *Light Source*

Solar simulator from Newport (Oriel Corporation) can be used. Item number 66477 with filter holder # 71260 and filter 1.5 AM # 81094. The power of the lamp can be adjusted by moving the lamp away or closer to the photochemical cell or by adjusting the power at the light source box.

G.1.5. *Contact for Oriel Lamps*

Roger Milson, Sales Engineer, Newport Corporation
Oriel Instruments 150 Long Beach Blvd Stratford CT 06615
Direct # 203.380.4227, Mobile # 203.913.4717, Main #'s 800.714.5393, 203.377.8282,
Fax # 203.378.2457
Email: roger.milson@newport.com

Appendix H. Variable Temperature UV-visible Spectroscopy with Unisoku Cryostat Setup

H.1. UV-vis Spectrometer with Unisoku cryostat

Temperature ranges: -80°C to 100°C

H.2. How to operate

H.2.1. Cooling

Flow house N₂ through the unisoku unit to avoid the condensation. Set the temperature controller to a desired temperature. Pour LN₂ into the reservoir, the LN₂ will flow in to cool the unisoku unit. Turn on the defroster to prevent condensation and only turn on the heater when the desired temperature is nearly reached to speed up the cooling down process. After the temperature is stable, the measurements can start.

Once the measurement is done, warm the unit up to room temperature using the heater. Make sure to empty out the LN₂ reservoir before turning everything off.

H.2.2. Heating

Flow house N₂ through the unisoku unit to avoid the condensation and to help stabilizing the temperature. The unit gets slightly heated by itself when the stirring is on. If you are not heating beyond 45°C, only defroster needs to be turned on and LN₂ can also be used to adjust the temperature when needed. Monitor the temperature closely and make sure it is stabilized before starting the measurements.

To turn off the system, let the unit cool down by turning all the heater/defroster off and let the house N₂ flow until it reaches room temperature.

Each Unisoku unit comes with a tool box with colorful handles. We currently have 2 unisoku; one that fits Cary 50 and the other one fits Agilent 8453. The unisoku should be aligned really well so that the beam of light is not blocked. To align the unit, turn on the align function so that you can see the visible light beam and project the light onto a blank sheet of paper. Move the unit until maximum amount of light projected on the paper and tightly screwed it down the platform.